UNITED NATIONS EDUCATIONAL, SCIENTIFIC AND CULTURAL ORGANIZATION
INTERNATIONAL ATOMIC ENERGY AGENCY
INTERNATIONAL CENTRE FOR THEORETICAL PHYSICS
I.C.T.P., P.O. BOX 586, 34100 TRIESTE, ITALY, CABLE: CENTRATOM TRIESTE

SMR.998c - 6

Research Workshop on Condensed Matter Physics
30 June - 22 August 1997
MINIWORKSHOP ON
PATTERN FORMATION AND SPATIO-TEMPORAL CHAOS
28 JULY - 8 AUGUST 1997

"Control of patterns in reaction-diffusion systems"

A.S. MIKHAILOV
Fritz-Haber-Institut der
Max-Planck-Gesellschaft
Faradayweg 4-6
Dahlem
D-14195 Berlin
GERMANY

These are preliminary lecture notes, intended only for distribution to participants.

Physica A, Physica B, Physica C and Physica D are published by Elsevier Science B.V., Amsterdam

Subscription data

Physica A (ISSN 0378-4371). For 1994, volumes 201–211 are scheduled for publication. Physica A is published semimonthly.
Physica B (ISSN 0921-4526). For 1994, volumes 192–202 are scheduled for publication. Physica B is published monthly.
Physica C (ISSN 0921-4534). For 1994, volumes 219–236 are scheduled for publication. Physica C is published two to three times per month.
Physica D (ISSN 0167-2789). For 1994, volumes 70–78 are scheduled for publication. Physica D is published semimonthly.
Subscription prices are available upon request from the publisher.
A combined subscription to Physica A, Physica B, Physica C and Physica D is available at a reduced rate.

Subscriptions are accepted on a prepaid basis only and are entered on a calendar year basis. Issues are sent by surface mail except to the following countries where air delivery via SAL is ensured: Argentina, Australia, Brazil, Canada, China, Hong Kong, India, Israel, Japan, Malaysia, Mexico, New Zealand, Pakistan, Singapore, South Africa, South Korea, Taiwan, Thailand, USA. For all other countries airmail rates are available upon request.
Please address all your requests regarding orders and subscription queries to: Elsevier Science B.V., Journal Department, P.O. Box 211, 1000 AE Amsterdam, The Netherlands. Telephone: +31-20-5803642, Telefax: +31-20-5803598. Claims for issues not received should be made within six months of our publication (mailing) date.

US mailing notice – Physica D (ISSN 0167-2789) is published semimonthly by Elsevier Science B.V., Molenwerf 1, P.O. Box 211, 1000 AE Amsterdam, The Netherlands. The annual subscription price in the USA is US$ 2048 (valid in North, Central and South America only), including air speed delivery. Second class postage paid at Jamaica, NY 11431. USA POSTMASTERS: Send address changes to Physica D, Publications Expediting, Inc., 200 Meacham Avenue, Elmont, NY 11003. Airfreight and mailing in the USA by Publication Expediting.

Printed in The Netherlands

Physica D 70 (1994) 1–39
North-Holland

SSDI 0167-2789(93)E0257-C

Review article

Complex dynamics of spiral waves and motion of curves

A.S. Mikhailov[a,b], V.A. Davydov[c] and V.S. Zykov[d,e]

[a] *Department of Physical Chemistry, Fritz Haber Institute of the Max Planck Society, Faradayweg 4–6, 14195 Berlin (Dahlem), Germany*
[b] *N.N. Semenov Institute for Chemical Physics, Russian Academy of Sciences, ul. Kosygina 4, 117334 Moscow, Russian Federation*
[c] *Department of Physics, MIREA, ul. Vernadskogo 78, 117454 Moscow, Russian Federation*
[d] *Institute for Molecular Physiology of the Max Planck Society, Rheinlanddamm 201, 4600 Dortmund 1, Germany*
[e] *Institute of Control Sciences, Russian Academy of Sciences, 117342 Moscow, Russian Federation*

Received 26 April 1993
Accepted 21 June 1993
Communicated by A.V. Holden

In this review paper we consider spiral waves in weakly excitable media where they can be described using a sim kinematical model. The model is formulated in terms of the motion of curves with free ends. These curves can grow contract while moving over a plane. A steadily rotating spiral is a dynamical attractor of such a system. Application spatial gradients or temporal modulation of the medium's properties induce drift of spirals. When interactions between curves are taken into account, this results in appearance of complex meandering regimes.

1. Introduction

Rotating spiral waves have been observed in a variety of chemical and biological excitable media (most remarkably, in the Belousov–Zhabotinskii reagent) and became a subject of intensive theoretical studies [1–8]. In the present paper we consider spiral waves in weakly excitable media. The weakly excitable kinetics is typical for the aging Belousov–Zhabotinskii reagent [9,10] and has been recently found in the surface reactions of the catalytic CO oxidation [11]. In the Winfree classification [5] it corresponds to the vicinity of the existence boundary ∂R of spiral waves in the parameter space.

The spiral waves in weakly excitable media are sparse: their pitch is much larger than the length of the recovery tail left by a propagating excitation pulse (such spirals were first found in numerical simulations [7,11]). They can be tained by breaking a continuous wave and producing a free tip. The tip then slowly gr until a steady regime is established in whic rotates along a large circle representing a cor the spiral wave. Generally, wave patterns weakly excitable media can be viewed as con ing of individual independently propaga fronts followed by a narrow excitation zone a short recovery tail. At a lower resolution, patterns may be pictured as a set of orie curves which perform motion in the plane. principal dynamical properties of these patt can be understood using simple kinema models formulated in terms of motion of curves with free ends.

Mathematical models dealing with motio

curves and surfaces are employed in various problems, ranging from growth of crystals [12,13] to flame propagation [14] and biological pattern formation [15,16]. Recently, this class of models has attracted new attention after a discovery [17,18] of their relationship to some completely integrable equations of nonlinear waves.

A kinematical model formulated in terms of motion of the curves has been first proposed for description of the process in excitable media in 1946 by N. Wiener and A. Rosenblueth [19]. They assumed that each small segment of an oriented curve moves in its normal direction with the same constant velocity. It was shown in [19] that such a curve rotating around an obstacle forms a spiral which represents an involute of this obstacle and approaches an Archimedian spiral far from it.

The subsequent analysis of wave propagation based on partial differential equations of excitable reaction–diffusion systems has revealed [20,21] that the propagation velocity of excitation waves actually depends on their local curvature and that a wave can even break when a certain maximal curvature is reached. The curvature dependence was incorporated into a kinematical model and used to determine the properties of steadily rotating spiral waves in [7,20].

A propagating excitation is followed in excitable media by a recovery tail. When the distance between two waves moving in the same direction is shorter than the length of such a tail the waves interact. In the Wiener–Rosenblueth (WR) model [19] it was assumed that an abrupt complete recovery occurs after a fixed time interval (the refractory time): a second wave cannot propagate through a given region of the medium until the time elapsed after the passage of the first wave exceeds the refractory time of the medium.

Investigations of wave propagation in realistic excitable reaction–diffusion systems (see, e.g., [6–8]) show that recovery represents rather a gradual process. The second wave may run into the tail left by the first one but then it moves with a smaller velocity. When periodic wave propagation is considered this gives rise to a dependence of the propagation velocity on the time period of a wave train which specifies a dispersion law for the wave propagation in a particular excitable medium. The dispersion laws have been calculated for a number of different reaction–diffusion systems [7,8,22–24].

The dispersion effects become important for spiral waves when their rotation period is comparable to the characteristic refractory time of the medium (or, more correctly speaking, when the propagation velocity of the waves separated by such a period becomes significantly different from the propagation velocity of a solitary wave). This happens when spiral waves are no longer sparse, i.e. the conditions of weakly excitable media are violated (the rotation period of spiral waves diverges near their existence boundary ∂R in the parameter space and hence can be indefinitely large in the media with sufficiently weak excitabilities). For the steadily rotating spirals, the combined effects of the dispersion and the curvature dependence of the propagation velocity were studied in detail by Keener and Tyson [4,25–27].

In their pioneering paper [19] Wiener and Rosenblueth considered only pinned spirals which rotated around an obstacle. The subsequent numerical simulations and experiments with chemical and biological excitable media have revealed however that the same systems may support free spirals, not associated with any material defects or impurities. A steadily rotating free spiral looks very similar to a pinned one: its tip moves around a circular core which plays the role of an effective obstacle. In essence, theoretical methods developed in [4,22–28] treat steady free spirals as if they were pinned by an appropriate obstacle; the radius of this circular obstacle is either considered as an *a priori* phenomenological parameter or is determined using stability arguments.

But free spirals do not always perform such fixed steady rotation. It has been known since some time (see, e.g., [7]) that there are parameter regions where a non-steady circulation develops with a tip moving along a complex trajectory in the plane. The systematic studies [5,29–34] of meandering regimes have shown that they are typical when sufficiently strong interactions between the coils of a spiral wave are present. The meandering boundary, denoted as ∂M in [5], usually lies not far from the boundary ∂R in the parameter space where the free spiral waves first appear.

Moreover, it has been found in the experiments and the numerical simulations that even steadily rotating free spirals can be destabilized and forced to perform motions through the medium by application of appropriate spatial gradients [35–39], by temporal modulation of the medium's properties [36,40], in the vicinity of the medium's borders [41,42] or in the presence of external fields [43]. Spiral waves, rotating in the opposite directions, can form stable pairs which slowly drift along the symmetry axis [41,44]. If steady rotation of a single spiral is stable it represents only an asymptotic regime which is established after a certain transient stage during which a broken wave curls into a spiral. To describe all these phenomena one should go beyond the approximations treating free spirals as being effectively pinned.

A consistent theoretical study of all these phenomena of complex dynamics of spiral waves requires an explicit analysis of the process taking place at a free tip of the spiral. From a mathematical viewpoint, this problem is similar to that encountered in the description of the dendrite crystal growth. It was suggested in [45] to consider *two* curves which specify the front and the back of the excited zone and should come into contact at a certain point in the tip region. Recently, a significant progress in the solution of this problem has been achieved [46,47]. However, the analysis relies on the particular properties of concrete models.

The absence of a complete solution of a free tip problem may be of less importance when weakly excitable media are considered. The boundary ∂R in the parameter space, in the vicinity of which such systems are located, is defined by a condition that a medium supports a solution representing a flat broken wave which steadily propagates in its normal direction without either sprouting or contraction of the free tip. The existence of such solutions was shown numerically in [48] (see fig. 1) and recently analytically demonstrated in [49]. Assuming that such a solution is known, one can take it as a basis for developing a singular perturbation theory (see [50] and the Appendix A to the present paper) which would describe motion of broken waves close to the boundary ∂R, i.e., in the weakly excitable media.

When a spiral wave is sparse it can be described at a low resolution by a *single* curve, not distinguishing the front and the back of the excited zone (note that in the WR model [19] the entire excitation zone was also pictured by

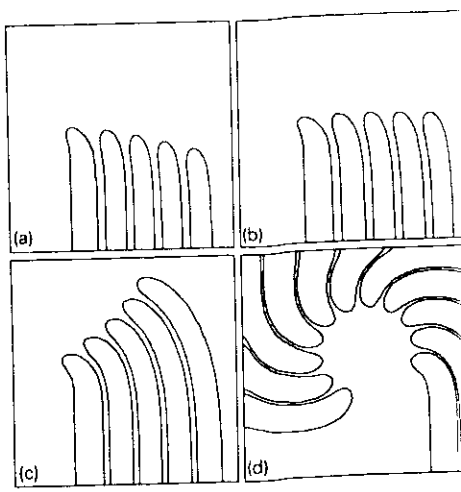

Fig. 1. Evolution of a broken excitation wave in a reaction-diffusion model of an excitable medium (from [48]). Contours of the constant activator concentration are shown at subsequent time moments for four different (a)–(d) excitabilities of the medium.

single curve). Then the free tip is represented by the end point of such a curve. To define motion of an entire curve with a free end, one additionally needs a law of sprouting (or contraction) at its end point.

A model [51] for the motion of a broken curve assumed that the end point always grows at a constant velocity. This assumption which adequately describes the first stage of formation of a spiral wave from a flat broken wave is however deficient in that it does not allow to describe a transition to the final regime of steady rotation of a spiral wave.

The geometrical properties of the curve may influence not only the normal propagation velocities of its small segments (as usually assumed), but also the growth velocity of its free end. Suppose we have two broken curves: the first which is flat and the second which has the form of an arc of a certain radius. Since the normal propagation velocity depends on the local curvature, the elements of the second curve move somewhat slower in their normal directions. But then, would it not be natural to expect that the tangential velocity of growth of the free end is also influenced by the curvature and is smaller for the second curve?

These arguments motivated us to propose in 1986 a phenomenological model [52] for motion of the curves with free ends. In this model which was later examined in detail in [8,53–56] we suggested that the normal propagation velocity V of the curve and the tangential velocity G of its free end depend linearly on the local curvatures:

$$V = V_0 - Dk\,, \tag{1.1}$$

$$G = G_0 - \gamma k_0 \tag{1.2}$$

where D and γ are some positive coefficients. The local curvature k_0 which appears in the second of these equations should be understood as a limit of the arc's curvature when the end point is approached. In this model the structure of the excitation zone is not spatially resolved and all this zone is represented by a single oriented curve, the end point of which is the free tip of the wave. According to (1.2), the growth velocity G of the tip decreases for higher curvatures k_0 and changes its sign (so that sprouting is replaced by contraction) at a certain critical curvature $k_c = G_0/\gamma$. It is this critical curvature which sets at the free end of a steadily rotating spiral.

In this review paper we show that a model employing eqs. (1.1) and (1.2) could describe simple steady rotation as well as more complex dynamical regimes of spiral waves in weakly excitable media. In section 2 we derive basic equations of the curve's motion which are used in the subsequent analysis. In section 3 we consider the Wiener–Rosenblueth limit obtained when the curvature dependence of the normal propagation velocity is neglected. We construct a complete analytical solution in this limit and show that it gives rise to a singularity: the curvature becomes infinite near the end point of a curve. It means that in this region the curvature dependence of the propagation velocity should be taken into account. Using such dependence, we derive in section 4 a solution for a steadily rotating spiral wave and analyze its stability in respect to small perturbations. The analysis reveals that only perturbations originating close to the free end of the curve are able to influence the motion of the end point. This result is further used in section 5 to construct a quasi-steady approximation which allows to determine the trajectory of motion of the end point by solving a separate system of several ordinary differential equations.

In the following sections these theoretical methods are applied to investigate particular problems of the spiral wave dynamics. In section 6 we consider behaviour of spiral waves in the presence of a periodic modulation of the medium's excitability. We show that a resonance effect is observed when the modulation frequency coincides with the own frequency of the spiral wave. In the same section we consider drift of spiral waves in media with spatial gradients.

The next section deals with a problem of motion of a spiral wave in the proximity of a boundary of the medium. A closely related effect also discussed in this section is formation of a bound state of a pair of counter-rotating spirals.

In section 8 we go beyond the approximation of a weakly excitable medium and take into account interactions between the curves caused by the presence of the refractory tails. Our analysis holds for such reaction–diffusion systems where the width of an excitation pulse is much shorter than that of the refractory tail. In this case the entire excitation zone could be approximately represented by a single curve. The moving curve is followed by an extended recovery zone where the effective excitability of the medium is significantly reduced. Thus a propagating curve creates spatial gradients in the medium. We show that such self-induced inhomogeneity indeed leads to an instability of steady rotation of spiral waves. By numerical integration of the equations of motion of the curves we demonstrate that this instability results in the emergence of various meandering regimes characterized by a rosette-like motion of the tip.

In the final section we discuss several other problems involving application of the kinematical models and formulate the conclusions. In Appendix A we show that the phenomenological model of motion of curves could be justified by a singular perturbation analysis of the broken waves in weakly excitable media. In Appendix B we provide a different derivation of the equations of motion valid for the waves on curved surfaces.

2. Motion of curves with free ends

Propagation of waves in a weakly excitable two-dimensional medium can be described by a simple phenomenological model. In this model a wave is represented by a single smooth oriented curve. Each small element of the curve moves in its normal direction with the velocity given by (1.1). When the curve has a free end, it smoothly grows or contracts with the tangential velocity (1.2).

This definition allows us to construct a curve at any later time moment if its initial form is known. To investigate the general properties of the curve's motion described by this model we must derive the respective equation which describes evolution of the curve in the process of its motion. To specify an arbitrary curve on a plane we use its *natural equation* $k = k(l, t)$ which gives curvature k of the curve as a function of its arc length l measured from a certain fixed point on it. The advantage of this description is its invariance in respect to any translations and rotations of the curve in the plane: all curves that differ only by a shift or a rotation are described by the same natural equation. Note that the arc length l provides thus an internal coordinate of the points on a curve.

Let us consider a curve at a certain time. Suppose that its curvature at point a is equal to k_a. After a short time interval dt a neighbourhood of point a is transferred due to the motion of the curve into a neighbourhood of another point b.

To calculate curvature k_b at the new point we introduce a local polar coordinate system (r, α) with the origin in the center of curvature of point a (i.e., in the center of a circle of radius $r_a = 1/k_a$ that touches the curve at point a). In the neighbourhood of point a, the curve is then given by a certain function $r = r(\alpha, t)$ the derivatives $dr/d\alpha$ and $d^2r/d\alpha^2$ of which vanish at a. In the same coordinate system, the form of the curve near point b at time $t + dt$ is given by

$$r(\alpha, t + dt) = r(\alpha, t) + V(\alpha)\, dt\,, \tag{2.}$$

where $V(\alpha)$ is the local velocity of motion in the normal direction.

When the form of a curve in the polar coordinates is known its local curvature can be determined as

$$k = (r^2 - 2r'^2 - rr'')(r^2 + r'^2)^{-3/2}\,, \tag{2.}$$

where a prime denotes differentiation with respect to angle α. Substituting (2.1) into (2.2) we obtain, to within terms of order dt,

$$k_b = k_a - \left(Vk_a^2 + k_a^2 \frac{\partial^2 V}{\partial \alpha^2}\right) dt . \tag{2.3}$$

Transforming to differentiation with respect to the arc length l ($dl = r_a\, d\alpha = d\alpha/k_a$) in (2.3), we obtain

$$k_b - k_a = dk = -\left(k_a^2 V + \frac{\partial^2 V}{\partial l^2}\right) dt . \tag{2.4}$$

Note that although both points b and a correspond to the same local polar angle α they have different internal coordinates l on the curve. The difference is caused by two factors. First, any increase in the curvature radius leads to local stretching of the curve. Second, when the arc lengths l are measured from the end point of a curve the growth of the curve results in an additional shift of all internal coordinates l. Due to these two effects, the internal coordinate l of point b at time $t + dt$ has an increment

$$dl = \left(\int_0^l kV\, d\xi\right) dt + G\, dt . \tag{2.5}$$

Therefore we get

$$dk = \left(\frac{\partial k}{\partial l}\right) dl + \left(\frac{\partial k}{\partial t}\right) dt . \tag{2.6}$$

Substituting this into (2.4) and using (2.5), one obtains

$$\frac{\partial k}{\partial t} + \left(\int_0^l kV\, d\xi + G\right) \frac{\partial k}{\partial l} = -k^2 V - \frac{\partial^2 V}{\partial l^2} . \tag{2.7}$$

This general equation of motion of curves has been independently derived in problems of wave propagation in excitable media [52–54,57] and of the dendridic growth of crystals [13]. Recently it has also attracted attention as a generator of different completely integrable equations of nonlinear waves [18].

In our model the normal propagation velocity V depends on the coordinate l only because $V = V_0 - Dk$ and k depends on l. Therefore, $\partial^2 V/\partial l^2 = -D\, \partial^2 k/\partial l^2$. Moreover, we consider only the curves with so small curvatures that $Dk \ll V_0$. Then one can approximately replace V by V_0 in all other terms in (2.7). This finally yields an evolution equation

$$\frac{\partial k}{\partial t} + \left(\int_0^l kV_0\, d\xi + G\right) \frac{\partial k}{\partial l} = -k^2 V_0 + D \frac{\partial^2 k}{\partial l^2} . \tag{2.8}$$

This equation should be supplemented by an initial condition and two boundary conditions. First we consider the boundary condition at a free end of the curve.

Without a short time interval δt the curve grows by $G\, \delta t$. It means that a new element of the curve appears. We assume that the curve grows *smoothly*, i.e., that the curvature in the newly formed element is given by a smooth extrapolation from the old part of the curve. Therefore, the curvature at the new tip position is

$$k(\delta l) = k(0) + \delta l \frac{\partial k(0)}{\partial l} + \cdots . \tag{2.9}$$

Note that we measure the arc length l from the free end of the curve and hence the positive values of l refer to the points that belong to the older part of the curve while the internal coordinates l for the new element of the curve are negative. Since the tip grows by $G\, \delta t$ within time δt, its new curvature $k_0(t + \delta t)$ is given by (2.9) for $\delta l = -G\, \delta t$. Dividing both parts of (2.9) by δt and taking limit $\delta t \to 0$ we obtain

$$\frac{dk_0}{dt} = -G \left(\frac{\partial k}{\partial l}\right)_{l=0} . \tag{2.10}$$

It can be verified that the same equation holds when the curve shrinks, i.e., if the tangential velocity G is negative. Equation (2.10) gives us a boundary condition at the free end[*1].

If the curve has two free ends then a similar boundary condition should be applied at the opposite end, i.e., at $l = L(t)$ where $L(t)$ is the total length of the curve at time moment t. It reads as

$$\frac{d\tilde{k}_0}{dt} = \tilde{G} \left(\frac{\partial k}{\partial l}\right)_{l = L(t)} . \tag{2.11}$$

Here $\tilde{k}_0$ is the curvature at the opposite end and $\tilde{G}$ is its tangential growth velocity. Note that the total length L of the curve changes with time as

$$\frac{dL}{dt} = \int_0^L kV_0\, d\xi + G + \tilde{G} . \tag{2.12}$$

One can also consider an infinite curve with a free end. If the curve asymptotically flattens far away the free end the second boundary condition is $k \to 0$ as $l \to \infty$.

A solution of (2.8) yields dependence $k = k(l, t)$ which determines the form of the curve but does not fix its position on the plane. To completely define the curve, one should additionally indicate absolute Cartesian coordinates $X_0(t)$ and $Y_0(t)$ of its end point and the angle $\alpha_0(t)$ between the tangent to the curve at the end point and the x-axis. It is also necessary to specify the initial orientation of the curve which determines the direction of rotation (clockwise or counterclockwise).

In the case of the counterclockwise rotation the motion of the free end of the curve is described by equations

$$\dot{X}_0 = -V_0 \sin \alpha_0 - G \cos \alpha_0 , \tag{2.13}$$

[*1] Although the arguments leading to the condition (2.10) look plausible, they do not constitute its rigorous derivation. Therefore, this boundary condition is rather postulated in our phenomenological model of the curve's motion. The situation is similar to that encountered in the theory of the crystal growth where additional selection conditions at the growing tip should be provided [58].

$$\dot{Y}_0 = V_0 \cos \alpha_0 - G \sin \alpha_0 , \tag{2.14}$$

$$\dot{\alpha}_0 = \left(\frac{\partial V}{\partial l}\right)_{l=0} + Gk_0 . \tag{2.15}$$

The last equation gives the rate of change of the angle α_0, i.e., the angular rotation velocity of the free end. Since $V = V_0 - Dk$ we have $\partial V/\partial l = -D\, \partial k/\partial l$ and therefore

$$\dot{\alpha}_0 = -D \left(\frac{\partial k}{\partial l}\right)_{l=0} + Gk_0 . \tag{2.16}$$

For a spiral that rotates in the clockwise direction, eqs. (2.13)–(2.16) are replaced by

$$X_0 = V_0 \sin \alpha_0 - G \cos \alpha_0 , \tag{2.13a}$$

$$Y_0 = -V_0 \cos \alpha_0 - G \sin \alpha_0 , \tag{2.14a}$$

$$\dot{\alpha}_0 = D \left(\frac{\partial k}{\partial l}\right)_{l=0} - Gk_0 . \tag{2.16a}$$

When one end of the wave moves along a boundary of the medium and this boundary is impermeable (so that there is no diffusion of the reacting substances through it), the wave is orthogonal to the boundary. Hence, the tangential component of the curve's velocity at this end of the curve is absent. The motion of the end point along the boundary obeys thus eqs. (2.13), (2.14) and (2.16) where we should put $G = 0$. Note that in this case the trajectory of motion is known, since it represents simply the boundary of the medium. The end point moves along it with linear velocity V. The angular velocity $\dot{\alpha}_0$ of the end point can be determined in this case in the following way.

Suppose that K is the local curvature of the boundary at a given point. By a definition of curvature, it is $K = d\phi/d\lambda$ where ϕ is the angle between the tangent to the boundary and the x-axis and λ is the length of the boundary curve. Since the end of the wave is orthogonal to the boundary, $\phi = \alpha_0 + \frac{1}{2}\pi$. Moreover, since the end point of the curve moves along this boundary with velocity V, we have $dl = V\, dt$. Hence, $d\alpha_0/dt = VK(t)$. Substituting this into (2.16) with

$G = 0$, we obtain the boundary condition for the end of a curve moving along a boundary

$$\left(\frac{\partial k}{\partial l}\right)_0 = -\frac{V}{D} K(t) . \tag{2.17}$$

Here $K(t)$ is the curvature of the boundary at a point which is being passed by the end of the curve at time t. This curvature is positive if the boundary is convex and negative if it is concave. Note that $V = V_0 - Dk_0$ in this equation. If the boundary is a straight line, this boundary condition reduces to $(\partial k/\partial l)_0 = 0$.

When a solution of eqs. (2.8), (2.13), (2.14) and (2.16) is known, the Cartesian coordinates of the curve points can be found as

$$X(l, t) = X_0(t) + \int_0^l \cos(\alpha_0 \pm \alpha)\, d\xi , \tag{2.18}$$

$$Y(l, t) = Y_0(t) + \int_0^l \sin(\alpha_0 \pm \alpha)\, d\xi , \tag{2.19}$$

where

$$\alpha(l, t) = \int_0^l k(\xi, t)\, d\xi . \tag{2.20}$$

Signs "+" and "−" in these equations should be taken if the free end rotates in the clockwise direction and the counterclockwise directions, respectively.

Figures 2a,b shows results of numerical integration of the kinematical equation (2.8) with boundary condition (2.10) and associated equations (2.13), (2.14) and (2.16). The initial conditions represented a flat curve with a small perturbation near its free end; different initial perturbations are taken in Figs. 2a and 2b. Independent of the initial conditions, the curve evolves to a steadily rotating spiral with the same form and rotation period. In section 4 an analytical solution for a steadily rotating spiral will be derived and stability of such solution will be investigated. Before this we examine, however,

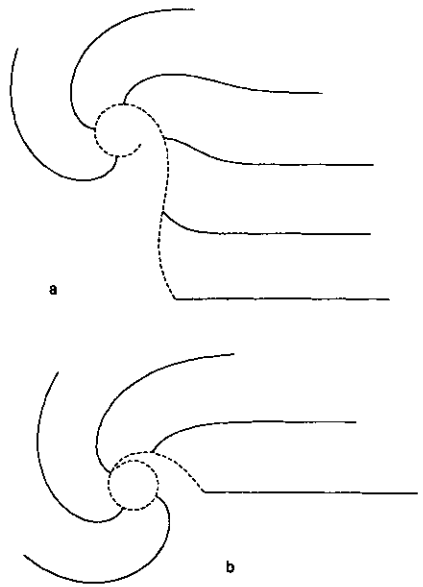

Fig. 2. Formation of a steadily rotating spiral from an initial flat curve with two different perturbations (a), (b) near its free end ($V_0 = 1.5$, $G_0 = 0.96$, $D = 1.0$, $\gamma = 1.5$).

motion of the curves in a special Wiener–Rosenblueth limit.

3. The Wiener–Rosenblueth limit

In the Wiener–Rosenblueth (WR) model the normal propagation velocity V is taken to be independent of the local curvature k. This corresponds to the limit $D \to 0$ in the kinematical equation (2.8). Since D is a coefficient at the highest (i.e. the second) derivative in (2.8), appearance of singularities could be expected in this limit.

Let us write eq. (2.8) in a slightly different but equivalent form so that it looks like a continuity equation for the variable k:

$$\frac{\partial k}{\partial t} + \frac{\partial J}{\partial l} = D \frac{\partial^2 k}{\partial l^2} , \tag{3.1}$$

where

$$J = k\left(\int_0^l kV_0\, d\xi + G\right) . \tag{3.2}$$

Substituting $k = \partial\alpha/\partial l$ into (3.1) and integrating over l, we obtain

$$\frac{\partial \alpha}{\partial t} + (\alpha V_0 + G)\frac{\partial \alpha}{\partial l} = K \frac{\partial^2 \alpha}{\partial l^2} + \omega(t) . \tag{3.3}$$

Here $\omega(t)$ is an integration constant which has the meaning of the momentary rotation velocity of the free end. Indeed, since $\alpha = 0$ at $l = 0$, eqs. (3.7) and (2.16) yield

$$\omega(t) = G\left(\frac{\partial \alpha}{\partial l}\right)_0 - D\left(\frac{\partial^2 \alpha}{\partial l^2}\right)_0 = Gk_0 - D\left(\frac{\partial k}{\partial l}\right)_0 = \dot{\alpha}_0 . \tag{3.4}$$

The WR limit is obtained if we neglect the term with the second derivative in (3.3), which then reduces to

$$\frac{\partial \alpha}{\partial t} + (\alpha V_0 + G)\frac{\partial \alpha}{\partial l} = \omega . \tag{3.5}$$

This nonlinear differential equation is completely integrable. Its general solution is constructed using the notion of characteristics. A characteristic of (3.5) is a curve in the plane (l, t) that satisfies the equation

$$\frac{dl}{dt} = \alpha V_0 + G . \tag{3.6}$$

As it follows from (3.5), the angle variable α changes along the characteristic as

$$\frac{d\alpha}{dt} = \omega . \tag{3.7}$$

Let us consider properties of characteristics of eq. (3.5) in the quarter $l \geq 0$ and $t \geq 0$ of the plane (l, t). It is useful to distinguish two different families of these characteristics which originate from the l- and t-axes, respectively. The first family of characteristics is generated by the elements of the curve which were already present at the initial moment $t = 0$. The second family corresponds to the new elements which have appeared at $t > 0$ due to growth of the curve at its free end. If a characteristic terminates at the t-axis, it means that the respective curve element has disappeared due to contraction of the curve.

According to the general theory of partial differential equations, the initial value of α on each characteristic at the point of its origination should be specified. Thus, for the characteristics belonging to the first family the initial condition at $t = 0$ should be indicated:

$$\alpha(l, t = 0) = f(l) \quad \text{for } 0 \leq l \leq \infty . \tag{3.8a}$$

The characteristics belonging to the second family originate at different time moments η from the t axis and, since $\alpha \equiv 0$ at $l = 0$, their initial conditions are

$$\alpha(l = 0, t = \eta) = 0 \quad \text{for } \eta > 0 . \tag{3.8b}$$

We first construct an explicit solution along the characteristics which belong to the second family. Integration of (3.6) and (3.7) yields in this case

$$l(\eta, t) = \int_\eta^t G(t_1)\, dt_1 + V_0 \int_\eta^t dt_1 \int_\eta^{t_1} dt_2\, \omega(t_2) , \tag{3.9}$$

$$\alpha(\eta, t) = \int_\eta^t \omega(t_1)\, dt_1 . \tag{3.10}$$

The first of these two equations determines the shape of a characteristic while the second provides the dependence of α on t on it.

The respective solutions for the characteristics of the first family are

$$l(\xi, t) = \xi + V_0 f(\xi) t + l_g(t) , \tag{3.11}$$

$$\alpha(\xi, t) = f(\xi) + \alpha_g(t) , \tag{3.12}$$

where $l_\kappa(t) \equiv l(\eta = 0, t)$ and $\alpha_\kappa(t) = \alpha(\eta = 0, t)$. Note that $f(0) = 0$.

Equations (3.9)–(3.12) determine a solution if functions $f(l)$, $\omega(t)$ and $G(t)$ are given. Here $f(l)$ specifies the initial form of the curve while $\omega(t)$ and $G(t)$ are the angular and the tangential linear velocities of the free end. As seen from (3.4), we have $\omega = Gk_0$ if $D = 0$. Thus, instead of providing the angular velocity ω of the free end we may give curvature $k_0(t)$ at the free end of the curve.

Proceeding from the constructed general solution, properties of the curve's motion in the WR limit can be discussed. Note that although this solution is constructed in terms of the angle variable α, it can be easily reformulated in terms of the curvature $k = \partial\alpha/\partial l$. Let us consider how k changes along a characteristic that belongs to the first family. Since t is fixed, we can write using (3.11) and (3.12)

$$k(\xi, t) = \frac{(\partial\alpha/\partial\xi)_t}{(\partial l/\partial\xi)_t} = \frac{\mathrm{d}f/\mathrm{d}\xi}{1 + V_0 t(\mathrm{d}f/\mathrm{d}\xi)} . \tag{3.13}$$

Here $\mathrm{d}f/\mathrm{d}\xi = k(\xi, 0)$ is the initial curvature of a curve element that was located at $t = 0$ at $l = \xi$. Similarly, if a characteristic belongs to the second family we have

$$k(\eta, t) = \frac{(\partial\alpha/\partial\eta)_t}{(\partial l/\partial\eta)_t} = \frac{\omega(\eta)}{G(\eta) + V_0\omega(\eta)(t - \eta)} = \frac{k_0(\eta)}{1 + V_0 k_0(\eta)(t - \eta)} . \tag{3.14}$$

Hence, if the initial curvature of a given element of the curve was positive, it monotonously decreases in time, so that the element becomes flat asymptotically at $t \to \infty$. However, if the initial curvature of an element was negative, it increases with time and becomes infinite after a finite time interval $\Delta t(\eta) = (V_0|k_0(\eta)|)^{-1}$.

The divergence of the solution, which occurs when the curve initially has a concave segment with negative curvature, is of the same nature as formation of caustics in the geometrical optics (see [59]). The singularity can be eliminated by retaining the curvature dependence of the normal propagation velocity.

Above it was assumed that the curve has a free tip which grows (or contracts) with a certain velocity G. If we try to apply this solution to a case where the end of a curve moves along a boundary of the medium we must take into account that the curve is always orthogonal to the boundary and therefore the tangential velocity G of the end point vanishes there. Since in the WR limit it follows from (3.4) that $\omega(t) = Gk_0$, we come to a surprising and unrealistic conclusion that the angular velocity of the tip must also vanish, i.e., that the end point of the curve may move only along a straight line! Fortunately, a closer inspection of the kinematical equation (3.4) shows that even in the WR limit the curve is still able to follow any bent of the medium's boundary.

Note that in the above analysis it was assumed that the curvature k remained finite when the tip of the curve was approached. This assumption was completely justified in the situations where the tangential velocity G was present (indeed, if k goes to infinity while G is nonvanishing, the angular velocity ω diverges). However, it should be reconsidered if $G = 0$. In this case eq. (3.5) yields

$$\frac{\omega}{V_0} = \lim_{l \to 0} \alpha\left(\frac{\partial\alpha}{\partial l}\right) \tag{3.15}$$

Note that $\alpha = 0$ at $l = 0$. We see that if curvature $k = \partial\alpha/\partial l$ becomes infinite at $l = 0$, the limit in (3.15) may still exist and, thus, the curve's tip may move with a nonvanishing angular velocity even if the tangential component of its velocity vanishes.

The solution for a curve whose tip moves along a boundary of the medium is obtained if we put $G = 0$ in eqs. (3.9)–(3.12). Despite the absence of growth, it still has two different families of characteristics. The characteristics which belong to the second family originate from the boundary, i.e., from the axis $l = 0$. In the vicinity of the boundary, i.e., for $t \to \eta$, they have the form

$$l(\eta, t) = \tfrac{1}{2} V_0\omega(t)(t - \eta)^2 . \tag{3.16}$$

Note that these characteristics *touch* the l-axis at the origination point, i.e., $\partial l/\partial t = 0$ at $t = \eta$. The angle α changes along such a characteristic as

$$\alpha(\eta, t) = \omega(t)(t - \eta) . \tag{3.17}$$

Eliminating $(t - \eta)$ from (3.16) and (3.17) we find for $l \to 0$

$$\alpha(l, t) = \left(\frac{2\omega(t) l}{V_0}\right)^{1/2} . \tag{3.18}$$

Curvature k near the tip can be found by differentiation (3.18) with respect to l which yields

$$k(l, t) = \left(\frac{\omega(t)}{2V_0 l}\right)^{1/2} . \tag{3.19}$$

It goes to infinity when l approaches zero. We conclude that *any curved boundary gives rise to a singularity of the solution in the WR limit.*

An important special case is a curve that rotates around a circular obstacle in the medium. In this case the rotation velocity is constant and equal to $\omega = V_0/R$ where R is the radius of the obstacle. Then eqs. (3.16)–(3.19) hold not only in the vicinity of the boundary but at any l. Particularly, eq. (3.19) takes the form

$$k(l) = (2Rl)^{-1/2} . \tag{3.20}$$

This functional dependence describes a curve that is an involute of the circle of radius R. When $l \gg R$, the involute approaches an Archimedian spiral with a pitch equal to $h = 2\pi R$, i.e., to the perimeter of the obstacle. This is a classical result first derived by Wiener and Rosenblueth in [19].

We see that the problem of motion of a broken curve is completely solvable in the formal limit $D \to 0$ where the normal propagation velocity V does not depend on the local curvature k. It follows from (1.1) that this approximation is applicable while the curvature k is sufficiently small so that $Dk \ll V_0$.

Our analysis of solutions obtained in the WR limit shows that the curvature actually diverges at a tip of the curve that moves without growth or contraction with a nonvanishing angular velocity. This occurs when the tip moves along a curved material boundary of the medium and, as we shall see in the next section, for freely rotating spiral waves. To eliminate such a singularity and obtain a smooth solution we must take now into account in this region the curvature dependence of the normal propagation velocity.

4. Spiral waves

In this section we derive the solutions for a spiral wave steadily rotating around a circular obstacle and for a free spiral wave and investigate their stability. It was found in the previous section following Wiener and Rosenblueth [19] that a steadily rotating spiral wave is an involute of the obstacle's boundary and approaches an Archimedian spiral far from it. However, the conditions of applicability of the WR approximation break down near the tip of a steadily rotating spiral because curvature diverges there. Therefore we return to the general equation (3.3) of motion of the curves which retains the curvature dependence $V = V_0 - Dk$ of the normal propagation velocity.

A curve that steadily rotates around an obstacle of radius R is described by the equation

$$D\frac{\mathrm{d}^2\alpha}{\mathrm{d}l^2} + \omega = \alpha V_0 \frac{\mathrm{d}\alpha}{\mathrm{d}l} , \tag{4.1}$$

which we obtain from (3.3) by putting $\partial\alpha/\partial t = 0$ and $G = 0$ there. We seek a solution of (4.1) that satisfies the boundary conditions

$$\alpha = 0 \quad \text{at } l = 0 , \qquad \frac{\mathrm{d}\alpha}{\mathrm{d}l} \to 0 \quad \text{as } l \to \infty . \tag{4.2}$$

Note that the angular velocity is related to the radius of the obstacle as $\omega = V/R$.

Let us introduce new variables q and s as

$$\alpha = \left(\frac{Dk_0}{V_0}\right)^{1/2} q\,, \quad l = \left(\frac{D}{k_0 V_0}\right)^{1/2} s\,, \tag{4.3}$$

where k_0 is a (yet unknown) curvature at $l = 0$. In the new variables eq. (4.2) takes the form

$$\frac{d^2q}{ds^2} + \zeta = q\frac{dq}{ds}\,, \tag{4.4}$$

where

$$\zeta = \omega(DV_0k_0^3)^{-1/2} \tag{4.5}$$

is a coefficient that remains indefinite since we do not know the value of k_0. We look for a solution of (4.4) that satisfies the conditions $q(0) = 0$, $dq(0)/ds = 1$, $dq/ds \to 0$ as $s \to \infty$. Note that since (4.4) is a differential equation of the second order these *three* boundary conditions can be simultaneously satisfied only for a certain value of the coefficient ζ in (4.4). In other words, they set a nonlinear eigenvalue problem for this equation.

Although (4.4) cannot be solved analytically it can be easily numerically integrated. Figure 3 shows the derivative $\psi(s) = dq_0/ds$ of the solution $q_0(s)$ that satisfies the above mentioned three boundary conditions; it corresponds to $\zeta = 0.685\ldots$. The dashed line in fig. 3 shows the respective dependence $\psi_\infty(s) = (\zeta/2s)^{1/2}$ which is found in the WR limit, by neglecting the term with the second derivative in (4.4). We see that the two functions are very close for $s \gg 1$. However, the WR function diverges at $s = 0$ whereas $\psi_0(s)$ approaches 1 at $s = 0$.

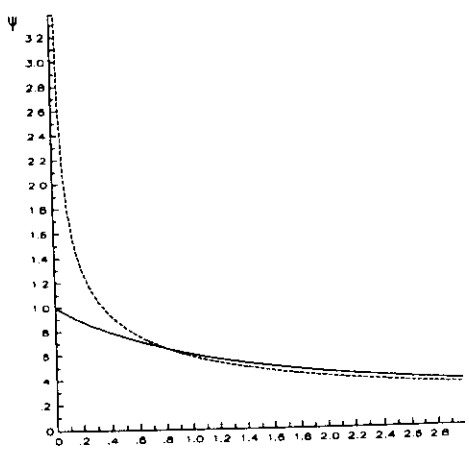

Fig. 3. Functions $\psi(s)$ and $\psi_\infty(s)$.

Since the coefficient ζ is known we can now inverse (4.5) to determine curvature k_0 at the boundary of the obstacle.

$$k_0 = \left(\frac{V_0}{\zeta^2 DR^2}\right)^{1/3}. \tag{4.6}$$

Thus, the solution for a spiral that rotates around a circular obstacle is

$$k(l) = k_0\psi(l/l_0)\,, \tag{4.7}$$

where the computed universal function $\psi(s)$ is shown in fig. 3 and the characteristic length l_0 is given by

$$l_0 = \left(\frac{D}{k_0V_0}\right)^{1/2}. \tag{4.8}$$

The form of the spiral differs from the Wiener–Rosenblueth involute given by $k_0\psi_\infty(l/l_0)$ only within a distance about l_0 from the boundary of the obstacle.

In the above derivation we have used only the fact that the tangential velocity G of the tip vanishes when it moves along a boundary of the obstacle. But this velocity can vanish, under certain circumstances, for a *free* tip too. According to (1.2) we have $G = G_0 - \gamma k_0$ and therefore $G = 0$ when the curvature k_0 at the free end of the curve is

$$k_c = G_0/\gamma\,. \tag{4.9}$$

It can be said that eq. (4.9) defines a *critical* curvature: when $k_0 < k_c$ the tip of the curve grows while for $k_0 > k_c$ it contracts. Note that we can write (1.2) as

$$G = \gamma(k_c - k_0)\,. \tag{4.10}$$

Since in our kinematical model we consider only slightly bent curves, such that $Dk \ll V_0$ for any element of them, the critical curvature must satisfy the same condition. Because of the relationship (4.9) this implies $G_0 \ll (\gamma/D)V_0$.

Suppose that the curvature at the free end of a curve is equal to the critical curvature k_c. Then the conditions for the curve's motion would be effectively the same as if a circular obstacle were present in the medium and the curve's tip were rotating around it. The curve represents then a spiral described by (4.7) where k_0 must be replaced by k_c. Its free tip rotates around an effective circular which may be called a *core* of the spiral wave. The core radius R_0 can be found by substituting k_c instead of k_0 in (4.6) and solving the resulting equation, which yields

$$R_0 = \left(\frac{V_0}{\zeta^2 Dk_c^3}\right)^{1/2}. \tag{4.11}$$

The rotation frequency $\omega_0 = V_0/R_0$ of a free spiral is

$$\omega_0 = \zeta(DV_0)^{1/2}k_c^{3/2}\,, \tag{4.12}$$

where the numerical factor is $\zeta = 0.685\ldots$. This solution was first derived by Zykov [7] using a different form of the kinematical equations and later independently obtained in [52,53]. Note that $\omega_0 \to 0$ and $R_0 \to \infty$ as $D \to 0$; therefore the solution for a free spiral is absent in the WR limit that was discussed in the previous section.

The form of the steadily rotating free spiral is given by the natural equation (4.7) where k_0 should be replaced by k_c. It differs from an involute of the core only within a distance l_0 from the free end, obtained by substitution of k_c instead of k_0 into (4.8). This distance is much smaller than the core radius R_0 when the conditions of applicability of the kinematical approximation are satisfied. Using (4.8) and (4.11) one finds $l_0/R_0 \sim Dk_c/V_0 \ll 1$.

The stability investigation is especially important for free spirals whose steady rotation is maintained not because of the presence of an obstacle but due to the properties of motion of a free tip. To analyze the stability of the spiral wave solution we go back to the full time-dependent kinematical equation (3.1) and use the boundary condition (2.10) at the free end. We introduce a small perturbation

$$k(l,t) = \bar{k}(l) + \delta k(l,t)\,, \tag{4.13}$$

where $\bar{k}(l)$ is the stationary solution given by (4.7) with $k_0 = k_c$ and consider its further evolution.

Since $\bar{k}(l=0) = k_c$ and $G(k_c) = 0$ the linearized boundary condition (2.10) yields

$$\frac{d\delta k_0}{dt} = \gamma\left(\frac{\partial\bar{k}}{\partial l}\right)_0 \delta k_0\,. \tag{4.14}$$

It follows from eq. (4.1) that

$$\left(\frac{\partial\bar{k}}{\partial l}\right)_0 = \left(\frac{\partial^2\alpha}{\partial l^2}\right)_0 = -\frac{\omega_0}{D}\,. \tag{4.15}$$

Therefore (4.14) can be written as

$$\frac{d\delta k_0}{dt} = -\frac{\gamma}{D}\omega_0\,\delta k_0\,. \tag{4.16}$$

Therefore the perturbations of k_0 fade away with a characteristic relaxation time

$$\tau_G = D/\gamma\omega_0\,. \tag{4.17}$$

Because of this damping of δk_0 we can further assume in our analysis that $\delta k_0 = 0$ and hence $G = 0$. Under this assumption the linearized equation (3.1) reads as

$$\frac{\partial\delta k}{\partial t} + \frac{\partial\delta J}{\partial l} = D\frac{\partial^2\delta k}{\partial l^2}\,, \tag{4.18}$$

where

$$\delta J = \left(\int_0^l \bar{k}V_0\,d\xi\right)\delta k + \bar{k}\int_0^l \delta k V_0\,d\xi \tag{4.19}$$

and the boundary conditions are $\delta k = 0$ at $l = 0$ and $\delta k \to 0$ at $l \to \infty$.

We can write eq. (4.18) in the equivalent form

$$\frac{\partial\delta k}{\partial t} + U(l)\frac{\partial\delta k}{\partial l} = F(\delta k) + D\frac{\partial^2\delta k}{\partial l^2}\,, \tag{4.20}$$

with

$$U(l) = \int_0^l \bar{k}(\xi)\, V_0\, \mathrm{d}\xi\,, \tag{4.21}$$

$$F(\delta k) = -2\bar{k}(l)\, V_0\, \delta k - \frac{\partial \bar{k}}{\partial l}\left(\int_0^l \delta k\, V_0\, \mathrm{d}\xi\right), \tag{4.22}$$

and apply general methods of the theory of quasi-linear equations [60]. In absence of the last diffusion-like term in (4.20), this equation describes propagation of a perturbation δk along the characteristics given by

$$\frac{\mathrm{d}l}{\mathrm{d}t} = U(l)\,. \tag{4.23}$$

Note that $U(l)$ is a positive monotonously increasing function of l and therefore any perturbation is driven away from the tip to the periphery of the spiral.

As was noticed above, the solution $\bar{k}(l)$ for a free spiral approaches the spiral solution in the WR limit outside of the boundary layer of the width about l_0 near the tip, i.e., $\bar{k}(l) \approx k_c(\zeta l_0/2l)^{1/2}$ for $l \gg l_0$ where $l_0 = (D/k_c V_0)^{1/2}$. In this region the characteristics of eq. (4.20) are

$$l = \tfrac{1}{2}\zeta(k_c V_0)^2 (t - t_0)^2 l_0\,, \tag{4.24}$$

where t_0 is an arbitrary constant. Thus, outside of the boundary layer perturbations move away from the core with an acceleration. On the other hand, inside the boundary layer, at $l \ll l_0$, we have approximately $\bar{k} \approx k_c$ and therefore the characteristics obey the equation

$$\frac{\mathrm{d}l}{\mathrm{d}t} = k_c V_0 l\,, \tag{4.25}$$

whose solution is

$$l = l_0 \exp[k_c V_0 (t - t_0)]\,. \tag{4.26}$$

Note that (4.26) is valid only for $l \ll l_0$, which implies $t < t_0$. According to (4.26), a perturbation originating within the boundary layer stays there for about time

$$\tau_0 = (k_c V_0)^{-1} \tag{4.27}$$

and only afterwards leaves it and is fastly driven away, as described by (4.24).

Until now we neglected the diffusion-like term in (4.20). We have found that in its absence a spiral wave solution is stable in respect to small perturbations, in a sense that all of them are eventually driven to the periphery ($l \to \infty$) and do not influence the motion of the tip. Introduction of the diffusion-like term results in an additional spreading of the perturbations. The characteristic time within which a perturbation spreads to a size about the width l_0 of the boundary layer can be estimated as $D/l_0^2 = (k_c V_0)^{-1}$. We see that it is exactly the same characteristic time τ_0 which has been defined in (4.27) and specifies the duration of stay within the boundary layer.

Hence, we find that a steadily rotating free spiral is stable in respect to small perturbations. Relaxation to the steady rotation involves two different characteristic times τ_0 and τ_G. The first of them is the time after which the stationary shape of the spiral near the tip (inside the boundary layer about l_0 from the end point) is established. The second property τ_G is the time after which curvature k_0 at the free end reaches k_c and sprouting or contraction is terminated.

It is interesting to compare these characteristic times τ_0 and τ_G with the rotation period $T_0 = 2\pi/\omega_0$ of the spiral wave. Using (4.12), we find

$$\tau_0 \omega_0 = \zeta\left(\frac{Dk_c}{V_0}\right)^{1/2} \ll 1\,. \tag{4.28}$$

Thus, the form of the spiral curve near its tip is recovered after a perturbation within a time interval which is much shorter than the rotation period T_0 of the spiral. On the other hand, eq. (4.17) yields

$$\tau_G \omega_0 = \frac{D}{\gamma}\,. \tag{4.29}$$

In the phenomenological theory, D and γ represent two independent parameters whose ratio is not restricted by any inner conditions. The analysis based on the reaction–diffusion equations, which is performed in Appendix A, allows us to express these properties (see (A.27) and (A.33)) in terms of certain eigenfunctions of the reaction–diffusion equations. Since both of them involve similar combinations of the model parameters, one can expect that generally D and γ have the same orders of magnitude. It means that sprouting (or contraction, depending on the initial condition) of the tip continues within a time which can vary from a fraction of a single rotation to a few rotations of the spiral wave.

Before proceeding to a study of more complex dynamical regimes of spiral waves which begins in the following section we consider a *hysteresis effect* [61] that clearly shows the difference between a pinned and a free spiral.

Suppose that we have a pinned spiral wave which rotates around a hole in the medium, in such a way that the tip touches the boundary of the hole. Let us start now to decrease radius R of the hole. If we do this slowly enough, the tip remains attached to the boundary and the rotation frequency increases as $\omega = V_0/R$. However, this does not continue indefinitely long: the numerical simulations [61] show that, when a certain critical radius R^* is achieved, the tip suddenly breaks away from the boundary and begins free motion through the medium. After some time, it settles to rotate around a circular core which is much larger than the hole located in its center. Now the hole could be completely removed without influencing the rotation regime.

On the other hand, we can start with a freely rotating spiral, place a very small hole in the center of its core and begin to increase its radius. In this case, the wave does not feel the presence of the hole until its tip comes into contact with the hole's boundary, which occurs when the radius of the hole is equal to the radius of the core, i.e., at $R = R_0$. After that the spiral is pinned and the rotation frequency begins to decrease in accordance with $\omega = V_0/R$, we see that in the interval $R^* < R < R_0$ the two rotation regimes are both possible, with the rotation frequency of the pinned spirals significantly larger than that of a free spiral.

To explain this effect, we notice that the conditions of the excitation propagation for a free tip and the tip which touches a boundary are different. Indeed, in the latter case the diffusional flow in the tangential direction (i.e. through the boundary) is absent and, therefore, the propagation conditions are the same as for a continuous (non-broken) excitation wave. It was shown [7,21] that, unless the diffusion constants of all reacting components are equal, a curved continuous excitation wave breaks spontaneously when its local curvature k exceeds a certain critical value k_c^* which for the weakly excitable media can be much larger than the critical curvature $k_c = G_0/\gamma$ for the free tip. Since the local curvature of a pinned spiral wave achieves its maximum at the hole boundary, the wave breaks and the free tip appears when this maximal curvature reaches the critical value k_c^*. Using (4.6) and (4.12), we find the relationship between the radius R^* of the minimal pinning hole and the core radius R_0 of a free spiral wave:

$$\frac{R^*}{R_0} = \left(\frac{k_c^*}{k_c}\right)^{3/2}. \tag{4.30}$$

It should be noted that in the early works on the kinematical theory (e.g. in [7]) the distinction between the two critical curvatures k_c^* and k_c was not understood. Use of a different critical curvature k_c for the free tip was first suggested in [52,53].

A simple estimate (4.30) is not quite correct because at $k = k_c^*$ the dependence of the normal propagation velocity on the curvature is no longer linear. The corrections were taken into account in [62] where the theoretical estimate for the radius of the minimal pinning hole was also compared with the data of numerical simulations of a reaction–diffusion model and a good quantitative agreement was found.

5. The quasi-steady approximation

The set of equations which includes the general kinematical equation (2.8) supplemented by boundary condition (2.10) and eqs. (2.13), (2.14) and (2.16) of motion of the end point describes not only a steadily rotating spiral. It can be also used to determine evolution of a curve starting from an arbitrary initial condition. Moreover, if the parameters of these equations are some functions of time and/or spatial coordinates, the same set of equations describes the behaviour of spiral waves in time-dependent or nonuniform weakly excitable media.

The description of the curve's motion can be further simplified when the conditions of the *quasi-steady approximation* are fulfilled. To formulate them, let us consider again the narrow boundary layer of width about l_0 near the free end of the propagating curve. It was shown in section 4 that outside this layer, in the external region $l \gg l_0$, the curvatures are so small that the curvature dependence of the normal propagation velocity V can be neglected and the motion of the curve can be satisfactorily described in the WR approximation. Moreover, we have seen that small perturbations, originating in this region, cannot influence the processes inside the boundary layer. When $Dk_c \ll V_0$, the width of the boundary layer is much smaller than the pitch of the spiral.

A similar situation is encountered in hydrodynamics where, in calculations of the velocity profiles, the viscosity of liquid should be taken into account only within a narrow boundary layer and the flow of liquid inside of this layer can be calculated independently. When the solution in the boundary layer is found, it can be used [63] to generate an effective boundary condition for the solutions in the external region where viscosity is neglected. In mathematical terms, it means that a variant of the singular perturbation theory is used here.

If we try to construct a solution within the boundary layer near the free tip of the curve, i.e., on the length scale about l_0 near $l = 0$, we must supply the boundary conditions at the ends of this interval. One of these conditions is natural: we require that curvature k vanishes when we enter the outer region, i.e., for all $l/l_0 \to \infty$. Another boundary condition should be placed at $l = 0$, i.e., at the free end of the curve. Generally, it is given by eq. (2.10) which implies that the curvature k_0 at the free end tends to approach the critical value k_c. Since $G = -\gamma(k_0 - k_c)$, the rate of the adjustment is determined by coefficient γ.

In the previous section we have estimated the characteristic time τ_0 within which the form of the spiral inside the boundary layer is established and the characteristic time τ_G which is required to approach the stationary value k_c of curvature at the free end of the spiral. The ratio of these two times is

$$\frac{\tau_0}{\tau_G} = \zeta \left(\frac{Dk_c}{V_0}\right)^{1/2} \frac{\gamma}{D} = \zeta \left(\frac{\gamma}{D}\right)^{1/2} \frac{G_0}{V_0}. \tag{5.1}$$

We see that if coefficient γ has the same order of magnitude as D (which can be expected for typical reaction–diffusion models) and, as it is assumed in the kinematical theory, condition $G_0 \ll V_0$ is satisfied this ratio is small. It means that sprouting (or contraction) of the curve is so slow that its form inside the boundary layer near the free end adjusts adiabatically to the momentary value of curvature k_0.

When condition $\tau_0 \ll \tau_G$ is satisfied the form of the curve in the boundary layer is the same as that of the rigidly rotating spiral with $k = k_0$ at $l = 0$. Particularly, its momentary angular velocity ω_0 is given by (4.12) and hence

$$\left(\frac{\partial k}{\partial l}\right)_{l=0} = -\frac{\omega_0}{D} = -\zeta \left(\frac{V_0}{D}\right)^{1/2} k_0^{3/2}. \tag{5.2}$$

This result can be further used to derive a closed equation for the evolution of k_0. By substituting (5.2) into (2.10) we obtain

$$\frac{dk_0}{dt} = -\gamma\zeta \left(\frac{V_0}{D}\right)^{1/2} k_0^{3/2}(k_0 - k_c). \tag{5.3}$$

When a solution of (5.3) is known, eqs. (2.15) and (4.12) can be used to determine the angular velocity of the motion of the tip:

$$\frac{d\alpha_0}{dt} = \zeta(DV_0)^{1/2} k_0^{3/2} - \gamma(k_0 - k_c)k_0. \tag{5.4}$$

The Cartesian coordinates X_0 and Y_0 of the tip obey the equations

$$\frac{dX_0}{dt} = -V_0 \sin\alpha_0 - G\cos\alpha_0, \tag{5.5}$$

$$\frac{dY_0}{dt} = V_0 \cos\alpha_0 - G\sin\alpha_0, \tag{5.6}$$

where $G = -\gamma(k_0 - k_c)$.

Hence, we see that when condition

$$\frac{G_0}{V_0} \ll \left(\frac{D}{\gamma}\right)^{1/2}, \tag{5.7}$$

holds, the trajectory of motion of the end point of a curve can be determined in the quasi-steady approximation by solving a system of ordinary differential equations (5.3)–(5.7). Note that these equations correspond to the case of the counterclockwise rotating spiral. For the spirals which rotate in the opposite clockwise direction they should be replaced by

$$\frac{d\alpha_0}{dt} = -\zeta(DV_0)^{1/2} k_0^{3/2} + \gamma(k_0 - k_c)k_0, \tag{5.4a}$$

$$\frac{dX_0}{dt} = V_0 \sin\alpha_0 - G\cos\alpha_0, \tag{5.5a}$$

$$\frac{dY_0}{dt} = -V_0 \cos\alpha_0 - G\sin\alpha_0. \tag{5.6a}$$

The form of the spiral whose tip moves along the trajectory given by (5.3)–(5.6) is approximately determined by (3.9) and (3.10) where we should substitute $\omega = \zeta(DV_0)^{1/2} k_0^{3/2}$ and $G = -\gamma(k_0 - k_c)$ with $k_0(t)$ given by a solution of (5.3).

The equations of the quasi-state approximation can be used to describe the process of formation of a steadily rotating spiral from an arbitrary broken initial curve or to consider relaxation to the steady rotation after a finite perturbation. Moreover, using this system of equations, one can easily determine the behaviour of the spiral in time-dependent or nonuniform media.

If the properties of a medium change in time and/or in space, the parameters of the kinematical model (i.e., V_0, D, γ and G_0 or $k_c = G_0/\gamma$) become certain functions of spatial coordinates and/or of time. In the quasi-steady approximation the motion of the tip is influenced only by the dependence of the properties of the medium along its trajectory. It means that the kinetical parameters in eqs. (5.3)–(5.6) would represent certain functions of X_0 and Y_0. When such functions are known, the system of these equations can be solved to determine the trajectory of motion of the tip and, hence, the behaviour of the spiral wave.

Note that the quasi-steady approximation can be applied for description of processes in time-dependent or nonuniform excitable media only if the characteristic time T and length L of variation of the medium's properties are not very small. Namely, we should require that $T \gg \tau_0$, $L \gg l_0$ and $L/V_0 \gg \tau_0$. However, these conditions are not very restrictive since τ_0 is much smaller than the rotation period of a spiral wave (cf. (4.28)) and l_0 is much smaller than the pitch of the spiral.

6. Resonance and drift of spiral waves

In this section we consider the typical behaviour of spiral waves in weakly excitable media whose properties vary in time or in space. It is assumed that variations of these properties are small enough and hence a perturbation theory could be used to determine responses of steadily rotating spiral waves to periodic temporal modulation or weak spatial gradients. Note that the solution for a steadily rotating spiral wave is invariant in respect to translations and rotations: any rotation of the spiral and any shift

of its center yield again a valid solution. Therefore, the respective components of the perturbations are not damped.

If one tries to develop a perturbation theory proceeding directly from the reaction–diffusion equations this meets with serious difficulties. They arise because translation and rotation perturbation modes for the spiral wave are not spatially localized. We bypass such difficulties by using the quasi-steady approximation formulated in the previous section. In this approximation the trajectory of the tip motion can be calculated by solving a system of ordinary differential equations which depend only on the local properties of the medium in the vicinity of the tip. The perturbations which originate outside a small neighbourhood of the end point propagate fastly to the periphery and do not influence the motion of the tip. The evolution of the entire curve can be then calculated in the WR approximation using the known trajectory of the tip motion as a dynamic boundary condition.

Although any of the four principal kinematical parameters of an excitable medium may be varied, below we consider only the effects caused by changes of the parameter G_0 which gives the tangential velocity of growth of a flat broken wave. When the kinematical theory is applicable this parameter is small and can be significantly modified even by slight changes in the local properties of a medium. In our model parameter G_0 effectively controls excitability of the medium.

We consider first a problem with uniform periodic temporal modulation of the medium's excitability

$$G_0(t) = \bar{G}_0 + G_1 \cos(\omega_1 t + \phi_1) . \tag{6.1}$$

It is assumed that the modulation amplitude is small, $G_1 \ll \bar{G}_0$, and the modulation frequency ω_1 is close to the eigenfrequency ω_0 of the spiral wave.

After putting $k_c(t) = G_0(t)/\gamma$ into eq. (5.3) of the quasi-steady approximation and linearizing this equation, one can find variations of curvature k_0 at the free end of the curve which are induced by modulation of G_0. Substitution of these variations into the linearized equation (5.4) yields a time dependence of angle α_0. The motion of the tip of the spiral wave can be then calculated from (5.5) and (5.6). We find that in the linear approximation the complex coordinate $Z_0 = X_0 + iY_0$ of the end point of the curve changes in time as

$$Z_0(t) = R_0 \exp(i\omega_0 t + i\phi_0) \pm R_1 \exp[i(\omega_0 - \omega_1)t + i(\delta + \phi_0 - \phi_1)] , \tag{6.2}$$

where $R_0 = V_0/\omega_0$ and

$$R_1 = \frac{\frac{1}{4}(G_1/\bar{G}_0)V_0}{|\omega_0 - \omega_1|[1 + (D/\gamma)^2]^{1/2}} , \tag{6.3}$$

$$\delta = -\arctan(\gamma/D) . \tag{6.4}$$

In (6.2) we should take the sign plus if $\omega_0 > \omega_1$ and the sign minus if $\omega_0 < \omega_1$. Equation (6.2) holds for a spiral wave rotating in the counterclockwise direction. For a spiral wave rotating in the opposite clockwise direction it must be replaced by

$$Z_0(t) = R_0 \exp(-i\omega_0 t - i\phi_0) \pm R_1 \exp[-i(\omega_0 - \omega_1)t - i(\delta + \phi_0 - \phi_1)] . \tag{6.2a}$$

Here we take a plus sign when $\omega_0 < \omega_1$ and a minus sign when $\omega_0 > \omega_1$.

The above results for the motion of the tip of a spiral wave induced by periodic modulation of properties of an excitable medium were first derived, in a slightly different form, in 1986 in [52] and later extensively discussed in [8,36,48,55,56]. They show that the tip performs a cycloidal motion that represents a superposition of a rotation around a circle of radius R_0 and of a circular motion with radius R_1 (hence the momentary rotation center of the spiral wave moves along a circle of this radius). The type of the cycloid depends on the relationship between the two frequencies. If $\omega_0 > \omega_1$, the center of the spiral wave moves in the direction which is opposite to the direction of its rotation (i.e. clockwise if the spiral wave rotates in the counterclockwise direction, see fig. 4a). When $\omega_0 < \omega_1$, these two rotation directions coincide (see fig. 4b).

Radius R_1 of the circular motion induced by periodic modulation is proportional to the modulation amplitude G_1. It is inversely proportional to the difference of the two frequencies and thus diverges when the condition $\omega_0 = \omega_1$ of complete resonance is reached.

Under the condition of complete resonance the rotation center of a spiral wave moves along a straight line, so that its tip performs motion described by

$$Z_0(t) = vt \exp[\pm i(\delta + \phi_0 - \phi_1)] + R_0 \exp[\pm i(\omega_0 t + \phi_0)] , \tag{6.5}$$

where the drift velocity v is given by

$$v = \frac{\frac{1}{4}V_0(G_1/\bar{G}_0)}{[1 + (D/\gamma)^2]^{1/2}} . \tag{6.6}$$

The minus sign in (6.5) should be taken for a wave rotating in the clockwise direction.

Hence, in the case of complete resonance the spiral wave drifts along a straight line. As we see from (6.5) the direction of such drift depends on the initial phase of the spiral wave ϕ_0, on the initial phase ϕ_1 of modulation and on the rotation direction of the spiral wave. Consequently, if several spiral waves are present in the medium they start to drift along different directions when the modulation is switched on.

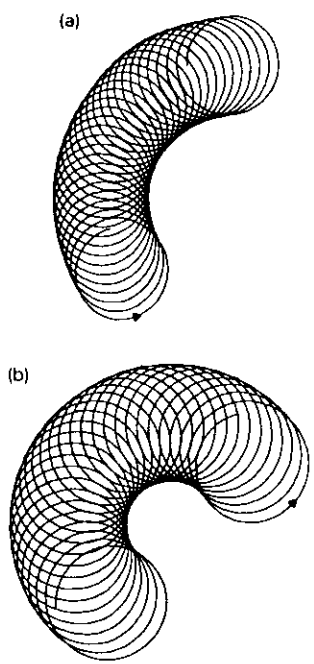

Fig. 4. Trajectories of the end point of a spiral under a periodic modulation of the medium's excitability with the frequency (a) $\omega_1 = 0.0196$ and (b) $\omega_1 = 0.202$. The rotation frequency of the spiral is $\omega_0 = 0.2$; the kinematical parameters are $V_0 = 1.0$, $G_0 = 0.15$, $D = 1.0$, $\gamma = 1.5$.

The predictions of the kinematical theory for the resonance of spiral waves were verified in [36,56] by performing a numerical simulation for a particular reaction–diffusion model. The resonance of spiral waves was first experimentally observed [40] in 1987 using the photosensitive modification of the Belousov–Zhabotinskii reaction. The annihilation of a pair of spiral waves rotating on the opposite directions after application of periodic resonant illumination was also seen in [40].

Recently resonance of a spiral wave has been observed [10,64] in a surface chemical reaction of CO oxidation. In this case, however, the modulation frequency was twice smaller than the eigenfrequency of the spiral wave. Such resonances, which occur when the condition $n\omega_1 = \omega_0$ with $n = 2, 3, \ldots$ is satisfied, are also described by the kinematical approach. They are yielded by higher-order terms of the perturbation theory which lead to products of the harmonics and thus to frequency multiplication. The magnitude of resonance (i.e. the drift velocity and the radius of cycloidal motion) are proportional to the nth

power of the modulation amplitude. Below we give without a derivation the results for the second-order resonance ($n = 2$). The motion of the tip of the spiral wave is described in this case by

$$Z_0(t) = R_0 \exp(\mathrm{i}\tilde{\omega}_0 t + \mathrm{i}\phi_0) + \frac{\nu_2 \varepsilon^2 V_0}{\tilde{\omega}_0 - 2\omega_1} \exp[\mathrm{i}(\tilde{\omega}_0 - 2\omega_1)t + \mathrm{i}(\phi_0 - 2\phi_1)] , \tag{6.7}$$

where $\varepsilon = G_1/\bar{G}_0$ and

$$\nu_2 = -\frac{(1 - \frac{3}{8}\mathrm{i})}{2(1 - \mathrm{i}D/2\gamma)^2} - \frac{(\frac{9}{8}\mathrm{i})(D/2\gamma)^2}{2(1 - \mathrm{i}D/2\gamma)^4(1 - \mathrm{i}D/\gamma)^2} . \tag{6.8}$$

In the second-order of the perturbation theory periodic modulation leads also to a nonlinear shift of the rotation frequency of spiral waves:

$$\tilde{\omega}_0 = \omega_0(1 + \varepsilon^2 \nu) , \tag{6.9}$$

$$\nu = \frac{15}{8[1 + (\omega_1 D/\omega_0 \gamma)^2]} . \tag{6.10}$$

This nonlinear shift changes the resonance frequency by an amount proportional to the square of the modulation amplitude. This quadratic effect holds also for the first-order resonance which was considered above.

Next we consider the drift of a spiral wave in a nonuniform excitable medium whose properties slowly change along a certain direction. It is again assumed that the parameter of the kinematical model which undergoes the variation is the tangential growth velocity G_0 of the flat broken wave which controls local excitability of the medium. We choose the direction of the gradient of G_0 as the x-axis and assume that the gradient is small,

$$\mathrm{grad}\, G_0 \ll \bar{G}_0/R_0 , \tag{6.11}$$

where R_0 is the core radius of the spiral wave. Hence in this case the medium becomes more excitable in the positive x-direction.

Since the gradient is weak its effect can again be calculated in the perturbation theory. In the zeroth order of the perturbation theory we have a steadily rotating spiral wave with a tip performing uniform rotation around a core of radius R_0 at an angular velocity ω_0 given by (4.12). Hence, its coordinate X_0 changes with time as

$$X_0 = R_0 \cos(\omega_0 t + \phi_0) . \tag{6.12}$$

While performing this motion the tip visits regions of the medium with different excitabilities. Because of this it effectively experiences time-dependent variation of parameter G_0 given by

$$G_0(t) = \bar{G}_0 + bX_0(t) = \bar{G}_0 + bR_0 \cos(\omega_0 t + \phi_0) , \tag{6.13}$$

where $b = \mathrm{grad}\, G_0$. It means that, for the tip, the situation is the same as in the case of periodic modulation of the medium's properties which was considered earlier in this section. Note that such nodulation occurs at exactly the same frequency as the eigenfrequency of the spiral wave and, moreover, its initial phase coincides with that of the spiral wave (i.e. $\omega_1 = \omega_0$, $\phi_1 = \phi_0$). The above analysis of the resonance of spiral waves reveals that under such circumstances the spiral wave performs drift described by (6.5). The complex coordinate $Z_0 = X_0 + \mathrm{i}Y_0$ of the wave's tip changes in time as

$$Z_0(t) = vt \exp(\pm \mathrm{i}\delta) + R_0 \exp[\pm \mathrm{i}(\omega_0 t + \phi_0)] , \tag{6.14}$$

where the drift velocity is given by (6.6) after replacement of G_1 by bR_0 and δ is given by (6.4). The plus sign should be taken for the waves rotating in the counterclockwise direction.

Thus, the center of the spiral wave slowly drifts along a straight line at angle $\pm\delta$ (plus sign refers to the counterclockwise rotating wave) to the x-axis, i.e., to the direction of the gradient of G_0. According to (6.4), δ is negative. Hence, the y-component of the drift velocity is negative for the counterclockwise rotating wave and positive for the clockwise rotating spiral wave which drift, respectively, downwards and upwards. Note that the x-components of the drift velocity are however identical (and positive) for both of these waves. It means that when the conditions of our approximations hold the spiral waves should move towards the region of higher values of G_0 which correspond to higher excitability of the medium.

The numerical simulations of spiral waves in nonuniform excitable media based on the reaction–diffusion models and the available experimental data for the Belousov–Zhabotinskii reaction show [35–38] however that the drift proceeds in some cases in the opposite direction, towards the regions with the smaller excitability. To clarify this issue we have performed an additional investigation.

We solved numerically the kinematical equation (2.8) with boundary condition (2.10) and eqs. (2.13), (2.14) and (2.16) determining the motion of the end point of the curve in presence of the gradient of G_0. We have found (fig. 5a) that the spiral wave indeed drifts in the direction of increase of G_0, i.e., towards the region with the higher excitability, while G_0 is smaller than a certain critical value which can be roughly estimated as $G^* \sim V_0(D/\gamma)^2$. At $G_0 = G^*$ the drift direction is orthogonal to the gradient of G_0, whereas for higher values $G_0 > G^*$ the drift proceeds (fig. 5b) in the direction opposite to that of the gradient, i.e., towards the region with the smaller excitability.

By looking at the condition of applicability of the quasi-steady approximation (5.7), we can notice that it is equivalent to $G_0 \ll G^*$. Hence, it is not surprising that the above effect of changing of the drift direction is not obtained in the equations derived using an approximation. When the terms proportional to small parameter $(\gamma/D)(G_0/V_0)^{1/2}$ are retained in eq. (6.4) it is replaced by

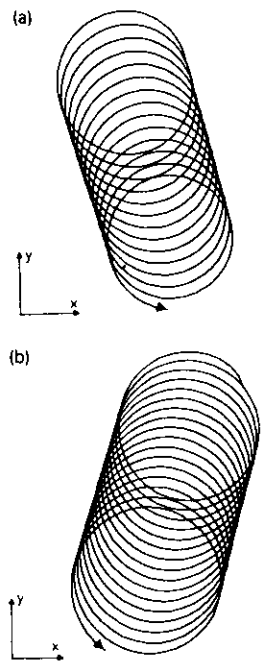

Fig. 5. Drift of spirals in the presence of an excitability gradient. Numerical integration of the kinematical equation for (a) $G_0 = 0.15$, $b = 0.0001$ and (b) $G_0 = 7.5$, $b = 0.005$; other parameters are $V_0 = 1.0$, $D = 1.0$, $\gamma = 1.5$.

$$\tan\delta = -\left[\frac{\gamma}{D} + \frac{2}{3\zeta}\left(\frac{G_0}{V_0}\right)^{1/2}\right] \times \left[1 - \frac{2}{3\zeta}\frac{\gamma}{D}\left(\frac{G_0}{V_0}\right)^{1/2} + \frac{4}{3}\left(1 + \frac{\gamma^2}{D^2}\right)\frac{G_0}{V_0}\right] \tag{6.15}$$

where $\zeta \approx 0.685\ldots$. We see that the denominator of (6.15) and, hence, $\tan\delta$ can change its sign with an increase of G_0. However this occurs when $G_0 \sim V_0(D/\gamma)^{1/2}$, i.e., outside the region of validity of the quasi-steady approximation.

The effect of the drift direction's reversal has an important experimental implication. Suppose that the excitability of a medium gradually in

creases in the positive direction of the x-axis, so that it reaches the above-defined critical value G^* at a certain coordinate $x = x^*$. Then all spiral waves located to the left from this boundary (i.e., at $x < x^*$) begin to drift towards this boundary. As they come closer to it, their drift direction is gradually rotated until the drift becomes orthogonal to the gradient at $x = x^*$. The same behaviour is found for the waves which start their motion to the right side from such boundary and drift closer to it against the gradient direction. It means that if initially the medium had several spiral waves located at different distances from $x = x^*$, all of them gather, after some time, on the boundary $x = x^*$ and slowly drift along it.

A remarkably similar behaviour of migration of spiral waves is found in the presence of real physical boundaries in excitable media. We discuss this phenomenon and a related effect of formation of bound states of spirals in the next section.

7. Migration along a border and bound states

It was found in numerical simulations of reaction–diffusion excitable systems [41] that, if a spiral wave is placed closely enough to a physical border of the medium, it may start to drift parallel to it. The distance from the medium's border at which such a drift takes place is fixed: if initially a spiral wave is a little farther away from the border it moves closer until a certain characteristic distance is reached. If a spiral wave is pushed slightly closer to the border it is repelled by it.

A closely related effect is formation of a bound state of two spiral waves [44]. Suppose that we have a pair of spiral waves which rotate in the opposite directions. This wave pattern is symmetric in respect to mirror reflection about a straight line which is orthogonal to the line connecting the centers of the two spirals and is located at an equal distance from each of them. The symmetry implies that the wave fronts are orthogonal to the central line when they come to it. But this is exactly the same condition which must be satisfied near a physical boundary of the medium. Hence, if we put a flat physical boundary at the central symmetry line the system would not be able to detect the difference. It means that the behaviour of each spiral in the pair is exactly the same as if it were placed at a certain distance from a physical straight boundary in the medium.

If the initial distance between the centers of two spirals is not very large, a *bound state* of these two spirals is formed. It was noted in [44] that the properties of a bound pair do not depend on the initial conditions. The pair slowly drifts at a constant velocity along its symmetry line while the distance between the two centers remains constant. Such stable bound pairs of oppositely rotating spirals were found in numerical simulations [44] not for any parameters of the excitable medium. A necessary condition was that a spiral should be loosely coiled, i.e., its pitch should be significantly larger than the recovery length in the medium.

The symmetry considerations require that the velocity of the drift of a bound pair of spiral waves should be the same as that of a single spiral wave migrating along a physical border. Obviously, the distance between the spiral wave centers is twice the distance between the center of a migrating spiral wave and the border of the medium.

A related effect for spiral waves inside small disks of excitable medium has been recently investigated [42,65]. The numerical simulations of a reaction–diffusion system showed that the dynamical regime with a spiral wave steadily rotating around the center of the disk (fig. 6a) is unstable in small disks. A slight shift of the initial position of the spiral wave leads to motion of the wave's core towards the boundary of the disk and the spiral wave begins to migrate (fig. 6b) along this boundary at a certain distance from it. When the radius of the disk is made

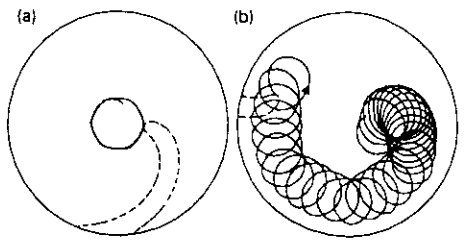

Fig. 6. Instability of a centered rotation of a spiral wave (from [65]). $R = 30$).

smaller, the tip moves closer to the center of the disk (figs. 7a–c). For very small disks, no migration is observed: the rotation center of the spiral wave coincides with the center of the disk (fig. 7d).

To see whether migration along boundaries could be described by the kinematical model we have performed numerical simulations of the kinematical equation (2.8) using the boundary condition (2.11) for the free end and the orthogonality condition on the boundary. The motion of the end point was then obtained by integration of eqs. (2.13), (2.14) and (2.16).

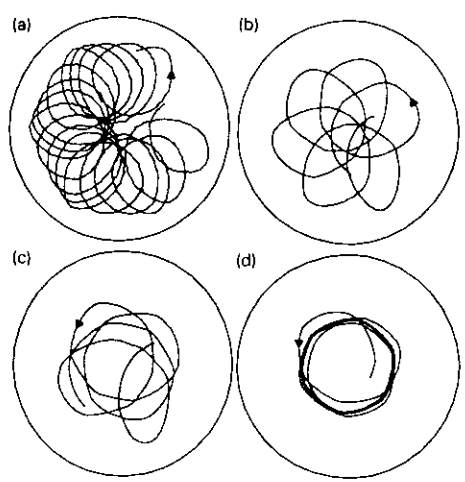

Fig. 7. Spiral waves in disks of different radii: (a) $R = 18$, (b) $R = 12$, (c) $R = 9.6$, (d) $R = 8.4$ (from [65]).

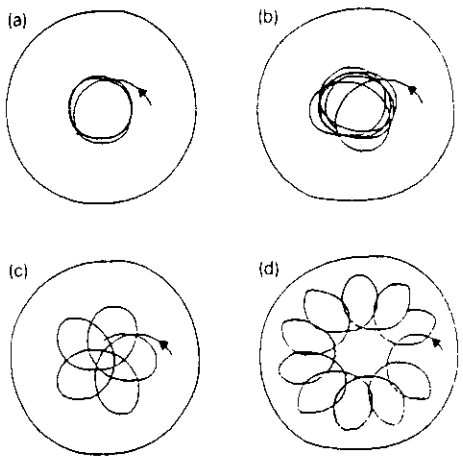

Fig. 8. Trajectories of motion of the end point of a curve inside a small circular region of radius. (a) $R = 1.5$, (b) $R = 2.0$, (c) $R = 2.5$ and (d) $R = 4.0$ obtained by numerical integration of the kinematical equations (from [65]). The kinematical parameters are $V_0 = 1.0$, $G_0 = 2.40$, $D = 0.5$, $\gamma = 2.0$.

The results of the numerical integration of the kinematical equations are presented in fig. 8 which shows trajectories of the free end point of the curve for different sizes of the disk. For small disks the trajectory is attracted to a circle (fig. 8a). It means that the rigid rotation regime is stable. But for the larger disks this regime loses its stability and the tip's trajectory becomes more complicated (figs. 8b,c). In a large disk the trajectory represents a rosette (fig. 8d) obtained by a superposition of the tip's rotation around a smaller circular core and the steady migration of the core along the boundary of the disk. Figure 9 shows migration of the spiral along a flat boundary obtained by numerical integration of the kinematical equations (note that formally this case corresponds to a disk of an infinite radius).

The migration of spirals can be qualitatively explained [43,65] in the following way: If a spiral curve is placed near the border, its tip comes periodically very close to the boundary of the medium (as seen from fig. 10 which shows the

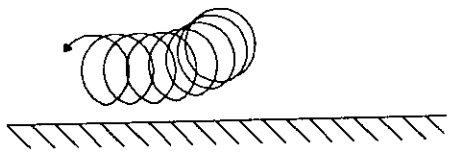

Fig. 9. Migration of a spiral wave along a flat boundary ($V_0 = 1.0$, $G_0 = 3.0$, $D = 1.0$, $\gamma = 2.0$). Only the trajectory of the tip motion is shown.

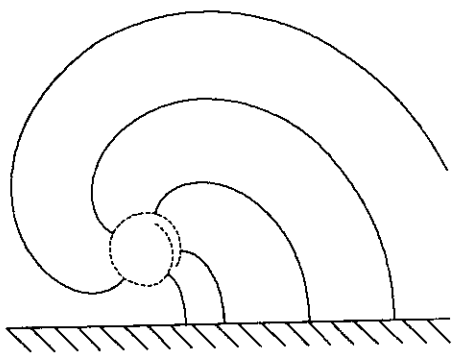

Fig. 10. Subsequent positions of a curve rotating near a flat boundary (time intervals $\Delta t = 15$, other parameters are the same as in fig. 9).

curve at several subsequent time moments). When the tip is close to the boundary, the total arc length L of the curve segment, from the free end to the border, is greatly reduced and may become comparable to the characteristic width l_0 of the boundary layer given by (4.8). In this situation, the motion of the free end of the curve can be influenced by the motion of its opposite end which slides along the border of the medium. Since $\partial k/\partial l$ vanishes at the border, this derivative becomes smaller also at the free end of the curve when it passes near the border of the medium. According to (2.16) the derivative $\partial k/\partial l$ determines the momentary angular velocity of the tip. This periodic variation is resonant since it occurs with the same period as the rotation of the spiral wave. Therefore, it is natural to expect that it produces a drift of the spiral wave which was seen above.

8. Meandering of spiral waves

In our previous analysis we neglected possible interactions between propagating waves (except for their annihilation after collisions). This is justified if the time interval between any two subsequent waves is much larger than the recovery time of the individual elements of excitable medium. Since the rotation period of spiral waves goes to infinity in the limit $G_0 \to 0$ of weakly excitable systems and thus the spirals become very sparse there, this condition can always be satisfied close enough to the existence boundary ∂R of spiral waves in the parameter space which was defined in [5]. The kinematical approach which was formulated above allows us to find the rotation frequency of free sparse spirals and to investigate relaxation to the regime of steady rotation.

However, when we move away from this existence boundary of spiral waves the rotation periods decrease and become comparable with the recovery time of the medium. It means that propagation of the next wave is now influenced by what is left after the propagation of the first wave, since the medium's elements had not enough time to return to the initial rest state. In other words, the subsequent curls of such less sparse spirals are interacting with one another.

Generally, such interactions result in breakdown of rigid rotation and emergence of *meandering regimes* for spiral waves. These regimes are characterized by complex motion of the wave tip. The trajectory of such motion is sensitive to the parameters of the medium. Near the onset of meandering it represents a cycloid obtained by a superposition of two independent circular motions. Meandering of spiral waves was observed in the numerical simulations [7,29–34]. An extensive study of the meandering regimes has been recently undertaken in [5].

The interactions between the subsequent waves are sensitive to the processes which take place inside an excitation pulse and lead to recovery of the initial state of rest (indeed, they arise because the next pulse runs into the tail of the previous propagating one). Therefore, the related phenomena are less universal and may significantly depend on the actual nonlinear dynamics and on the diffusion constants of various reacting components. This makes the analytical theory of the meandering regimes more complicated.

The studies of interactions between the propagating pulses in different reaction–diffusion systems reveal a large variety of behaviours. For instance, the individual pulses have sometimes the oscillating tails [6]. Moreover, the "bound states" of two propagating pulses are known to exist in some systems, so that the pulses can form stable pairs propagating at a fixed distance one from another [6,66]. Obviously, all these effects can contribute into the complex rotation dynamics of the tightly wound spirals [6,66–68]. When the investigation of a given reaction–diffusion system must be performed, the direct numerical simulations may be complemented by application of the semi-numerical methods of the perturbation theory. As recently demonstrated [69], this technique can be successfully used to determine the onset of meandering in concrete systems and to analyze its properties in the context of the bifurcation theory.

Generally, the width of the excitation zone is of the same order of magnitude as the width of the recovery tail. Therefore, when a spiral ceases to be sparse with an increase in the excitability of the medium its pitch is no longer large as compared to the width of the propagating excitation pulse. It means also that the width of the wave's tip becomes comparable with the radius of the core of the spiral wave. Obviously, in this situation the kinematical description, developed above for the weakly excitable media and picturing the entire wave as a *single curve* with a free end, is not applicable.

There is however a special class of systems where, after certain modifications, the kinematical description could be still applied to describe interactions between the propagating waves. These are the systems where a propagating pulse is narrow but its recovery tail is long. In terms of the reaction–diffusion equations it means that the motion of the portraying point along the recovery branch of the null-cline takes much more time than the respective motion along the excitation branch of the same null-cline. This condition can be realized by a proper choice of the nonlinear terms in a reaction–diffusion model. When it is fullfilled, the entire excitation zone of the propagating wave can be represented by a single (infinitely thin) curve in the same manner as we did before.

The effect of a gradual recovery can be incorporated into the kinematical description by assuming that the velocity of the normal propagation of a flat curve is a certain function $V_0(T)$ of the time T that has elapsed after the previous curve had passed the same point of the medium. The actual form of this function depends on a particular reaction–diffusion system which is described by the kinematical model. It must approach the propagation velocity V_0 of a solitary excitation pulse and should become smaller for shorter time intervals T between the waves.

Not only is the normal propagation velocity of the next wave changed. Suppose that a broken flat wave is placed at a certain distance after the first propagating wave. Since the elements of the medium have not yet recovered, the properties of the medium are modified and the tangential velocity G_0 of the growth of the wave tip is altered: it is a certain function $G_0(T)$ of the time interval between the two waves. Since the effective excitability diminishes for smaller times T one can expect that $G_0(T)$ decreases with a decrease in T. In the limit of large time intervals T this function approaches the tangential velocity of growth G_0 of a solitary flat broken wave.

When the recovery effects are taken into account, motion of the curves is thus described by the normal propagation velocity $V = V_0(T) - Dk$ and the tangential velocity of the free tip $G = G_0(T) - \gamma k_0$. We discuss first how this in

fluences the regime of a steady rigid rotation of spiral waves.

If a spiral wave performs rigid rotation, each point of the medium (outside the core region) is visited by an excitation front at time intervals equal to the rotation period $T_0 = 2\pi/\omega_0$ of the spiral. Substituting $V_0(T_0)$ and $G_0(T_0)$ into expression (4.12) for the rotation frequency of spiral waves (and using the relationship $k_c = G_0/\gamma$) we arrive at the equation

$$\frac{2\pi}{T_0} = \zeta \left(\frac{D}{\gamma^3}\right)^{1/2} [V_0(T_0)]^{1/2} [G_0(T_0)]^{3/2} . \qquad (8.1)$$

Its solution yields the rotation period of free spiral waves. Two functions $V_0(T)$ and $G_0(T)$ which enter into (8.1) can be numerically calculated for any particular reaction–diffusion system (see, e.g., [62]).

The stability analysis of a rigidly rotating spiral is much more complicated when the interactions between the subsequent coils of the spiral are present. The stability can be however easily numerically tested by performing integration of the time-dependent equations of the curve's motion modified to include the recovery effects. Now it should be additionally assumed that the parameters V_0 and G_0 in the kinematical equations are some functions of the time T elapsed after the last passage of the curve through a given point of the medium.

In the regime of rigid rotation the waves pass through all points of the medium with the same time interval T equal to the rotation period of the spiral. When more complex regimes are considered this time interval may be different for different points of the medium and may also vary in time so that $T = T(x, y, t)$ where x and y are the Cartesian coordinates of a point. To find $T(x, y, t)$ one must keep in memory the moments $T^*(x, y)$ of the last arrival to the curve at any point (x, y) of the medium. Then the function $T(x, y, t)$ is calculated as

$$T(x, y, t) = t - T^*(x, y) . \qquad (8.2)$$

To compute the moment $T^*(x, y)$ of passing the curve through a given point (x, y) we solve the kinematical equation (2.8) and obtain the function $k = k(l, t)$ which yields the shape of the curve at a given time moment t. The motion of the free tip is then determined by integrating eqs. (2.13), (2.14) and (2.16). Finally, the Cartesian coordinates $X(l, t)$ and $Y(l, t)$ of the curve on the plane are given by the integrals (2.18)–(2.20). They yield the coordinates of the points which are being passed by the front at a given time moment.

We have performed [30,56,70] the numerical simulations of the revised kinematical equations. The last moments of the curve's passage through all points of the medium were stored in the computer memory and updated each time when a new front went through a given point. The function $T(x, y, t)$ was thus calculated at the nodes of a square grid with a distance H between the nodes. The linear interpolation of $1/T$ was used between the nodes (this is necessary because the calculated coordinates X_0 and Y_0 of the tip may take a continuous range of values since they are obtained by numerical integration of a separate set of ordinary differential equations). The velocities of the motion of the wave fronts, as well as the tangential velocity of the free tip, were then systematically corrected using the recorded distributions of the passage times. As a simple approximation for functions $V_0(T)$ and $G_0(T)$ we have used

$$V_0(T) = V_0(1 - aT_r/T) , \qquad (8.3)$$

$$G_0(T) = G_0(1 - T_r/T) , \qquad (8.4)$$

where T_r is a characteristic recovery time; coefficient $a < 1$ in (8.3) takes into account that generally the normal propagation velocity V_0 does not vanish when $G_0 = 0$. Note that our simulations were aimed only to demonstrate appearance of meandering regimes in the kinematical model and therefore we did not try to fit the parameters of the functions $G_0(T)$ and $V_0(T)$ to a particular reaction–diffusion system.

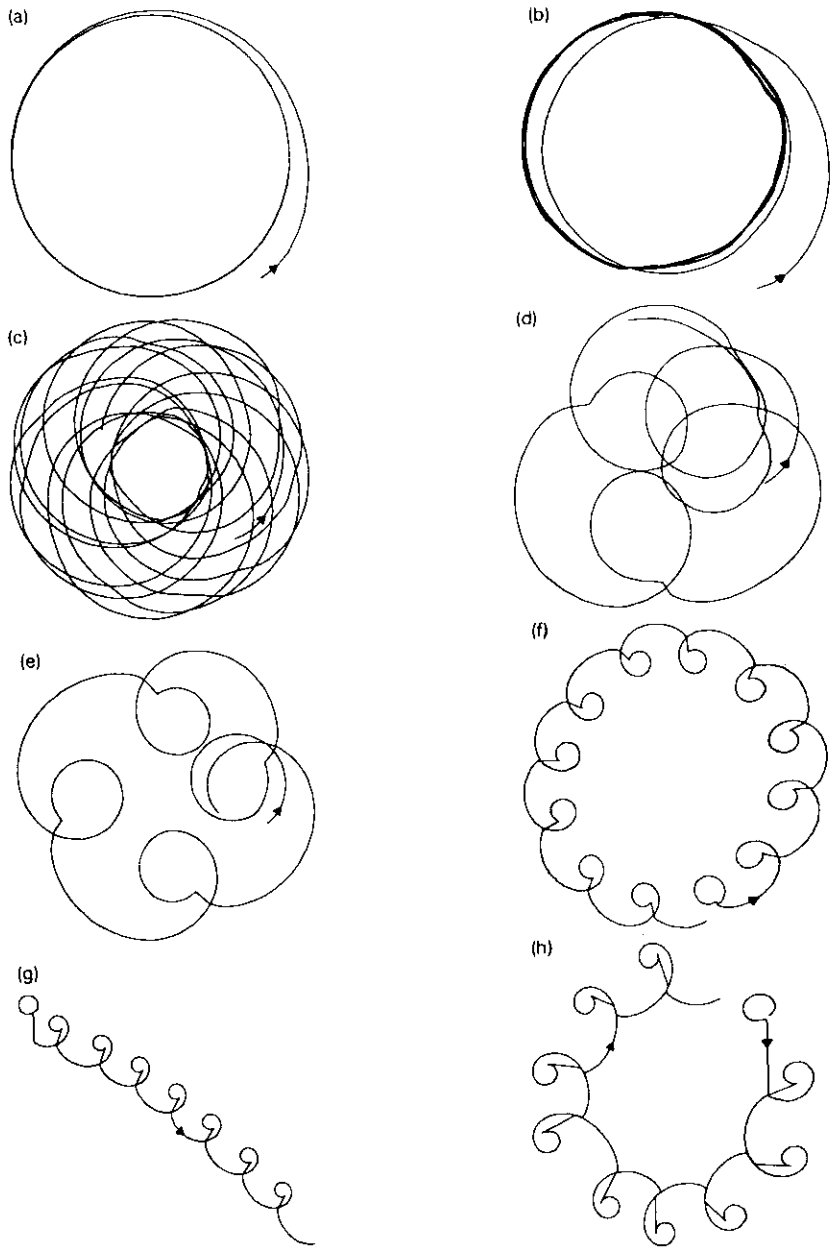

Fig. 11. Complex meandering motion of the curves in media with slow recovery. The trajectories of the tip motion obtained by numerical integration of the kinematical equations at $V_0 = 1.5$, $G_0 = 3.2$, $D = 1.0$, $\gamma = 5.0$ and different values of the recovery time $T_r = 1$ (a), 5 (b), 10 (c), 20 (d), 30 (e), 50 (f), 70 (g) and 100 (h).

By varying T_r we can control the degree of interaction between the subsequent coils of the spiral. Figures 11a–h displays evolution of properties of spiral waves under an increase of recovery time T_r. Only the trajectory of motion of the free tip of a spiral wave is shown; the initial positions of the tip are indicated by arrows.

If T_r is small stable rigid rotation is established (fig. 11a). When $T_r = 5$ (fig. 11b) small-amplitude beatings of the circular trajectory develop. At $T_r = 10$ their amplitude increases and a two-period motion is clearly seen (figs. 11c). If T_r is further increased (fig. 11d,e) the trajectory gradually approaches a rosette form. A cycloidal orbiting is observed at $T_r = 50$ (fig. 11f). With a further increase of the recovery time the larger radius grows and the spiral wave drifts almost along a straight line through the medium (fig. 11g). At still larger values of T_r the character of meandering is changed: now the trajectory represents a pivoting cycloid (fig. 11h). Hence, numerical simulations of the kinematical model reveal the same sequence of meandering regimes which is known for the systems described by full reaction–diffusion equations [5,29].

Within the kinematical approach, the onset of meandering can be explained by simple qualitative arguments. Suppose that we have a spiral whose rotation period is not very large and therefore the wave moves through the region which has not completely recovered. It means that the effective excitability of the medium is reduced. Note however that inside the core region, not visited by the wave, the excitability remains unchanged. Thus the wave's tip moves exactly along the border between the two regions with different effective excitabilities. If, as a result of a small perturbation, the tip enters the core region it begins to move faster in its normal direction and starts to grow. In doing this, it performs a quick rotation inside the former core region, until it runs into its own tail. In this manner, a short petal of the meandering flower is produced. Afterwards, the tip motion slows down and it moves along a less curved trajectory forming the base of the flower. Later another diving of the tip into the core region occurs and the cycle is repeated.

To make clear the mechanism responsible for meandering we have plotted in fig. 12 the subsequent positions of the moving curve obtained by numerical integration of the kinematic equations. We see that the tip starts to grow and performs a quick rotation around a circle of a smaller radius. This rotation is ended when the curve runs into the refractory tail left in the medium (this would occur at the next moment for the last of the curves shown in fig. 12). Since the refractory tail represents an effective obstacle, the curve breaks there. A small disconnected part of it, near the center of the quick rotation, disappears after some time. A newly formed free tip retracts fastly along the border of the effective obstacle until the properties of the medium in the tail are recovered and the front propagation is again possible. After that the entire cycle is repeated.

The emergence of meandering is thus related to the presence of an effective radial gradient of excitability in the central region of the rotating spiral. The above arguments describe however only the initial stage of the meandering onset. Since the effective inhomogeneity of the medium's properties is produced by the propagating wave itself, the spatial distribution of excitability is coupled to its motion. When meandering develops, it results in complex dependence of the excitability distribution in the medium.

In the kinematical model the tip represents a point which is the free end of a moving curve. Therefore, its motion produces an abrupt change of excitability along the core boundary which separates the region visited by the wave and the core where propagation is absent. The actual free tips of spiral waves in reaction–diffusion systems are smooth and thus the gradients created by their motion should be finite. This difference can lead to some disagreements between the predictions of the kinematical model and the behaviour of spiral waves in reaction–diffusion systems.

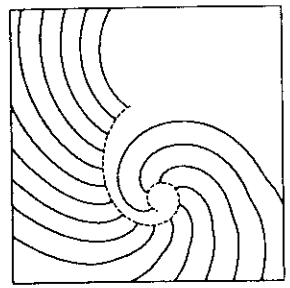

Fig. 12. Subsequent positions of the curve corresponding to the second loop in fig. 11(h), $\Delta t = 100$.

Below a related model problem is considered [30,56] where a spiral wave is assumed to rotate in the presence of an externally imposed smooth radial gradient of excitability. We describe the spiral wave in the kinematical approximation by a single moving curve with a free end. The gradient of excitability is modelled assuming that the kinematical parameter G_0, which gives the tangential velocity of growth of a flat curve, is radius-dependent, i.e., $G_0 = G_0(r)$.

Suppose that we know a solution for a steadily rotating spiral which has rotation frequency ω_0 and core radius R_0. Let us investigate the behaviour of small radial perturbations of this steady rotation regime. If the free end of the spiral has moved by a distance δR closer to the rotation center, it experiences a change of excitability by $\delta G_0 = -b\,\delta R$ where $b = -\partial G_0/\partial r$ at $r = R_0$. On the other hand, this motion of the free end of the curve should be a result of its smooth growth and, therefore, the curvature k_0 at the free end should change then by $\delta k_0 = -(\partial k/\partial l)_0\,\delta R$ where the derivative $(\partial k/\partial l)_0$ is taken at $l = 0$ for the steadily rotating spiral. Since $(\partial k/\partial l)_0 = -\omega_0/D$, we get $\delta k_0 = (\omega_0/D)\,\delta R$. But the tangential velocity G of the free end depends on the curvature k_0 at the free end as $G = G_0 - \gamma k_0$. It means that an increase of this curvature produces a decrease of G by $\gamma\,\delta k_0$. The combination of the two effects yields that, if the tip comes closer by δR to the rotation center, its tangential velocity is changed by $\delta G = -b\,\delta R + \gamma(\omega_0/D)\,\delta R$. Since in the regime of steady rotation $G = 0$, it means that δG gives us the actual tangential velocity of the tip's motion, i.e., we have

$$\delta \dot{R} = (b - \gamma\omega_0/D)\,\delta R\,. \tag{8.5}$$

Hence, stability in respect to radial perturbation is maintained only while $b < \gamma\omega_0/D$. If the radial gradient b exceeds the threshold $b_c = \gamma\omega_0/D$, the regime of rigid steady rotation becomes unstable.

This result which is derived (following [30]) for a spiral rotating in a fixed radial gradient of excitability could be used to obtain a rough estimate of the stability condition for free spiral waves where the radial gradient is produced by the wave itself. For such waves the magnitude of b can be estimated as $b \sim \Delta G_0/H$. Here ΔG_0 is the difference between the growth velocities G_0 in the core region, not visited by the wave, and inside the region filled by the propagating waves where the growth velocity is reduced due to the recovery effect. Using (8.4) we can estimate this difference as $\Delta G_0 \sim G_0(T_r/T_0)$ where T_r is the recovery time and T_0 is the period of steady rotation of the spiral wave.

To find the radial gradient b, we must also know the length H within which the decrease of G_0 takes place. It is given by the length within which the excitation fades down to zero in the radial direction. This is an important property of broken waves in reaction-diffusion systems determined by diffusion of the activator from the excitation zone.

Taking all this into account, the threshold of meandering instability can be roughly estimated as $T_r \sim 2\pi\gamma H/DG_0$. Since $G_0 = \gamma k_c$ this condition can also be written as

$$T_r > \frac{2\pi H}{Dk_c}\,. \tag{8.6}$$

In fig. 13 we have plotted the diagram of meandering regimes on the parameter plane (T_r, k_c) of the kinematical model which are obtained by numerical integration of the kinematical equations. To compare the computation data with the results of our stability analysis, we have shown in fig. 13 by the dashed line the boundary given by condition (8.6). When this condition is formally applied to the kinematical model, a difficulty in determination of the parameter H appears. Strictly speaking, such a length must be zero in this model because the motion of the curve creates a boundary with an abrupt change of G_0. In the numerical calculations this boundary was, however, smoothed. The spatial distribution of passage times T_r which determined according to (8.5) the local values of $G_0(T)$, was first computed in the nodes of a square lattice and then linearly interpolated between the nodes. We take this lattice length as the parameter H in (8.6). Looking at fig. 13 we see that the instability boundary obtained in this way qualitatively agrees with the computed behaviour of spiral waves in the kinematical theory. The general trend in the dependence of T_r on k_c on the boundary seems to be accurately produced by the inverse proportionality law (8.6).

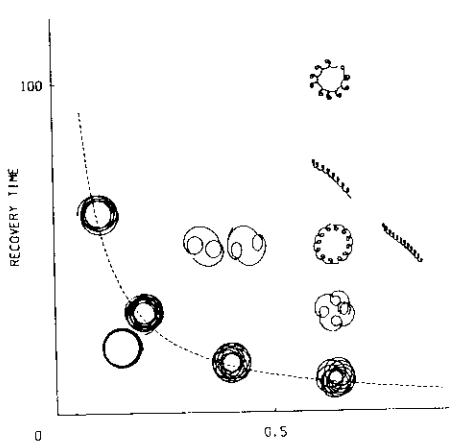

Fig. 13. Schematic diagram of meandering regimes in the parameter plane (T_r, k_c) of the kinematical model ($V_0 = 1.5$, $D = 1.0$, $\gamma = 5.0$; $G_0 = \gamma k_c$). The dashed line shows the theoretical estimate for the instability boundary.

The deficiency of this stability analysis is that it does not predict an *oscillatory* instability. As follows from (8.5), small perturbations behave as $\delta R \sim \exp(\mu t)$ near the stability threshold and the increment $\mu = b - b_c$ is real. In contrast to this, both the numerical simulations of the reaction–diffusion systems and of the kinematical model show that the actual instability must be oscillatory.

The oscillatory behaviour of the perturbation could not have been reproduced in our analysis because it obviously required at least two dynamical variables while in our analysis we had only one variable, the radial perturbation δR.

The second dynamical variable may be provided by the angular perturbations of the tip's motion. After such a perturbation the curve near the tip is shifted in its normal direction by a small distance and thus goes deeper into the recovery tail left by the preceding wave. These perturbations were recently considered in [71] where it was shown that they are always damped. The nature of such damping is clear: when the wave comes closer to the previous one, its normal propagation velocity $V_0(T)$ is decreased and therefore the wave slows down its motion.

But the radial and the polar perturbation modes are actually coupled together. Indeed, if the curve has advanced closer to the previous coil of the spiral, it experiences not only a smaller normal propagation velocity V_0 but also a smaller tangential velocity G_0. Therefore, this perturbation will induce also a contraction of the curve at its free end, i.e., the radial motion of the tip.

The origin of the oscillations at the meandering instability threshold can be qualitatively understood as follows. When, after a slight initial perturbation, the tip comes closer to the rotation center, it experiences higher excitability and, therefore, begins to move faster. But, in doing so, it moves closer to the previous coil of the spiral. This decreases the effective excitability experienced by the tip and forces it to slow its motion, thus providing the negative feedback which is essential for the onset of oscillations. Hence, one can expect that the emergence of oscillations is a consequence of the dynamical coupling between the radial and the angular perturbation modes.

We see that the generalized kinematical model which takes into account interactions between the curves contains the meandering instability and demonstrates patterns of meandering regimes which closely resemble those found in the reaction–diffusion models.

9. Discussion and conclusions

In this paper we have considçred a number of mathematical problems related to the motion of oriented curves with free ends. We have found that even under the simplest assumptions the motion of such curves may be very complicated. We have seen that the curves can form spirals and these spirals can wander on the plane in presence of gradients or under time variation of the propagation parameters. We have also found that interactions between the coils forming a spiral can destabilize its steady rotation and give rise to complex meandering regimes.

The kinematical model can be generalized to describe spiral waves in anysotropic media (see [56,72]) and on the curved surfaces (this is briefly discussed in Appendix B). A similar kinematical theory has been developed in [8,48,50,55–56,73] for three-dimensional media. In the latter case a fundamental notion of the theory is an oriented curved surface with a free edge. The surface elements move in their normal directions with the velocity depending on the local mean curvature of the surface. The surface can grow or contract along its edge with a tangential velocity depending both on the mean curvature of the surface near the edge and the local geodesic curvature of the edge line.

Within the kinematical model, we have analyzed in [8,48,50,55–56] properties of scroll rings and calculated the rates of their expansion or contraction which are accompanied by drift of the ring along its symmetry axis. We have also shown [8,48] that in a narrow interval of parameters stable scroll rings should exist. The resonance of a scroll ring under periodic modulation of the medium's properties was investigated in [74].

Acknowledgements

The authors are grateful to J. Keener for his comments on the construction of the boundary condition at the free end of a moving curve. We thank H. Levine, E. Meron, S. Muller, P. Pelcé and A.T. Winfree for valuable discussions. One of us (A.S.M.) acknowledges financial support from the Fritz Thyssen Foundation.

Appendix A. Wave propagation in weakly excitable media

The reaction–diffusion equations of an excitable medium can be written in a general form:

$$\frac{\partial \boldsymbol{w}}{\partial t} = \boldsymbol{F}(\boldsymbol{w}, \mu) + \hat{D}\nabla^2 \boldsymbol{w}\,. \tag{A.1}$$

Here $\boldsymbol{w} = (w_1, \ldots, w_N)$ is a vector whose components $w_n = w_n(r, t)$ give spatial distributions of N reacting species. The set of nonlinear functions $\boldsymbol{F}(\boldsymbol{w}) = (F_1(\boldsymbol{w}), \ldots, F_n(\boldsymbol{w}))$ specifies the local dynamics within an individual small volume of the medium. The diagonal matrix $\hat{D}$ gives diffusion constants for all the components. Generally, functions $\boldsymbol{F}$ may depend also on some control parameter μ.

Equations (A.1) define an *excitable medium* if they satisfy two additional conditions:

(i) The system has an attractive stationary

state of rest where all components w_n are constant across the medium. This state is stable in respect to sufficiently small perturbations. One can always choose reference values for the components w_n in such a way that $w = 0$ in the state of rest.

(ii) In the one-dimensional case the system has a special time-dependent solution which describes a solitary travelling pulse,

$$w = f(\xi), \quad \xi = x - V_0 t - x_0,$$
$$f(\xi) \to 0 \quad \text{for } \xi \to \pm\infty. \tag{A.2}$$

Both before and after the pulse the medium is in the state of rest. The pulse moves with velocity V_0 and is centered at $x = x_0 + V_0 t$. We assume that the pulse is localized, i.e., all its components $f_n(\xi)$ exponentially vanish outside a region of a certain width a. In contrast to the nonlinear waves in the conservative media, such as the solitons of the Kordeweg–de Vries equation, both the amplitude and the velocity of a travelling excitation pulse are uniquely determined by the properties of the medium. Its initial location x_0 remains arbitrary. The travelling pulse is stable: its shape is recovered after a perturbation. However, the perturbation can result in a small change of the pulse location x_0. The collision of any two pulses results in their mutual annihilation.

In two dimensions (A.2) describes a flat excitation wave which propagates along the x-axis. If the medium is isotropic, the same solutions can be constructed for the flat waves that move along an arbitrary direction.

We suppose that at a certain value $\mu = \mu_0$ of the control parameter eqs. (A.1) have a special two-dimensional solution which represents a broken flat wave which propagates without either growth or contraction,

$$w = g_0(\xi, \eta), \quad \xi = x - V_0 t - x_0,$$
$$\eta = y - y_0, \tag{A.3}$$

such that

$$g_0(\xi, \eta) \to 0 \quad \text{for } \xi \to \pm\infty,$$
$$g_0(\xi, \eta) \to 0 \quad \text{for } \eta \to +\infty,$$
$$g_0(\xi, \eta) \to f(\xi) \quad \text{for } \eta \to -\infty. \tag{A.4}$$

This solution represents a flat travelling *half-wave*. This wave moves at a constant velocity in the x-direction but it does not grow or contract at its end in the orthogonal y-direction. The existence of such a solution which is located on the boundary ∂R in the parameter space in the Winfree notations [5] was first demonstrated in the numerical simulations [48]. This solution was analytically investigated [49] in a model of a reaction–diffusion system. We assume that the components of this solution vanish exponentially fast when $|x - x_0 - V_0 t| \to \infty$ and $(y - y_0) \to \infty$. It is therefore localized within a strip at $x = x_0 + V_0 t$ which terminates near the coordinate point $y = y_0$ that can be chosen as the end of such broken wave. The special solution (A.4) is stable in a sense that its profile is recovered after a small perturbation. However, the parameters x_0 and y_0 are arbitrary and they can slightly change as a result of the perturbation.

We define *weakly* excitable media by assuming that, for the chosen values of their parameters, they are close to the conditions of existence of the travelling half-wave solution (A.4), i.e., $\mu = \mu_0 + \delta\mu$ where $\delta\mu \ll \mu_0$ (one can take $\delta\mu$ as the distance from the boundary ∂R).

When the medium is weakly excitable the nonlinear terms F in (A.1) can be expanded around $\mu = \mu_0$. Keeping only the correction which is proportional to variation $\delta\mu$, we have

$$F(w, \mu) = F_0(w) + \delta\mu\, F_1(w), \tag{A.5}$$

where $F_0(w) = F(w, \mu_0)$ and $F_1(w) = \partial F / \partial \mu$ is taken at $\mu = \mu_0$. Hence, we can write (A.1) as

$$\frac{\partial w}{\partial t} = F_0(w) + \hat{D}\,\nabla^2 w + \delta\mu\, F_1(w). \tag{A.6}$$

Since $\delta\mu$ is small, the last term in (A.6) can be treated as a weak perturbation. Let us investigate how it influences the half-wave solution $w = g_0(x - V_0 t, y)$.

We first go to the moving coordinate system $x' = x - V_0 t$ where the wave is at rest. Then eqs. (A.6) take the form

$$\frac{\partial w}{\partial t} = F_0(w) + V_0 \frac{\partial w}{\partial x} + \hat{D}\left(\frac{\partial^2}{\partial x^2} + \frac{\partial^2}{\partial y^2}\right) w + \delta\mu\, F_1(w). \tag{A.7}$$

Here and below we drop the prime in x'.

The effect of the perturbation described by the last term in (A.7) is two-fold. Firstly, this leads to a small change in the profile of the wave. Secondly, it results in a slow gradual change in the parameters x_0 and y_0 that fix the position of the wave on the plane. Thus, we can write

$$w = g_0(x - x_0(t), y - y_0(t)) + \delta w(x, y, t). \tag{A.8}$$

Substitution of (A.8) into (A.7) yields an equation for the evolution of δw:

$$\frac{\partial \delta w}{\partial t} = \hat{\Gamma}\,\delta w + \delta\mu\, F_1(g_0) + \dot{x}_0 \frac{\partial g_0}{\partial x} + \dot{y}_0 \frac{\partial g_0}{\partial y}. \tag{A.9}$$

Here $\hat{\Gamma}$ is a linear differential operator with matrix elements

$$(\hat{\Gamma})_{nm} = B_{nm}(x, y) + V_0 \delta_{nm} \frac{\partial}{\partial x} + D_{nm}\left(\frac{\partial^2}{\partial x^2} + \frac{\partial^2}{\partial y^2}\right), \tag{A.10}$$

where

$$B_{nm} = \left.\frac{\partial F_{0,n}}{\partial w_m}\right|_{w = g_0(x,y)}. \tag{A.11}$$

Note that the linear operator $\hat{\Gamma}$ is not self-adjoint, $\hat{\Gamma}^+ \neq \hat{\Gamma}$. Therefore, its eigenvectors $u_{(\alpha)}$ that correspond to different eigenvalues $\lambda_{(\alpha)}$, i.e., satisfy the equation

$$\hat{\Gamma} u_{(\alpha)} = \lambda_{(\alpha)} u_{(\alpha)}, \tag{A.12}$$

are not orthogonal. Still they form a complete set and we can, for instance, decompose δw as

$$\delta w(x, y, t) = \sum_{\alpha} C_{(\alpha)}(t)\, u_{(\alpha)}(x, y). \tag{A.13}$$

Since any shift of the flat half-wave (A.3) along the directions x or y yields also a valid solution, the spectrum of the linear operator $\hat{\Gamma}$ must include a (doubly degenerate) zero eigenvalue. The respective two eigenvectors are simply

$$u_{(0,x)} = \frac{\partial g_0}{\partial x}, \quad u_{(0,y)} = \frac{\partial g_0}{\partial y}. \tag{A.14}$$

Because the displacements along these two directions induced by the perturbation $\delta\mu\, F_1$, are already taken into account in (A.8) by assuming that x_0 and y_0 slowly change in time, the term δw cannot include the projections on these two eigenvectors, i.e., $C_{(0,x)} = C_{(0,y)} = 0$ in (A.13).

Since eigenvectors are not orthogonal, we should employ a more complicated procedure for finding the decomposition coefficients. Namely, we first consider the eigenvalue problem

$$\hat{\Gamma}^+ u^{(\alpha)} = \lambda^{(\alpha)} u^{(\alpha)} \tag{A.15}$$

for the adjoint linear operator $\hat{\Gamma}^+$. Its eigenvalues are related to eigenvalues of $\hat{\Gamma}$ as $\lambda^{(\alpha)} = \lambda^*_{(\alpha)}$, while its eigenvectors are orthogonal to the respective eigenvectors of $\hat{\Gamma}$, so that the scalar products of these eigenvectors vanish,

$$(u^{(\alpha)}, u_{(\alpha')}) = \int\int dx\, dy \sum_{n=1}^{N} u_n^{(\alpha)}(x, y)\, u_{n,(\alpha')}(x, y) = 0 \quad \text{for } \alpha \neq \alpha', \tag{A.16}$$

Particularly, there are two eigenvectors which correspond to the doubly degenerate zero eigenvalue. We can choose these eigenvectors $u^{(0,x)}$ and $u^{(0,y)}$ in such a way that

$$(u^{(0,x)}, u_{(0,y)}) = 0, \quad (u^{(0,y)}, u_{(0,x)}) = 0. \tag{A.17}$$

Now we can multiply both sides of (A.9) by $u^{(0,y)}$. Since $(u^{(0,y)}, \delta w) = 0$, this yields

$$\delta\mu\,(u^{(0,y)}, F_1(g_0)) + \dot{y}_0 (u^{(0,y)}, u_{(0,y)}) = 0, \tag{A.18}$$

where we have used (A.14).

It follows from (A.18) that when the control parameter is changed by $\delta\mu$ from its critical value μ_0 the flat half-wave grows (or contracts) in its tangential y-direction. The velocity $G_0 = \dot{y}_0$ of such growth is given according to (A.18) by

$$G_0 = (\mu_0 - \mu)\frac{(\boldsymbol{u}^{(0,y)}, \boldsymbol{F}_1(\boldsymbol{g}_0))}{(\boldsymbol{u}^{(0,y)}, \boldsymbol{u}_{(0,y)})}. \tag{A.19}$$

If $G_0 > 0$ the wave grows while if $G_0 < 0$ it contracts.

Until now we considered only flat waves, but the waves can also be curved. When the local curvature k of the wavefront is so small that the curvature radius $R = 1/k$ is much larger than the wave width a, the effects of the curvature can be studied using the perturbation theory, in a manner similar to the above analysis.

We consider first a wave segment which lies far away from the end point. This segment of the curved front can be locally approximated by a circular front of radius R. We use a polar coordinate system (r, ϕ) with the origin in the center of such a circle. In this coordinate system the reaction–diffusion equations take the form

$$\frac{\partial \boldsymbol{w}}{\partial t} = \boldsymbol{F}(\boldsymbol{w}) + \frac{\hat{D}}{r}\frac{\partial \boldsymbol{w}}{\partial r} + \hat{D}\frac{\partial^2 \boldsymbol{w}}{\partial r^2}. \tag{A.20}$$

Note that the angle derivatives are absent because of our choice of the origin of the coordinates. As the next step, we take into account that components w_n of the vector $\boldsymbol{w}$ change only within the wave, i.e., inside a region of width a near its front. Since a is assumed to be much smaller than curvature radius $R = 1/k$, one can approximately replace $\hat{D}/r$ by $\hat{D}k$ in (A.20) and write it as

$$\frac{\partial \boldsymbol{w}}{\partial t} = \boldsymbol{F}(\boldsymbol{w}) + \hat{D}\frac{\partial^2 \boldsymbol{w}}{\partial r^2} + \hat{D}k\frac{\partial \boldsymbol{w}}{\partial r}. \tag{A.21}$$

Since curvature k is small, the last term in (A.21) can be treated as a weak perturbation. We introduce a new radial coordinate $\rho = r - V_0 t$ and seek a solution in the form:

$$\boldsymbol{w} = \boldsymbol{f}(\rho - \rho_0(t)) + \delta\boldsymbol{w}(\rho, t), \tag{A.22}$$

where $\boldsymbol{f}(\rho)$ gives the profile of a solitary travelling pulse (see (A.2)) and $\rho_0(t)$ describes a slow drift due to the perturbation. The correction $\delta\boldsymbol{w}$ obeys then the equation

$$\frac{\partial \delta\boldsymbol{w}}{\partial t} = \hat{A}\,\delta\boldsymbol{w} + \hat{D}k\frac{\partial \boldsymbol{f}}{\partial \rho} + \dot{\rho}_0\frac{\partial \boldsymbol{f}}{\partial \rho}, \tag{A.23}$$

where matrix elements of the linear differential operator $\hat{A}$ are

$$(\hat{A})_{nm} = A_{nm}(\rho) + V_0\delta_{nm}\frac{\partial}{\partial \rho} + D_{nm}\frac{\partial^2}{\partial \rho^2}, \tag{A.24}$$

$$A_{nm}(\rho) = \left.\frac{\partial F_n(\boldsymbol{w})}{\partial w_m}\right|_{\boldsymbol{w}=\boldsymbol{f}(\rho)}. \tag{A.25}$$

Now the problem is clearly similar to the one which was solved above. Since $\delta\boldsymbol{w}$ should not include a projection to the shift mode $\boldsymbol{v}_{(0)} = \partial \boldsymbol{f}/\partial \rho$, the condition

$$k(\boldsymbol{v}^{(0)}, \hat{D}\,\partial \boldsymbol{f}/\partial \rho) + \dot{\rho}_0(\boldsymbol{v}^{(0)}, \boldsymbol{v}_{(0)}) = 0 \tag{A.26}$$

must be satisfied where $\boldsymbol{v}_{(0)}$ is the eigenvector of the adjoint operator $\hat{A}^+$ with the zero eigenvalue. Hence, the propagation velocity $V(k) = V_0 + \dot{\rho}_0$ of a slightly curved wave is $V(k) = V_0 - Dk$ where

$$D = \frac{(\boldsymbol{v}^{(0)}, \hat{D}\,\partial \boldsymbol{f}/\partial \rho)}{(\boldsymbol{v}^{(0)}, \boldsymbol{v}_{(0)})}. \tag{A.27}$$

As the last step, we determine the curvature dependence of the tangential growth velocity. We fix the value of the control parameter at $\mu = \mu_0$, so that the tangential velocity of a flat half-wave is zero. We consider now however a *curved* half-wave which is produced by taking a circular wave and removing a half of it. After such an operation we have a circular segment with two free ends (i.e. two tips). We want to determine the velocity of growth (or contraction) of the end point as a function of the curvature k_0 of the segment.

Let us introduce polar coordinates (r, ϕ) with the origin in the center of the circle. The reaction–diffusion equations in this coordinate system have the form

$$\frac{\partial \boldsymbol{w}}{\partial t} = \boldsymbol{F}_0(\boldsymbol{w}) + \frac{\hat{D}}{r}\frac{\partial \boldsymbol{w}}{\partial r} + \hat{D}\frac{\partial^2 \boldsymbol{w}}{\partial r^2} + \frac{\hat{D}}{r^2}\frac{\partial^2 \boldsymbol{w}}{\partial \phi^2}, \tag{A.28}$$

where $\boldsymbol{F}_0(\boldsymbol{w}) = \boldsymbol{F}(\boldsymbol{w}, \mu_0)$. Since the components of $\boldsymbol{w}$ undergo a significant change only within an interval of width a at $r = R$ and, as we assume, $R \gg a$, we can approximately replace r by R in the second and the fourth terms in (A.28). Furthermore, because of the symmetry we can consider only the evolution of one of the segment tips. It is convenient to introduce $y = R\phi$ which gives us the length of the arc measured from the center $\phi = 0$ of the segment. With these notions we obtain

$$\frac{\partial \boldsymbol{w}}{\partial t} = \boldsymbol{F}_0(\boldsymbol{w}) + \hat{D}\left(\frac{\partial^2 \boldsymbol{w}}{\partial r^2} + \frac{\partial^2 \boldsymbol{w}}{\partial y^2}\right) + \hat{D}k_0\frac{\partial \boldsymbol{w}}{\partial r}. \tag{A.29}$$

Since the curvature k_0 is small, the last term here can be treated as a weak perturbation. Thus, the problem is similar to (A.6).

We seek a solution to (A.29) in the form

$$\boldsymbol{w} = \boldsymbol{g}_0(x - x_0(t), y - y_0(t)) + \delta\boldsymbol{w}(x, y, t), \tag{A.30}$$

where $\boldsymbol{g}_0$ is a nonperturbed solution (A.3) for a flat half-wave and $x = r - V_0 t$. The correction $\delta\boldsymbol{w}$ satisfies then the equation

$$\frac{\partial \delta\boldsymbol{w}}{\partial t} = \hat{\Gamma}\,\delta\boldsymbol{w} + \hat{D}k_0\frac{\partial \boldsymbol{g}_0}{\partial x} + \dot{x}_0\frac{\partial \boldsymbol{g}_0}{\partial x} + \dot{y}_0\frac{\partial \boldsymbol{g}_0}{\partial y}, \tag{A.31}$$

where the linear operator $\hat{\Gamma}$ is defined by (A.10). Since (A.31) differs from (A.9) only in the form of the perturbation term, we can use now the same arguments as above and derive the following expression for the tangential velocity $G(\mu_0, k) = \dot{y}_0$ of the broken curved front:

$$G(\mu_0, k_0) = -\gamma k_0, \tag{A.32}$$

where the proportionality factor γ is

$$\gamma = \frac{(\boldsymbol{u}^{(0,x)}, \hat{D}\,\partial \boldsymbol{g}_0/\partial x)}{(\boldsymbol{u}^{(0,x)}, \boldsymbol{u}_{(0,x)})}. \tag{A.33}$$

When the control parameter μ is different from μ_0, this changes the tangential velocity. If the variation $\delta\mu$ is small, its effect can be determined using the linear perturbation theory. Since within the linear theory the corrections due to different perturbations are independent and additive, the velocity $G(\mu, k_0)$ of the growth (or retraction) of a curved broken wave is a sum of G_0 given by (A.19) and of the term $G(\mu_0, k_0)$. For simplicity, it was assumed above that the broken curved wave represented a segment of a circular front (with constant curvature k_0). However, since the form a curved broken front near its end can always be approximated by a piece of a circle, our result holds in this general case too, if we interpret k_0 as a curvature of the wave front in the immediate vicinity of the end point.

Thus, we see that the motion of a curved broken wave in a weakly excitable medium obeys simple dynamical laws. Namely, the wave can be portrayed by an oriented curve with a free end. As time goes on, each small segment of the wave moves in the normal direction with velocity

$$V = V_0 - Dk, \tag{A.34}$$

where k is the local curvature of the wave. In addition to its normal motion, the wave can also grow or contract at its free end. The velocity G of growth (or contraction) is

$$G = G_0 - \gamma k_0, \tag{A.35}$$

where G_0 is this velocity for a flat broken wave and k_0 is the curvature near the free end. The medium is *weakly* excitable if condition $G_0 \ll V_0$ holds. Note that, although eqs. (A.34) and (A.35) were derived above only for convex waves with positive curvature k, the same dependencies hold if the wavefront is locally concave, so that its curvature is negative.

Equations (A.34) and (A.35) take into account only the first terms in the decomposition of V and G in powers of the curvature k. As follows from their derivation, these approximate expressions can generally be used only while $k \ll 1/a$, where a is a characteristic width of the excitation wave. For some special reaction–diffusion models the applicability condition may be, however, less stringent. For instance, if the system includes a number of components which do not diffuse, the characteristic width a that enters into the condition is determined only by the diffusing components.

A special class of reaction–diffusion models consists of the systems where the diffusion coefficients of all the components are the same, i.e., $\hat{D} = D\hat{I}$ where $\hat{I}$ is the unit matrix. Since, by the definition, $\partial f/\partial x = v_{(0)}$, eq. (A.27) implies that for such a system the proportionality coefficient D in dependence (A.34) coincides with the (common) diffusion constant of the components. On the other hand, eq. (A.33) yields in this case

$$\gamma = D\frac{(u^{(0,y)}, \partial f_0/\partial x)}{(u^{(0,y)}, u_{(0,y)})} = 0\,, \tag{A.36}$$

because, by the definition, $\partial g_0/\partial x = u_{(0,x)}$ and this vector is orthogonal to $u^{(0,y)}$. Thus, in the reaction–diffusion systems with the same diffusion constant for all the components the coefficient γ should vanish. It means that the expansion in powers of k_0 for the tangential velocity G must begin for such systems with quadratic terms,

$$G = G_0 - \gamma_1 k_0^2\,. \tag{A.37}$$

Therefore, the case of equal diffusion constants has special properties and should be separately investigated.

Appendix B. Waves on curved surfaces

In this appendix we derive following [54] a basic equation of motion of curves on curved surfaces and briefly discuss the relevant effects for spiral waves. Suppose we have a curve moving over a two-dimensional surface. If we take a series of snapshots of propagation of this curve at different times t we obtain a one-parameter family of curves with time t as a parameter. We introduce a curvilinear orthogonal coordinate system (ϕ, t) where each coordinate lines $t = \text{const.}$ coincides with the moving curve at time t. In this coordinate system the first quadratic form of the surface (yielding the square of differential arc length) is

$$\mathrm{d}s^2(t,\phi) = V^2(t,\phi)\,\mathrm{d}t^2 + B^2(t,\phi)\,\mathrm{d}\phi^2\,, \tag{B.1}$$

where V and B are the Lamé coefficients and V is obviously the velocity of the normal propagation of the curve. The local Gaussian curvature Γ of the surface can be expressed through the Lamé coefficients as [75]

$$\Gamma = -\frac{1}{VB}\left[\left(\frac{B_t}{V}\right)_t + \left(\frac{V_t}{B}\right)_\phi\right], \tag{B.2}$$

where the subscripts t and ϕ denote the corresponding partial derivatives. The geodesic curvature k of a coordinate line on the surface can also be expressed [75] in terms of the Lamé coefficients as $k = B_t/VB$. Then using (B.2) we get

$$\Gamma = -k^2 - \frac{1}{V}\frac{\partial k}{\partial t} - \frac{1}{VB}\frac{\partial}{\partial \phi}\left(\frac{1}{B}\frac{\partial V}{\partial \phi}\right). \tag{B.3}$$

We perform next a change of variables and go from ϕ to the arc length l measured from a fixed point on the curve. This is done using the relation $\mathrm{d}/\mathrm{d}t \to \partial/\partial t + (\mathrm{d}l/\mathrm{d}t)\,\partial/\partial l$. Here $\mathrm{d}l/\mathrm{d}t$ is the rate of elongation of the curve's arc between a fixed reference point and the point with coordinate ϕ. Since according to (B.1) $\mathrm{d}l = B\,\mathrm{d}t$ we obtain

$$\frac{\mathrm{d}l}{\mathrm{d}t} = \int_{\phi_0}^{\phi} B_t\,\mathrm{d}\phi = \int_{\phi_0}^{\phi} kVB\,\mathrm{d}\phi = \int_0^l kV\,\mathrm{d}\xi\,. \tag{B.4}$$

If the end of the curve is chosen as the reference point and the curve can grow, this leads to the appearance of the additional tangential growth velocity G in the right hand side of (B.4). In the new valuables we finally obtain from (B.3)

$$\frac{\partial k}{\partial t} + \left(\int_0^l kV\,\mathrm{d}\xi + G\right)\frac{\partial k}{\partial l} + k^2V + \frac{\partial^2 V}{\partial l^2} = -\Gamma V\,. \tag{B.5}$$

This is the basic kinematical equation of motion of curves on a curved surface with the local Gaussian curvature Γ. In the special case of a plane we have $\Gamma = 0$ and then (B.5) reduces to the kinematical equation (2.7) that was derived in section 2.

An immediate important conclusion which can be made by looking at (B.5) is that the motion of the curves is influenced by the local Gaussian curvature of the surface which is a product $\Gamma = k_1k_2$ of its local two principal curvatures k_1 and k_2 but *not* by its mean curvature $H = \frac{1}{2}(k_1 + k_2)$. This implies, for instance, that the motion of curves on cones or cylinders has exactly the same properties as on a plane.

We have used (B.5) in [54,56] to calculate the rotation frequency of a pair of spiral waves occupying the opposite poles of a sphere. It was noted in [54] that the kinematical equations do not possess a solution which would have described a single steadily rotating spiral wave on a sphere. The experimental study [76] of spiral waves in the Belousov–Zhabotinskii chemical reaction on the surfaces of small spherical beads revealed that single spirals are still possible; however, their rotation is not steady but irregular.

Since properties of spiral waves are influenced by the Gaussian curvature Γ, its variation can induce drift of spirals. We have considered in [56,77] a problem of a spiral wave on a periodically "breathing" large spherical surface under the resonant condition that the modulation frequency of the radius of the sphere is close to the own rotation frequency of the spiral wave.

Note that if the surface is not uniformly curved (like a sphere, a cone or a cylinder) its local Gaussian curvature changes from one point of the surface to another. When this happens, the moving tip of the wave passes through the regions with different values of the Gaussian curvature and thus experiences an effective time variation of this property. This variation is resonant and, as in the case of a spiral wave in the presence of a spatial gradient of excitability, it induces drift [77] of the spiral wave on such nonuniformly curved surface. This effect was confirmed [56] by numerical simulations of spiral waves on the surface of a prolate spheroid with two different semi-major axes.

References

[1] A.T. Winfree, When Time Breaks Down (Princeton Univ. Press, Princeton, 1987).

[2] J.D. Murray, Mathematical Biology (Springer, Berlin 1989).

[3] P.C. Fife, Propagator-controller systems and chemical patterns, in: Non-Equilibrium Dynamics in Chemical Systems, eds. C. Vidal and A. Pacault (Springer, Berlin 1984) pp. 76–88.

[4] J.P. Keener and J.J. Tyson, Spiral waves in the Belousov–Zhabotinskii reaction, Physica D 21 (1986) 1039.

[5] A.T. Winfree, Varieties of spiral wave behavior: An experimentalist's approach to the theory of excitable media, Chaos 1 (1991) 303.

[6] E. Meron, Pattern formation in excitable media, Phys. Rep. 218 (1992) 1.

[7] V.S. Zykov, Simulation of Wave Processes in Excitable Media (Nauka, Moscow, 1984) [English translation Manchester Univ. Press, Manchester, 1987].

[8] A.S. Mikhailov, Foundations of Synergetics I. Distributed Active Systems (Springer, Berlin, 1990).

[9] Zs. Nagy-Ungvarai, J. Ungvarai, S.C. Muller and B. Hess, The role of curvature and pulse width for transition to unstable wave fronts in the Belousov–Zhabotinskii reaction, J. Chem. Phys. 97 (1992) 1004.

[10] S. Nettesheim, A. von Oertzen, H.H. Rotermund and G. Ertl, Reaction diffusion patterns in the catalytic CO-oxidation on Pt(110) – Front propagation and spiral waves, J. Chem. Phys. 98 (1993) 3377.

[11] A.M. Pertsov and A.V. Panfilov, Spiral waves in active media. Reverberator in the FitzHugh–Nagumo model, in: Autowave Processes in Systems with Diffusion, A.M. Grekhova, ed. (Institute of Applied Physics Publications, Gorky, 1981) pp. 77–84 [in Russian].

[12] W.K. Burton, N. Cabrera and F.C. Franck, Crystal growth, Phil. Trans. R. Soc. (London) 243 (1951) 299.
[13] R.C. Brower, D. Kessler, J. Koplik and H. Levine, Geometrical models of interface evolution, Phys. Rev. A 29 (1984) 1335.
[14] G.I. Sivashinsky, Instabilities, pattern formation and turbulence in flames, Am. Rev. Fluid Mech. 15 (1983) 179.
[15] P. Nelson and T. Powers, Rigid chiral membranes, Phys. Rev. Lett. 69 (1992) 3409.
[16] P. Pelcé and A. Pocheau, Geometrical approach to the morphogenesis of unicellular algae, J. Theor. Biol. 156 (1992) 197.
[17] R.E. Goldstein and D.M. Petrich, The Korteweg-de Vries hierarchy as dynamics of closed curves in the plane, Phys. Rev. Lett. 67 (1991) 3202.
[18] K. Nakayama, H. Segur and M. Wadati, Integrability and motion of curves, Phys. Rev. Lett. 69 (1992) 2603.
[19] N. Wiener and A. Rosenblueth, The mathematical formulation of the problem of conduction of impulses in a network of connected excitable elements, specifically in cardiac muscle, Arch. Inst. Cardiol. Mexico 16 (1946) 205.
[20] V.S. Zykov, Kinematics of steady circulation in excitable medium, Biophysics (USSR) 25 (1980) 329.
[21] V.S. Zykov, Analytical estimate of the dependence of the excitation wave velocity on the curvature of its front in a two dimensional excitable medium, Biophysics (USSR) 25 (1980) 906.
[22] R.N. Miller and J. Rinzel, The dependence of impulse propagation speed on firing frequency and dispersion for the Hodgkin–Huksley model, Biophys. J. 34 (1981) 227.
[23] A.S. Mikhailov and V.I. Krinsky, Rotating spiral waves in excitable media: the analytical results, Physica D 9 (1983) 346.
[24] J.D. Dockery, J.P. Keener and J.J. Tyson, Dispersion of travelling waves in the Belousov–Zhabotinskii reaction, Physica D 30 (1988) 177.
[25] J.P. Keener, A geometrical theory for spiral waves in excitable media, SIAM J. Appl. Math. 46 (1986) 1039.
[26] J.J. Tyson and J.P. Keener, Spiral waves in a model of miocardium, Physica D 29 (1987) 215.
[27] J.J. Tyson and J.P. Keener, Singular perturbation theory of travelling waves in excitable media, Physica D 32 (1988) 327.
[28] A.S. Mikhailov, A theory of spiral waves, in: Self-Organization: Autowaves and Structures far from Equilibrium, ed. V.I. Krinsky (Springer, Berlin, 1984) pp. 92–95.
[29] V.S. Zykov, Cycloidal circulation of spiral waves in an excitable medium, Biophysics (USSR) 31 (1986) 940.
[30] V.S. Zykov and O.L. Morozova, Computer simulations and investigation of spiral autowave stability, J. Nonlin. Biol. 1 (1991) 127.
[31] E. Lugosi, Analysis of meandering in Zykov kinetics, Physica D 40 (1989) 331.
[32] G.S. Skinner and H.L. Swinney, Periodic to quasi-periodic transition of chemical spiral rotation, Physica D 48 (1990) 1.
[33] A. Karma, Meandering transition in two-component excitable medium, Phys. Rev. Lett. 65 (1990) 2824.
[34] D. Barkley, M. Kness and L.S. Tuckerman, Spiral wave dynamics in a simple model of excitable media: Transition from simple to compound rotation, Phys. Rev. A 42 (1990) 2489.
[35] A.N. Rudenko and A.V. Panfilov, Drift and interaction of vortices in two-dimensional heterogeneous active media, Stud. Biophys. 98 (1983) 183.
[36] V.A. Davydov, V.S. Zykov, A.S. Mikhailov and P.K. Brazhnik, Drift and resonance of spiral waves in excitable media, Radiophys. Quantum Electron. 31 (1988) 574.
[37] M. Markus, Zh. Nagy-Ungvarai and B. Hess, Phototaxis of spiral waves, Science 257 (1992) 225.
[38] M. Braune and H. Engel, Spiral drift in a light-sensitive active medium with spatial gradient of excitability, in: Spatio-Temporal Organization in Nonequilibrium Systems (Projekt Verlag, Dortmund, 1992) pp. 34–35.
[39] X. Zou, H. Levine and D.A. Kessler, Interaction between a drifting spiral and defects, preprint (1993).
[40] K.I. Agladze, V.A. Davydov and A.S. Mikhailov, Observation of a spiral-wave resonance in an excitable distributed medium, JETP Lett. 45 (1987) 767.
[41] E.A. Yermakova and A.M. Pertsov, Interaction of rotating spiral waves with a boundary, Biophysics (USSR) 31 (1986) 855.
[42] V.A. Davydov and V.S. Zykov, Spiral waves in a small disk and on a small sphere, in: Spatio-Temporal Organization in Nonequilibrium Systems, eds. S.C. Muller and Th. Plesser (Projekt Verlag, Dortmund, 1992) pp. 63–64.
[43] O. Steinbock, J. Schutze and S. Muller, Electric-field-induced drift and deformation of spiral waves in an excitable medium, Phys. Rev. Lett. 68 (1992) 248.
[44] E.A. Yermakova, A.M. Pertsov and E.E. Shnol, Pairs of interacting vortices in two-dimensional active media, Sov. Phys. Dokl. 33 (1988) 519.
[45] P. Pelcé and J. Sun, Wavefront interactions in steadily rotating spirals, Physica D 48 (1991) 353.
[46] A.J. Bernoff, Spiral wave solutions for reaction-diffusion equations in a fast reaction/slow diffusion limit, Physica D 53 (1991) 125.
[47] D. Kessler, H. Levine and W.N. Reynolds, Spiral core in singly diffusive excitable media, Phys. Rev. Lett. 68 (1992) 401.
[48] V.A. Davydov, A.S. Mikhailov and V.S. Zykov, Kinematical theory of autowave patterns in excitable media, in: Nonlinear waves in active media, eds. A. Crighton and Yu. Engelbrecht (Springer, Berlin, 1989) pp. 38–51.
[49] A. Karma, Universal limit of spiral wave propagation in excitable media, Phys. Rev. Lett. 66 (1991) 2274–2277.
[50] P.K. Brazhnik, V.A. Davydov, V.S. Zykov and A.S. Mikhailov, Vortex rings in distributed excitable media, JETP 66 (1987) 984.
[51] E. Meron and P. Pelcé, Model for spiral wave formation in excitable media, Phys. Rev. Lett. 60 (1988) 1880.

[52] P.K. Brazhnik, V.A. Davydov and A.S. Mikhailov, Spiral waves and vortex rings in combustion with subsequent recovery of the initial properties of the medium, in: Kinetics and Combustion, Proc. VIII Soviet Symp. on Combustion and Explosion, Tashkent, 1986 (Inst. Chem. Phys. Publ., Chernogolovka, 1986) pp. 39–43.
[53] V.A. Davydov and A.S. Mikhailov, Spiral waves in distributed active media, in: Nonlinear Waves. Structures and Bifurcations, eds. A.V. Gaponov-Grekhov and M.I. Rabinovich (Nauka, Moscow, 1987) pp. 262–279.
[54] P.K. Brazhnik, V.A. Davydov and A.S. Mikhailov, Kinematical approach to description of autowave processes in active media, Theor. Math. Phys. 74 (1988) 300.
[55] A.S. Mikhailov, Kinematics of wave patterns in excitable media, in: Nonlinear Wave Processes in Excitable Media, eds. A.V. Holden, M. Markus and H.G. Othmer (Plenum Press, New York, 1991) pp. 127–144.
[56] V.A. Davydov, V.S. Zykov and A.S. Mikhailov, Kinematics of autowave structures in excitable media, Sov. Phys. Usp. 34 (1991) 665.
[57] V.S. Zykov, Investigation of some properties of self-sustained activity in excitable media, in: Control of Complex Systems, ed. Ya. A. Tsypkin (Nauka, Moscow, 1975) pp. 59–66.
[58] D. Kessler, J. Koplik and H. Levine, Adv. Phys. 37 (1988) 255.
[59] V.I. Arnold, Catastrophe Theory (Springer, Berlin, 1986).
[60] I.M. Gel'fand, Some problems in the theory of quasilinear equations, Usp. Mat. Nauk 14 (1959) 87 [Am. Math. Soc. Transl., Ser. 2, 29 (1963) 295].
[61] A.M. Pertsov, A.V. Panfilov and E.A. Yermakova, Numerical simulations of spiral waves in active media, Physica D 14 (1984) 117–125.
[62] A.S. Mikhailov and V.S. Zykov, Kinematical theory of spiral waves in excitable media: comparison with numerical simulations, Physica D 52 (1991) 379.
[63] L.D. Landau and E.M. Lifshitz, Fluid Mechanics (Pergamon Press, London, 1959).
[64] S. Nettesheim, A. von Oertzen, H.H. Rotermund and G. Ertl, Reaction-diffusion patterns in the catalytic CO oxidation on Pt(110)–Front propagation and spiral waves, in: Spatio-Temporal Organization in Nonequilibrium Systems, eds. S.C. Muller and Th. Plesser (Projekt Verlag, Dortmund, 1992) pp. 184–186.
[65] V.A. Davydov and V.S. Zykov, Spiral waves in a round excitable medium, JETP 76 (1993) 414.
[66] C. Elphik, E. Meron, J. Rinzel and E.A. Spiegel, Impulse patterning and relaxational propagation in excitable media, J. Theor. Biol. 146 (1990) 249.
[67] E. Meron, The role of curvature and wavefront interactions in spiral wave dynamics, Physica D 49 (1991) 98.
[68] M. Courtemanche, L. Glass and J.P. Keener, Instabilities of a propagating pulse in a range of excitable media, Phys. Rev. Lett. 70 (1993) 2182.
[69] D. Barkley, Linear stability analysis of rotating spiral waves in excitable media, Phys. Rev. Lett. 68 (1992) 2090.
[70] V.S. Zykov, Kinematics of nonsteady circulation of spiral waves, Biophysics (USSR) 32 (1987) 385.
[71] P. Pelcé and J. Sun, On the stability of steadily rotating waves in the free boundary formulation, Physica D 6 (1993) 273.
[72] V.A. Davydov and V.S. Zykov, Spiral waves in anisotropic excitable media, JETP 68 (1989) 80–84.
[73] P.K. Brazhnik, V.A. Davydov and A.S. Mikhailov, Twisted scroll in excitable medium, Radiophys. Quantum Electron. 32 (1989) 219.
[74] A.Yu. Abramychev, V.A. Davydov and A.S. Mikhailov, On the theory of resonance in excitable media, Biofizik 34 (1990) 979 [Biophysics (USSR) 34 (1990)].
[75] W. Blaschke, Differential Geometry (Springer, Berlin, 1945).
[76] J. Maselko and K. Showalter, Chemical waves on spherical surfaces, Nature 339 (1989) 609.
[77] A.Yu. Abramychev, V.A. Davydov and V.S. Zykov, Drift of spiral waves on the nonuniformly curved surfaces, JETP 70 (1990) 666.

Reprinted from

PHYSICAL REVIEW
E

STATISTICAL PHYSICS, PLASMAS, FLUIDS, AND RELATED INTERDISCIPLINARY TOPICS

JUNE 1995
PART A

Traveling-wave fragments in anisotropic excitable media

F. Mertens, N. Gottschalk, M. Bär, M. Eiswirth, and A. Mikhailov
Fritz-Haber-Institut der Max-Planck-Gesellschaft, Faradayweg 4-6, D-14195 Berlin (Dahlem), Germany

R. Imbihl
Institut für Physikalische Chemie und Elektrochemie, Universität Hannover, Callinstrasse 3-3a, D-30167 Hannover, Germany

RC R5193-R5196

Published by
THE AMERICAN PHYSICAL SOCIETY
through the
American Institute of Physics

Volume 51 Third Series Number 6-A

Traveling-wave fragments in anisotropic excitable media

F. Mertens, N. Gottschalk, M. Bär,* M. Eiswirth, and A. Mikhailov
Fritz-Haber-Institut der Max-Planck-Gesellschaft, Faradayweg 4-6, D-14195 Berlin (Dahlem), Germany

R. Imbihl
Institut für Physikalische Chemie und Elektrochemie, Universität Hannover, Callinstrasse 3-3a, D-30167 Hannover, Germany
(Received 24 February 1995)

Experiments with an anisotropic chemical excitable medium—a catalytic chemical reaction on a single crystal surface—reveal a kind of stable wave pattern representing single traveling-wave fragments. Their existence is attributed to the presence of a strong state-dependent diffusion anisotropy in the medium. A simple theory of traveling fragments setting general conditions for their observation is proposed. Its conclusions are confirmed by numerical simulations of a reaction-diffusion model. Our analysis suggests that traveling-wave fragments are a general property of excitable media with strong state-dependent anisotropy.

PACS number(s): 05.40.+j, 82.20.Mj, 82.65.Jv

Phenomena of spatiotemporal self-organization in excitable media have attracted considerable interest in various fields from physics to biology. In chemical systems, wave formation has been extensively studied with various reaction systems of the Belousov-Zhabotinskii (BZ) type and the properties of target patterns, spiral waves, and stationary spots have been investigated [1–3]. These reactions occur in the fluid phase where diffusion is isotropic, and hence a question arises whether different kinds of patterns can be expected if the medium is anisotropic. When the diffusion constants of all species are made anisotropic by the same factor, the result would be an elliptical distortion of the patterns. The situation is different when the anisotropic varies depending on the state of the system. This is the situation realized in catalytic surface reactions. Such an anisotropy cannot in general be removed by rescaling the coordinates and the effects which are not found in isotropic media may therefore be observed [4–7]. In this paper we present experimental examples of different types of structures along with a theoretical analysis.

The standard method for initiating spiral waves in the BZ reaction consists of breaking a propagating excitation wave [8]. The appearing wave fragment grows, curls at its open ends, and eventually forms a pair of spiral waves. This evolution of a wave fragment is observed when the excitability of the medium is not too small. If the excitability is low, the wave fragment contracts and finally disappears [9]. Hence wave fragments in usual excitable media, such as the BZ reaction, are unstable: they either transform into a rotating spiral wave or vanish.

Here we report on the observation of single wave fragments in a surface reaction that are steadily traveling along a certain crystallographic direction. The reaction studied is the catalytic reduction of NO with hydrogen on a Rh(110) surface. The Rh(110) surface easily dissociates NO into atomic oxygen, O(ad), and atomic nitrogen, N(ad), and the dissociation products then recombine and react with dissociatively adsorbed hydrogen, H(ad), to the product molecules N_2 and H_2O. At low pressure in the 10^{-6} mbar range the process is truly isothermal. Under these conditions the reaction system represents an excitable medium, i.e., we observe target patterns and spiral waves. For imaging these patterns we employ photoemission electron microscopy (PEEM) [10]. This method, which yields a resolution of 0.1–1 μm, is sensitive to local work function variations. A strongly electronegative adsorbate such as oxygen is therefore imaged as a dark area while the nitrogen-covered and bare surface appear bright in PEEM.

In previous investigations, we have demonstrated that rectangularly shaped chemical wave patterns whose sides are oriented along two main crystallographic directions of Rh(110), i.e., along $[1\bar{1}0]$ and [001], can be observed in this system [4]. If we first generate such target patterns and then decrease the partial pressure p_{H_2} of hydrogen, we observe that those parts of the pattern which are oriented along the $[00\bar{1}]$ direction dissolve and only the parts oriented along the $[1\bar{1}0]$ direction remain. A further decrease of p_{H_2} leads to shrinking of fragments. If we wait until the fragments reach the size of a small nucleus and then increase back the hydrogen partial pressure, steadily traveling wave fragments are produced which are shown in Fig. 1.

Motion and evolution of individual wave fragments for different reaction conditions are demonstrated in Fig. 2. When the partial pressure p_{H_2} is high, the fragment evolves into a pair of counterrotating spirals [Fig. 2(a)]. For slightly lower partial pressure, steadily traveling and expanding wave fragments are observed [Fig. 2(b)]. When the pressure is further decreased, the fragments shrink [Fig. 2(c)].

The fragments shown in Fig. 2(b) travel at a constant velocity of 1.28 μm/s in the [001] direction while simultaneously expanding in the orthogonal direction, i.e., along $[1\bar{1}0]$. The bright area (low work function) forming the head of a traveling-wave fragment can be attributed to adsorbed nitrogen, while the black areas (high work function) are indicative of adsorbed oxygen. The triangular-shaped gray

*Present address: Department of Chemical Engineering, Princeton University, Princeton, NJ 08544.

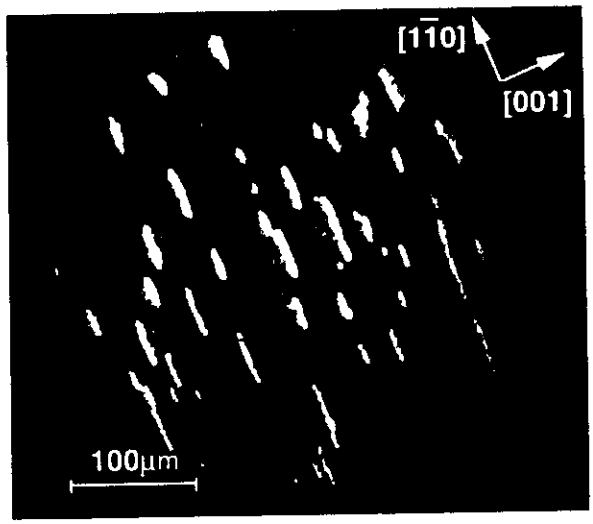

FIG. 1. Traveling-wave fragments in the catalytic NO-H_2 reaction on Rh(110) ($p_{H_2}=4.6\times10^{-6}$ mbar, $p_{NO}=1.8\times10^{-6}$ mbar, $T=620$ K). The fragments are moving in the [001] direction. The excited bright zone in the front is followed by the light gray refractory tail.

zones (intermediate work function) following the bright white stripes correspond to refractory tails of the wave fragments. The leading edges of the fragments exhibit a slight curvature. The trajectories of the fragment ends represent straight lines forming a cone symmetric to the [001] direction. For given parameters, the angular width of the cone is the same for any wave fragment in a medium; it is somewhat less than that of the cone formed by the refractory tail of a fragment. If two wave fragments traveling in the opposite direction collide, they annihilate each other. Note that traveling-wave fragments have previously been seen in experiments with a different catalytic surface reaction [11,12]; however, they were present in large numbers and interacted in a complicated way so that a study of the properties of an individual fragment was not possible.

In the following we construct a phenomenological model explaining the appearance of traveling-wave fragments and demonstrate by numerical simulations that these phenomena are reproduced when the state-dependent anisotropy is included in a typical reaction-diffusion model to reflect the microscopic picture of surface diffusion.

The observed wave patterns can be explained qualitatively, if the excitability of the medium is effectively angle dependent [6]. Suppose that along a certain direction the excitability is sufficient to induce growth and curling of the wave fragment while in the orthogonal direction it is so low that a fragment with this direction of motion should shrink. A flat wave fragment propagating in the high excitability direction would then first grow and curl. But, as curling proceeds and the propagation direction of the wave near its tip is changed, the speed of the growth would diminish because the medium's excitability experienced by the moving tip is decreased. Since at larger angles the growth is replaced by contraction, the tip would not complete in this case a full rotation and produce a spiral wave. Instead, a curved wave fragment traveling through the medium would be produced.

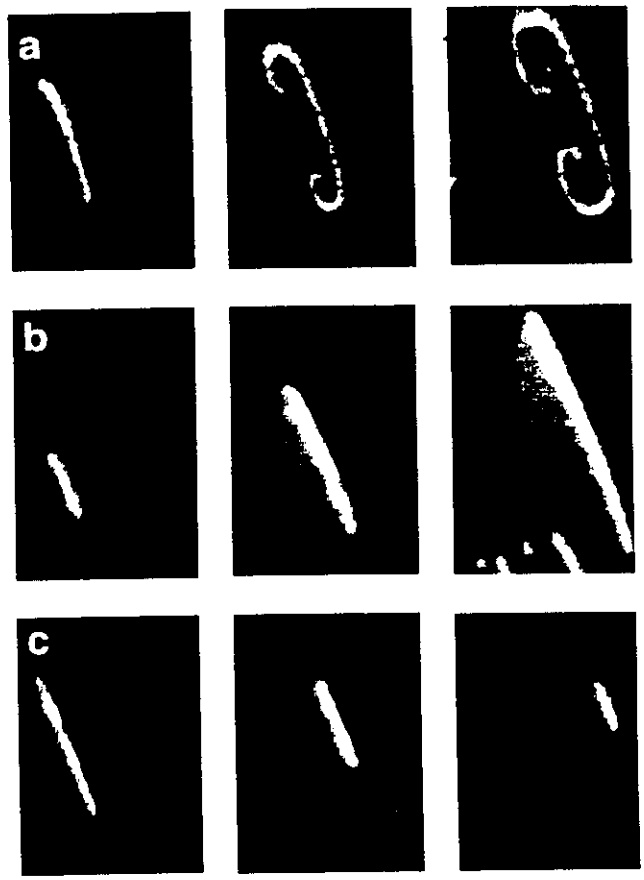

FIG. 2. Evolution of a single wave fragment for different experimental conditions in the catalytic surface reaction: (a) $p_{H_2}=5.5\times10^{-6}$ mbar, $p_{NO}=1.8\times10^{-6}$ mbar, $T=580$ K, the time interval Δt between the frames is 3 s; (b) $p_{H_2}=4.6\times10^{-6}$ mbar, $p_{NO}=1.8\times10^{-6}$ mbar, $T=620$ K, $\Delta t=30$ s; (c) $p_{H_2}=4.4\times10^{-6}$ mbar, $p_{NO}=1.8\times10^{-6}$ mbar, $T=620$ K, $\Delta t=30$ s. Subsequent frames are shifted to accommodate the entire traveling object. The size of the frames is 75×100 μm.

In the kinematic theory of wave propagation in excitable media [13,14] the narrow excitation zone is modeled by a single curve. If a wave is broken, its tip corresponds to an open end of this curve. Any element of the curve moves in its normal direction with velocity $V=V_0-Dk$ depending on the local curvature k of this element. Moreover, the curve can grow or shrink at its open end with velocity $G=G_0-\gamma k_0$ that depends on the curvature k_0 at the end point; note that G_0 reflects the effective excitability of the medium [6]. If a medium is anisotropic, both V and G also depend on the angle α between the local propagation direction and the anisotropy axis. Suppose that the velocity G changes its sign at a certain angle α_0. Then, for higher angles, sprouting of the tip is replaced by its contraction, When this occurs, sprouting and curling of the wave fragment continues only until this angle is reached and steadily traveling wave fragments with a constant angular width of $2\alpha_0$ are thus produced. Figure 3 shows the evolution of wave fragments obtained by the numerical integration of the kinematic equations for anisotropic excitable media [5,6].

Since simple anisotropy could be scaled out by stretching the coordinates—a transformation which does not change the

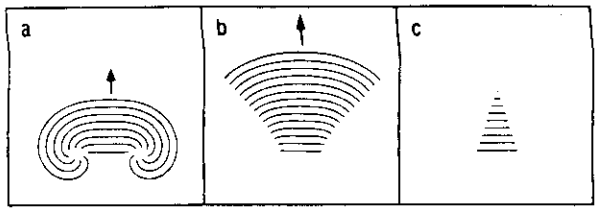

FIG. 3. Kinematics of wave fragments. Time evolution of an initially flat fragment with small perturbations near its open ends is shown. The angular dependence of the tangential tip velocity is $G_0 = A - B(\sin\alpha)^2$, the normal propagation velocity is constant. The vertical direction represents $\alpha = 0$. The kinematical parameters are $V_0 = 1.5$, $D = 1.0$, $\gamma = 1.5$, $B = 1.0$, and (a) $A = 1.5$, (b) $A = 0.5$, (c) $A = -0.5$.

sign of the tip velocity—such behavior of the wave fragments is possible only in reaction-diffusion systems with the state-dependent anisotropy. In the catalytic surface reaction considered here a state-dependent anisotropy is realized by two different types of surfaces reconstructions induced by atomic oxygen and nitrogen, respectively. While atomic oxygen generates so-called missing-row type reconstructions consisting of atomic troughs along the $[1\bar{1}0]$ direction, atomic nitrogen gives rise to the Rh-N chains which are oriented perpendicular to the direction of oxygen-induced troughs [15–17]. Assuming that diffusional anisotropy is merely determined by the substrate geometry, the change from oxygen to nitrogen which occurs in the reaction front causes a rotation of the anisotropy axis by 90°.

Pattern formation on catalytic surfaces can be described by a two-component model with a fast activator variable (u) representing an adsorbate coverage (changing rapidly due to adsorption and reaction processes) and a slow inhibitor variable (v) representing the degree of surface reconstruction and acting as a negative feedback on the coverage [18]. In order to demonstrate that a state-dependent diffusion anisotropy explains the appearance of steadily traveling wave fragments, we have numerically integrated a modification of the well-known FitzHugh-Nagumo model for an excitable medium given by equations

$$\partial_t u = (u - u^3/3 - v)/\varepsilon + \partial_x[D_x(v)\partial_x u] + \partial_y[D_y(v)\partial_y u],$$

$$\partial_t v = u + b - av. \tag{1}$$

Because surface reconstructions are nondiffusive, we assume that spatial coupling is only due to diffusion of the adsorbate represented here by the activator species u. As noted above, under our experimental conditions the diffusional anisotropy of the adsorbate (activator) species is controlled by the surface structure. This state-dependent anisotropy of diffusion due to adsorbate-induced reconstructions is modeled in (1) by introducing a steplike dependence of diffusion coefficients on the surface reconstruction variable v,

$$D_x = D_0, \quad D_y(v) = \begin{cases} D_1, & v \le v_{\text{crit}} \\ D_2, & v > v_{\text{crit}}. \end{cases} \tag{2}$$

Diffusion in the x direction is kept constant, but in the y direction we switch the diffusion constant between two values, depending on the degree of reconstruction (v).

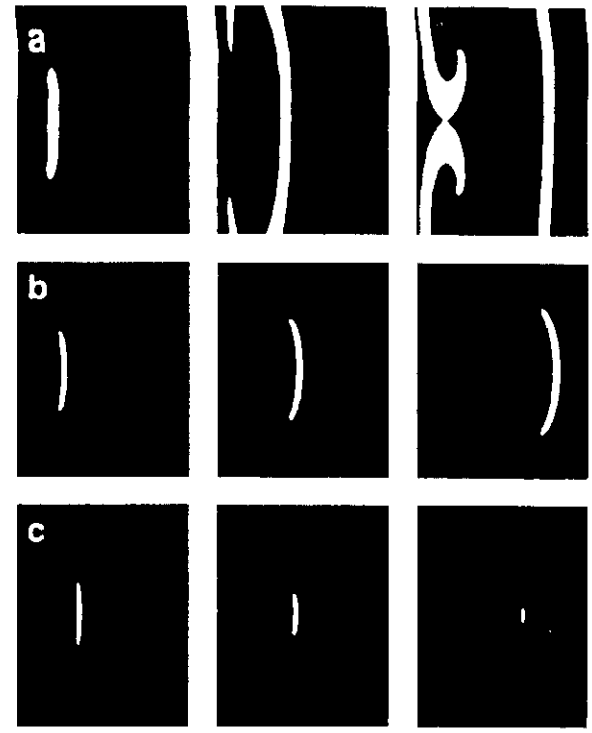

FIG. 4. Evolution of fragments in a numerical simulation of the surface reaction. The model parameters are $a = 0.5$, $\varepsilon = 0.25$, $D_0 = 0.25$, $D_1 = 1.0$, $D_2 = 3.0$, $v_{\text{crit}} = -0.4415$ and (a) $b = 0.97$, (b) $b = 1.12$, (c) $b = 1.18$. The y direction (which exhibits state-dependent diffusion) is parallel to the vertical axis. The time step is 0.000 18, the coordinate step is 0.04, and the grid length is 345×512. Subsequent frames are separated by time intervals $\Delta t = 2.0$.

The results of numerical simulations are shown in Fig. 4. When the excitability of the medium (controlled by parameter b in this model) is sufficiently high, a pair of counterrotating spiral waves develops from the initial flat wave segment [Fig. 4(a)]. Upon decreasing excitability, traveling-wave fragments are found [Fig. 4(b)] which transform, at still lower excitabilities, into the shrinking fragments [Fig. 4(c)]. The angular width of the traveling fragments shown in Fig. 4(b) depends on the parameter b, and the parameter window within which these patterns exist increases with the degree of the state-dependent anisotropy in the system characterized by the difference between D_1 and D_2.

As shown above, traveling-wave fragments represent another type of persistent pattern in excitable media with state-dependent anisotropy. Though the reported experiments have been performed for a particular system with a catalytic surface reaction, the theory is general and applies for excitable systems with state-dependent diffusion anisotropy of various origins.

Financial support from the Alexander-von-Humboldt Stiftung and from the Volkswagen Stiftung is gratefully acknowledged.

[1] A. M. Zhabotinskii and A. N. Zaikin, Nature (London) **225**, 535 (1970).
[2] A. T. Winfree, Science **175**, 634 (1972).
[3] K.-J. Lee, W. D. MacCormick, J. E. Pearson, and H. L. Swinney, Nature (London) **369**, 215 (1994).
[4] F. Mertens and R. Imbihl, Nature (London) **370**, 124 (1994).
[5] A. Mikhailov, Phys. Rev. E **49**, 5875 (1994).
[6] A. Mikhailov and V. Zykov, in *Chemical Waves and Patterns*, edited by R. Kapral and K. Showalter (Kluwer, Dordrecht, 1995), pp. 119–162.
[7] N. Gottschalk, F. Mertens, M. Bär, M. Eiswirth, and R. Imbihl, Phys. Rev. Lett. **73**, 3483 (1994).
[8] G. R. Ivanitsky, V. I. Krinsky, A. N. Zaikin, and A. M. Zhabotinskii, Sov. Sci. Rev. **2D**, 280 (1980).
[9] Zs. Nagy-Ungvarai, J. Ungvarai, S. C. Müller, and B. Hess, J. Chem. Phys. **97**, 1004 (1992).
[10] W. Engel, M. E. Kordesch, H. H. Rotermund, S. Kubala, and A. von Oertzen, Ultramicroscopy **36**, 148 (1991).
[11] H. H. Rotermund, S. Jakubith, A. von Oertzen, and G. Ertl, Phys. Rev. Lett. **66**, 3083 (1991).
[12] M. Bär, M. Eiswirth, H. Rotermund, and G. Ertl, Phys. Rev. Lett. **69**, 945 (1992).
[13] A. Mikhailov, *Foundations of Synergetics*, 2nd revised ed. (Springer, Berlin, 1994), Vol. 1.
[14] A. Mikhailov, V. A. Davydov, and V. S. Zykov, Physica D **70**, 1 (1994).
[15] F. M. Leibsle, P. W. Murray, S. M. Francis, G. Thornton, and M. Bowker, Nature (London) **363**, 706 (1993).
[16] P. W. Murray, F. M. Leibsle, G. Thornton, M. Bowker, V. R. Dhanak, A. Baraldi, M. Kiskinova, and R. Rosei, Surf. Sci. **304**, 48 (1994).
[17] P. W. Murray, G. Thornton, M. Bowker, V. R. Dhanak, A. Baraldi, R. Rosei, and M. Kiskinova, Phys. Rev. Lett. **71**, 4369 (1993).
[18] M. Eiswirth and G. Ertl, in *Chemical Waves and Patterns*, edited by R. Kapral and K. Showalter (Kluwer, Dordrecht, 1995), pp. 447–484.

Bifurcation to Traveling Spots in Reaction-Diffusion Systems

K. Krischer[1] and A. Mikhailov[1,2]

[1]*Fritz-Haber-Institut der Max-Planck-Gesellschaft, Faradayweg 4-6, 14195 Berlin (Dahlem), Germany*
[2]*N.N. Semenov Institute for Chemical Physics, Russian Academy of Sciences, ul. Kosygina 4, 117333 Moscow, Russia*
(Received 6 June 1994)

A bifurcation leading to the onset of translational motion of localized particlelike structures (spots) in two-dimensional excitable media with long-range inhibition and global coupling is analytically and numerically investigated. Properties of slowly traveling spots and effects of collisions between these objects are studied.

PACS numbers: 82.20.Wt, 47.54.+r, 82.20.Mj

Recent experiments and numerical simulations [1–4] brought attention to the phenomena of pattern formation in two-dimensional reaction-diffusion systems which involve localized particlelike structures (spots). A spot represents a region filled with activator and surrounded by a larger inhibitor cloud. Localized one-dimensional patterns (standing and moving pulses or filaments) have been also observed in semiconductor materials [5,6], in gas discharge phenomena [7], and in chemical systems [8]. Explicit analytical solutions for stationary and moving pulses [9–11] and for stationary two-dimensional spots [12] have been constructed, and instabilities of one-dimensional localized patterns [10,13] and the onset of breathing and static deformations of two-dimensional spots [12] have been analyzed.

The aim of the present Letter is to investigate the spontaneous onset of translational motion of stationary two-dimensional spots. This instability may be viewed as an analog of the meandering transition for spiral waves (see, e.g., [14]) or mobility onset for defects in coupled chaotic map lattices [15], which play an important role in the transition to developed reaction-diffusion turbulence. We find that the bifurcation is supercritical only in the presence of sufficiently strong global coupling. Near such a bifurcation an excitable two-dimensional medium with long-range inhibition exhibits a special kind of pattern—localized steadily moving spots filled with activator and surrounded by a large cloud of the inhibitor. As the bifurcation point is approached, their velocity gradually decreases and they transform into stable static spots.

We consider a reaction-diffusion system described by the equations:

$$\dot{u} = -u + H(u - a) - v + \nabla^2 u,$$
$$\tau \dot{v} = \mu u - v + L^2 \nabla^2 v, \qquad (1)$$

where $H(z)$ is the step function, $H(z) = 0$ for $z < 0$ and $H(z) = 1$ for $z > 0$. This system represents a variant of the Rinzel-Keller model [16] with additional diffusion of the inhibitor v. We study the case when the diffusion length L of the inhibitor is much larger than the diffusion length of the activator u, which is equal to unity in our notation. Therefore, we choose $L = \varepsilon^{-1}$ and $\tau = (\varepsilon\sigma)^{-1}$, where $\varepsilon \ll 1$ and $\sigma = L/\tau$ is an independent parameter. The system has a stable uniform stationary state ($u = v = 0$) with the excitation threshold a. Global coupling is introduced similar to Refs. [8] and [17] by assuming that the threshold a depends on the total activator and inhibitor concentrations in the medium, i.e., that $a = a_0 + \alpha(s - s_0)$ where

$$S = \int (u + v)\, dx, \qquad (2)$$

and α is a positive coefficient.

We look first at the one-dimensional case where stationary and propagating pulse solutions could be explicitly constructed using the singular perturbation approximation [10,11]. We generalized this construction in order to include the effects of global coupling. Figure 1 shows the obtained bifurcation diagram for localized stationary and traveling solutions of Eq. (1) in the limit $\varepsilon \to 0$. As long as parameter $\sigma = L/\tau$ is large, a stationary pulse (with velocity $c = 0$) is the only nontrivial stable solution. When σ is decreased, the stationary solution loses its stability and at $\sigma = 0.179$ it gives rise to two traveling pulses with opposite velocities. In the absence of global coupling the bifurcation is subcritical so that moving and standing pulses can coexist in a certain parameter interval (cf. [11]). Sufficiently strong global coupling makes it supercritical (it also suppresses the breathing instability of pulses not shown in Fig. 1). When the bifurcation is supercritical, the velocity of pulses is vanishingly small at the critical point and their profile is close to that of a stationary pulse.

Standing one-dimensional pulses correspond to stationary spots in two-dimensional media. However, not every moving pulse gives rise to a traveling spot in two dimensions. To suppress spots from blowing up into spatially extended patterns (i.e., into propagating excitation waves), sufficiently strong global inhibitory coupling is required.

A mathematical method for the stability analysis of two-dimensional localized patterns in excitable media with long-range inhibition has been proposed by Ohta *et al.* [12]. Since the boundary of the excited domain, forming the core of the spot pattern, is narrow when the parameter ε in Eq. (1) is small, its width can be neglected and it can be represented approximately by a

0031-9007/94/73(23)/3165(4)$06.00

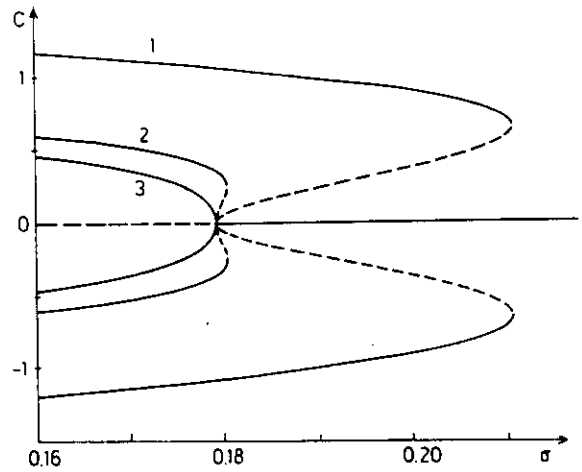

FIG. 1. Velocity of traveling pulse solutions of Eq. (1) as a function of σ in the limit of $\varepsilon \to 0$ for the one-dimensional case. Curves 1, 2, and 3 correspond to different coupling strengths ($\alpha = 0$, 0.1, and 0.2, respectively). Dashed lines indicate unstable solutions. A stationary pulse ($c = 0$) is stable for $\sigma > 0.179$.

single closed curve Γ. Since the boundary of the core is essentially an activator front, its motion is controlled by the local inhibitor concentration. The activator is produced inside the region bounded by curve Γ but can diffuse out of this region. Because the second equation in model (1) is linear, a closed dynamical equation for the motion and time-dependent deformations of the curve Γ could be constructed. Because of inhibitor diffusion, it contains retarded interactions between distant elements of the boundary curve. The stability analysis is thus reduced to the investigation of small perturbations of the steady solution of this equation describing a stationary spot. This method was used to investigate the stability of stationary spots with respect to their radial breathing and asymmetric static deformations [12]. We have applied it to analyze the instability leading to translational motion of spots in the presence of global coupling.

Omitting the derivation, which is performed following the steps outlined above in close analogy to Ref. [12], we find that the increment z of growth of perturbations representing a small shift of the activator core is given by the root of the equation $F(z) = 0$ where

$$F(z) = \sigma z - \xi\rho[I_1(\rho)K_1(\rho) - I_1(\rho\sqrt{1+z})K_1(\rho\sqrt{1+z})]. \quad (3)$$

Here $I_n(x)$ and $K_n(x)$ are the modified Bessel functions, $\rho = (1+\mu)^{1/2}R$ is the rescaled radius R of the stationary spot, and the coefficient ξ is approximately given by $\xi = 4\mu(1+\mu)^{-3/2}$. The radius is determined by the same set of matching equations as in Ref. [12] with the only change that in the presence of global coupling the threshold a in these equations becomes a function of the radius, i.e., $a = a_0 + \alpha(s - s_0)$, where s is the total excited area [when only one spot is found in the medium, $s = \pi\rho^2(1+\mu)^{-1}$]. Note that the radius of the spots does not depend on the parameter σ.

Equation $F(z) = 0$ always has a root $z = 0$ due to the invariance with respect to translations of the whole localized solution. A nontrivial perturbation mode consists of a shift of the activator core against a fixed background of the inhibitor distribution. At the onset of translational motion, the real root z associated with this mode changes its sign and becomes positive. Thus, the function $F(z)$ must have a doubly degenerate root $z = 0$ at the critical point. Requiring that $dF/dz = 0$, we find that stationary spots become absolutely unstable with respect to the onset of translational motion for $\sigma < \sigma_c$ where

$$\sigma_c = \frac{1}{4\xi\rho}\{I_1(\rho)[K_0(\rho) + K_2(\rho)] - K_1(\rho)[I_0(\rho) + I_2(\rho)]\}. \quad (4)$$

For the system without global coupling, Fig. 2 shows the boundary for the onset of translational motion given by Eq. (4) and the boundaries of instabilities with respect to breating and static deformations of the spot derived in Ref. [12]. We see that upon decreasing the control parameter σ the bifurcation leading to the onset of translational motion is preceded by the breathing instability of stationary spots. When the excitation threshold a is decreased at fixed σ, the radius of stationary spots grows, and they undergo static deformations (which may lead to the development of labyrinthine patterns, cf. [18]).

Note that the excitation threshold $a = a_0 + \alpha(s - s_0)$ is not changed by any transformation that conserves the total excited area s given by (2). If s_0 is chosen equal to the value of s for a stationary spot without global coupling, stationary spots under strong global coupling have the same shape and radius as in its absence (i.e., for $\alpha = 0$). At the bifurcation leading to the onset of translational motion, the spots are moving slowly (with $c \to 0$) and have practically the same shape and total excited area as the stationary ones. Therefore, the boundary of this bifurcation (given by curve t in Fig. 2) is not sensitive to global coupling when this choice is made. However, it stabilizes slowly moving (and stationary) spots by preventing their blowup.

We performed numerical simulations of spots in the vicinity of the boundary t of the bifurcation to translational motion for different values of the global coupling coefficient α. The numerical simulations of spots in model (1) meet certain difficulties. They are caused by a large difference in the diffusion lengths of activator and inhibitor species (in our simulations the ratio of two diffusion lengths was $\varepsilon = 0.125$). When a standard forward Euler scheme is chosen, this would lead to enormous computation times. The computational speed can be much enhanced if the grid size of the inhibitor is adjusted, so that the resolutions of activator and inhibitor are equal with respect to their characteristic lengths. Moreover, we speed up the simulations by using different time

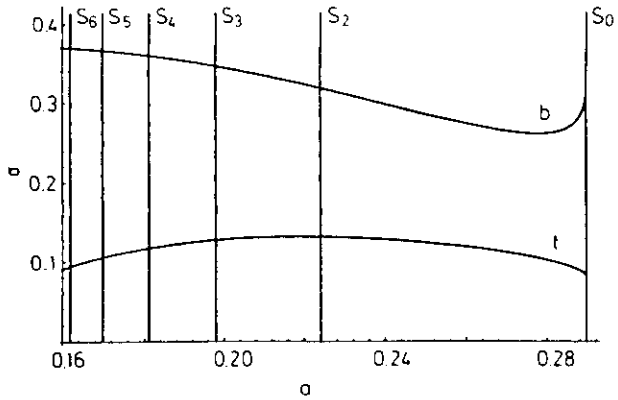

FIG. 2. Bifurcation diagram in the plane (a, σ) for the two-dimensional case without global coupling, $\varepsilon = 0.125$. Stationary spots exist to the left of the vertical boundary s_0. A stationary spot is unstable with respect to the breathing instability below boundary b; it is unstable with respect to static deformations of angular symmetry $n = 2, 3, 4, 5, \ldots$ to the left of the vertical boundaries s_n. Curve t gives the boundary of the instability resulting in translational motion.

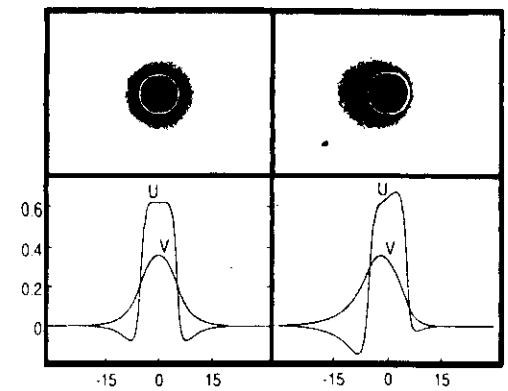

FIG. 3. Gray-level representation and profiles of a stationary spot (left, $\sigma = 1.0$) and a traveling spot close to the onset of translational motion (right, $\sigma = 0.0975$); other parameters are $\mu = 3.0$, $L = 8.0$, $a_0 = 0.275$, $\alpha = 5.0$, and $s_0 = 0.03$. The gray-scale representations show the distribution of the inhibitor; the white contours show the activator interface.

steps for the integration of u and v, each time step given by the stability boundary of the numerical scheme. In this way not only do we reduce the number of grid points for the inhibitor field by nearly 2 orders of magnitude, it also allows us to use 10^2–10^3 times larger time steps. To obtain the values of v at grid points and time steps at which they are not calculated explicitly, linear interpolation is applied. A further increase in the speed of calculations is achieved by altering the original variable u to the new variable $\bar{u} = u + v$ in Eq. (1). It could be shown that this combination (exponentially) vanishes outside the spot. This means that we can use in this region an "active" procedure for the calculation of the Laplacian proposed by Barkley [19]; i.e., we do not compute it whenever the value of $\bar{u}$ falls below a preset value (which was 10^{-4} in our calculations).

Our simulations demonstrate that breathing instability is suppressed by strong global coupling and that the system exhibits a supercritical bifurcation leading to the onset of translational motion of spots. Figure 3 shows (i) a stationary spot and (ii) a slowly moving spot slightly below the critical point $\sigma_c = 0.108$ for $\alpha = 5.0$. We see that the transformation to moving spots is accompanied by a shift of the activator domain (white contour in Fig. 3) with respect to the inhibitor cloud, which makes the pattern asymmetric. The presence of strong global coupling is essential for the existence of traveling spots: If we gradually decrease the coupling coefficient α while keeping other parameters fixed, the moving spot expands, elongates in the transverse direction, and finally transforms into an extended propagating wave pattern (Fig. 4).

Steadily moving spots obtained as a result of the bifurcation represent a special type of spatiotemporal pattern in two-dimensional excitable media. We have numerically investigated collisions between such spots. Close to the bifurcation point, elastic scattering of slowly moving spots has been found [Fig. 5(a)]. The spots approach one another, slow down, change the direction of their motion, and move away. Characteristically, the regions filled with the activator do not come into contact in such a collision. Bouncing results from an increase of the inhibitor concentration in the region between two colliding activator cores. Under the same conditions, slowly moving spots were found in our simulations to scatter from no-flux boundaries of the medium.

Frontal collisions between faster moving spots found farther away from the bifurcation point [Fig. 5(b)] lead to the formation of a single bound state where the cores of two spots are fused together. After a while this bound state breaks apart and gives rise to spots which move away in a direction perpendicular to the original direction of motion of the particles. In contrast to this, an oblique collision [Fig. 5(c)] ends with the formation of one larger stable moving spot; i.e., the collision between the particles is in this case inelastic. The effect of inelastic collisions demonstrates also the multiplicity of traveling spot solutions: instead of a few smaller spots the medium

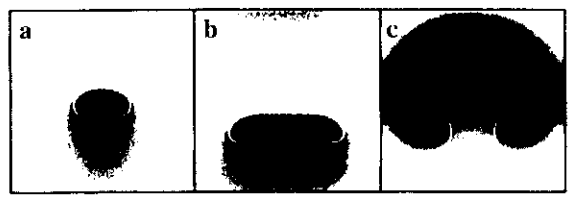

FIG. 4. Transition from a localized moving spot to an extended propagating wave pattern as the coupling strength is decreased: (a) $\alpha = 5.0$, (b) $\alpha = 1.0$, (c) $\alpha = 0$; $\sigma = 0.05$; other parameters are the same as in Fig. 3. For the activator (inhibitor) field, 400×400 (50×50) grid points were used.

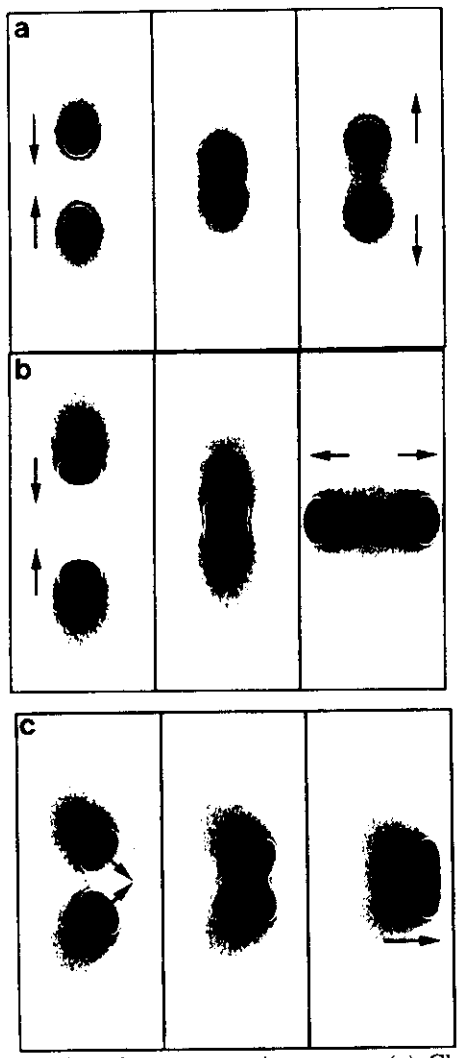

FIG. 5. Collisions between moving spots. (a) Close to the onset of translational motion ($\sigma = 0.0975$), colliding spots are elastically scattered. (b) Frontal collision of fast-moving spots ($\sigma = 0.05$) leads to a 90° change of the direction of motion. (c) Oblique collision of fast-moving spots ($\sigma = 0.05$) results in a single-moving spot of a larger size. The parameters were chosen as in Fig. 3, but $s_0 = 0.06$ (activator field: 800×400, inhibitor field: 100×50).

may form a larger spot, providing that the total excited area s remains approximately constant. When inelastic scattering is possible, a moving spot can stick to a no-flux boundary and continue motion along it.

Though our study has been confined to a particular model, we believe that its results illustrate generic properties of excitable media with long-range slow inhibition and global coupling. Traveling spots may represent fundamental elementary patterns in such distributed dynamical systems, as typical as spiral waves in more usual excitable media with short-range slow inhibition. Remarkably, a population of traveling spots would behave as a reactive gas of self-moving particles. A challenge is to construct the statistical mechanics and "chemistry" of these objects.

The authors are grateful to M. Lübke for preparation of some of the drawings. The financial support from Alexander von Humboldt-Stiftung and Deutsche Forschungsgemeinschaft is acknowledged.

[1] K.-J. Lee, W. D. McCormick, J. E. Pearson, and H. L. Swinney, Nature (London) **369**, 215 (1994).
[2] J. E. Pearson, Science **261**, 189 (1993).
[3] E. Anmelt, D. Schweng, and H.-G. Purwins, Phys. Lett. **173**, 348 (1993).
[4] U. Middya and D. Luss, J. Chem. Phys. **100**, 6386 (1994).
[5] B. S. Kerner and V. F. Sinkevich, JETP Lett. **36**, 436 (1982).
[6] F.-J. Niedernostheide, B. S. Kerner, and H.-G. Purwins, Phys. Rev. B **46**, 7559 (1992).
[7] H. Willebrand, T. Hunter, F.-J. Niedernostheide, R. Dohmen, and H.-G. Purwins, Phys. Rev. A **45**, 8766 (1992).
[8] U. Middya, M. D. Graham, D. Luss, and M. Sheintuch, J. Chem. Phys. **98**, 2823 (1993).
[9] A. S. Mikhailov, *Foundations of Synergetics I* (Springer, Berlin-Heidelberg, 1990; 2nd revised edition 1994).
[10] S. Koga and Y. Kuramoto, Prog. Theor. Phys. **63**, 106 (1980); see also, J. D. Dockery and J. P. Keener, SIAM J. Appl. Math. **49**, 539 (1989); P. Ortoleva and R. Sultan, Chem. Physics **148**, 47 (1990).
[11] A. Ito and T. Ohta, Phys. Rev. A **45**, 8374 (1992).
[12] T. Ohta, M. Mimura, and R. Kobayashi, Physica (Amsterdam) **34D**, 115 (1989); this method is further developed in D. M. Petrich and R. E. Goldstein, Phys. Rev. Lett. **72**, 1120 (1994).
[13] See B. Kerner and V. V. Osipov, Sov. Phys. Usp. **32**, 101 (1989), and references therein.
[14] D. Barkley, Phys. Rev. Lett. **72**, 164 (1994).
[15] K. Kaneko, Physica (Amsterdam) **34D**, 1 (1989).
[16] J. Rinzel and J. B. Keller, Biophys. J. **13**, 1313 (1973).
[17] G. Veser, F. Mertens, A. S. Mikhailov, and R. Imbihl, Phys. Rev. Lett. **77**, 975 (1993); F. Mertens, R. Imbihl, and A. Mikhailov, J. Chem. Phys. **99**, 8668 (1993).
[18] A. Hagberg and E. Meron, Phys. Rev. Lett. **72**, 2494 (1994).
[19] D. Barkley, Physica (Amsterdam) **49D**, 61 (1991).

Reprinted from

PHYSICA D

Physica D 90 (1996) 84–95

Controlling turbulence in the complex Ginzburg–Landau equation

D. Battogtokh,[1] A. Mikhailov

Fritz-Haber-Institut der Max-Planck-Gesellschaft, Faradayweg 4-6, 14195 Berlin (Dahlem), Germany

Received 26 April 1995; revised 26 June 1995; accepted 10 July 1995
Communicated by Y. Kuramoto

N·H

ELSEVIER

PHYSICA D

Nonlinear Phenomena

Aims and Scope

Physica D contains papers and review articles reporting experiments, techniques and ideas which, although they may be derived and explained in the context of a particular field, advance the understanding of nonlinear phenomena in general. Contributions of this type in the literature have dealt with: wave motion in physical, chemical and biological systems; chaotic motion in models relevant to turbulence; quantum and statistical mechanics governed by nonlinear field equations; instability, bifurcation, pattern formation and cooperative phenomena.

Abstracted/indexed in:
ACN Computing Reviews; Applied Mechanics Reviews; Current Contents: Physical, Chemical & Earth Sciences; EI Compendex Plus; Engineering Index; INSPEC; Physics Briefs

Subscription Information 1995
Physica A (ISSN 0378-4371). For 1996, Volumes 223–234 are scheduled for publication. Physica A is published semimonthly.
Physica B (ISSN 0921-4526). For 1996, Volumes 215–228 are scheduled for publication. Physica B is published semimonthly except in July, August, September, November and December.
Physica C (ISSN 0921-4534). For 1996, Volumes 256–279 are scheduled for publication. Physica C is published two to three times per month.
Physica D (ISSN 0167-2789). For 1996, Volumes 89–98 are scheduled for publication. Physica D is published semimonthly.
Subscription prices are available upon request from the Publisher. Combined subscriptions to Physica A, Physica B, Physica C and Physica D are available at a reduced rate. Subscriptions are accepted on a prepaid basis only and are entered on a calendar year basis. Issues are sent by SAL (Surface Air Lifted) wherever this service is available. Airmail rates are available upon request. Please address all your requests regarding orders and subscription queries to: *Elsevier Science B.V., Order Fulfilment Department, P.O. Box 211, 1000 AE Amsterdam, The Netherlands, Tel. + 31 20 4853642, Fax. + 31 20 4853598.* Claims for issues not received should be made within six months of our publication (mailing) date.

US mailing notice - Physica D (ISSN 0167-2789) is published semimonthly by Elsevier Science B.V., Molenwerf 1, P.O. Box 211, 1000 AE Amsterdam, The Netherlands. The annual subscription price in the USA is US$ 2836 (valid in North, Central and South America only), including air speed delivery. Second class postage paid at Jamaica, NY 11431.
USA POSTMASTERS: Send address changes to Physica D, Publications Expediting, Inc., 200 Meacham Avenue, Elmont, NY 11003. Airfreight and mailing in the USA by Publication Expediting.

⊗ The paper used in this publication meets the requirements of ANSI/NISO 239.48-1992 (Permanence of Paper).

Printed in The Netherlands

North-Holland, an imprint of Elsevier Science

ELSEVIER

Physica D 90 (1996) 84–95

PHYSICA D

Controlling turbulence in the complex Ginzburg–Landau equation

D. Battogtokh,[1] A. Mikhailov

Fritz-Haber-Institut der Max-Planck-Gesellschaft, Faradayweg 4-6, 14195 Berlin (Dahlem), Germany

Received 26 April 1995; revised 26 June 1995; accepted 10 July 1995
Communicated by Y. Kuramoto

Abstract

We suggest that diffusion-induced turbulence in distributed dynamical systems near a supercritical Hopf bifurcation can be controlled by means of global delayed feedback. Analytical and numerical investigations of this method for a system described by the complex Ginzburg–Landau equation are performed. Suppression of phase and amplitude turbulence is found inside a window of delay times under increasing the intensity of the control signal.

1. Introduction

Suppression of spatiotemporal chaos (turbulence) in distributed dynamical systems is a problem of much practical interest. When only a few unstable spatial modes are present, this problem can be solved by identifying the unstable directions and computing the corrective perturbations [1]. The amount of needed computation, however, rapidly grows with the number of unstable modes and therefore such approach becomes intractable for developed turbulence. For dynamical systems with a few degrees of freedom, an alternative empirical method [2,3] is known which is based on introduction of delayed feedbacks and does not require computer processing. In this paper we suggest a similar method for controlling turbulence in distributed dynamical systems. We show that developed turbulence in the system described by the one-dimensional complex Ginzburg–Landau equation can be suppressed by introduction of global delayed feedback. The synchronization is achieved by adjusting only two parameters: the intensity of the control signal and the delay time.

The complex Ginzburg–Landau equation (CGLE) represents a normal form for distributed dynamical systems with local diffusion coupling near the supercritical Hopf bifurcation [4,5]. When the Benjamin–Feir condition is satisfied, synchronous uniform oscillations in this system are unstable and turbulence develops. 'Phase turbulence' is characterized by small variations of real amplitudes and slow irregular

[1] On leave from the Institute for Mathematics, Mongolian Academy of Sciences, Zhukov av. 51, Ulan Bator, Mongolia, and Department of Physics, Moscow State University, 117234 Moscow, Russia.

SSDI 0167-2789(95)00232-4

drift of local oscillation phases [6]. 'Amplitude turbulence' displays rapid local variations of both the real amplitude and the phase, which can be attributed to the presence of defects [6,7]. The oscillation amplitude is greatly reduced in the center of a defect and the oscillation phases on the left and right sides of it are considerably different; the defects are closely related to the family of exact solutions obtained by Bekki and Nozaki [8]. Extensive statistical investigations of such chaotic regimes have been performed in Refs. [9,10]; they show that these regimes are characterized by the presence of only short-range spatial correlations and by a great number of unstable modes.

Recently, the action of external periodic forces on the system described by CGLE has been studied [11,12]. By applying a sufficiently strong force, the stabilization of uniform oscillations could be achieved. However, the efficiency of such external control is too sensitive to the choice of the modulation frequency: large forces are needed out of the complete resonance.

It is known that the behaviour of large oscillatory populations can be modified by introduction of global coupling between the oscillators. Such coupling is equivalent to application of a periodic force which is collectively produced by all elements in the population. Strong global coupling can synchronize oscillations in heterogeneous systems with a random distribution of oscillation frequencies [6]. In uniform populations, global coupling can lead to formation of clusters and emergence of chaotic collective dynamics [13,14].

In some experimental situations, a distributed oscillatory system may have both local and global couplings between its elements. In surface chemical reactions, the local coupling between the surface elements is due to diffusion in the surface plane while the global coupling is produced by interactions through the gas phase, where rapid mixing is realized [15]. The effect of global coupling in such oscillatory chemical reactions have been considered in [16–21]. A simple model of global coupling is oscillatory chemical reactions [17,18] represents the complex Ginzburg–Landau equation with an additional linear term that is proportional to the spatial average of the complex oscillation amplitude. Under certain conditions, global coupling can suppress turbulence, leading to standing waves and uniform oscillations [19].

Global coupling can be viewed as a form of the feedback. Though in some experimental situations such global interaction is a natural property of the system, it can also be artificially implemented to control the behaviour of systems of various origins. In practice, however, the control methods based on artificial global coupling would meet serious difficulties. Indeed, the global feedback can be introduced in many different ways and, generally, it would be characterized by a large number of free parameters. How to choose these parameters and which of them should be varied in order to produce synchronization is far from clear. Alternatively, one can try first to derive the complex Ginzburg–Landau equation for a considered system near the Hopf bifurcation and then use the computed CGLE coefficients to fix the control parameters. But calculation of these coefficients is a cumbersome procedure. Moreover, analytical knowledge of full dynamical equations describing the experimental system would then be required.

In this paper we suggest to use the *delayed* global feedback. We show that in this case there are two simple parameters whose variation is sufficient to impose the synchronization. They are the intensity of the control signal and the delay time. By varying them, turbulence can be suppressed, irrelevant to the values of the CGLE coefficients and the coupling parameters.

In the next section we formulate the method and perform preliminary analysis of the dynamical equations. The stability investigation of uniform oscillations in the presence of the control signal is carried out in Section 3. The numerical simulations of the control problem are the subject of Section 4. The paper ends with

conclusions and discussion of the obtained results.

2. Formulation of the control method

Suppose that we have a dynamical system described by a set of reaction-diffusion equations for the concentrations w_i of various reacting species ($i = 1, \ldots, N$),

$$\dot{w}_i = Q_i(w_1, \ldots, w_N; q) + D_i \nabla^2 w_i , \qquad (1)$$

where $Q_i(w)$ are nonlinear functions, D_i are the diffusion constants and q is some variable parameter. We assume that, as shown from experiments or preliminary theoretical studies, the system undergoes a supercritical Hopf bifurcation leading to the diffusion-induced turbulent regime at a certain threshold given by $q = q_0$. Below the threshold, the system has a stable stationary state with constant concentrations w_i^0, while slightly above it small-amplitude variations $w_i = w_i^0 + \delta w_i$ of the concentrations around their steady values are observed. Though the local oscillations are fairly harmonical, the oscillation phases in different spatial areas fluctuate randomly in this case; a careful analysis of the experimental data may also reveal the presence of phase singularities related to the amplitude defects. Thus, the system is in the turbulent state.

Our conjecture is that, in order to control this system and eventually suppress turbulence, it would often suffice to apply a weak uniform time-dependent signal $S(t)$, so that the dynamical equations of the controlled system become

$$\dot{w}_i = Q_i(w_1, \ldots, w_N; q) + D_i \nabla^2 w_i + g_i(w_1, \ldots, w_N) S(t) , \qquad (2)$$

where g_i are coefficients that may also depend on concentrations w_i. The control signal is constructed as a combination of average concentration variations $\delta \bar{w}_i$ taken at a delayed time moment, i.e., as

$$S(t) = s \sum_i c_i \, \delta \bar{w}_i(t - \tau) . \qquad (3)$$

The spatial average $\delta \bar{w}_i$ is given, for a one-dimensional system, by an integral

$$\delta \bar{w}_i(t) = \frac{1}{L} \int_0^L \delta w_i(x, t) \, dx , \qquad (4)$$

where L is the total length of the system, and c_i give the weights of contributions by various reacting species into the global control signal. The parameter s specifies the intensity of the control signal. We expect that, by taking a sufficiently strong signal and varying only the delay time τ, suppression of turbulence can be achieved.

Indeed, after performing the transformation to complex oscillation amplitudes $A(x, t)$, retaining only the leading resonant terms [6] and choosing appropriate units for the measurement of time and spatial coordinates, one would obtain for this system in the presence of the weak control signal the following dynamical equation:

$$\dot{A} = (1 - i\omega)A - (1 + i\beta)|A|^2 A + (1 + i\varepsilon)\frac{\partial^2 A}{\partial x^2} + F(t) . \qquad (5)$$

This is the complex Ginzburg–Landau equation (CGLE) modified by an additional term

$$F(t) = \mu \, e^{i\chi_0} \bar{A}(t - \tau) . \qquad (6)$$

Here $\bar{A}$ is the spatial average of the complex oscillation amplitude,

$$\bar{A} = \frac{1}{L} \int_0^L A(x, t) \, dx . \qquad (7)$$

The average amplitude is taken in (3) at a delayed moment $t - \tau$. The coefficient μ specifies the intensity of control and χ_0 determines the phase shift between $\bar{A}$ and F. Further coefficients in Eq. (5) are β, characterizing the intensity of the nonlinear frequency shift, and ε, specifying the degree of cross-coupling between real and imaginary components of oscillation amplitudes for the neighbouring oscillators. Note that this equation holds near the Hopf bifurcation, while the increment of growth of the uniform oscillatory mode (equal to unity after the performed rescaling) is much smaller than the (linear) oscillation frequency ω. Without the control signal ($F = 0$), the uniform oscillations are unstable and the turbulence develops when the Benjamin–Feir condition $1 + \varepsilon\beta < 0$ is satisfied.

It should be emphasized that, though the general structure of Eq. (5) is clear, the actual computation of its coefficients for a concrete reaction-diffusion system is a tedious task which requires explicit knowledge of nonlinear functions $Q_i(w)$ and diffusion constants D_i, as well as of functions $g_i(w)$ and weights c_i. When experimental systems are considered, such functions and parameters are often known only to some extent and thus the parameters in (5) cannot be theoretically determined.

Fortunately, the detailed knowledge of coefficients in Eq. (5) is not essential for the control problem. The results of our subsequent analysis show that, by varying only the overall intensity of the control signal and its delay, the synchronization of oscillations in the system can be reached.

In our paper we do not directly derive Eq. (5) from full reaction–diffusion equations of any concrete problem. The complex Ginzburg–Landau equation (5) with the control terms (6) and (7) is taken here as the *initial model* for the subsequent analysis. The above comments were aimed to illustrate the general context in which this equation may arise.

It is convenient to introduce in (5) slowly varying complex amplitudes $\eta(x, t)$ as

$$\eta(x, t) = A(x, t) \exp(i\omega t) . \qquad (8)$$

After such a transformation, the considered system is reduced to

$$\dot{\eta} = \eta - (1 + i\beta)|\eta|^2 \eta + (1 + i\varepsilon)\frac{\partial^2 \eta}{\partial x^2} + f(t) , \qquad (9)$$

where the new control signal is

$$f(t) = \mu \exp[i(\chi_0 + \omega\tau)] \, \bar{\eta}(t - \tau) \qquad (10)$$

and

$$\bar{\eta} = \frac{1}{L} \int_0^L \eta(x, t) \, dx . \qquad (11)$$

Note that now the phase shift $\chi = \chi_0 + \omega\tau$ between the spatial average of the complex oscillation amplitude $\bar{\eta}$ and the control signal f has received a correction proportional to the delay time τ.

When delays are short ($\tau \ll 1$), the slowly varying average amplitude $\bar{\eta}(t)$ does not significantly change within the delay time and the delays in this term could be neglected. Then the system is described by an equation with effective global coupling,

$$\dot{\eta} = \eta - (1 + i\beta)|\eta|^2 \eta + (1 + i\varepsilon)\frac{\partial^2 \eta}{\partial x^2} + \mu \, e^{i\chi} \bar{\eta}(t) . \qquad (12)$$

The principal effect of the delays consists here in providing an additional phase shift $\Delta\chi = \omega\tau$ between the average slow oscillation amplitude and the signal, which can be easily manipulated by changing the delay time. Eq. (12) was introduced earlier as a model for global coupling in surface chemical reactions [17]. Below we analyze how the phase shift variations influence the properties of this system and find windows of delay times where synchronization occurs. Though we consider mainly the system described by Eq. (12), numerical simulations of the full problem, given by Eqs. (5)–(7), are also discussed in Section 4.

3. The stability of uniform oscillations

When turbulence is suppressed, uniform oscillations should be stable in the presence of the feedback control signal at least in respect to small perturbations. The uniform oscillations in

the distributed dynamical system (12) have the frequency

$$\Omega = \omega_0 - \mu(\sin\chi - \beta\cos\chi) \tag{13}$$

and the amplitude

$$\rho_0 = (1 + \mu\cos\chi)^{1/2} . \tag{14}$$

To investigate their stability, evolution of small inhomogeneous perturbations must be considered.

The local phase $\phi(x,t)$ and (real) amplitude $\rho(x,t)$ of the oscillations, defined by

$$\eta(x,t) = \rho(x,t)\exp[-i\Omega t - i\phi(x,t)] , \tag{15}$$

satisfy the dynamical equations

$$\dot\rho = (1-\rho^2)\rho + \frac{\partial^2\rho}{\partial x^2} - \rho\left(\frac{\partial\phi}{\partial x}\right)^2 + \varepsilon\rho\frac{\partial^2\phi}{\partial x^2} + 2\varepsilon\frac{\partial\rho}{\partial x}\frac{\partial\phi}{\partial x} + \mu R\cos(\phi - \Psi + \chi) , \tag{16}$$

$$\dot\phi = \beta\rho^2 - \Omega + \frac{2}{\rho}\frac{\partial\rho}{\partial x}\frac{\partial\phi}{\partial x} + \frac{\partial^2\phi}{\partial x^2} - \frac{\varepsilon}{\rho}\frac{\partial^2\rho}{\partial x^2} + \varepsilon\left(\frac{\partial\phi}{\partial x}\right)^2 - \frac{\mu R}{\rho}\sin(\phi - \Psi + \chi) . \tag{17}$$

Here, the global oscillation phase Ψ and (real) global amplitude R are defined by

$$R(t)\exp[-i\Psi(t)] = \frac{1}{L}\int_0^L \rho(x,t)\exp[-i\phi(x,t)]\,dx . \tag{18}$$

The uniform oscillations correspond to the steady state of equations (16)–(18) with $\rho(x,t) = R = \rho_0$ and $\phi(x,t) = \Psi = \phi_0$. To investigate the stability of this steady state, we add small perturbations $\delta\rho(x,t)$ and $\delta\phi(x,t)$. The solution of the linearized equations (16)–(18) is then given by a sum of independent spatial modes. When no-flux boundary conditions are put at $x = 0$ and $x = L$, these modes are

$$\delta\rho(x,t) = \delta\rho_k\exp(\gamma_k t)\cos(kx) , \tag{19}$$

$$\delta\phi(x,t) = \delta\phi_k\exp(\gamma_k t)\cos(kx) , \tag{20}$$

where $k = 2\pi n/L$, $n = 1, 2, \ldots$. Substitution of (19) and (20) into the linearized evolution equations yields an equation for the increment γ_k of growth of the mode with the wave number k,

$$(\gamma_k + 2 + 3\mu\cos\chi + k^2)(\gamma_k + \mu\cos\chi + k^2) + (\varepsilon k^2 + \mu\sin\chi)[2\beta(1 + \mu\cos\chi) + \varepsilon k^2 + \mu\sin\chi] = 0 . \tag{21}$$

Its solutions are

$$(\gamma_k)_{1,2} = -1 - k^2 - 2\mu\cos\chi \pm\{1 - 2\varepsilon\beta k^2 - \varepsilon^2 k^4 + 2\mu\cos\chi - 2\varepsilon\beta\mu k^2\sin\chi + \mu^2\cos(2\chi) - 2\beta\mu\sin\chi - 2\varepsilon\mu k^2\sin\chi - \beta\mu^2\sin(2\chi)\}^{1/2} . \tag{22}$$

When the Benjamin–Feir condition $1 + \varepsilon\beta < 0$ is satisfied, the uniform oscillations are unstable at $\mu = 0$, i.e., when the control signal is absent[2]. They become stable if, starting from a certain critical control intensity $\mu = \mu_c$, we have $\mathrm{Re}(\gamma_k) < 0$ for all wave numbers k. The last unstable group of modes in the considered system has $\mathrm{Im}(\gamma_k) = 0$ and its wavenumbers are close to a certain wave number k_0 (Figs. 1a and b). Because the spatial profiles of real amplitude ρ and phase ϕ are periodic in space but do not undergo temporal oscillations, these modes represent standing waves (see also [19]).

Besides of the standing waves, the system may have oscillatory modes with nonvanishing $\mathrm{Im}(\gamma_k)$ that correspond to periodic spatio-temporal modulation of the uniform oscillations. As follows from (22), the increment of growth of these modes is

$$\mathrm{Re}(\gamma_k) = -1 - 2\mu\cos\chi - k^2 . \tag{23}$$

Hence, they can be unstable only if the condition $\cos\chi < 0$ is satisfied. When such modes are present, their increment of growth *increases* with the intensity μ of the control signal. The most unstable modes have then the wavenumber near $k = 0$ (see Fig. 1c).

Thus, when determining the stability boundary of uniform oscillations, possible growth of standing waves and development of periodic modulation with large wavelengths should both be considered.

The stability diagram of uniform oscillations, calculated using the exact analytical solution (22), is shown in Fig. 2. The stability windows of uniform oscillations lie above the two curves in the figure. These windows approximately correspond to the intervals[3] of the phase shift $0 < \chi < \pi/2$ and $3\pi/2 < \chi < 5\pi/2$, where the negative feedback is realized. In the middle of such intervals, uniform oscillations are stabilized already by very weak control signals. The stabilization threshold is however significantly increased in the right side of the intervals.

The windows extend slightly beyond these two intervals. An interesting behaviour is found near the left and right ends of them. Here, if we keep the phase shift fixed and begin to increase the intensity of the control signal, uniform oscillations first become stable in respect to small perturbations but later lose again their stability: Crossing of the lower boundary corresponds to disappearance of standing waves (as in Fig. 1b); periodic modulation with large wavelengths (as in Fig. 1c) develops when the higher boundary is crossed.

The stability boundary of uniform oscillations in the plane $(\mu, -\beta)$ at fixed χ and ε is shown in Fig. 3. The critical intensity μ_c vanishes at the point $\beta = -1/\varepsilon$ of the Benjamin–Feir instability and monotonously increases with $-\beta$. On this

[2] In the opposite case, when the Benjamin–Feir instability is absent, uniform oscillations can be destabilized by global coupling for the phase shifts that give rise to a positive feedback (see [18,21]).

[3] Phase shifts differing by 2π are physically identical.

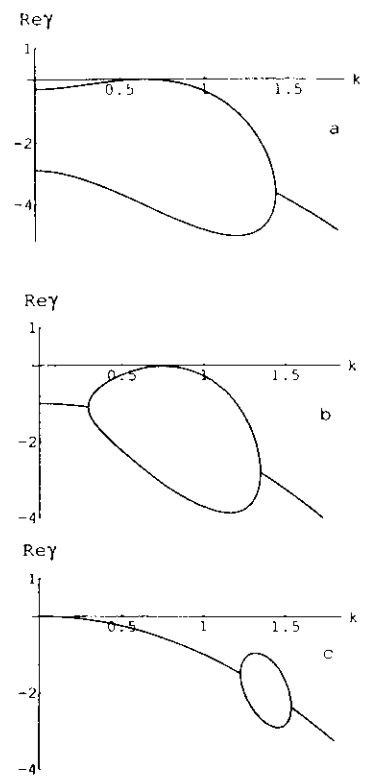

Fig. 1. The increment of growth $\mathrm{Re}\,\gamma$ as function of the wavenumber k. The parameters are $\beta = -1.4$, $\varepsilon = 2.0$ and (a) $\mu = 0.3$, $\chi = 0$, (b) $\mu = 0.5$, $\chi = 3\pi/2$, (c) $\mu = 3.2$, $\chi = 1.45\pi$.

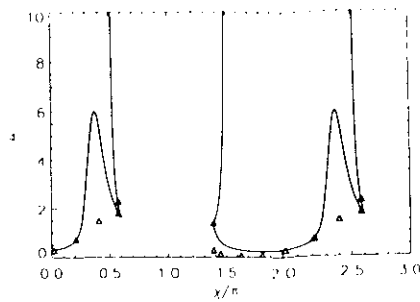

Fig. 2. The stability diagram in the plane (μ, χ) at $\beta = -1.4$ and $\varepsilon = 2.0$. Uniform oscillations are stable in respect to small perturbations above the boundary shown by the solid curve. The triangles indicate where the defects disappear in numerical simulations.

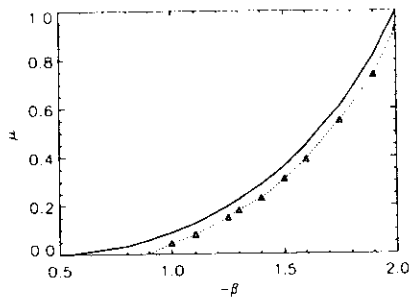

Fig. 3. The stability boundary of uniform oscillations (bold line) and the boundary of the amplitude turbulence (dash line) at $\epsilon = 2.0$ and $\chi = 0$. The triangles indicate where the defects disappear in numerical simulations.

boundary, growth of standing waves begins. The computed wavelength $\lambda = 2\pi/k_0$ of growing standing waves is shown as function of β for two values of the parameter ε in Fig. 4. The wavelength of standing waves diverges at the boundary of the Benjamin–Feir instability.

Thus, our general stability analysis reveals that stabilization of uniform oscillations can be achieved by taking sufficiently strong control signal and adjusting only the phase shift, i.e., the delay time of the control signal.

However, the stability in respect to small perturbations, which has been discussed above, does not yet guarantee that uniform oscillations

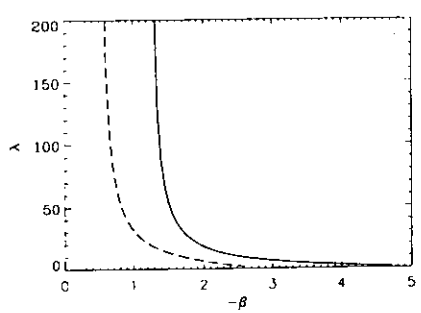

Fig. 4. The wavelength $\lambda = 2\pi/k_0$ of standing waves at the stability boundary of uniform oscillations as function of β for $\epsilon = 0.8$ (bold line) and $\epsilon = 2.0$ (dash line).

would also be stable in respect to finite-size perturbations. On the other hand, the state of the system below the instability threshold of the uniform oscillations is not necessarily turbulent. Indeed, it may also represent a regular wave pattern. Hence, further numerical simulations of the control problem are desired.

4. The numerical simulations

Our main numerical simulations have been performed for the one-dimensional system described by Eq. (12). The total length of the system was $L = 128$. We used an explicit integration algorithm with a constant time step $\Delta t = 0.01$ and the grid size $\Delta x = 0.5$. No-flux boundary conditions were applied at the ends $x = 0$ and $x = L$ of the integration interval. To visualize evolution of the system, the real oscillations amplitude $\rho(x, t)$ or the flux

$$j = \frac{1}{2i}\left(\eta \frac{\partial \eta^*}{\partial x} - \eta^* \frac{\partial \eta}{\partial x}\right) = \rho^2 \frac{\partial \phi}{\partial x} \tag{24}$$

have been displayed as functions of time in gray scale. The initial conditions were prepared by adding small random perturbations to the uniform state with $\rho = 1$ and $\phi = \text{const.}$ and then allowing the system to evolve to its developed turbulent state, while the control signal was absent. In choosing the parameter values for our simulations, we make use of the detailed phase diagram for CGLE constructed in Ref. [9].

Fig. 5 shows an example of the system's evolution from the developed turbulent state as intensity μ of the control signal is gradually increased with time. The initial turbulent state is characterized by the presence of multiple defects. In the center of a defect the real oscillation amplitude ρ is reduced, though it does not completely vanish (Fig. 5a). The flux j changes its direction on a defect (Fig. 5b). As μ is increased, the number of defects decreases and their distribution becomes more intermittent: groups of defects appear on a more regular

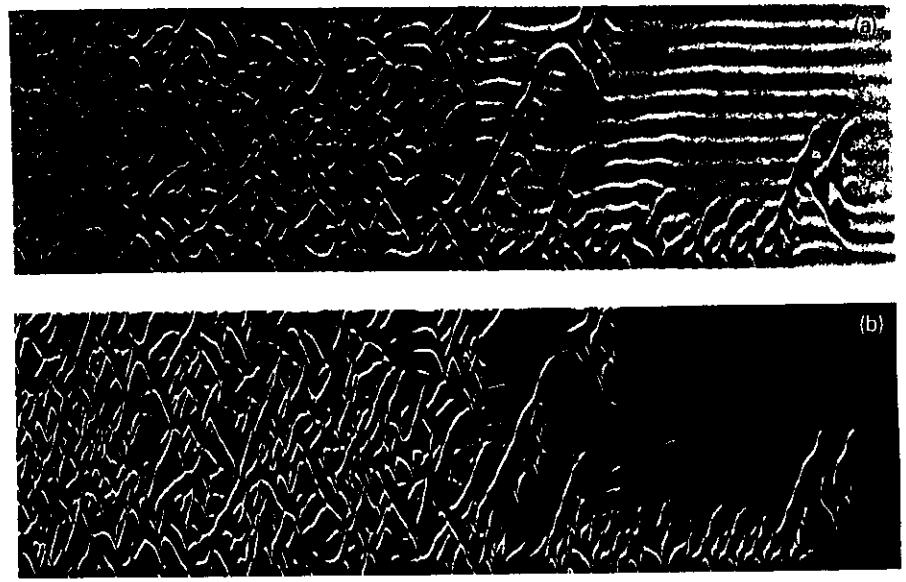

Fig. 5. Suppression of amplitude turbulence under increase of the control intensity. The real oscillation amplitude (a) and the flux (b) are shown in gray scale, the vertical coordinate corresponds to the spatial dimension, time is running from the left to the right. The parameter μ is increased as $\mu = ct$ with $c = 1.4 \times 10^{-4}$, other parameters are $\beta = -1.4$, $\epsilon = 2.0$ and $\chi = 0$; the shown time interval is $1200 < t < 2400$.

background. For the smaller values of μ, the background is in the state of phase turbulence. When μ is higher, it is filled with standing waves. Starting from a certain intensity of the control signal, the defects completely disappear. When μ is further increased, the amplitude of standing waves slowly decreases and they finally fade away so that the system is found in the state with uniform oscillations.

Since the amplitude turbulence in the system is associated with the presence of defects, its boundary in the parameter space can be determined by the condition that the defects disappear. Absence of the defects can be checked by taking a certain threshold $\rho = \rho_c$ and verifying that the real oscillation amplitude ρ never goes below it, within a sufficiently long simulation. The numerical experiments showed that this procedure yields approximately the same boundaries while the threshold ρ_c is varied between 0.5 and 0.8. The dashed line in Fig. 3 shows the boundary of amplitude turbulence in the parameter plane (μ, β), which was obtained by applying this procedure.

We see that the turbulence boundary lies below the stability boundary of the uniform oscillations indicated by the solid curve in Fig. 3. It could also be noted that, in a certain interval of β near the Benjamin–Feir point $\beta = -1/\varepsilon = 0.5$, the defects do not develop. In the absence of the control feedback ($\mu = 0$) the system is here in the state of phase turbulence. When the control is switched on and its intensity is gradually increased, such phase turbulence transforms

Fig. 6. Time evolution of the phase turbulence under increasing control intensity. The square of the flux j is shown in gray scale; the parameter μ is increased with speed $c = 3 \times 10^{-5}$ from zero (the left side) to $\mu = 0.03$ (the right side), other parameters are $\beta = -0.8$, $\varepsilon = 2.0$ and $\chi = 0$.

into uniform oscillations through the regime of standing waves. This is seen in Fig. 6 where the square of the flux j is plotted in gray scale as function of time, as μ is slowly increased at a constant rate.

Note that j^2 vanishes where the phase has its minima. The thin black curves, corresponding to $j = 0$ in this figure, show the trajectories of the points with the minimal phase. These trajectories are irregular in the state of phase turbulence, but arrange into a more regular pattern as the intensity μ of the control signal is increased. At still higher values of μ, the curves become horizontal – the phase minima do not change their positions with time. This is the regime of standing waves. The amplitude of standing waves slowly decreases, and they disappear when the stability boundary of uniform oscillations is reached.

Because the phase shift χ is a parameter that can be easily manipulated in an experiment, we have performed a detailed study of how the boundary of amplitude turbulence is influenced by variation of the phase shift. The same procedure as above was used to verify absence of the defects. The values of the control signal intensity μ, where the amplitude turbulence disappeared in our simulations, are marked by triangles in Fig. 2.

In the middle of the synchronization window, the boundary of the amplitude turbulence lies close to the stability boundary of uniform oscillations shown by the solid curve in Fig. 2. However, near the right end of the window, where this curve has a maximum, the amplitude turbulence develops only for much weaker control signals. Our simulations show that here the system has a wide range of existence of standing waves.

The gradual disappearance of turbulence has been observed in the simulations of $\varepsilon = 2.0$ whose results are shown in Figs. 3, 5, 6. As the boundary of the amplitude turbulence is approached, the number of defects decreases. Moreover, no hysteresis is found here. When one starts from the state with uniform oscillations at a high intensity of the control signal and then slowly decreases the control parameter μ, the defects first appear at the same boundary where they die out, as the control parameter is changed in the opposite direction.

Numerical studies of turbulence in the one-dimensional CGLE without global coupling [9,22] reveal that at smaller values of the parameter ε the behaviour of this system is different. Then, the amplitude turbulence can be initiated even on the other side of the Benjamin–Feir boundary, where the uniform oscillations are

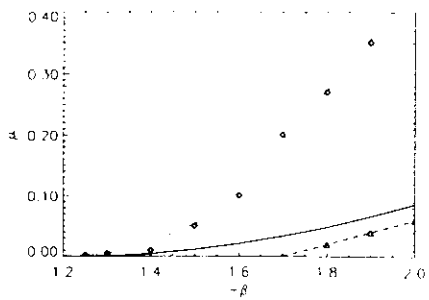

Fig. 7. Hysteresis in the transition to and from turbulence. The dot line shows the boundary where the turbulence is replaced by uniform oscillations as μ is increased at a constant speed $c = 1.7 \times 10^{-4}$. The dash line shows the boundary where the defects begin to spontaneously develop under the gradual decrease of the parameter μ. The solid line is the theoretical stability boundary of uniform oscillations. Other parameters are $\varepsilon = 0.8$ and $\chi = 0$.

stable in respect to small perturbations. In order to investigate how such turbulent regime is influenced by the global feedback we have performed a series of simulations at the parameter value $\varepsilon = 0.8$.

Fig. 7 shows that transition to turbulence is characterized now by a strong hysteresis. If we start from the developed turbulent state at $\mu = 0$ and slowly increase the feedback intensity, the amplitude turbulence is maintained until the boundary shown by the dot line in Fig. 7 is reached. Generally, this boundary is much higher than the stability boundary of uniform oscillations in respect to small perturbations (the solid line in the same figure). But when we start from the uniform oscillations at a high intensity of the control signal and slowly decrease μ with time, the defects first appear only below the stability boundary of uniform oscillations, i.e. when the dash line in Fig. 7 is crossed.

Fig. 8 displays the time evolution of the local flux j when the feedback intensity μ is increased at a constant speed. The essential difference from the behaviour found at higher values of the parameter ε is that new defects are produced here only by the defects already present in the system, i.e. no spontaneous defect generation occurs. Uniform oscillations occupy the background, outside of the defect bursts. When the turbulence dies out, the system is found immediately in the state of uniform oscillations. The destabilization of uniform oscillations, leading to appearance of standing waves, is observed only when the control signal is changed in the opposite direction, so that the control intensity is decreased.

The above numerical study has been performed for a reduced version (12) of the original feedback control problem (5)–(7), where the transformation to the slowly varying complex amplitudes η has been made and the delays in the control signal (10) have been after that neglected. This is justified while the delay τ is

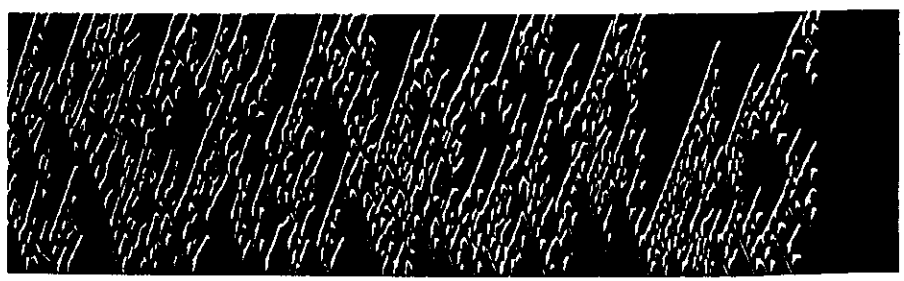

Fig. 8. Disappearance of turbulence under increasing control intensity. The parameter μ is increased with speed $c = 1.7 \times 10^{-4}$, the time interval from $t = 2000$ to $t = 3000$ is shown. Other parameters are $\beta = -1.8$, $\varepsilon = 0.8$ and $\chi = 0$.

small. In this case the principal effect of the delay in the original equation (5) consists in the introduction of an additional phase shift $\Delta\chi = \omega\tau$. Note that, if the oscillation frequency is high, a significant renormalization of the phase shift could be produced already by applying very short delays.

If the oscillation frequency is not large, such approximate reduction is not valid and full dynamical equations (5)–(7) with the delay should be investigated. To demonstrate that suppression of turbulence can also be achieved in this case by adjusting the delay time, we have performed simulations of the system with a moderate frequency $\omega = 5$.

In the simulation shown in Fig. 9 the delay time τ was slowly increased at a constant speed, while the feedback intensity μ was kept constant. Initially, at $\tau = 0$, the system was in the state of developed turbulence characterized by the presence of multiple defects. As the delay τ was gradually increased, the system entered the synchronization window. Abruptly, the defects died out and uniform oscillations were observed. They persisted in a wide interval of delay times, yielding the synchronization window. At the end of this window, standing waves slowly emerged. They gave rise to the amplitude turbulence as the delay time was further increased.

Though the delays τ is this numerical experiment were of the same order of magnitude as the characteristic relaxation time for the amplitudes, its results could still be qualitatively interpreted using the above analysis of the reduced problem. The main effect of the gradual increase in the delay time apparently consists in the increase of the effective phase shift $\chi = \chi_0 + \omega\tau$. Indeed, the observed sequence of transitions agrees with crossing the stability diagram (Fig. 2) from the initial value $\chi = \pi$ at a constant intensity μ of the control signal in the direction to larger phase shifts.

4. Discussion

Both phase and amplitude turbulence in the considered system are entirely due to local diffusional coupling between individual oscillatory elements. The principal role in the stabilization of uniform oscillations in our method is played by introduction of additional global coupling between the oscillators, which is realized by means of a global control feedback. Under certain conditions, when effective negative feedback is realized, this is equivalent to the presence of additional attractive infinite-range interactions between the phases of individual oscillators. Such interactions can counterbalance the distabilizing diffusional coupling and bring about the synchronization. The use of time delays provides a way for varying the phase shift between the global control signal and the average oscillation phase in the medium. By adjusting the delay time, and hence the phase shift, the synchronization condition can be reached.

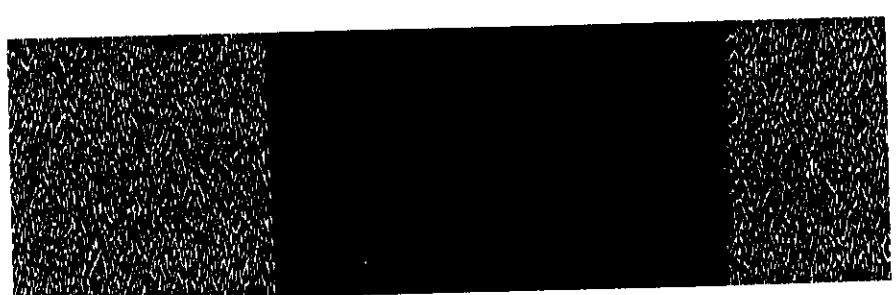

Fig. 9. Evolution of the controlled system under gradual increase of the delay from $\tau = 0$ to $\tau = 1.2$ within the time interval from $t = 0$ to $t = 3000$. The real oscillation amplitude $|A|^2$ is shown in gray scale. The constant intensity $\mu = 0.3$ of the control signal is maintained during sweeping; the chosen system parameters are $\omega = 5.0$, $\chi_0 = \pi$, $\varepsilon = 2.0$, and $\beta = -1.4$.

Thus, we have shown that by introducing delayed global feedback one can suppress both phase and amplitude turbulence in the complex Ginzburg–Landau equation, bringing the system to the state of uniform oscillations. The synchronization is realized in a window of delay times. In the middle of the window, the synchronization is produced already by weak control signals. We note that the synchronization can be achieved by varying only two parameters, i.e. the intensity of the control and the delay time. These two parameters have a simple physical interpretation and could be relatively easily manipulated in an experiment.

The actual coefficients of the complex Ginzburg–Landau equation, that describes the system near the Hopf bifurcation, are not needed to apply this control method. Therefore, no analytical derivation of this equation for a considered system must first be undertaken. It should only be verified that the system is indeed near the onset of persistent oscillations, i.e. at the threshold of the supercritical Hopf bifurcation. The complex computer processing of the dynamical data is also not required. Because of these features, the proposed method appears to be applicable for the experimental control of turbulence in distributed oscillatory systems of various origins.

Acknowledgements

The authors thank R. Imbihl, M. Bär and F. Mertens for useful discussions. The financial support from the Volkswagen-Stiftung is gratefully acknowledged.

References

[1] E. Ott, C. Grebogi, and J.A. Yorke, Phys. Rev. Lett. 64 (1990) 1196.
[2] K. Pyragas, Phys. Lett. A 170 (1992) 421.
[3] K. Pyragas and A. Tamasevicius, Phys. Lett. A 180 (1993) 99.
[4] A. Newell, Lect. Appl. Math. 15 (1974) 157.
[5] Y. Kuramoto and T. Tsuzuki, Prog. Theor. Phys. 55 (1976) 356.
[6] Y. Kuramoto, Chemical Oscillations, Waves, and Turbulence (Springer, Berlin, 1984).
[7] P. Coullet, L. Gil, and J. Lega, Physica D 37 (1989) 91.
[8] N. Bekki and K. Nozaki, Phys. Lett. A 110 (1985) 133.
[9] B.I. Shraiman, A. Pumir, W. van Saarloos, P.C. Hohenberg, H. Chaté and M. Holen, Physica D 57 (1992) 241.
[10] D.A. Egolf and H.S. Greenside, Phys. Rev. Lett. 74 (1995) 1751.
[11] P. Coullet and K. Emilsson, Physica A 88 (1992) 190.
[12] P. Coullet and K. Emilsson, Physica D 61 (1992) 119.
[13] H. Hakim and W.-J. Rappel, Phys. Rev. A 46 (1992) 7347.
[14] N. Nakagawa and Y. Kuramoto, Physica D 75 (1994) 74; D 80 (1995) 307.
[15] R. Imbihl, Prog. Surf. Sci. 44 (1993) 185.
[16] H. Levine and X. Zou, Phys. Rev. Lett. 69 (1992) 204.
[17] G. Veser, F. Mertens, A. Mikhailov and R. Imbihl, Phys. Rev. Lett. 77 (1993) 975.
[18] F. Mertens, R. Imbihl and A. Mikhailov, J. Chem. Phys. 99 (1993) 8668.
[19] F. Mertens, R. Imbihl and A. Mikhailov, J. Chem. Phys. 101 (1994) 9903.
[20] M. Falke and H. Engel, J. Chem. Phys. 101 (1994) 6255.
[21] M. Falke, H. Engel and M. Neufeld, Phys. Rev. E 52 (1995) 763.
[22] H. Chaté, Nonlinearity 7 (1994) 185.

PHYSICA D

Nonlinear Phenomena

Instructions to Authors

Submission of papers

Manuscripts should be sent in triplicate to one of the editors or coordinating editors with preference given to those whose interests appear to be close to the subject of the paper (addresses given on the inside front cover page).

Submission of a paper will be taken to imply that it represents original work not previously published, that it is not being considered elsewhere for publication, and that if accepted for publication it will not be published elsewhere in the same form, in any language without the consent of the publisher.

The master copy and original drawings will be returned to the authors in case their paper is not accepted for publication.

Proposals for review articles (approximately 500-1000 words) should be sent to any one of the editors. The editors will evaluate each proposal on the basis of (1) subject matter and (2) presentation and readability.

Refereeing. Submitted papers will be refereed and, if necessary, authors may be invited to revise their manuscript. If a submitted paper relies heavily on unpublished material, it would be helpful to have a copy of that material for the use of the referee.

Manuscript preparation

All manuscripts should be written in good English. The paper copies of the text should be prepared with double line spacing and wide margins, on numbered sheets.

Structure. Please adhere to the following order of presentation: Article title, Author(s), Affiliation(s), Abstract, PACS codes and keywords, Main text, Acknowledgements, Appendices, References, Figure captions, Tables.

Corresponding author. The name, complete postal address, telephone and fax numbers and the e-mail address of the corresponding author should be given on the first page of the manuscript.

PACS codes/keywords. Please supply upto four relevant PACS-1995 classification codes and approximately four keywords of your own choice for indexing purposes.

References. References to other work should be consecutively numbered in the text using square brackets and listed by number in the Reference list.

Illustrations

Illustrations should also be submitted in triplicate: one master set and two sets of copies. The *line drawings* in the master set should be original laser printer or plotter output or drawn in black india ink, with careful lettering, large enough (3-5 mm) to remain legible after reduction for printing. The *photographs* should be originals, with somewhat more contrast than is required in the printed version. They should be unmounted unless part of a composite figure. Any scale markers should be inserted on the photograph, not drawn below it.

Colour plates. Figures may be published in colour, if this is judged essential by the Editor. The Publisher and the author will each bear part of the extra costs involved. Further information is available from the Publisher.

After acceptance

Notification. You will be notified by the Editor of the acceptance of your article and invited to supply an electronic version of the accepted text, if this is not already available.

Copyright transfer. You will be asked to transfer the copyright of the article to the Publisher. This transfer will ensure the widest possible dissemination of information.

Proofs. Proofs will usually be printed on low-quality paper. Proofs will be sent to the author 4-6 weeks after acceptance. Please note that the proofs have been proofread by the Publisher and only a cursory check by the author is needed; we are unable to accept changes in, or additions to, the edited manuscript at this stage. In order to guarantee the fastest possible production times, the proofs must be returned within 48 hours after receipt, preferably by fax. If no reply is received from the author, the Publisher assumes that there are no further corrections to be made and will proceed with publication of the article.

Electronic manuscripts

The Publisher welcomes the receipt of an electronic version of your accepted manuscript (encoded in LaTeX). If you have not already supplied the final, revised version of your article (on diskette) to the Editor, you are requested herewith to send a file with the text of the accepted manuscript directly to the Publisher by e-mail or on diskette (allowed formats 3.5" or 5.25" MS-DOS, or 3.5" Macintosh) to the address given below. Please note that no deviations from the version accepted by the Editor are permissible without the prior and explicit approval by the Editor. Such changes should be clearly indicated on an accompanying printout of the file.

The Elsevier LaTeX package (including detailed instructions to authors) can be obtained using anonymous FTP from the Comprehensive TeX Archive Network (CTAN) from the directory /tex-archive/macros/latex/contrib/supported/elsevier. The participating hosts in the Comprehensive TeX Archive Network are: ftp.shsu.edu (TX, USA), ftp.dante.de (Germany), ftp.tex-.ac.uk (UK).

For a WWW interface to CTAN with the possibility to search the archive, visit the URL http://www.ucc.ie/cgi-bin/ctan/. For a list of hosts maintaining a (partial) mirror of the CTAN archive, do finger CTAN@pip.shsu.edu. In order to reduce network load, it is recommended that you use the CTAN host which is located in the closest network proximity to your site.

Questions concerning the LaTeX author-prepared article project and requests for the booklet with instructions to authors should be directed to the address below.

Author benefits

No page charges. Publishing in Physica D is free.

Free offprints. The corresponding author will receive 50 offprints free of charge. An offprint order form will be supplied by the Publisher for ordering any additional paid offprints.

Discount. Contributors to Elsevier Science journals are entitled to a 30% discount on all Elsevier Science books.

Contents Alert. Physica D is included in Elsevier's pre-publication service Contents Alert.

Further information (after acceptance)

Elsevier Science B.V., Physica D
Desk Editorial Department
P.O. Box 103, 1000 AC Amsterdam
The Netherlands
Tel.: + 31 20 4852 631
Fax: + 31 20 4852 319
E-mail: physdesk@elsevier.nl

ELSEVIER North-Holland, an imprint of Elsevier Science

Cellular Structures in Catalytic Reactions with Global Coupling

K. C. Rose,[1] D. Battogtokh,[1,*] A. Mikhailov,[1] R. Imbihl,[2] W. Engel,[1] and A. M. Bradshaw[1]
[1]*Fritz-Haber-Institut der Max-Planck-Gesellschaft, Faradayweg 4-6, 14195 Berlin (Dahlem), Germany*
[2]*Institut für Physikalische Chemie und Elektrochemie, Universität Hannover, Callinstrasse 3-3a, 30167 Hannover, Germany*
(Received 26 December 1995)

By employing mirror electron microscopy (MEM) to image the Pt(110) surface during the catalytic oxidation of CO we observe that a fine cellular structure (typical dimension 1–5 μm) develops under conditions at which rate oscillations occur. Based on an analysis using the complex Ginzburg-Landau equation, it is demonstrated that such a structure forms generally in an oscillatory medium in the presence of global coupling. [S0031-9007(96)00111-1]

PACS numbers: 61.16.–d, 82.20.Mj, 82.65.Jv

Global coupling plays an important role in a large number of dynamical systems ranging from the biological [1,2] and chemical [3] to phenomena more familiar to physicists such as gas discharges and transport processes in semiconductors [4–6]. Its effect can also be studied in oscillatory catalytic surface reactions where different reacting parts of a surface are coupled via partial pressure variations in the gas phase. In these reactions a large variety of spatiotemporal patterns have been observed in low pressure ($p < 10^{-3}$ mbar) single crystal experiments [7,8] using photoelectron emission microscopy (PEEM), a technique which allows parallel imaging of the surface with, typically, a field of view of 200 μm and a resolution of 1–10 μm [9]. Global coupling results in a type of pattern that is not seen in simple reaction-diffusion systems and has the form of a standing wave. An example is provided by the oxidation of CO on a Pt(110) surface [10–13]. Using mirror electron microscopy (MEM) at a resolution better than 0.1 μm we report in this Letter the observation of a fine cellular structure which develops during the latter reaction. We attribute the formation of such a structure to global coupling since it only exists under conditions at which rate oscillations are observed. Using simulations based on the modified complex Ginzburg-Landau (CGL) equation, which describes an oscillatory medium, we demonstrate that a cellular structure similar to the one seen in the experiment can indeed be observed if global coupling is taken into account.

During catalytic CO oxidation molecular oxygen readily dissociates on the Pt(110) surface into adsorbed atomic oxygen (O_{ad}) which reacts with adsorbed CO (CO_{ad}) to form the product CO_2 which in turn rapidly desorbs from the surface. Rate oscillations arise in this system through the coupling of the reaction with the $1 \times 1 \leftrightarrow 1 \times 2$ phase transition which is controlled by a critical coverage of CO [8].

As in previous investigations we study the reaction under isothermal conditions at low pressure ($p < 10^{-3}$ mbar) such that the UHV system is operated as a gradient-free flow reaction. Global coupling is present under these conditions as a consequence of mass balance in the reaction system requiring that oscillations in the reaction rate are accompanied by variations in the partial pressures of the reactants (typically ca. 1% of p_{CO}) [7,8,14]. The MEM measurements were performed in a low energy electron reflection microscope essentially similar to the instrument described by Telieps and Bauer [15]. MEM is extremely sensitive to both surface topography and differences in work function; it provides sufficient intensity for high temporal (0.04 s) and spatial ($\leq$0.1 μm) resolution. The method is thus ideally suited for investigations of dynamic phenomena at surfaces [16,17]. The electron energy in the present experiments was chosen such that depending on the local work function some electrons actually penetrate the surface and are not reflected. Areas with low work function then appear black, i.e., the contrast relative to PEEM is reversed. The Pt(110) sample used was freshly prepared and cleaned by a combination of Ar ion sputtering, heating in oxygen at 700 K ($p_{O_2} = 1 \times 10^{-5}$ mbar) and annealing to 950 K.

For partial pressures of the reactants in the 10^{-5} mbar range at $T = 430$ K, the reaction rate was initially stationary and target patterns as well as rotating spiral waves were observed [10,17]. For a certain set of parameters, however, the rate did not remain stationary but oscillations developed within a few minutes. These were accompanied by the formation of the spatiotemporal patterns shown in Fig. 1. The first frame shows an oxygen-covered Pt(110) surface with a large structural defect imaged as a dark circular area. The step bunch structure of the surface is clearly visible [16,18]. Small CO islands, which are imaged as dark areas, now begin to nucleate (frame 2) and, as they grow, a cellular structure develops (frame 3). This is more clearly seen in frame 4. (Note that in PEEM the reverse contrast pertains: oxygen-covered areas are dark and CO-covered areas light [10].) A network of thin bright lines ("membranes"), which do not necessarily coincide with the step bunch structure, divides the CO-covered surface into an array of individual cells. The cells then merge (frame 5) and a relatively uniform state of the CO-covered surface is established. After that the surface gradually returns to the state where it is covered with oxygen (an

 0031-9007/96/76(19)/3582(4)$10.00

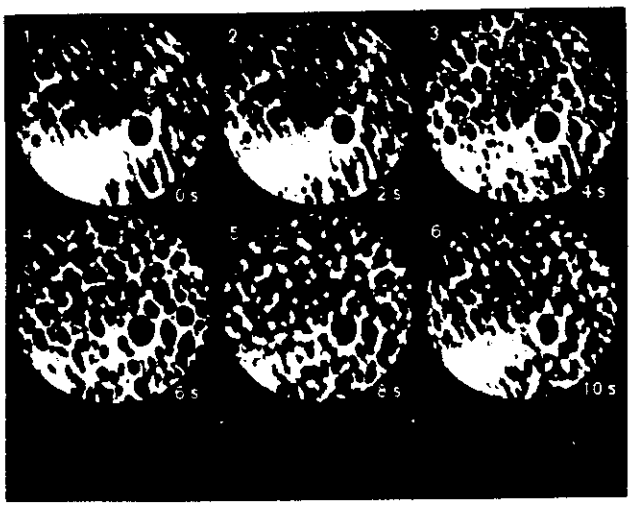

FIG. 1. MEM images showing the development of a cellular structure during rate oscillations in catalytic CO oxidation on Pt(110). Depicted is a cycle of 10 s duration which is smaller than the period of the rate oscillations (24 s). Experimental conditions: $T = 430$ K, $p_{CO} = 0.54 \times 10^{-5}$ mbar, $p_{O_2} = 1.3 \times 10^{-5}$ mbar.

FIG. 2. Transformation of a target pattern into a cellular structure occurring as rate oscillations develop, time in minutes. Experimental conditions essentially identical with those of Fig. 1.

intermediate stage is shown in frame 6). In this particular experiment the cycle just described took 12 s and, subsequently, the surface remained oxygen covered for another 11 s. Then, in a very rapid cycle of only about 1 s duration, the surface again goes through the sequence of patterns displayed in Fig. 1 but in the reverse order. The total time of 24 s is also the period observed for the measured rate oscillations corresponding to some kind of integral behavior over the whole surface.

The process through which global coupling gains control over the reacting surface is illustrated in Fig. 2. The first frame shows the situation where the reaction rate is still stationary and target patterns are present on the surface. With the onset of oscillatory behavior, the target pattern breaks up and a complex pattern of propagating waves is formed (frame 2). Subsequently, small CO islands begin to nucleate in the region directly in front of the propagating CO wave (frame 3). This further results in the complete disintegration of the CO waves and leads to the formation of the cellular structure shown above in Fig. 1. The whole process can be regarded as an induction period since the development of the rate oscillations takes place without any further change of the parameters.

For understanding the nature of the cellular structure, it is important to note that the network only forms when rate oscillations develop, i.e., when global coupling is effective. In this respect, the situation resembles the occurrence of standing waves that were found earlier in the same system at higher temperature (540–550 K) [10]. However, in contrast to the standing waves which form a rapidly oscillating stripe pattern with a wavelength of ca. 20–50 μm and a period of a few seconds, the cellular structure exhibits a characteristic size of about 1 μm and a period of the order of 1 min.

In the experiment shown in Fig. 1 the cellular structure was observed to stay at exactly the same position for over 80 oscillatory cycles (ca. 30 min), showing that the structure is probably pinned by the structural defects of the substrate. On the other hand, the propagation of the chemical waves is not significantly influenced by structural defects, as shown by the smooth boundaries of the fronts in frame 1 of Fig. 2. Further, the structure of the "membranes" does not necessarily correspond to that of the surface microtopography, as we have noted above. We thus conclude that although the cellular structure may be pinned by the defects, their influence alone is not a sufficient explanation of the origin and properties of the structure and that the effects of global coupling have to be taken into consideration.

In order to demonstrate that global coupling can indeed lead to cellular structures we have performed simulations with the CGL equation which we have modified to take global coupling into account. Our previous investigations of this model have shown that it describes qualitatively the various effects of global coupling in oscillatory systems, such as the breakdown of synchronization caused by defects [19,20], spontaneous formation of phase domains [20], and development of standing waves [13].

The modified CGL equation is given by

$$\dot{\eta} = (1 - i\omega)\eta - (1 + i\beta)|\eta|^2\eta + (1 + i\varepsilon)\nabla^2\eta + \mu e^{i\chi}\overline{\eta}, \quad (1)$$

where

$$\overline{\eta} = \frac{1}{S}\int \eta(\mathbf{x}, t)\, d\mathbf{x} \quad (2)$$

is the spatial (surface) average of the local complex oscillation amplitude $\eta(\mathbf{x}, t)$ and S is the total surface area. This equation describes a population of small-amplitude limit-cycle oscillators which are coupled both locally (due to diffusion) and globally. The nonlinearity in a single oscillator is specified by the parameter β,

while the local coupling is characterized by the parameter ε. The last integral term in Eq. (1) can be interpreted as a driving force that is produced collectively by all oscillators in the population and applied back on each of them. The intensity of global coupling is characterized by the coefficient μ; the factor χ in the last term takes into account a phase shift between the driving force and the average amplitude $\overline{\eta}$.

If the condition $1 + \varepsilon\beta < 0$ is satisfied, uniform oscillations in this system are stable at sufficiently strong intensities μ of global coupling inside a window of the parameter χ. When μ is decreased, they first become unstable with respect to the growth of a mode with a certain wave number k_0 and the same frequency as that of uniform oscillations [12]. The growth of this mode is limited due to further nonlinear interactions. In a two-dimensional system, a simple extension of such a mode yields a periodic stripe pattern. Although such patterns are occasionally seen in our numerical simulations, the typical pattern is a hexagonal array of cells, as in the case of external periodic forcing [21]. The origin of a cellular structure lies in the fact that, in two dimensions, the whole family of modes with the wave numbers $\mathbf{k}$ satisfying the condition $|\mathbf{k}| = k_0$ becomes simultaneously unstable. The nonlinear interactions may then enhance the growth of triplets of such modes with wave vectors satisfying the condition $\mathbf{k}_1 + \mathbf{k}_2 + \mathbf{k}_3 = 0$. These give rise to a hexagonal cellular structure (Fig. 3).

In contrast to cellular structures formed by a Turing instability in chemical reaction-diffusion systems [22,23], a cellular structure in the oscillatory system considered does not correspond to a stationary distribution of reactants. In such a pattern, both the modulus of the local oscillation amplitude and its phase are spatially modulated.

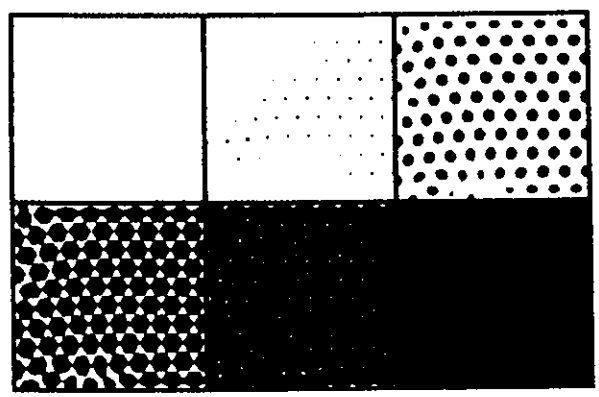

FIG. 3. Time-dependent cellular structure obtained by numerical integration of Eq. (1) with $\beta = -1.4$, $\varepsilon = 2.0$, $\mu = 0.245$, $\chi = 1.8\pi$, and $\omega = 0.1$ for the system of linear size $L = 100$ with no-flux boundary conditions. Spatial distributions of the local oscillation phase $\phi(x,t) = \arg[\eta(x,t)]$ at subsequent time moments within one oscillation cycle are shown (from top left to right bottom). The phase varies from 0 to 2π and the darker regions correspond to its smaller values.

We have found that oscillations in different cells are synchronized in time. Starting from random initial conditions, irregular patterns representing strongly distorted hexagonal arrays are produced (the relatively regular pattern shown in Fig. 3 is obtained after a long transient process). The characteristic time scale for motion of cell boundaries in the process of relaxation towards a more ordered state are, however, much larger than the oscillation period.

Comparing the typical evolution of a cellular structure in Fig. 3 with the behavior of cellular structures in the experiment, a number of similarities can be noted. As a new cycle of oscillations begins, small "islands" are formed in the centers of the cells (frame 2 in Fig. 3). They grow (frame 3) and form a hexagonal network (frame 4). After that, the islands merge (frame 5) and a relatively uniform state (frame 6) is established. This state then gradually transforms into the initial state shown in the first frame. However, there is also a difference. Each cycle in the experiment consists of two subcycles of significantly different durations. The model (1) is constructed assuming oscillations are almost harmonic; it therefore cannot reproduce such more complex situations. Only the main part of the experimental cycle thus agrees with the simulation.

The exact nature of the cellular pattern in terms of surface structure and adsorbate coverages in the system Pt(110)/CO + O_2 is not yet quite clear. Although the pressure range of our experiment was below ca. 10^{-4} mbar beyond which a faceting of the Pt(110) surface is known to occur, it cannot be ruled out that a certain amount of reaction-induced roughening (on a microscopic length scale) might play a role [24,25]. This would not, however, invalidate our theoretical analysis as long as the structure still originates from the effect of global coupling on an oscillatory medium and not from specific properties of the system investigated.

In summary, by employing MEM we have demonstrated that a cellular structure develops under oscillatory conditions in the system Pt(110)/CO + O_2. Since a theoretical analysis with a rather general model yields similar cellular structure, we conclude that the experimentally observed structure represents a new type of pattern existing in oscillatory media in the presence of global coupling. Analogous patterns can be expected in other systems.

The financial support of the Volkswagen-Stiftung and the Deutsche Forschunggemeinschaft through the Sonderforschungsbereich 290 is acknowledged.

*On leave from the Department of Physics, Moscow State University, 117234 Moscow, Russia, and the Institute for Mathematics, Zhukov av. 51, Ulan Bator, Mongolia.

[1] A.T. Winfree, *The Geometry of Biological Time* (Springer, Heidelberg, 1980).

[2] P.C. Matthews and S.H. Strogatz, Phys. Rev. Lett. **65**, 1701 (1990).

[3] U. Middya and D. Luss, J. Chem. Phys. **100**, 6386 (1994).
[4] H. Willebrand, T. Hünteler, F.-J. Niedernostheide, R. Dohmen, and H.-G. Purwins, Phys. Rev. A **45**, 8766 (1992).
[5] E. Anmelt, D. Schweng, and H.-G. Purwins, Phys. Lett. A **173**, 348 (1993).
[6] E. Schöll and A. Wacker, in *Nonlinear Dynamics and Pattern Formation in Semiconductors and Devices*, edited by F.-J. Niedernostheide (Springer, Heidelberg, 1995), p. 21.
[7] G. Ertl, Science **254**, 1756 (1991).
[8] R. Imbihl and G. Ertl, Chem. Rev. **95**, 697 (1995).
[9] O.H. Griffith and W. Engel, Ultramicroscopy **36**, 1 (1991).
[10] S. Jakubith, H.-H. Rotermund, W. Engel, A. von Oertzen, and G. Ertl, Phys. Rev. Lett. **65**, 3013 (1990).
[11] H. Levine and X. Zou, Phys. Rev. Lett. **69**, 204 (1992); Phys. Rev. E **48**, 50 (1993).
[12] M. Falcke and H. Engel, J. Chem. Phys. **101**, 6255 (1994).
[13] F. Mertens, R. Imbihl, and A. Mikhailov, J. Chem. Phys. **101**, 9903 (1994).
[14] M. Eiswirth, P. Möller, K. Wetzl, R. Imbihl, and G. Ertl, J. Chem. Phys. **90**, 510 (1989).
[15] W. Telieps and E. Bauer, Ultramicroscopy **17**, 57 (1985).
[16] W. Swiech, B. Rausenberger, W. Engel, A.M. Bradshaw, and E. Zeitler, Surf. Sci. **294**, 297 (1993).
[17] K.C. Rose, R. Imbihl, B. Rausenberger, C.S. Rastomjee, W. Engel, and A.M. Bradshaw, Surf. Sci. (to be published).
[18] B. Rausenberger, W. Swiech, C.S. Rastomjee, M. Mundschau, W. Engel, E. Zeitler, and A.M. Bradshaw **215**, 109 (1993).
[19] G. Veser, F. Mertens, A. Mikhailov, and R. Imbihl, Phys. Rev. Lett. **71**, 935 (1993).
[20] F. Mertens, R. Imbihl, and A. Mikhailov, J. Chem. Phys. **99**, 8668 (1993).
[21] P. Coullet and K. Emilsson, Physica (Amsterdam) **61D**, 119 (1992).
[22] D. Walgraef, G. Dewel, and P. Borkmans, Adv. Chem. Phys. **49**, 311 (1982).
[23] Q. Quyang and H.L. Swinney, Chaos **1**, 411 (1991).
[24] S. Ladas, R. Imbihl, and G. Ertl, Surf. Sci. **197**, 153 (1988); **198**, 42 (1988).
[25] J. Falta, R. Imbihl, and M. Henzler, Phys. Rev. Lett. **64**, 1409 (1990).

Microscopic Self-Organization of Enzymic Reactions in Small Volumes

A. Mikhailov and B. Hess

Fritz-Haber-Institut der Max-Planck-Gesellschaft, Faradayweg 4-6, 14195 Berlin (Dahlem), Germany Max-Planck-Institut für medizinische Forschung, Jahnstrasse 29, 69120 Heidelberg, Germany

The Journal of Physical Chemistry®

Reprinted from
Volume 100, Number 49, Pages 19059–19065

Microscopic Self-Organization of Enzymic Reactions in Small Volumes

A. Mikhailov and B. Hess*

Fritz-Haber-Institut der Max-Planck-Gesellschaft, Faradayweg 4-6, 14195 Berlin (Dahlem), Germany
Max-Planck-Institut für medizinische Forschung, Jahnstrasse 29, 69120 Heidelberg, Germany

Received: June 5, 1996[⊗]

Using an enzymic reaction with allosteric product activation as example, we show that allosterically regulated reactions in small volumes may develop strong microscopic correlations between individual molecular reaction events. Such correlations lead to coherent synchronous activity of the enzymic molecular population which is revealed in frequent periodic spiking of the reaction.

1. Introduction

The best known examples of self-organization in chemical reactions are provided by the waves in the Belousov−Zhabotinsky reaction,[1,2] the glycolytic oscillations,[3] and the spatiotemporal patterns formed in the processes of heterogeneous catalysis.[4] Their theoretical description is based on the rate equations for concentrations of reacting species and the reaction−diffusion models. But such phenomena do not represent the only possible kind of self-organization. As shown in this paper, strong deviations from equilibrium can under certain conditions develop already at the kinetic molecular level, leading to the microscopic coherence in a reacting system.

The difference between macroscopic and microscopic self-organization can be illustrated by using an example of optical oscillations. Coherence of light, generated by lasers, results from synchronous transitions between energy levels in a large number of optically active atoms. The characteristic property of this process is the presence of strong microscopic correlations between individual photon emission events in the atoms.

An optical system can also be constructed where the intensity of the generated light would periodically vary with time, but the light would not be coherent. In this system the individual atomic emission events would not be correlated, and only their mean rate, i.e., the intensity of the generated light, would be modulated with time. Simple oscillations in the light intensity represent an example of macroscopic self-organization, whereas the coherence of individual atomic transitions, typical for the lasers, indicates the existence of microscopic self-organization in the considered system.

Analogous phenomena can be found in systems of chemical reactions. Let us suppose that a reaction results in the release of product P by molecules X. When oscillations in the reaction rate are observed, the mean number of the released product molecules varies with time. However, if we look at the individual molecular reaction events (i.e., the release of molecules P by molecules X) within a short time interval, we would find that they are statistically independent and follow the Poisson distribution. Such local equilibrium is characteristic for all macroscopic chemical self-organization phenomena.

The microscopic self-organization of a chemical reaction means that individual molecular reaction events should be strongly correlated at microscopic scales, about the duration of a single reaction event. In the considered example, it means that a large part of molecules X in the entire molecular population would synchronously release the product molecules P, and thus a spike in their concentration would be created. This coherent reactivity would be an analog of coherent light generation by lasers.

To reach microscopic self-organization, certain conditions should be satisfied. In laser generation, the fundamental role is played by the phenomenon of stimulated quantum emission, in which a photon released by an atom can increase the probability of photon emission by a different atom, provided the latter is found in the excited state. It is also essential that the photons have long free path lengths, and therefore distant correlations can be established in the system.

In this paper we consider a hypothetical enzymic reaction

$$S + E \rightarrow ES \rightarrow P, \quad [P] \rightarrow 0 \qquad (1)$$

where binding of substrate S by enzyme E is allosterically activated by product P. If the substrate concentration is constant, this reaction does not exhibit macroscopic rate oscillations.[5] However, in small spatial volumes for sufficiently high intensities of the allosteric regulation periodic coherent spiking of the catalytic activity of the enzymic population in such reaction can develop. The onset of spiking represents an effect of microscopic self-organization in the considered chemical system.

In the next section we formulate the conditions under which spiking can appear. The regulatory part of the reaction should be fast. Such a reaction in large volumes would have been diffusion-controlled. When, however, the size of the volume is less than the correlation length of the reaction, correlations extend over the whole volume. It is also important that the duration of individual molecular catalytic cycles in such small volumes is much larger than the characteristic diffusion-controlled time scales, such as the mixing or the transit time for the regulatory molecules.

When these conditions are satisfied, the population of enzymes together with their regulatory molecules represents a "molecular network". A simple stochastic model of the reaction 1 in the regime of a molecular network is constructed in the third section. Investigations of this model allow us to analyze the onset of spiking and its basic properties. The paper ends with the discussion of the obtained results and their possible importance for the biochemistry of a living cell.

2. Molecular Networks

The microscopic molecular mechanism of the reaction 1 includes several stages. An enzyme molecule E binds a molecule S of the substrate, and the substrate−enzyme complex ES begins a sequence of conformational changes that ends, after some time T_1, in the release of the product molecule P. When the product molecule has left, the conformation of the enzyme

[⊗] Abstract published in *Advance ACS Abstracts,* November 1, 1996.

S0022-3654(96)01662-0 CCC: $12.00

molecule returns to the initial state. This recovery stage takes some time T_2 during which binding of a substrate molecule cannot occur. Hence, only after the time $T_0 = T_1 + T_2$, which represents the duration of a molecular catalytic cycle, the enzyme molecule can begin a new cycle. Note that thus the molecular cycle has much in common with the sequence of transitions in an excitable neuron.[6]

The initial binding of a substrate molecule is allosterically regulated. We assume that the probability of binding of a substrate by an enzyme in its resting conformation is small. It becomes, however, greatly increased if an additional regulatory molecule is bound to a different site on the surface of the enzyme, and this, by means of cooperative interactions within the enzyme macromolecule, facilitates the binding of the substrate. It is assumed that the enzyme has only one binding site for a regulatory molecule, and its binding can only take place when an enzyme is in its resting state, i.e., when the previous catalytic cycle is finished.

In the considered hypothetical reaction 1, the regulatory role is played by the product molecules, and thus the reaction is effectively autocatalytic. The product molecules decay, and therefore their lifetimes are finite. To exclude immediate triggering of a new molecular catalytic cycle by the product molecule that has just been released by the enzyme, we assume that the lifetime of a product molecule is shorter than the molecular recovery time T_2. Under this condition, the product molecules can execute their regulatory roles only by traveling through the volume and initiating the catalytic cycles of other enzymes in the population.

Since traveling of regulatory product molecules is realized by means of a random diffusion walk through the reaction volume, characteristic diffusion times are important in determining the actual kinetics of this reaction.

The mixing time t_{mix} is defined as the time after which a regulatory molecule, released at some point in the volume, can be found with equal probability anywhere inside it. If the volume has the linear size L and the diffusion constant of the regulatory molecules is D, the mixing time can be estimated, on the order of magnitude, as

$$t_{mix} = L^2/D \tag{2}$$

Another important characteristic time of the process is the traffic time $t_{traffic}$, which is defined as follows: Suppose that we have released a regulatory particle somewhere inside the volume that contains only one target enzyme molecule. Then $t_{traffic}$ represents the characteristic time after which the regulatory particle will find this enzyme molecule and bind itself to the atomic target group on its surface.

It should be noted that the last stage of this process could actually be quite complicated and involve docking by electrostatic interactions and two-dimensional diffusion of the regulatory molecule over the surface of the enzyme until the target site is reached.[7,8] In our simple treatment we neglect all these possible complications and assume that the regulatory molecule performs free Brownian motion in the volume until it touches a small target of radius R attached to the surface of the enzyme molecule. Once touching has occurred, the regulatory molecule becomes bound to the target site.

Because the molecular weight of enzymes is larger than that of the regulatory molecules, the targets can be viewed as immobile. Under these conditions, the characteristic traffic time can be estimated using the concepts of the theory of diffusion-controlled reactions.[9,10] In the order of magnitude, it is given by (cf. refs 11−13)

$$t_{traffic} = L^3/DR \tag{3}$$

where R is the radius of a target. (If the size of the atomic target group in the enzyme is comparable to the size of a regulatory molecule, it should be replaced by the sum of the two respective radii.)

Since the volume contains a population of N enzymes of the same kind, we can also introduce the transit time $t_{transit}$ that is the time after which, on the average, the regulatory molecule will find the first target (and bind to it). Assuming that targets are independently and uniformly distributed through the reaction volume, we have

$$t_{transit} = (1/N)t_{traffic} \tag{4}$$

or, explicitly,

$$t_{transit} = L^3/NDR \tag{5}$$

Note that $L_{corr} = (Dt_{transit})^{1/2}$ yields the mean distance passed by the regulatory molecule before it finds a target, and this characteristic length can be considered as the correlation radius of the reaction. This distance can be compared with the linear size L of the reaction volume.

When $L \gg L_{corr}$, the target will be found in a close proximity of the point where the regulatory product molecule has been released. Since the regulatory molecules, conveying information about the reaction events, are trapped in this case not far from the points where they have been produced, they cannot maintain long-range correlations in the reacting system.

A completely different situation is found if the condition $L \ll L_{corr}$ is satisfied. Now, the first target is found by the regulatory molecule only after it has traveled extensively through the reaction volume and has crossed it many times. It means that the regulatory molecule would be able, with equal probability, to bind any of N enzymes in the population, no matter where they are located inside the volume.

The latter condition can also be expressed in terms of the characteristic times of the diffusion problem, i.e., can be written as

$$t_{mix} \ll t_{transit} \tag{6}$$

When the transit time is much larger than the mixing time, the first target is found with equal probability anywhere in the volume.

According to eq 5, the transit time is inversely proportional to the total number N of enzyme molecules. Therefore, the condition (6) can be satisfied only for sufficiently small numbers of the enzymes. By putting $t_{mix} = t_{transit}$, we derived the estimate for the critical number of the enzyme molecules,

$$N_{cr} = L/R \tag{7}$$

Thus, it is controlled in the order of magnitude only by two parameters: the linear size L of the reaction volume and the radius R of the atomic target group on the surface of the enzyme molecule. When the number N of enzyme molecules is less than N_{cr}, the product-mediated allosteric interactions between the enzymes extend over the entire reaction volume. Note that eq 7 yields the critical enzyme concentration

$$c_{cr} = 1/L^2R \tag{8}$$

which decreases with the linear size L of the volume.

Taking $R = 1$ nm as the characteristic size of the atomic target group, we see that the critical number of enzyme molecules in the volume of size $L = 0.1$ μm is $N_{cr} = 100$, and the respective enzyme concentration is $c_{cr} \approx 10^{-4}$ M. If the diffusion constant of the product molecules is $D = 10^{-6}$ cm^2/s, we find from eqs 3−5 that the mixing time is $t_{mix} = 0.1$ ms, the traffic time is $t_{traffic} = 10$ ms, and the transit time for $N = N_{cr}$ is $t_{transit} = 0.1$ ms.

The above characteristic diffusion times can be compared with the duration T_0 of a single catalytic molecular cycle. This time has not been directly measured, but some estimates of its magnitude could be obtained by measuring the maximal turnover rate of an enzymic reaction. It is believed that this rate, reached under the condition of the substrate saturation, is controlled only by the molecular turnover.[8] Hence, T_0 can be roughly estimated as the inverse of the maximal turnover rate. Thus derived, the estimates for T_0 may range, depending on a particular enzyme, from as small as fractions of a microsecond to several seconds.[14] However, the fairly typical value would be about $T_0 = 10$ ms.

Hence, for the reactions in submicrometer volumes involving hundreds of enzyme molecules, this time is much larger than both the mixing and the transit times in the reaction volume,

$$T_0 \gg t_{transit}, t_{mix} \tag{9}$$

This is a remarkable result. In a macroscopic system, all characteristic kinetic times of a chemical reaction are usually much longer than the duration of a single molecular reaction event, and therefore these events can be treated as instantaneous. This forms the basis of the traditional kinetic theory formulated in terms of the Markov random processes. We see, however, that in very small spatial volumes for enzymic chemical reactions the opposite limit may be realized, so that the characteristic times of internal molecular dynamics of the enzymes become larger than the kinetic times of the reaction. When this occurs, the theoretical description of a chemical reaction should be essentially modified.

The considered system can be viewed as a population of active macromolecules that operate like molecular machines. Each internal molecular cycle of an enzyme results in the conversion of a substrate molecule into a molecule of the product. The cycle represent a sequence of conformation changes that can be understood as continuous motion along an internal reaction coordinate. For allosteric enzymes, the molecular cycles can be externally controlled by binding of regulatory molecules. Generally, arrival of a regulatory molecule can lead either to acceleration or slowing down at some stages of a molecular cycle.

When regulatory molecules are produced by enzymes in the same population, this leads to interactions (or communication) between the cycles of different enzyme molecules. If condition (9) holds, the characteristic transport times of regulatory molecules between the enzymes are short as compared with the molecular cycle duration. Furthermore, if the transit time is larger than the mixing time in the volume, a regulatory molecule released by a given enzyme can influence, with equal probability, the catalytic cycle of any other enzyme in the population. We have earlier suggested[13,15] that such interacting populations of active macromolecules should be called *molecular networks*.

In the presence of strong allosteric interactions, the internal dynamics of individual enzyme molecules in such a network can be so significantly influenced by the dynamics of other enzymes that the whole system would perform coherent collective evolution in the multidimensional phase space of internal reaction coordinates, i.e., behave as a single dynamical object.

This coherence would be manifested in rigid correlations between the individual catalytic cycles and the moments when the product molecules are released by different enzymes. It means that the catalytic activity of the network would represent a sequence of sharp spikes, each corresponding to synchronous firing of the product by a large fraction of enzyme molecules.

3. Stochastic Automata

To illustrate the general analysis of molecular networks, we consider a simple stochastic model.[16] In this model each enzyme molecule is treated as an automaton that performs a sequence of transitions between its internal states. The states of this automaton are described by an integer phase variable ϕ which takes values between 0 and K_0. The value $\phi = 0$ corresponds to the rest state of the enzyme, where it is ready to bind a substrate molecule; $\phi = 1$ is the first state of the substrate−enzyme complex. Firing of the product molecule occurs at the state $\phi = K_1$; the next K_2 states until $\phi = K_0$ correspond to the enzyme's recovery ($K_0 = K_1 + K_2$). From the state $\phi = K_0$ the enzyme goes to the rest state $\phi = 0$.

Transitions can occur only at discrete time moments $t_n = n\Delta t$, $n = 1, 2, 3, \ldots$. The transition from $\phi = 0$ to $\phi = 1$, i.e., binding of a substrate molecule by an enzyme, is stochastic and characterized by a certain probability w. The subsequent motion inside the cycle is deterministic: at each next time moment $n + 1$ the phase ϕ is increased by one until the state $\phi = K_0$ is reached.

The population consists of N enzymes; the phase variables of different enzyme molecules are denoted as ϕ_i, with $i = 1, 2, \ldots, N$. The phase dynamics is described by the algorithm

$$\phi_i(n+1) = \begin{cases} \phi_i(n) + 1, & \text{if } 0 < \phi_i(n) < K_0 \\ 0, & \text{if } \phi_i(n) = K_0 \\ 1, & \text{with probability } w, \text{ if } \phi_i(n) = 0 \\ 0, & \text{with probability } 1 - w, \text{ if } \phi_i(n) = 0 \end{cases} \tag{10}$$

Whenever an enzyme passes through the state $\phi_i(n) = K_1$, a new product molecule is created. On the other hand, if the decay rate of the product molecules per unit time step is g, any product molecule can die with the probability g at each step. If $m(n)$ is the number of product molecules in the system at moment n, their number at the next moment $n + 1$ is therefore given by

$$m(n+1) = m'(n) - k \tag{11}$$

where

$$m'(n) = m(n) + \sum_{i=1}^{N} \Delta(\phi_i(n) - K_1) \tag{12}$$

takes into account new product molecules that has been released by the enzymes and k is the number of the product molecules that have died. Since each product molecule can die per unit time step with the probability g, the probability $\pi(k|m')$ that k out of $m'(n)$ molecules would die is given by the binomial distribution

$$\pi(k|m') = \frac{m'!}{k!\,(m'-k)!}\, g^k (1-g)^{m'-k} \tag{13}$$

Equations 11−13 give the stochastic algorithm for the product molecules in the system.

We must also include into the model the effects of allosteric activation by the product molecules. Assuming that the

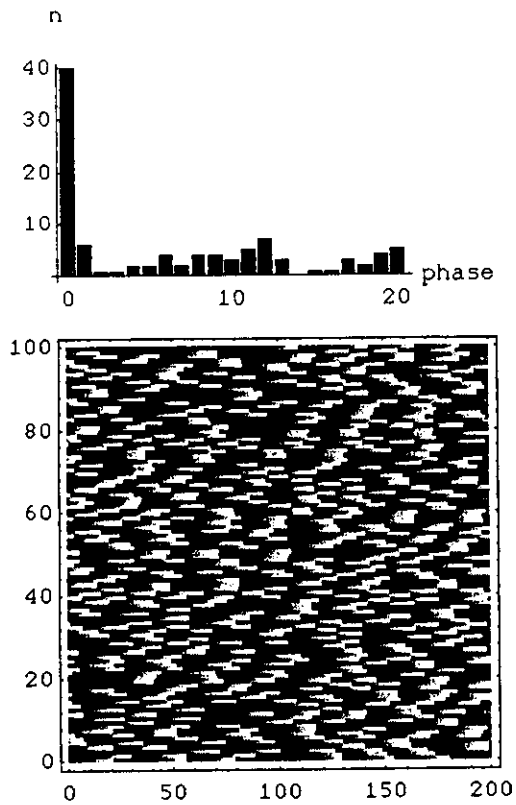

Figure 1. Molecular chaos. The histogram of the distribution of the enzymes over the cycle phases at a fixed time (a, top) and the evolution of the states of all 100 enzymes during 200 subsequent time steps (b, bottom); $K_0 = 20$, $K_1 = 11$, $w_0 = 0.01$, $w_1 = 0.01$, and $g = 0.3$.

conditions

$$T_0 \gg t_{\text{transit}} \gg t_{\text{mix}} \tag{14}$$

are satisfied for the considered reaction, each of the product molecules in the volume can activate with equal probability the catalytic cycle of any given enzyme.

Let w_0 be the probability of the spontaneous cycle initiation, i.e., the probability that, per one time step, the enzyme in the rest state $\phi = 0$ binds a substrate molecule and hence a transition to $\phi = 1$ occurs. Suppose that if only one product molecule is present inside the volume, there is a probability w_1 per one time step that this product molecule would activate the cycle, i.e., produce a transition from $\phi = 0$ to $\phi = 1$. Thus, the parameter w_1 characterizes in this model the intensity of the allosteric activation.

If the volume contains m product molecules, the total probability w of cycle initiation in a given enzyme per one time step can be found by first calculating the probability q that the initiation *does not* occur, and the enzyme remains in the rest state. Since this can take place only if the spontaneous initiation has not occurred and any of m product molecules has not activated the cycle, we can write

$$q = (1 - w_0)(1 - w_1)^m \tag{15}$$

Because the probability of the cycle initiation is $w = 1 - q$, we have at moment n

$$w = 1 - (1 - w_0)(1 - w_1)^{m(n)} \tag{16}$$

This completes the definition of the stochastic automaton model of the reaction 1 in the regime of a molecular network.

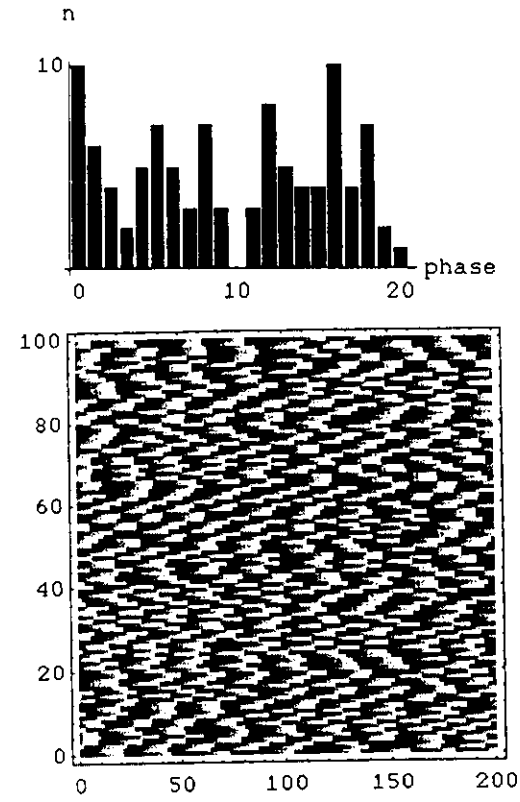

Figure 2. Enhanced fluctuations ($w_1 = 0.03$ and $K_1 = 11$, other parameters are the same as in Figure 1).

In the simulations of the stochastic reaction model, we take $T_0 = 20$ ms and choose $\Delta t = 1$ ms, so that the total number of phase steps in the cycle is $K_0 = 20$. The system consists of $N = 100$ enzyme molecules, and the probability of spontaneous cycle initiation is $w_0 = 0.01$ ms^{-1}. The decay rate of the product molecules is chosen to be $g = 0.3$ ms^{-1}, so that their mean lifetime is significantly shorter than the duration T_0 of the cycle. The parameters w_1, characterizing the intensity of allosteric regulation, and $K_1 = T_1/\Delta t$, specifying the phase inside the cycle where the product molecule is released, are varied.

4. From Molecular Chaos to Coherent Spiking

By repeatedly applying the stochastic algorithm described in the previous section, the evolution of the reaction system is reproduced and can be investigated. In the first series of simulations we fix $K_1 = 11$ (note that thus the product is released in the middle of the cycle of the total duration $K_0 = 20$) and study how the reaction properties are changed as the intensity of allosteric regulation, characterized by the parameter w_1 in the model, is gradually increased.

As the initial condition in our simulations, we have always chosen a state with random distribution over the cycle phases and a small number of the product molecules. To eliminate the transient effects, the iterations have typically been continued for several thousands of time steps before the kinetic properties of the reaction have been analyzed.

Figure 1a shows the histogram of the distribution of enzymes over cycle phases at a fixed moment for the situation with weak allosteric regulation ($w_1 = 0.01$). We see that about half of the enzyme population is found in the rest state ($\phi = 0$), waiting to bind a substrate. The remaining enzymes are uniformly, though with some fluctuations, distributed over the cycle phases. The cycles of individual enzymes are not correlated. This is clearly

seen in Figure 1b that shows the cycles of all enzymes in the population.

Each horizontal stripe in Figure 1b presents subsequent phases ϕ_i of a certain enzyme i as a function of time. The gray scale representation is used to display the phase values, with the black pixels corresponding to $\phi = 0$ and the bright pixels indicating the maximal possible phase $\phi = 20$. The vertical coordinate gives the number i assigned to an enzyme in the population. Note that, under the conditions of a molecular network, each enzyme may interact with equal probability with any other enzyme in the population, and hence the enumeration order is arbitrary and irrelevant.

The reaction regime in Figure 1b has no significant correlation between the cycles of individual enzymes, so that their phases are random. It can therefore be classified as the state of molecular chaos.

We increase now the intensity of allosteric regulation to $w_1 = 0.03$. This has a strong effect on the reaction conditions. As seen in Figure 2a, the occupation number of the state with $\phi = 0$ is not much larger than the occupations numbers of others phase states. Therefore, the enzymes do not long wait now before they bind a substrate molecule, and the cycle is initiated. Since the probability w_0 of the nonactivated, spontaneous cycle initiation is the same here as in Figure 1a, this implies that the cycles are already to a large extent allosterically activated. The fluctuations in the phase distribution in Figure 2a are enhanced (and bursts of spiking occasionally occur). However, no permanent temporal order can yet be discerned in the system's behavior (Figure 2b).

When the intensity of allosteric regulation is further increased to $w_1 = 0.05$, a qualitative change in the system's behavior occurs (Figure 3a). The enzymic population breaks now into two approximately equal groups. All enzymes belonging to the same group have close cycle phases, and the shift of half the cycle period is found between the mean phases of these two groups.

Though the histogram in Figure 3a is given only for one moment, it is fairly typical. As time goes on, two enzyme groups oscillating with the phase shift of a half a period persist in the system (Figure 3b). Occasionally, an enzyme may change its allocation and move to the other group. Moreover, the phases of enzymes inside a given group display some statistical fluctuations.

Apparently, this kinetic regime is different from the state with random, uncorrelated reaction events as shown in Figure 1. It is characterized by the presence of strong correlations between microscopic cycles of individual molecules in the enzymic population. Since the product molecules are released when enzymes pass through a fixed phase state, the product generation rate would show in this case sharp narrow spikes (see also the discussion below). The width of each spike is determined by the phase variation within an enzymic group, and the time period, separating two subsequent spikes, is half of the duration of a single molecular cycle T_0. Thus, coherent microscopic spiking in the enzymic activity is the characteristic property of such microscopically organized reaction regime.

To understand why two enzyme groups become formed in the system, we should recall that, in the above series of simulations, the product molecule is released at about the middle of the reaction cycle (i.e., $T_0 \approx 2T_1$). Because the lifetimes of the product molecules are much shorter than the cycle duration, synchronous oscillations of the entire population (formation of single phase group) are not here possible (indeed, the product molecules released in a spike would then have died before the enzymes return to their rest states and can be again activated).

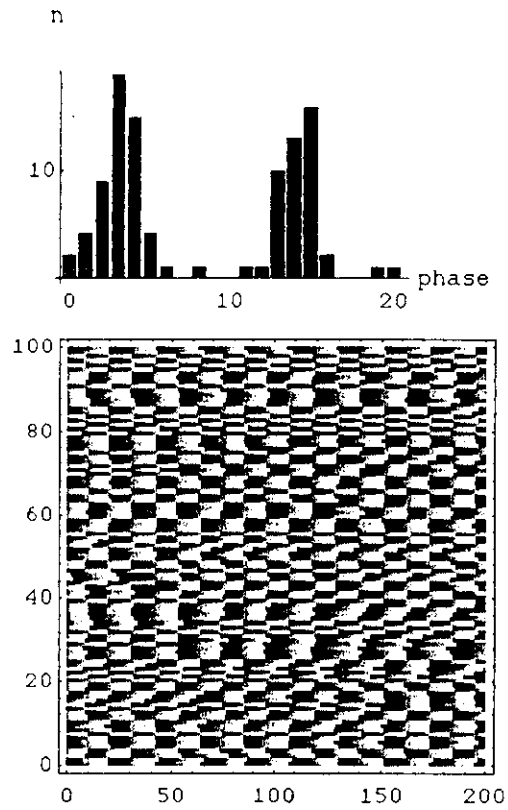

Figure 3. Spiking with two enzymic groups ($w_1 = 0.05$ and $K_1 = 11$).

However, the enzymes may still break into phase groups with the shift of half the oscillation period between them. In this case, which is realized for the simulation in Figure 3, the product molecules released by enzymes of the first group activate the cycles of the enzymes belonging to the second group, and vice versa.

These arguments indicate that the pattern of microscopic self-organization in the considered reaction may depend on the relationship between T_1 and T_0 (i.e., between $K_1 = T_1/\Delta t$ and $K_0 = T_0/\Delta t$). Therefore, in the second simulation series the parameter K_1 has been varied.

The simulations have revealed the existence of spiking regimes with a larger number of the enzymic groups. Figure 4 shows an example of spiking with three groups of enzymes that has been observed at $K_1 = 15$. Because the phases of these three groups are shifted by a third of the cycle period, they form a loop where each group activates the cycle of the next one. Since the number of the enzymes belonging to a group is now smaller, they release less product molecules in each spike, and therefore, higher intensity of allosteric regulation is needed for the onset of spiking.

The synchronous activity of the entire population (i.e., spiking with only one group) has been observed for $K_1 = 19$. In this case the recovery time is shorter than the lifetime of the product molecules, and therefore the products released by the same group can again activate it.

It is interesting that the synchronous activity has also been found (Figure 5) in the situation when the product molecules are released at an early stage of the cycle, i.e., for $K_1 = 3$. This effect has a different explanation. As seen in Figure 5a, the phases of the enzymes inside the group now significantly vary. When the "precursor" part of the group passes through the phase stage $\phi = K_1$, it releases the product molecules that activate the cycles in the central part of the enzymic group. Note that the synchronization threshold ($w_1 = 0.15$) is then larger than for the transition to spiking with two groups (cf. Figure 1).

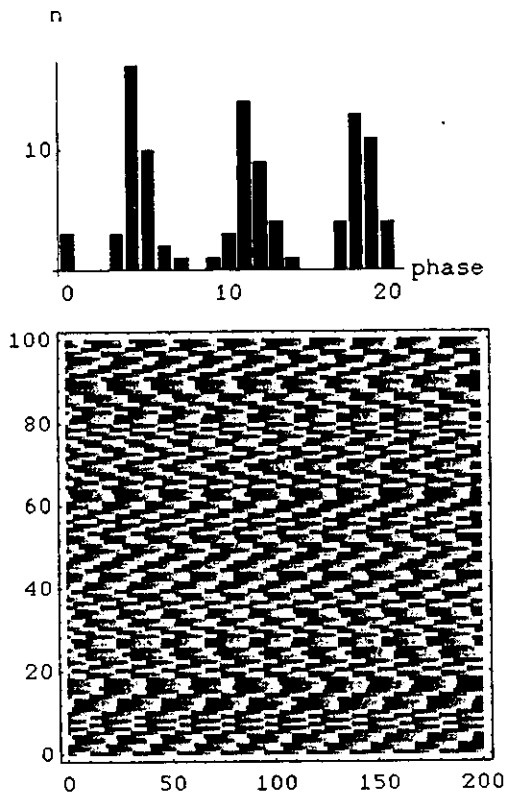

Figure 4. Spiking with three enzymic groups ($w_1 = 0.15$ and $K_1 = 15$).

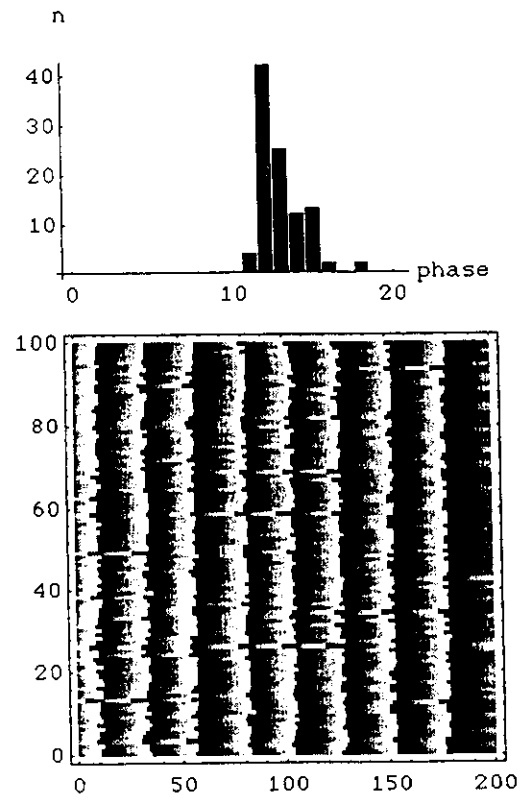

Figure 5. Synchronous spiking of the entire enzymic population ($w_1 = 0.15$ and $K_1 = 3$).

During the transient leading from the initial distribution with random phases to the stable spiking regime with a certain number of groups, a larger number of enzyme groups is first formed. However, such additional groups later disappear by a process which looks like competition between the groups. For some parameter values, the intermittent behavior has been

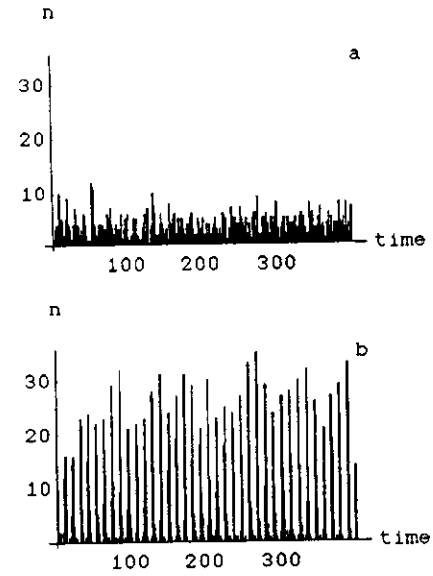

Figure 6. Time-dependent generation rate of the product molecules (a) in the regime of molecular chaos ($w_1 = 0.01$ and $K_1 = 11$) and (b) for the spiking with two enzymic groups ($w_1 = 0.07$ and $K_1 = 11$).

observed: the bursts of coherent spiking alternated with the periods of apparently chaotic activity.

An important property characterizing the kinetics of an enzymatic reaction is the time-dependent product generation rate, i.e., the number of new product molecules appearing at each time step. When the molecular cycles of individual enzymes in the population are not correlated, this rate randomly fluctuates around a certain mean level (Figure 6a). The intensity of such fluctuations agrees with that predicted by the Poissonian statistics.

In contrast to this, when strong correlations between individual molecular cycles are present, the product is released only in short narrow spikes separated by time intervals where the entire enzymic population is practically silent (Figure 6b). Each spike is produced by action of the enzymes in a certain group. The interval between two subsequent spikes is therefore equal to the duration of a single molecular cycle divided by the number of the synchronous enzymic groups in the system. Note that random phase variations within an enzymic group lead to the fluctuations in the amplitudes of the spikes that are seen in Figure 6b.

5. Discussion and Conclusions

A living biological cell is a tiny chemical reactor where tens of thousands of chemical reactions can simultaneously go on. The very fact that these reactions proceed in a regular and predictable manner, and properly respond to variations in environmental conditions, already indicates a high degree of organization in this system.

The biochemical activity of a cell can be compared with the operation of a large industrial factory or an assembly line where certain parts are produced by a system of machines. The products of one machine are then used by other machines for manufacturing of their products.

Two possible general modes of operation of such a factory can be imagined. In the asynchronous mode, the parts produced by a given machine are first deposited in a common store and then taken from the store by other machines, when these parts are needed for further production. This kind of the organization is not however optimal, since it requires large storage facilities and many transactions. It becomes deficient when the inter-

mediate products are unstable and can easily be damaged or destroyed during the storage process.

When the synchronous operation mode is employed, the intermediate products, required for a certain operation step in a given machine, are released by other machines and become available exactly at the moment when they are needed. Hence, large storage facilities can be eliminated, and the entire production process may run much faster. Apparently, such synchronous manufacturing process implies much more complicated management than the asynchronous operation mode. In a real factory, this is achieved by careful planning and external control of the production.

For a living cell, the role of the "machines" is played by individual enzyme molecules. The asynchronous mode of operation corresponds here to the usual kinetic regime of a chemical reaction, where intermediate products or regulatory molecules are stored in the solution. The synchronous mode would represent a kinetic regime with strong temporal correlations between the individual molecular cycles of different enzymes. An example of such behavior is provided by the phenomenon of coherent spiking, which has been considered in this paper.

Remarkably, we have found that as the strength of the allosteric regulation is increased, the synchronous kinetic regime can spontaneously emerge in the reacting system, and despite the stochastic nature of the process, no external control is necessary to maintain this mode. This is a clear effect of self-organization, which is however different from the macroscopic phenomena of pattern formation in systems with chemical reactions.

Our simple estimates have been performed for very small volumes, which are characteristic of the intracellular compartments. For the larger volumes, the mixing and traffic times rapidly increase and become larger than the duration of a molecular catalytic cycle. Therefore, similar synchronous activity of the reaction in the volume of the micrometer size would be possible only for the enzymes with the slower turnover rates, of about 1 Hz. The critical number of the enzymes in such a volume is then about 1000, which corresponds to the concentration of 10^{-6} M.

The analysis given in this paper is only a first step toward the detailed examination of microscopic self-organization in biochemical reactions. This must be followed by the detailed analysis of concrete reactions and particular mechanisms of the allosteric regulation.

Acknowledgment. The authors acknowledge valuable discussions with M. Eigen and A. Goldbeter.

References and Notes

(1) Belousov, B. P. A periodic reaction and its mechanism (1951, from his archives). English translation in: Field, R. J., Burger, M., Eds.; *Oscillations and Traveling Waves in Chemical Systems*; Wiley: New York, 1985; p 605.

(2) Kapral, R., Showalter, K., Eds. *Chemical Waves and Patterns*; Kluwer: Dordrecht, 1995.

(3) Hess, B.; Boiteux, A. *Annu. Rev. Biochem.* **1971**, *40*, 237.

(4) Imbihl, R.; Ertl, G. *Chem. Rev.* **1995**, *95*, 697.

(5) Goldbeter, A. *Biochemical Oscillations and Cellular Rhythms*; Cambridge University Press: New York, 1996.

(6) Wiener, N.; Rosenblueth, A. *Arch. Inst. Cardiol. Mex.* **1946**, *16*, 205.

(7) Berg, H. C. *Random Walks in Biology*; Princeton University Press: Princeton, NJ, 1983.

(8) Gutfreund, H. *Kinetics for the Life Sciences. Receptors, Transmitters and Catalysts*; Cambridge University Press: Cambridge, 1995.

(9) von Smoluchowski, M. *Phys. Z.* **1916**, *17*, 557.

(10) Eigen, M. *Z. Phys. Chem. (Munich)* **1954**, *1*, 176.

(11) Adam, G.; Delbruck, M. Reduction of dimensionality in biological diffusion processes. In *Structural Chemistry and Molecular Biology*; Rich, A., Davidson, N., Eds.; Freeman: San Francisco, 1968; p 198.

(12) Wittenberg, J. B.; Wittenberg, B. A. *Annu. Rev. Biophys. Biophys. Chem.* **1990**, *19*, 217.

(13) Hess, B.; Mikhailov, A. *J. Theor. Biol.* **1995**, *176*, 181.

(14) Stryer, L. *Biochemistry*, 3rd ed.; Freeman: New York, 1988.

(15) Hess, B.; Mikhailov, A. *Science* **1994**, *264*, 223.

(16) Hess, B.; Mikhailov, A. *Biophys. Chem.* **1996**, *58*, 365.

JP9616627

Submitted to Physica D, 13.9.96

Controlling Turbulence in the Complex Ginzburg-Landau Equation II. Two-Dimensional Systems

D. Battogtokh[1,*] A. Preusser[2], and A. Mikhailov[1]

[1]Fritz-Haber-Institut der Max-Planck-Gesellschaft,
Faradayweg 4-6, 14195 Berlin (Dahlem), Germany
[2]Gemeinsames Rechenzentrum der Berliner Max-Planck-Institute,
Faradayweg 4-6, 14195 Berlin (Dahlem), Germany

Abstract

Turbulence in oscillatory distributed systems can be controlled by introducing delayed global feedback and adjusting the feedback intensity and the delay time. We investigate, numerically and analytically, suppression of turbulence in two-dimensional systems described by the complex Ginzburg-Landau equation. Different scenarios leading to the onset of uniform oscillations are outlined. They involve destruction of phase flips and spiral waves, appearance of breathing and stationary cellular structures, and development of localized turbulent bubbles on the background of uniform oscillations.

* On leave from the Mathematics Institute, Mongolian Academy of Sciences, Zhukov av. 51, Ulanbator, Mongolia

1. Introduction

The complex Ginzburg-Landau equation (CGLE) represents a normal form of a distributed dynamical system in the vicinity of a supercritical Hopf bifurcation [1,2]. Though individual elements of a medium have in this case simple regular dynamics, i.e. perform harmonical limit-cycle oscillations, local diffusional coupling between them can produce turbulence [3]. Because of its generality, CGLE has been extensively studied both in its regular and turbulent parameter domains [4-14]. Using this model, such concepts as phase, amplitude, and defect turbulence have been introduced [3,8].

In the previous publication [15], hereafter referred as Part I, we have shown that turbulence in one-dimensional systems, described by CGLE, can be controlled by introducing delayed global feedback and adjusting the feedback intensity and the delay time. The aim of the present paper is to formulate principal scenarios leading to suppression of turbulence by global feedback in two-dimensional systems.

The dimensionality of a system is known to play an essential role in the phenomena related to fluctuations and spatiotemporal chaos near bifurcation points. For example, statistical fluctuations destroy long-range order in one-dimensional equilibrium systems [16]. On the other hand, resonant interactions between triplets of plane wave modes, leading to the appearance of hexagonal structures under the Turing instability [17,18], are first possible only in two dimensions. Indeed, our numerical and analytical studies of two-dimensional systems show new patterns - stationary and breathing cellular structures, turbulent bubbles on the background of uniform oscillations, and strings representing extended amplitude defects.

Under delayed global feedback, elements of a distributed oscillatory system collectively generate a control signal that is applied back to each of them after adding a certain delay. Depending on the phase shift of the control signal, the feedback can be either negative or positive, and thus it may alternatively suppress spatiotemporal chaos or destabilize uniform oscillations. The principal role of delays is that they modify phase shifts between the control signal and the oscillating pattern. By changing the delay, the phase shift can be directly varied.

Though global feedbacks can be artificially introduced to control the system's behaviour, such feedbacks may also represent an intrinsic feature of a system. Particularly, global coupling is typical for low-pressure experiments with surface chemical reactions where it is due to strong mixing of reactive components in the gas phase, while local coupling is provided by surface diffusion [19]. Effects of global coupling have been observed in oscillatory surface reactions and discussed in the framework of CGLE with instantaneous global feedback [20-25]. Hence, results of our investigations can be helpful in the analysis of pattern formation by such surface chemical reactions.

Extensive numerical simulations, performed by monitoring responses of the considered system to variations of its parameters and feedback properties, represent the main part of this work. Our primary task is to adequately describe these observations.

The framework for our analysis is provided by previous studies of GCLE in absence of global feedback and, especially, by the recently constructed phase diagram for turbulence in this equation [13]. We also use results of earlier investigations of CGLE with global coupling and perform a more detailed stability investigation of uniform oscillations, to analytically determine boundaries of the synchronization window and properties of first unstable modes.

Caution is needed when theoretical notions are applied to describe properties of reaction-diffusion turbulence. Such basic concepts as spiral waves, shocks, phase flips and Bekki-Nozaki holes, can safely be used only in the parameter regions where the respective structures are stable. However, these terms are also frequently employed to characterize elements of irregular and chaotic patterns in a turbulent state. Of course, in this case it can only be said that an object, *resembling* a respective elementary structure, appears and exists for some time, but later fades away or is replaced by another pattern.

For example, an object representing a shock is normally produced in a collision of two traveling waves. Inside a narrow spatial region, where annihilation of the waves takes place, the oscillation amplitude is then increased and the oscillation phase has a local minimum. But objects with similar properties are also observed in phase turbulence, where they form boundaries of irregular cells, or in turbulent bubbles, where they form membranes separating these bubbles from the area with uniform oscillations. We still describe them as 'shocks', though such objects are no longer associated with collisions of traveling waves.

There is uncertainty concerning the question which objects in a turbulent state should be classified as spiral waves. Except for the state of frozen turbulence, where a medium is occupied by a few steadily rotating spirals, spiral-shaped arms are not seen in turbulence simulations. Spiral waves are sometimes attributed to the presence of phase singularities, so that whenever phase singularities, i.e. topological defects, are found in a medium, it contains fragments of spiral waves. Such a description can, however, be misleading. Though phase singularities can indeed lie inside small cores with a decreased oscillation amplitude, like in the center of a steadily rotating spiral,

such singularities may also be attached to an extended amplitude defect, better classified as a 'string'.

Visualization of data is important to provide an adequate description of complex turbulent patterns. When one-dimensional systems were investigated in Part I, gray-scale representations with time running along the horizontal axis and the spatial coordinate plotted along the vertical axis were usually employed. In two dimensions, the pattern evolution is best seen when a computer animation or a video are generated. Hence, production and recording of such videos has been a significant element of this work. In the paper we present selected frames from these videos and also show, when appropriate, time evolution of a pattern in one of its spatial cross-sections, using the same representation as in Part I.

Much insight into the behaviour of a distributed dynamical system can be reached when transitions between different kinds of patterns or different turbulent regimes are observed. Keeping this in mind, our numerical experiments have usually been performed under ramping conditions, when the intensity of global feedback has been slowly increased with time. We tried to perform the experiments in an almost adiabatic manner, so that properties of observed patterns did not significantly differ from what would have been found under fixed parameter values. The minimal ramping speed was, however, limited by considerations of the computation time.

Below in this section we introduce the basic model of CGLE with global feedback and present a short summary of elementary dynamical structures and principal turbulent regimes in CGLE. Theoretical analysis of CGLE with global feedback is performed in Section 2. Results of systematic numerical simulations are described in Section 3. The paper ends with discussion of obtained results.

1.1. Global feedback in the complex Ginzburg-Landau equation

Using dimensionless time, coordinate and amplitude variables, the Ginzburg-Landau equation for local complex oscillation amplitudes A(r,t) in the presence of an additive force F(t) is written in the form

$$\dot{A} = (1 - i\omega)A - (1 + i\beta)|A|^2 A + (1 + i\varepsilon)\nabla^2 A + F(t) \ . \qquad (1)$$

In this equation β characterizes the nonlinear frequency shift of individual oscillators and ε controls dispersion of traveling waves.

The linear oscillation frequency of individual oscillators in equation (1) is ω. The derivation of CGLE as a normal form near a supercritical Hopf bifurcation (see [3]) is based on the assumption that the considered system is close to the bifurcation point and therefore the oscillation frequency is large as compared to the characteristic increment of growth of first unstable mode. Because the increment is made equal to unity in equation (1) by rescaling of time, this assumption is equivalent to the condition $\omega >> 1$.

When global feedback is present, force F(t) is constructed by taking global average

$$\overline{A}(t) = \frac{1}{S}\int_{(S)} A(\mathbf{r},t)d\mathbf{r} \qquad (2)$$

of local complex oscillation amplitudes at a delayed time moment t - τ (here S is the total area of the system) and multiplying this by a complex proportionality coefficient, i.e. as

$$F(t) = \mu e^{i\alpha_0}\overline{A}(t-\tau) \ . \qquad (3)$$

Hence, μ specifies the intensity of global feedback, χ_0 characterizes the phase shift between the delayed average oscillation amplitude and the (complex) control signal, and τ represents the delay time.

It is convenient to introduce slowly varying complex oscillation amplitudes as

$$\eta(\mathbf{r},t) = A(\mathbf{r},t)\exp(i\omega t) \ . \tag{4}$$

With this transformation, equation (1) takes the form

$$\dot{\eta} = \eta - (1+i\beta)|\eta|^2\eta + (1+i\varepsilon)\nabla^2\eta + f(t) \ , \tag{5}$$

where

$$f(t) = \mu\exp\left[i(\chi_0 + \omega\tau)\right]\overline{\eta}(t-\tau) \tag{6}$$

and

$$\overline{\eta}(t) = \frac{1}{S}\int_{(S)}\eta(\mathbf{r},t)d\mathbf{r} \ . \tag{7}$$

Characteristic evolution times of thus defined slow complex oscillation amplitudes $\eta(r,t)$ are of order unity. Therefore, when only short delays ($\tau << 1$) are considered, as assumed throughout this paper, a delay between the slowly varying complex control signal f(t) and the slowly varying global oscillation amplitude $\overline{\eta}$ in equation (6) can already be neglected.

Once this approximation is made, the only (but very important) remaining effect of delays is that they control the effective phase shift,

$$\chi = \chi_0 + \omega\tau \ , \tag{8}$$

between the global oscillation amplitude and the control signal. Note that since $\omega >> 1$ the renormalization of the phase shift can be significant even for short delays, less than an oscillation period.

When such conditions are satisfied, the system is approximately described by the equation

$$\dot{\eta} = \eta - (1+i\beta)|\eta|^2\eta + (1+i\varepsilon)\nabla^2\eta + \mu e^{i\chi}\bar{\eta} \qquad (9)$$

where $\bar{\eta}$ is given by the spatial average (7) of the complex oscillation amplitude. This equation has earlier been formulated to model effects of global coupling in oscillatory surface reactions [21-25]. Below we use equation (9) as a basic model for our analytical and numerical investigations.

Since elementary structures of CGLE play an important role in the subsequent analysis, brief summary of such structures and their properties is next presented.

1.2. Elementary structures and turbulence in CGLE

Steady uniform oscillations have frequency $\omega_0 = \omega - \beta$ and amplitude $\rho = 1$. Traveling plane waves $\eta(x,t) = \rho_k \exp(ikx - i\omega_k t)$ with $\rho_k = 1 - k^2$ and $\omega_k = \omega_0 + (\varepsilon - \beta)k^2$ are unstable in respect to the modulational Eckhaus instability [26] when their wavenumber k is greater than k_E given by the equation

$$k_E^2 = \frac{1+\varepsilon\beta}{2(1+\beta^2)+1+\varepsilon\beta} . \qquad (10)$$

The critical wavenumber k_E goes to zero at $1 + \varepsilon\beta = 0$. When $1 + \varepsilon\beta < 0$, uniform oscillations with $k = 0$ are unstable in respect to the Benjamin-Feir (BF) instability.

Front collisions of traveling plane waves lead to their annihilation. The annihilation takes place within a narrow region with an increased oscillation amplitude that represents a *shock*. If both colliding waves have the same wavenumber k, the width of a shock is estimated [18] as

$$\delta x \approx \frac{1+\varepsilon\beta}{2(\varepsilon-\beta)k} . \qquad (11)$$

In the center of a shock, the local modulus ρ of the complex oscillation amplitude is increased by

$$\delta\rho = \frac{\varepsilon(\varepsilon-\beta)k^2}{2(1+\varepsilon\beta)} . \qquad (12)$$

Equations (11) and (12) are valid for $1 + \varepsilon\beta > 0$ while $\delta\rho << 1$.

Bekki-Nozaki (BN) holes [7,27-29] are a family of exact one-dimensional solutions of CGLE that represent standing or steadily moving local depressions of the oscillation amplitude. Below we formulate principal properties of such solutions.

This family is parameterized by the velocity of holes c. If a hole is standing, the amplitude modulus ρ in its center vanishes. When the amplitude is zero, the phase is not defined in the center which represents therefore a point of the phase singularity. For a standing BN hole the phase differs by π on both sides of this singularity point. Such an object emits two waves with wavenumbers k_h that propagate in opposite directions.

For a slowly moving hole the minimal modulus of the oscillation amplitude does not reach zero (Fig. 1a). Since ρ does not vanish, the phase singularity is then absent. Instead, the phase rapidly changes within a narrow coordinate interval where the amplitudes are small (Fig. 1b). The asymptotic wavenumbers $k_+(c)$ and $k_-(c)$ are different - the forward wave has a shorter wavelength than the rear wave.

At a certain velocity c^*, the wavenumber of the rear wave left behind a moving hole reaches zero, $k_-(c^*) = 0$. This hole represents thus a front of transition from uniform oscillations to a plane wave moving in the direction of the plane wave.

Fig. 2 shows the profiles of the amplitude modulus and the phase for a BN hole that moves at a velocity slightly larger than c^*. The plane waves behind and before of a moving hole are now propagating in the same direction, but k_+ is larger than k_-. The difference between k_+ and k_- diminishes as the velocity v grows and the magnitude of the amplitude suppression in the central region separating two plane waves becomes progressively smaller. When a maximal velocity c_{max} is reached, $k_+ = k_- = k_{max}$ and the moving hole gradually transforms into a plane wave with a certain wavevector k_{max}.

Though the general BN solution is complicated, simple estimates for some of its characteristic properties are available:

$$k_s = \left[1 + \frac{3(1+\varepsilon^2)}{r(\varepsilon-\beta)}\right]^{-1/2}, \quad k_{max} = \left[1 + \frac{3r(1+\beta^2)}{(1+r^2)(\varepsilon-\beta)}\right]^{-1/2}, \tag{13}$$

$$c_{max} = 2(\varepsilon-\beta)k_{max}, \; c^* = \frac{2(\varepsilon-\beta)k_0}{\sqrt{k_0^2 + k_{max}^2}}, \tag{14}$$

where

$$r = \begin{cases} b + \sqrt{2 + b^2}, \text{ if } \varepsilon > \beta \\ b - \sqrt{2 + b^2}, \text{ if } \varepsilon < \beta \end{cases}, \quad b = -\frac{3(1 + \varepsilon\beta)}{2(\varepsilon - \beta)} . \tag{15}$$

Note that equations (13) - (15), describing a BN hole, are valid on both sides of the BF boundary given by the condition $1 + \varepsilon\beta = 0$.

In the limit when ε is close to β, so that the difference $\delta = \varepsilon - \beta$ is small, we have

$$k_h \approx \frac{\sqrt{2}\delta}{3(1 + \varepsilon^2)}, \; k_{max} \approx \frac{1}{\sqrt{3}} . \tag{16}$$

In this limit k_h is small and k_{max} coincides with the boundary k_E of the Eckhaus instability for plane waves.

Though BN holes are solutions for a one-dimensional system, they can be used to generate patterns in two dimensions. BN stripes are obtained by extending this one-dimensional solution along the second coordinate. BN stripes may also be bent and closed into loops [30].

Spiral waves in two-dimensional systems are associated with localized wave sources. Such a source represents a small core lying in the center of the spiral pattern. The oscillation phase changes by 2π after going around any surrounding it contour. Hence, the core includes a point of a phase singularity where the oscillation amplitude is zero. An approximate analytical solution for spiral waves in CGLE is available in the limit when $\delta \to 0$. In this case the asymptotic wavenumber k_{sw} of plane waves far from the center of a rotating spiral wave is given by [6,18]

$$k_{sw} \approx \frac{\zeta}{\delta}\sqrt{1 + \varepsilon^2}\exp\left[-\frac{\pi}{2\delta}(1 + \varepsilon^2)\right] \tag{17}$$

where $\zeta \approx 1.018...$. The rotation frequency of the spiral wave is

$$\omega_{sw} = \omega_0 + \delta k_{sw}^2 . \qquad (18)$$

Thus, in the considered limit the spiral wave is a much more long-wave source than the standing BN stripe, i.e. $k_{sw} << k_h$. Intriguingly, the dependence on the small parameter δ in equations (16) and (18) for k_{sw} and k_h formally coincides with the dependence of the energy of a localized state of a quantum particle in a potential well on the depth of this potential well, as yielded by the perturbation theory for the Schrödinger equation [31].

When the condition $1 + \varepsilon\beta < 0$ is realized, uniform oscillations, traveling plane waves and, therefore, any pattern that emits such waves, are unstable. Note, however, that special CGLE solutions describing such patterns continue to exist even in this parameter region. Indeed, traveling waves or BN holes, for which exact solutions are constructed, do not undergo any significant change as this boundary is crossed. The same may be true for spiral waves, though no analytical description for such patterns in this parameter region is available.

Turbulence in CGLE is a subject of intensive research in the last two decades, starting from the early numerical simulations [2,3] where the basic concepts of amplitude and phase turbulence have already been introduced. Various chaotic spatiotemporal regimes have been investigated [8, 9, 11]. A detailed phase diagram for turbulence in the two-dimensional CGLE is constructed [13].

When the BF boundary $1 + \varepsilon\beta = 0$ is crossed, the uniform state becomes unstable and phase turbulence develops. In this chaotic regime the medium is filled with an irregular set of cells. Inside a cell, the oscillation phase slightly decreases from the center to the periphery, so

that oscillations spread from the center to the cell's boundary. However, the phase difference between the center and the boundary of a cell is always much less than 2π. The modulus ρ of the oscillation amplitude is slightly increased on the boundaries of the cells. Therefore, the cell boundaries can roughly be characterized as formed by shocks.

Though the cells in the phase turbulence regime are not regular and their sizes vary with time and in space, there is a certain typical size of a cell determined by the wavelength of the most unstable perturbation mode of the uniform state. The increment of growth of perturbations in the form of plane waves with a wavevector k is given by

$$\gamma_k = -1 - k^2 + \sqrt{1 - 2\varepsilon\beta k^2 - \varepsilon^2 k^4} \ . \qquad (19)$$

It reaches a maximum at the wavenumber k_{KS} that satisfies the equation

$$\varepsilon k_{KS}^2 = -\beta - \sqrt{\frac{1+\beta^2}{1+\varepsilon^2}} \ . \qquad (20)$$

Near the BF boundary this yields

$$k_{KS}^2 \approx \frac{\nu}{1+\varepsilon^2} - \frac{\nu^2}{2(1+\varepsilon^2)^2} \qquad (21)$$

where $\nu = -1 - \varepsilon\beta$ is a small parameter ($\nu << 1$). The typical size of cells in phase turbulence is $\lambda_{KS} = 2\pi/k_{KS}$; it goes to infinity when the BF boundary is approached.

If, after crossing the BF-boundary, we pass the phase turbulence state and move further into the BF-unstable region, amplitude turbulence is found. This turbulence is characterized by strong

variations of both the phase and the modulus of the complex oscillation amplitude. Transition to amplitude turbulence proceeds through formation of a small seed on the background of phase turbulence. This seed grows until the new regime occupies the entire medium. The transition is characterized by a hysteresis: starting from this state and moving back towards the BF boundary, amplitude turbulence may be found in the parameter regions where phase turbulence has been present under motion in the opposite direction. Amplitude turbulence can even extend into the region where uniform oscillations are stable in respect to small perturbations (however, in our simulations we never choose the parameters in this part of the parameter plane).

For the amplitude turbulence, different states are distinguished. Closer to the BF boundary, frozen states are observed [13]. In such states the medium is filled with a few spiral waves. These waves are steadily rotating and their centers retain positions they have reached at the end of the initial transient process. The areas occupied by individual spirals are separated by shock lines, along which emitted waves collide and annihilate. These shocks are also approximately stationary. The entire pattern resembles frozen structures observed by Kaneko [32] in his simulations of coupled logistic maps. If the spatial distribution of the modulus ρ is plotted for a frozen state, point-like defects, where the modulus reaches zero, are clearly seen. They correspond to centers of spiral waves and are surrounded by flat regions where the modulus is constant. The state of defect turbulence is generally found farther away from the BF boundary [13]. In this state, multiple topological defects representing singularities of the phase field and therefore zeros of the oscillation amplitude, are observed. These defects randomly move through the medium.

2. Analytical investigations

Our analysis is based on the equation (9) for slow oscillation amplitudes. The delays are absent in this equation, though they determine [see eq. (8)] the phase shift between the average oscillation amplitude and the driving force. Global feedback modifies the frequency and the amplitude of uniform oscillations. Substituting $\eta(t) = \rho_0 e^{-i\Omega t}$ into equation (9), we find that in the presence of global feedback the oscillation frequency is shifted from ω_0 by

$$\Omega = -\mu(\sin\chi - \beta\cos\chi) , \qquad (22)$$

and the modulus of the complex amplitude for uniform oscillations is

$$\rho_0 = (1 + \mu\cos\chi)^{1/2} . \qquad (23)$$

When intensity μ of global feedback is low, these corrections are small.

It is convenient to introduce the local modulus ρ of the complex oscillation amplitude and the local oscillation phase ϕ as

$$\eta(\mathbf{r},t) = \rho(\mathbf{r},t)\exp(-i\Omega t - i\phi(\mathbf{r},t)) . \qquad (24)$$

The average (7) of the complex oscillation amplitude can also be written as

$$\overline{\eta}(t) = R(t)e^{-i\Omega t - i\Psi(t)} . \qquad (25)$$

Here $\Psi(t)$ represents the global oscillation phase. The variable R(t) is called below the *synchronization parameter*. Indeed, it is given by the equation

$$R(t) = \frac{1}{S}\left|\int_{(S)} \eta(\mathbf{r},t)d\mathbf{r}\right| \quad . \tag{26}$$

Therefore, it vanishes when oscillations in different parts of the medium are not correlated and approaches its maximal value ρ_0 for the uniform oscillations.

2.1. Stability of uniform oscillations

Assuming periodic boundary conditions, complex oscillation amplitudes can be decomposed into a superposition of plane waves:

$$\eta(\mathbf{r},t) = \sum_{\mathbf{k}} \eta_{\mathbf{k}}(t) e^{i\mathbf{kr}} \quad . \tag{27}$$

The equations determining evolution of amplitudes $\eta_{\mathbf{k}}$ are obtained by performing a Fourier transformation of equation (9), which yields

$$\dot{\eta}_{\mathbf{k}} = \left(1 + \mu e^{i\alpha}\Delta(\mathbf{k}) - k^2 - i\varepsilon k^2\right)\eta_{\mathbf{k}} - (1+i\beta)\sum_{\mathbf{k}_1,\mathbf{k}_2,\mathbf{k}_3} \eta^*_{\mathbf{k}_1}\eta_{\mathbf{k}_2}\eta_{\mathbf{k}_3}\Delta(\mathbf{k}+\mathbf{k}_1-\mathbf{k}_2-\mathbf{k}_3) \quad . \tag{28}$$

The mode with $\mathbf{k} = 0$ corresponds to uniform oscillations. As follows from (28), its amplitude η_0 obeys the equation

$$\dot{\eta}_0 = (1+\mu e^{i\alpha})\eta_0 - (1+i\beta)|\eta_0|^2\eta_0 - 2(1+i\beta)\sum_{\mathbf{k}\neq 0}|\eta_{\mathbf{k}}|^2\eta_0$$

$$-(1+i\beta)\sum_{\mathbf{k}\neq 0}\eta_{\mathbf{k}}\eta_{-\mathbf{k}}\eta_0^* - (1+i\beta)\sum_{\mathbf{k}_1,\mathbf{k}_2,\mathbf{k}_3\neq 0}\eta^*_{\mathbf{k}_1}\eta_{\mathbf{k}_2}\eta_{\mathbf{k}_3}\Delta(\mathbf{k}_1-\mathbf{k}_2-\mathbf{k}_3) \quad . \tag{29}$$

When the stability of uniform oscillations is investigated, the plane wave modes with $\mathbf{k} \neq 0$ represent small perturbations. Examining equation (29), it can be seen that in the linear approximation the dynamics of uniform oscillations is not influenced by such perturbations.

This means that in this approximation the plane-wave modes are decoupled from uniform oscillations and, when their evolution is investigated, we should put $\eta_0 = \rho_0 e^{-i\Omega t}$ where ρ_0 and Ω are given, respectively, by equations (23) and (22). By keeping only linear terms in the evolution equations for plane waves, we obtain:

$$\dot{\eta}_{\mathbf{k}} = \left[1-(1+i\beta)\rho_0^2-(1+i\varepsilon)k^2\right]\eta_{\mathbf{k}} - 2(1+i\beta)\rho_0^2 e^{-2i\Omega t}\eta^*_{-\mathbf{k}} \ . \qquad (30)$$

Thus, so far as the linear stability analysis is performed, the problem is identical to an investigation of CGLE with external periodic forcing and corresponds to the case n = 1 of Refs. 33-34.

We see that, according to equation (30), pairs of modes with opposite wave vectors **k** and **-k** are coupled in the linear approximation and therefore all unstable modes should represent their symmetrical superpositions, i.e. standing waves. To investigate properties of such standing waves, it is more convenient to perform the linear stability analysis not for complex oscillation amplitudes but for variables $\rho(\mathbf{r},t)$ and $\phi(\mathbf{r},t)$. This immediately yields spatial distributions of the phase and the oscillation amplitude modulus in such a pattern (of course, the same results could be obtained after some algebraic transformations directly from equations for the amplitudes $\eta_{\mathbf{k}}$).

When written for the variables $\rho(\mathbf{r},t)$ and $\phi(\mathbf{r},t)$, the model (9) gives a set of two equations:

$$\dot{\rho} = (1-\rho^2)\rho + \nabla^2\rho - \rho(\nabla\phi)^2 + \varepsilon\rho\nabla^2\phi + 2\varepsilon\nabla\rho\nabla\phi + \mu R\cos(\phi - \Psi + \chi) \ , \quad (31)$$

$$\dot{\phi} = \beta\rho^2 - \Omega + \frac{2}{\rho}\nabla\rho\nabla\phi + \nabla^2\phi - \frac{\varepsilon}{\rho}\nabla^2\rho + \varepsilon(\nabla\phi)^2 - \frac{\mu R}{\rho}\sin(\phi - \Psi + \chi) \ . \quad (32)$$

Linearizing these equations near uniform oscillations with $\rho = R = \rho_0$ and $\phi = \Psi$, evolution equations for perturbations $\delta\rho(r,t)$ and $\delta\phi(r,t)$ are obtained:

$$\delta\dot{\rho} = -2\rho_0\delta\rho + \nabla^2\delta\rho + \varepsilon\rho_0\nabla^2\delta\phi - \mu\rho_0\delta\phi\sin\chi \ , \quad (33)$$

$$\delta\dot{\phi} = 2\beta\rho_0\delta\rho + \nabla^2\delta\phi - \frac{\varepsilon}{\rho_0}\nabla^2\delta\rho - \mu\delta\phi\sin\chi + \frac{\mu}{\rho_0}\delta\rho\cos\chi \ . \quad (34)$$

Solutions of these equations are linear superpositions of standing waves,

$$\delta\rho(x,t) = \delta\rho_k \exp(\gamma_k t)\cos(kx) \ , \quad (35)$$

$$\delta\phi(x,t) = \delta\phi_k \exp(\gamma_k t)\cos(kx), \quad (36)$$

where the coordinate axis x is chosen to be oriented along the vector k. The increments of growth γ_k satisfy the equation

$$(\gamma_k + 2 + 3\mu\cos\chi + k^2)(\gamma_k + \mu\cos\chi + k^2)$$

$$+(\varepsilon k^2 + \mu\sin\chi)\left[2\beta(1+\mu\cos\chi) + \varepsilon k^2 + \mu\sin\chi\right] = 0 \ . \quad (37)$$

Depending on the parameters and the wavenumber k, this equation may have either two real or two complex conjugated roots γ_k [in the latter

case the complex conjugate terms should be added to the right sides of equations (35) and (36) to obtain real quantities]. Variations of the phase and the modulus in a growing standing wave mode are related as

$$\delta\phi_k = -\frac{\gamma_k + 2\rho_0 + k^2}{\varepsilon\rho_0 k^2 + \mu\rho_0 \sin\chi}\delta\rho_k \,. \tag{38}$$

We first consider the situation where both roots γ_k of the characteristic equation (37) are real. Then the instability threshold of uniform oscillations is reached when the largest of the roots for the modes with all possible wavevectors k crosses zero and becomes positive. It means that at the threshold the conditions

$$\gamma_k = 0\,,\quad \frac{\partial\gamma_k}{\partial k} = 0\,,\quad \frac{\partial^2\gamma_k}{\partial k^2} < 0 \tag{39}$$

should be satisfied for a mode with a certain wavevector $k = k_0$.

Differentiating equation (37) in respect to variable $q = k^2$ and using conditions (39), the critical intensity of global coupling is determined as

$$\mu_c = -\frac{1 + \varepsilon\beta + (1+\varepsilon^2)k_0^2}{(2+\varepsilon\beta)\cos\chi + \varepsilon\sin\chi} \,. \tag{40}$$

The wavevector k_0 of the first unstable mode is then found from equation (37), taking into account that $\gamma_k = 0$ at $k = k_0$ and that the intensity of global feedback at the threshold should be given by equation (40).

Note that the first unstable mode is in this case a standing wave. Indeed, it has the same frequency as that of the uniform oscillations (since $\mathrm{Im}\gamma_k = 0$) and represents a growing periodic spatial variation [see

(35) and (36)] of the phase and the amplitude modulus of such oscillations.

Although in general the solutions for k_0 and μ_c are complicated and can be only numerically analyzed, simple expressions for these properties are available near the BF boundary where the parameter $\nu = -1 - \varepsilon\beta$ is small. By keeping only the terms up to the second order in ν, we find

$$k_0^2 \approx \frac{\nu}{1+\varepsilon^2} - \frac{\varepsilon\nu^2(\cos\chi + \varepsilon\sin\chi)}{2(1+\varepsilon^2)^2(\varepsilon\cos\chi - \sin\chi)} \quad , \tag{41}$$

$$\mu_c \approx \frac{\varepsilon\nu^2}{2(1+\varepsilon^2)(\varepsilon\cos\chi - \sin\chi)} \, . \tag{42}$$

In the limit of small ν's variations of the phase and of the modulus in the first unstable standing wave mode are related as

$$\delta\phi \approx -\frac{2(1+\varepsilon^2)}{\varepsilon\nu}\delta\rho \quad . \tag{43}$$

We see that in the linear order in the parameter ν, specifying the distance from the BF boundary, the wavelength $\lambda_0 = 2\pi/k_0$ coincides with the characteristic size λ_{KS} of the cells in the phase turbulence regime of CGLE [cf. equations (21) and (41)] and does not depend on the phase shift parameter χ. The difference between the two characteristic lengths is revealed in the second-order corrections, already sensitive to the phase shift. The critical intensity μ_c of global coupling is proportional in this limit to ν^2. According to the equation (43), variations of ρ and ϕ in the standing wave are shifted by half of the spatial period, i.e. the phase ϕ has its maxima where the modulus ρ is minimal.

Fig. 3 shows the dependence of k_0^2 as function of ν, obtained by numerical solution of equations (37) and (39), together with its quadratic approximation (41). We see that though this approximation has been derived assuming that $\nu << 1$, it remains satisfactory even at larger values of this parameter.

The instability threshold μ_c rapidly increases as the phase shift $\chi = \arctan\varepsilon$ is approached[1]. This is accompanied by a decrease of the wavenumber k_0 of the first unstable standing wave. As seen from (41), this wavenumber reaches zero at certain point χ^* shortly before μ_c diverges. Above this point, equation (41) yields $k_0^2 < 0$ which is unphysical. Returning to equations (37) and (39), we find that for $\chi > \chi^*$ they have a solution where the maximal increment of growth is achieved at $k = 0$ and therefore the first unstable mode has $k_0 = 0$. In this region the instability threshold is

$$\mu_c = -\frac{2(\beta\sin\chi + \cos\chi)}{1 + 2\cos\chi(\beta\sin\chi + \cos\chi)} . \qquad (44)$$

This branch meets at $\chi = \chi^*$ the branch with $k_0 \neq 0$, described by equations (41) and (42) . When $\chi > \chi^*$, the increment of growth γ_k is minimal at $k = 0$ for μ given by equation (44).

A note of caution should now be made. As follows from equation (29), the uniform mode with $k = 0$ is always stable in the linear approximation. The characteristic equation (37) is derived by considering small nonuniform perturbations of the uniform oscillations. Therefore, any unstable mode determined by this equation must have a nonvanishing wavenumber. If periodic boundary conditions are used, the

---

[1] Here and below, unless specially noted, we consider the phase shifts inside the interval $-\pi < \chi < +\pi$. We restrict our analysis to the case of positive values of the parameter ε.

minimal wavenumber is $k_{min} = 2\pi/L$ where L is the spatial size of the medium.

For large systems $L \to \infty$ and therefore the limit $k \to 0$ can be considered. Thus, when modes with k = 0 are considered, we actually mean the modes with the minimal possible wavenumber, specified by the size of the medium and the boundary conditions. In our numerical simulations, described below, we see that, when such an instability occurs, the medium breaks into large domains whose sizes are about the dimension of the medium.

Finally, unstable modes with $\mathrm{Im}\gamma_k \neq 0$ are also possible. As follows from equation (37), for such modes we have

$$\mathrm{Re}\,\gamma_k = -1 - k^2 - 2\mu\cos\chi \,. \tag{45}$$

Therefore, the least stable mode is always the mode with k = 0 (i.e. it has the maximal possible wavelength for a given medium). The instability occurs only if $\cos\chi < 0$. In contrast to the instabilities related to growth of standing waves, this instability develops under an *increase* of the feedback intensity μ, i.e. when $\mu > \mu_0$ where

$$\mu_0 = -\frac{1}{\cos\chi} \,. \tag{46}$$

Therefore, for some phase shifts χ uniform oscillations may be stable inside an interval of the global feedback intensity μ. They become stabilized as a certain low boundary $\mu_c^{(1)}$, given by equations (42) or (44), is crossed but lose again their stability a higher value $\mu_c^{(2)}$, given by equation (46), and are then replaced by turbulence.

Fig. 4 shows the stability diagram of uniform oscillations in the plane (χ, μ) which has been obtained by direct numerical solution of the

characteristic equation (37). In this diagram the parameters $\varepsilon = 2$ and $\beta = -1.4$ has been chosen, so that the parameter $\nu = -1 - \varepsilon\beta$ is no longer small ($\nu = 1.8$). Uniform oscillations are stable above the boundary consisting of curves AB, BC, CE and AD.

When the curve AB is crossed, standing waves with $k_0 \neq 0$ appear. The dependence of their wavelength $\lambda_0 = 2\pi/k_0$ on the phase shift χ is shown in Fig. 5 (the horizontal line in this figure shows the respective typical size λ_{KS} of the cells in the phase turbulence regime in absence of the global feedback). This wavelength diverges as the point B, corresponding to $\chi^* \approx 0.275\ \pi$, is approached. The wavelength monotonously decreases when the phase shift is decreased.

When the curve BC, determined by the equation (44), is crossed, a large-scale domain structure develops in the medium, with the characteristic size of domains about the size of the entire medium. This domain structure has at the threshold the same frequency as that of the uniform oscillations and is therefore 'standing', or static, in the coordinate frame rotating with the frequency of the uniform oscillations.

In contrast to this, if curves DA or CE are crossed, long-wavelength oscillatory perturbations start to grow. These two curves asymptotically approach $\mu = \infty$ at $\chi = \pm\ \pi/2$. For $\chi_- < \chi < -\pi/2$ and for $\pi/2 < \chi < \chi_+$, where $\chi_- \approx -0.6235\ \pi$ and $\chi_+ \approx 0.599\ \pi$, uniform oscillations are stable only inside certain intervals of the feedback intensity μ.

Of course, the linear stability analysis does not yet allow to determine, whether a bifurcation is supercritical or subcritical. This can only be found by investigating the role of nonlinear terms, giving rise to interactions between the modes. When an instability of uniform oscillations leads to growth of a mode with $k_0 \neq 0$, the characteristic

equation (37) fixes only the magnitude $|\mathbf{k}| = k_0$ of the wavevector, but leaves its direction arbitrary. Therefore, all such modes grow in the linear approximation. Nonlinear interactions may select a group of modes that eventually dominates over the medium. Due to mutual enhancement, the modes in this group can grow even when single modes already die out. This changes the nature of the bifurcation, making it subcritical and characterized by a hysteresis.

The nonlinearly selected groups often represent, as known in the theory of stationary Turing patterns [17,18], triplets of modes with the wavevectors satisfying the conditions $\mathbf{k}_1 + \mathbf{k}_2 + \mathbf{k}_3 = 0$, where $|\mathbf{k}_1| = |\mathbf{k}_2| = |\mathbf{k}_3| = k_0$. A superposition of such three modes gives rise to a hexagonal cellular structure. Similar cellular structures may appear near the instability boundary AB in Fig. 4. They have indeed been observed in our preliminary study [25] and will be discussed in detail in Sect. 3.

It should be emphasized that, in contrast to the usual Turing instability, the considered system is oscillatory and individual modes forming a cellular structure are standing waves. When such a structure is established in the medium, all its elements continue to perform oscillations. However, the modulus and the phase of these oscillations depend on the location of a given element inside a cell.

Though the cells result from nonlinear interactions, insight into their properties (later confirmed by numerical simulations) can be gained from the linear theory. As follows from equation (43), in a single standing wave mode the oscillation phase ϕ reaches its maximum at a point where the amplitude modulus ρ is minimal. When a superposition of three such modes, representing a cellular structure, is constructed, this point would correspond to the center of a cell. Since the phase is maximal there, oscillations originate in the center and spread towards

the cell's boundary. On the boundary, oscillation fronts coming from two neigbouring cells meet and annihilate. Thus, the cells behave as if there were a pacemaker sitting in each of their centers. Note, however, the phase gradients inside a cell are small, i.e. the cell's size is shorter than the wavelength of produced waves. As a result, only single fronts spreading from the center and annihilating at the boundary are seen. Since waves are colliding at the boundary, a shock-like object can be expected there. Indeed, according to equation (43), the modulus is increased where the phase has its minimum, i.e. on the boundary of a cell.

2.2. Phase flips

Phase flips are new elementary structures that appear in CGLE under negative global feedback. Inside a flip the oscillation phase makes full 2π rotation. Such objects travel at a constant velocity preserving their spatial profile. Phase flip solutions are constructed below using a reduced phase description for the system with global feedback. The BF-stable case where the condition $1 + \varepsilon\beta < 0$ holds and local diffusional coupling tends to stabilize uniform oscillations is here considered.

Suppose that the local oscillation phase $\phi(r,t)$ slowly varies in space and in time and that the modulus $\rho(r,t)$ of the oscillation amplitude only slightly deviates from its constant value ρ_0 characteristic for uniform oscillations. Then the modulus adiabatically adjusts to the local spatial derivatives of the phase, i.e.

$$\rho = \rho_0 + \frac{\varepsilon}{2}\nabla^2\phi - \frac{1}{2}(\nabla\phi)^2 , \qquad (47)$$

and the phase description is applicable [3,35]. In this approximation evolution of the phase variable obeys the equation [22]

$$\dot{\phi} = g(\phi - \Psi) + (\varepsilon - \beta)(\nabla\phi)^2 + (1 + \varepsilon\beta)\nabla^2\phi \qquad (48)$$

that differs from the usual phase dynamics equation for CGLE (see [18]) by the presence of an additional term,

$$g(\phi - \Psi) = \mu\sqrt{1+\beta^2}\left[\sin\chi_1 - \frac{R}{\rho_0}\sin(\phi - \Psi + \chi_1)\right] , \qquad (49)$$

taking into account action of global feedback and depending on the difference between local oscillation phase ϕ and global phase Ψ. Assuming that $\mu << 1$ we keep only the terms up to the first order in μ; the notation $\chi_1 = \chi$ - arctanβ is employed.

Depending on the phase shift χ, the feedback can be either positive or negative, i.e. it can destroy uniform oscillations or increase their stability. To find the conditions for a negative global feedback, behaviour of small local perturbations of the uniform state should be considered.

Suppose that the local oscillation phase is slightly shifted ($\phi = \Psi + \delta\phi$) in some region in respect to the global oscillation phase Ψ, fixed by uniform oscillations in the rest of the medium. This region is small in comparison to the total size of the medium but larger than the diffusion length, so that the terms with spatial derivatives in (48) can be neglected. Evolution of such perturbations is described by the linearized equation

$$\frac{d\delta\phi}{dt} = g'(0)\delta\phi , \qquad (50)$$

where

$$g'(0) = \left.\frac{\partial g}{\partial \phi}\right|_{\phi=\Psi} = -\mu\sqrt{1+\beta^2}\cos\chi_1 \,. \qquad (51)$$

We see that the sign of the derivative g'(0) determines whether a perturbation would grow or fade.

If $\cos\chi_1 < 0$ (or, explicitly, $\cos\chi + \beta\sin\chi < 0$), global feedback is positive and the local phase tends to deviate from the global phase. Numerical simulations show that in this case the medium breaks into a few large domains with different oscillation phases [22]. This situation is reminiscent of spontaneous breaking of ferromagnets into individual magnetic domains, leading to disappearance of the total magnetization. We find below that similar behaviour is also observed in the BF-unstable region.

When negative global feedback is realized (i.e. $\cos\chi_1 > 0$), small local phase variations are damped. In this case, however, traveling phase flips are possible [21-22]. If a large medium contains a single phase flip, its presence does not significantly influence the global oscillation phase Ψ determined by uniform oscillations in the rest of the medium and, moreover, $R \approx \rho_0$. It can be said that the rest of the medium generates in this case a periodic driving force. Hence, the situation is similar to the problem with external forcing where phase flips have earlier been considered [33,34] . An important difference is, however, that the driving force produced by a global feedback is always resonant.

The phase dynamics equation (49) has an infinite number of phase-locked states with phases $\phi_m = \Psi + 2\pi m$, where m = 1, 2, 3,... . Though

such states are physically indistinguishable, traveling waves of *transitions* between them are possible. They represent phase flips

$$\phi(x,t) = \Phi(\xi)\ ,\ \xi = x - Vt\ \ , \tag{52}$$

satisfying the conditions $\Phi \to \Psi$ for $\xi \to \infty$ and $\Phi \to \Psi + 2\pi$ for $\xi \to -\infty$. Inside a flip the phase undergoes a full 2π rotation; V is the propagation velocity of the flip.

To construct these solutions and analyze their properties, we perform in equation (49) a nonlinear transformation to the new variable u, defined by

$$\phi - \Psi = \frac{1+\varepsilon\beta}{\varepsilon-\beta}\ln u\ , \tag{53}$$

which yields for the variable u the evolution equation

$$\dot{u} = Q(u) + (1+\varepsilon\beta)\nabla^2 u \tag{54}$$

with the nonlinear source function given by

$$Q(u) = \mu u\sqrt{1+\beta^2}\,\frac{\varepsilon-\beta}{1+\varepsilon\beta}\left[\sin\left(\chi_1 + \frac{1+\varepsilon\beta}{\varepsilon-\beta}\ln u\right) - \sin\chi_1\right]. \tag{55}$$

An equation of the same form describes propagation of trigger waves in bistable one-component reaction-diffusion systems [18] and results of the respective analysis are directly applicable here.

The equation (54) has traveling wave solutions u = U(ξ) with ξ = x - Vt that satisfy asymptotic conditions

$$U(\xi) \to u_1 \text{ for } \xi \to -\infty \text{ and } U(\xi) \to 1 \text{ for } \xi \to \infty \ , \tag{56}$$

where

$$u_1 = \exp\left[\frac{2\pi(\varepsilon - \beta)}{(1 + \varepsilon\beta)}\right] . \tag{57}$$

This solution, including its propagation velocity V, is uniquely determined by the conditions (56). Particularly, the velocity sign is controlled by the integral (cf. [18])

$$J = \int_1^{u_1} Q(u)du \ . \tag{58}$$

Calculating this integral, we find after some transformations that an important role is played by the parameter combination

$$A = \sin\chi_1 + \frac{2(\varepsilon - \beta)}{(1 + \varepsilon\beta)}\cos\chi_1 \ . \tag{59}$$

The velocity V is positive when A < 0 and negative if A > 0. Note that for the solution (56) the positive propagation velocity means that phase ϕ is increased by 2π after a phase flip has passed through a given point of the medium; it is decreased by 2π if V is negative. In other words, the phase inside a phase flip may rotate either the clockwise or the counterclockwise direction, depending on the sign of A. The phase flips are standing if A = 0.

Though the variable u changes from 1 to u_1 inside a propagating phase flip, these values correspond to a phase change of 2π and therefore the states of the medium before and after the passage of the

flip are physically identical. The pattern is therefore visible only in a narrow region where the phase varies.

The width of a phase flip is estimated from equation (55) as

$$\delta x \approx \left[\frac{1+\varepsilon\beta}{\mu(\varepsilon-\beta)(1+\beta^2)^{1/2}} \right]^{1/2} . \qquad (60)$$

It is inversely proportional to the square root of the feedback intensity μ. The phase gradient inside a phase flip can be approximately estimated as $\nabla\phi = 2\pi/\delta x$.

According to equation (47), variation of the phase leads to variation of the modulus ρ inside a phase flip. Taking as the center of the flip the point x where $\partial^2\phi/\partial x^2 = 0$, we find that the amplitude modulus is decreased there by $\delta\rho = -(\nabla\phi)^2/2$ or, explicitly, by

$$\delta\rho = -\frac{2\pi^2\mu(\varepsilon-\beta)(1+\beta^2)^{1/2}}{1+\varepsilon\beta} . \qquad (61)$$

This can be taken as the characteristic magnitude of the modulus variation in a phase flip. The amplitude depression in a flip becomes stronger when the BF boundary $1 + \varepsilon\beta = 0$ is approached. It also increases for higher feedback intensities μ.

Note that the reduced phase description, i.e. the equation (47), is applicable while $\delta\rho << 1$. To investigate the behaviour of phase flips at higher feedback intensities, numerical simulations based on the equation (9) have been performed. These simulations have been carried out for the one-dimensional medium of length L = 102.4 with periodic boundary conditions, using a small coordinate step dx = 0.1 and a short time step $dt = 10^{-5}$. To create a phase flip, we used periodic boundary conditions and started with the initial condition where the modulus of

the oscillation amplitude was constant over the medium but the phase gradually decreased by 2π from the left to the right sides of the interval (i.e. the winding number was equal to 1).

Fig. 6 displays phase and modulus profiles in a traveling phase flip at a moderate intensity of global feedback. This object is stable and travels at a constant velocity, though the modulus depression in it is already considerable. Note also that the depression of the amplitude modulus is actually preceded by its small increase.

Numerical simulations have shown that further increase of the feedback intensity leads to destruction of phase flips which disappear transforming to uniform oscillations. When the simulation is started from the described above initial condition, the profile similar to that of a steadily traveling phase flip (Fig. 6) first appears. Then the flip slightly accelerates and the amplitude depression in its center increases (T = 112.5 in Fig. 7a). At the same time, the phase profile gets steeper (T = 112.5 in Fig. 7b). Within a very short time, the amplitude in one point inside the flip region sharply falls down and a jump develops in the phase profile. In the frame T = 113.07 of Fig. 7a the minimal value of the amplitude modulus is $\rho = 0.0012$. The respective phase distribution, shown at T = 113.07 in Fig. 7b, displays a large phase jump. Since integration is performed with a small, but still finite time step, we cannot see the exact moment when the amplitude vanishes (i.e. $\rho = 0$). However, it seems that such a moment exists and lies very close to the time T = 113.07.

If the oscillation amplitude vanishes in a certain point, the oscillation phase is not defined there. The phase distributions in the regions lying on the left and right sides of this point become then disconnected and the phase can be changed by 2π while passing this point. Thus, the part of the phase distribution on the left side of the

singularity point may be shifted down by 2π, so that the phase levels at both ends $x = 0$ and $x = L$ of the medium become equal.

Note that this operation, i.e. cutting off the 2π jump at a certain time moment, is needed only when the phase distribution is constructed for visualization purposes. The computed variables are real and imaginary parts of the complex oscillation amplitude. When a phase singularity appears, both of them vanish in a certain point but remain continuous there.

At a later moment, the amplitude modulus is again everywhere positive, though it has a strong depression near the point where it has reached zero (frame T = 113.22 in Fig. 7a). The phase slowly decreases as this point is approached and then sharply grows, forming a local maximum. Farther away from the former singularity point, the phase slowly returns to its initial value (frame T = 113.22 in Fig. 7b). Subsequently, this local pattern smears out (frame T = 114.5 in Fig. 7) and uniform oscillations are established.

Thus, the winding number is not conserved in this one-dimensional system in the presence of strong global feedback. Destruction of phase flips proceeds through the formation of a phase singularity.

In two-dimensional media, curved traveling waves of phase flips are possible. As intensity of global feedback is increased, destruction of these waves, similar to the described above process in a one-dimensional system, may occur. A phase singularity would appear at a certain point on the front, where ρ would reach zero, and the phase-flip wave would break at this point. The rupture would then spread to the left and the right sides. Both ends of a ruptured phase-flip front would represent phase singularities: when going around a contour that surrounds such a point, the phase variation of 2π would be found. Hence, destruction of a phase-flip wave in the two-dimensional oscillatory

medium may be similar to break-up of waves in excitable systems [14]. The tip of the excitation wave corresponds now to the end-point singularity of a broken phase-flip wave.

The above analysis of phase flips has been performed in the BF-stable region, i.e. where the condition $1 + \varepsilon\beta > 0$ holds. However, similar objects are found below in numerical simulations in the parameter region where the opposite condition is satisfied and uniform oscillations are unstable in absence of global feedback.

3. Numerical investigations

To study nonlinear processes in the system, numerical simulations were performed. We employed an explicit integration method with constant time and coordinate steps $dt \leq 0.01$ and $dx = 0.5$ on a square grid of 200 x 200 elements. The integration process was numerically stable and the results did not change when smaller integration steps have been chosen. The medium of size $L = 100$ was sufficiently large to contain many elementary structures. No-flux boundary conditions were used, though some simulations were repeated with periodic boundary conditions. As the initial condition, the unstable uniform state $\eta = 0$ with weak random perturbations has usually been taken.

Since we wanted to examine how the system responds to global feedback in different parameter regions, in a numerical experiment we often started from the system in absence of global feedback ($\mu = 0$) and then slowly increased its intensity μ at a constant speed, until uniform oscillations appeared (if we were inside the synchronization window of phase shifts). To make the system's evolution approximately adiabatic, sufficiently low speeds of ramping have been chosen, though the

minimal speed has been obviously limited by the computation time requirements. When a particularly interesting phenomenon had been observed, we returned and repeated the simulation at a fixed intensity of global feedback.

The data of each evolution case has been used to generate computer animations consisting from 200 to 2000 single frames. In this paper, only selected frames from such animations are presented. Short videos, illustrating basic synchronization scenarios, are available via Internet [36].

For visualization of computed patterns, we employed different variables, i.e. the real part u = Re η of the complex oscillation amplitude η, its modulus ρ and the phase ϕ. The spatial distributions of these variables at subsequent time moments have been plotted using different color codes or gray-scale coding. The spatial distribution of the amplitude modulus ρ is always slowly changing with time, whereas the variables u and ϕ undergo large variation within a single oscillation period. To eliminate as much as possible such obvious rapid variation, we used coordinate frames which rotated at a frequency which was only slightly less than the actual frequency of oscillations. Therefore, the plotted distributions correspond rather to the variables $\tilde{u} = \mathrm{Re}(\eta e^{i\Omega_0 t})$ and $\tilde{\phi} = \phi + \Omega_0 t$ where Ω_0 is the rotation frequency of the coordinate frame. Note that the our basic equation (9) is already written in the coordinate frame that rotates at the frequency Ω of uniform oscillations. However, when the oscillations in the medium are not uniform, their frequency differs, due to the effects of global feedback, from that of the uniform oscillations. In practice, we adjusted the rotation frequency Ω_0 used in the visualization for each sequence of frames after it has been computed.

The phase was calculated as

$$\phi = -\arctan\left(\frac{\mathrm{Im}\,\eta}{\mathrm{Re}\,\eta}\right) + \pi H(\mathrm{Re}\,\eta) + \frac{\pi}{2}\ , \qquad (62)$$

where the step function is defined as H(z) = 1 for $z \geq 0$ and H(z) = 0 for $z < 0$. Hence, the phase varies inside the interval from 0 to 2π. When it reaches its maximal possible value 2π, the phase abruptly falls to the minimal bound 0. As a result, visualizations employing continuous gray-scale coding in the interval from zero to 2π for the phase variable show sharp phase fronts that represent lines of the constant phase $\phi = 0$.

Note that the phase variable (62) is often better suited for visualization of oscillations than real or imaginary parts of the complex oscillation amplitude. Since $\mathrm{Im}\eta = \rho\cos\phi$, the phases that differ by π yield the same value of the imaginary part $\mathrm{Im}\eta$. Therefore, if only the imaginary part of the oscillation amplitude is plotted, it is impossible to see whether a full phase rotation or only a variation of the phase inside the interval from 0 to π takes place along a certain direction. This can be determined if, in parallel, the respective variation of the real part of the oscillation amplitude is traced. This is automatically done when the definition (62) is employed.

To monitor the degree of synchronicity of oscillations, we followed the time dependence of the synchronization parameter R(t), defined by equation (26) and representing the modulus of the averaged oscillation amplitude.

In a recent publication [13], a detailed phase diagram for turbulence in the two-dimensional CGLE has been given and examples of the typical turbulent regimes have been discussed. As a test, we have checked that our simulations correctly reproduced all turbulent states reported in Ref. 13. The simulations described in the next section thus

show what happens with these turbulent states as the global feedback is introduced and its intensity μ is gradually increased. The phase diagram of Ref. 13 with the points corresponding to our simulations is given in Fig. 8.

3.1. Destruction of spiral waves

On the right side of the line T in the phase diagram (Fig. 8) frozen states are observed in the system without global feedback. In such states the medium is filled by a number of steadily rotating spiral waves. These spiral waves develop after a transient from the chaotic state, which first appears when the initial condition $\eta = 0$ with small random perturbation is used. In our simulations we have investigated evolution of such spiral waves as global feedback described by equation (9) is introduced and its intensity μ is gradually increased. Fig. 9 shows destruction of spiral waves by increasing global feedback. The solid curve in the upper part of this figure displays the time evolution of the synchronization parameter R defined by equation (26); the dash line indicates the respective (linear) increase of the feedback intensity μ with time. In the lower part of the figure, characteristic spatial distributions of the variable $\cos\phi$ at six subsequent moments are shown. Parameters ε and β in this simulation correspond to the point 1 in the phase diagram of Fig. 8.

While μ is small, several spiral waves are present. Then one of these waves begins to dominate and spreads its activity over the entire medium. When the spiral wave covers the whole medium, the synchronization parameter R is close to zero because different parts of this pattern oscillate with different phases. Inside the synchronization window, the growing global feedback tends to establish synchronous

oscillations and thus suppress the spiral wave. This occurs in the following way: The waves, traveling from the core of the spiral wave, become destroyed at a certain distance from its center and are replaced there by relatively uniform oscillations. As a result, the rotating spiral is confined inside a roughly circular spatial region surrounded by the area with synchronous oscillations. This region slowly shrinks and the process is accompanied by growth of the parameter R, showing a higher degree of synchronization in the medium.

We sometimes observed that, depending on the choice of the system's parameters, spiral waves spread again its influence over almost the entire medium and thus destroyed the synchronization. Then the synchronization parameter R was decreased. This resembled the intermittency found in numerical simulations [37] of CGLE without global feedback - the difference was, however, that the area outside of the spiral wave was occupied not by the defect turbulence, but by almost uniform oscillations.

As the intensity of global feedback is further increased, the spiral wave becomes localized inside a small circular region which quickly shrinks and disappears. This stage is characterized by monotonous growth of the synchronization parameter R until uniform oscillations are established in the entire medium. If the global feedback intensity μ is increased at a high rate, the intermittent stage is not found and the spiral wave dies immediately out.

Similar evolution under increasing intensity of global feedback was found in the numerical simulations for a different choice of the parameters (point 2 in Fig. 8) where, in absence of global feedback, a large number of rotating spiral waves was observed. As displayed in Fig. 10, a population of spiral waves responds to an increase of global feedback by confining the activity of individual spiral waves inside

islands bounded by certain 'membranes'. Outside of these islands, the oscillations are approximately uniform. The islands populated by wave fragments are not stationary - they change their shapes, move through the medium and can merge. As the intensity of global coupling grows, the islands get smaller and acquire more regular circular shapes. Spiral fragments disappear from the interior of the islands and they collapse, giving way to synchronous oscillations.

It should be noted that, though this phenomenon has not been specifically investigated, spiral waves rotating inside islands surrounded by uniform oscillations have earlier been described in an experiment [38] with catalytic surface chemical reactions, where the global feedback was intrinsically present because of the global coupling via the gas phase.

To analyze in more detail the processes that accompany destruction of a spiral wave by increasing global feedback, we show in Fig. 11 the spatial distributions of (a) the oscillation amplitude modulus ρ and (b) the phase ϕ at subsequent time moments during the process. No-flux boundary conditions have been used in this simulation. The speed of increase of the feedback intensity is now higher than in Fig. 9 and the intermittency does not develop. The contrast in the frames of Fig. 11(a-b) is increased, so that variations of the modulus and the phase are better discernible for small values of these variables.

The frame T = 0 in Fig. 11 displays a spiral wave in absence of global feedback (μ = 0). The modulus ρ is significantly decreased only inside a small core region of the rotating wave and reaches zero in its center. Outside of this region the variable ρ is practically constant, as indeed should be expected for harmonical oscillations.

The black-white spiral interface in the spatial distribution of the oscillation phase in the frame T = 0 indicates the line, along which the

phase reaches the value 2π (white area) and switches to the value 0 (black area). This sharp interface is a consequence of the definition (62) used for plotting of the phase variable. It does not correspond itself to any physical singularity. This form of visualization is however convenient: if a closed contour crosses such an interface, the phase increment along this contour is equal to 2π. The interface ends in the central point where the phase singularity is located.

When the global feedback is switched on but it remains relatively low, the properties of a spiral wave are changed. As seen in the frame T = 73, the spiral is visible now not only in the phase distribution, but also in the spatial distribution of the amplitude modulus. Inside a narrow curled dark stripe, repeating the shape of the phase front, the modulus ρ is somewhat decreased. Examination of the figure also reveals that the dark front is preceded by a slightly brighter area with an increased oscillation amplitude. This is similar to the profile of ρ in the spatial cross-section of a traveling phase flip (Fig. 6). Therefore, we approximately describe this object as a spiral wave formed by a phase-flip wave. Though the amplitude modulus is diminished inside the phase flip, forming the arm of a spiral wave, it vanishes only in one point near the center of the spiral wave, where the phase singularity is located. The other end of the phase flip reaches the boundary of the medium.

As μ is further increased, the outer part of the phase flip, rotating along the system boundary, becomes destroyed. This is preceded by the development of a front instability, already visible at T = 73. We see in this frame that the amplitude modulus ρ gets smaller in the front close to the boundary. Moreover, its distribution along the front is here nonuniform, i.e. at some points on the front the values of ρ are lower. Later, the amplitude vanishes in these points, the phase singularity

develops and the phase flip breaks, similar to what has been described in Sect. 2.

At the moment T = 80, destruction of the phase front in the periphery region is already visible. In the frame, showing the spatial phase distribution at this moment, the sharp interface is absent in the area adjacent to the right boundary of the medium. In this entire area the phase does not reach the value 2π.

At T = 86 we see a long black curled stripe that begins approximately at the end of the sharp phase boundary and extends, along the phase flip front, towards the center of the rotating spiral. Inside this stripe, the local level of the oscillation amplitude modulus is strongly reduced, though it does not yet reach zero. The point where the sharp black-white boundary for the phase distribution ends should correspond to a phase singularity and the oscillation amplitude must vanish there. By comparing spatial distributions of the phase and the modulus in this region, we notice that the modulus ρ indeed becomes very small here, i.e. the local black level is the same as that characteristic for the core of the spiral wave. However, in contrast to the core, a strong depression of the amplitude modulus is not localized near a certain point. It represents an extended amplitude defect which contains a topological defect, i.e. the phase singularity point, near its end.

When such black stripe has just appeared, it is relatively short and does not come close to the center of the spiral, where the profile characteristic for a phase flip with a smaller magnitude of the amplitude reduction persists. However, the stripe moves closer to the core of the spiral (T = 88) and, at the same time, its back retrieves, leaving after it the region with approximately uniform oscillations

(note that the stripe is followed by a long curled bright tail with the increased oscillation amplitude).

At a certain moment (T = 90) the black stripe enters the core of the spiral wave. The phase distribution at this time moment shows that the pattern characteristic for a rotating spiral wave is visible only near the center of the medium, and it is surrounded by the area with the approximately uniform oscillation phase. Later the stripe forms a shortening black tail (T = 92).

At T = 94 a small elongated and slightly curved black drop is seen in the spatial distribution of the amplitude modulus in the center of the medium. The respective phase distribution shows a small dark area, separated by a sharp boundary from the area with uniform oscillations. This phase domain grows and the modulus of the oscillation amplitude inside it does not reach zero now (T = 97).

At the last stage, not shown in Fig. 11, a ring-shaped amplitude domain develops in the center of the medium. It is surrounded by a bright membrane, where the oscillation amplitude modulus is increased. The ring breaks into parts contained inside the membrane. These parts shrink and disappear, so that uniform oscillations are established in the entire medium.

Though the process, illustrated by Fig. 11, is recorded under a gradual increase of the global feedback intensity μ, similar behaviour leading to the destruction of a spiral wave has been found when this intensity has been kept at a fixed high level. These simulations at a fixed feedback intensity have shown, moreover, that merging of the extended amplitude defect and the core of the spiral wave is a very important event. If this has not occurred, the spiral wave can spread again its activity over the medium, as found under the intermittent conditions.

Break-up of the phase flip front, forming the arm of the spiral wave, is locally similar to the process which leads to the destruction of the phase flip in one-dimensional systems (Sect. 2.2). To make the comparison easy, we show in Fig. 12 (a,b) the space-time diagram for the latter process, using the same gray-scale coding as in Fig. 11. We see that the sharp black-white interface ends and the phase flip disappears after the oscillation amplitude has dropped down in the center of such an object.

3.2. Suppression of phase turbulence

Phase turbulence is found near the BF boundary. Fig. 13 (point 3 in the phase diagram in Fig.8) shows several subsequent spatial distributions of the phase ϕ in the medium, when global feedback is absent. We see that an irregular pattern is formed by a system of cells. Inside a cell, the phase is slightly larger at its center. Therefore, new oscillation cycles initiate in the middle of a cell and then the phase fronts quickly propagate towards its periphery. The fronts coming from neigbouring cells collide on the boundary separating these cells and annihilate. Hence, this boundary can be viewed as formed by a shock. Indeed, if the spatial distribution of the amplitude modulus ρ is plotted, one observes that the modulus is slightly increased on the boundary, as it should be for a shock.

When the global feedback is introduced and its intensity μ is gradually increased, the cells tend to form a more regular arrangement (this is however a slow process and therefore the arrangement is not completed if the speed of ramping is too high). At the same time, the magnitude of variations of the phase and the modulus of the oscillation amplitude inside the cells slowly diminishes. Eventually, the cells fade

away and uniform oscillations are established in the medium. This process is very similar to suppression of standing waves in one-dimensional systems, described in Part I.

3.3. Three synchronization scenarios

Farther away from the BF boundary in the unstable region, the state of developed defect turbulence is reached. Our numerical simulations indicate that suppression of such defect turbulence by increasing global feedback is achieved by different scenarios, depending on the phase shift χ of the global feedback: Synchronous oscillations emerge through appearance of a spatial cellular structure, through the regime of localized turbulence, or through formation of large phase domains. In the simulations described below we always start from the same initial state of defect turbulence (point 3 in Fig. 8) but choose different values of the phase shift for the ramped global feedback.

An example of evolution following the first scenario is given in Fig. 14 (point 5 in the phase diagram in Fig. 8). The dash line in the top part of this figure shows growth of the feedback intensity μ, the solid curve presents the respective evolution of the synchronization parameter R. The middle part shows time development for the spatial distribution of the modulus ρ of the local oscillation amplitude along the vertical spatial cross-section drawn through the center of the medium. At the bottom, characteristic spatial distributions of the modulus in the entire medium at three different subsequent time moments are shown. The gray scale coding is chosen, so that darker regions correspond to smaller values of ρ. Almost black small regions indicate amplitude defects where ρ is close to zero. Boundaries of the

cells are formed by shocks with an increased modulus of the oscillation amplitude, which look therefore like thin light membranes.

As the intensity of global feedback increases, shocks surrounding amplitude defects become less mobile and arrange into more regular cellular structures. Inside some cells, amplitude defects disappear and thus empty cells are produced. The cells populated by defects have larger sizes. Occasionally, the defects destroy a cell boundary formed by a shock and penetrate into neighbouring cells. The competing influences of the global feedback, tending to impose synchronization, and of the defects, tending to spread turbulence, balance for some time each another, despite a steady increase of the feedback intensity. Inside this time interval, as seen from Fig. 14, the synchronization parameter R remains near to 0.3.

Under an increase of μ, the number of defects gets smaller and they gradually lose their ability to destroy the cell boundaries. Finally, the growing global feedback completely eliminates the defects and the medium becomes filled only with the hexagonal cells seen in the second frame in the bottom of Fig. 14. In the spatial cross-section, such cellular structures correspond to standing waves in the one-dimensional system.

As μ is further increased, the cell boundaries are gradually washed out and the amplitude variation between the center and the boundaries of a cell gets less pronounced. This process leads to an almost monotonous increase of the synchronization parameter R, until uniform oscillations are established and a constant value of R is reached.

The second scenario of the synchronization onset is illustrated by Fig. 15 where a different value of the phase shift is taken. The growth of the synchronization parameter R is accompanied now by large

fluctuations. They are related to bursts in the number of defects, as seen in the time evolution in the central cross-section.

In comparison to the previously described case, a higher intensity of global feedback is needed here to establish uniform oscillations. Empty cellular structures, forming the background, dissolve now before the disappearance of the cells populated by defects has taken place. As a result, active cells containing defects form clusters, or islands, on the background of uniform oscillations. Sizes and shapes of such turbulent islands vary in time, and they can move through the medium.

When the intensity of global coupling is further increased, these turbulent islands get smaller and the fraction of the medium covered by them decreases. Finally, all turbulent islands die out and uniform oscillations are established in the medium.

The third scenario is observed when we take the phase shift χ inside the interval between χ^* and χ_+ in Fig. 4. In this case, the linear stability analysis predicts that, when the global feedback intensity is decreased, the uniform oscillations should first give rise to large phase domains. Note that this occurs at much larger values of the feedback intensity μ.

In the simulation shown in Fig. 16 we slowly increase the feedback intensity. The initial stage of the pattern evolution is similar to that found in the second scenario. A cellular structure first appears that later transforms into clusters of cells surrounded by the area with uniform oscillations. Later, however, the shock boundaries between the cells in a cluster dissolve and a large single domain is formed. Initially, this domain has a complex shape and nonuniform amplitude activity is observed inside it. As the intensity of global feedback is further increased, the domain acquires an almost elliptical shape and its

interior becomes approximately uniform. At still higher intensities, the domain shrinks and finally disappears.

Note that if we stop increasing the global feedback and fix its intensity, the phase domains are stable and this pattern is persistent. The modulus is slightly decreased inside such a steady domain. The phase slightly decreases from the center towards the boundary and then abruptly drops on the boundary reaching its level for uniform oscillations in the outside region.

Numerical simulations performed under gradual increase of the global feedback intensity, which have been mainly described above, yield a general view of the processes leading to the synchronization onset in the medium. Below we investigate in more detail the typical properties of appearing patterns under the conditions when the global feedback intensity and other parameters of the system are kept constant.

3.4. Cellular structures

Cellular structures are formed by triplets of standing wave modes, whose wave vectors satisfy the condition $\mathbf{k}_1 + \mathbf{k}_2 + \mathbf{k}_3 = 0$ and $|\mathbf{k}_1| = |\mathbf{k}_2| = |\mathbf{k}_3|$. Nonlinear effects saturate growth of these modes and thus a steady hexagonal cellular structure becomes formed. Note that the pattern, that develops from random initial conditions or when going from the turbulent state in a ramping experiment, is very irregular. Long time should pass until a slow relaxation process leading to ordering of the cellular pattern is finished.

In contrast to the Benard or Turing instabilities, cellular structures in the considered oscillatory system are not stationary. Fig. 17 shows the pattern evolution during a single oscillation period. Here the spatial distribution of the local oscillation phase ϕ at subsequent

time moments under fixed global feedback intensity is displayed. A cycle begins with appearance of a relatively regular array of islands. They slowly grow and, shortly before they merge, a hexagonal network is clearly seen. This network is further discernible on the dark background until it fades out and the oscillation cycle is repeated. Cellular structures with such properties have recently been experimentally observed in oscillatory catalytic surface reactions [25].

Note that the dynamical pattern formed by a cellular structure is therefore similar to that of the phase turbulence (cf. Fig. 12). The differences are that the cells forming this structure have equal sizes and are ordered into a hexagonal array.

We performed systematic numerical studies of cellular structures. Because the system may possess several global attractors in the considered parameter region, only one of which corresponds to a cellular structure, the following simulation procedure was adopted: By going from the region of developed defect turbulence, the feedback intensity μ was gradually increased until a cellular structure first appeared. Then we fixed the respective value of μ and continued integration to check whether the observed structure was persistent. If a stable structure was found, it was used as the initial condition for the next simulation where the parameters μ and χ were slightly changed. If this again yielded a stable structure, it was used as the initial condition for the next step, etc. In this manner, boundaries for the existence of stable cellular patterns and other steady spatiotemporal regimes have been determined.

The results of a large series of numerical simulations are summarized in Fig. 18. The solid curve in this figure indicates the stability boundary of uniform oscillations, yielded by the perturbation analysis (cf. Sect. 2.1). Nonlinear effects, i.e. interactions between the

modes, lead however to the hysteresis phenomena. Therefore the uniform oscillations first appear, when going from the region with a weak feedback, only when the border of the region UO, shown by the dot line in Fig. 18, is crossed.

Stable hexagonal cells are observed in the interval between the curves connecting symbols + and * in Fig. 18. The cells appearing at χ = -0.6 π are shown at three subsequent time moments in Fig. 19a where the spatial distribution of the oscillation amplitude modulus ρ is displayed in gray scale. We see that in the membranes forming boundaries between the cells the oscillation amplitude is increased, as it can be expected for the shocks. Note also that the structure formed by the spatial distribution of ρ is almost stationary. The linear size of the cells approximately corresponds to the wavelength λ_0 of the first unstable mode, as yielded by the linear stability analysis (cf. Fig. 5). When the phase shift is increased to χ = -0.2 π, the cells get larger (Fig. 19b).

Inside the narrow region BH in Fig. 18, breathing cellular structures are observed. In such a structure, sizes of the cells change periodically with time, as shown in Fig. 19c. These structures are stable. Note that the width of this region becomes very small for larger phase shifts.

On the left side of the synchronization window, the hysteresis becomes weaker and approximately at the point χ_- = -0.6 π in Fig. 5 the existence boundary of hexagonal cells merges, within the simulation accuracy, with the stability boundary of uniform oscillations. Further to the left from this point, the cells are replaced by stripes (Fig. 19d). One of the three modes, needed to produce a cellular structure, begins to dominate and eliminates here the two other modes. This process has

analogs in the investigations of stationary Turing structures in reaction-diffusion systems [17].

On the right side of the synchronization window, the cell sizes increase as the point $\chi^* = 0.275\ \pi$ is approached and become comparable with the total size of the medium. Large phase domains are observed near the stability boundary of uniform oscillations inside the interval $\chi_+ < \chi < \chi^*$ where $\chi_+ = 0.599\ \pi$. Note that the boundaries separating different regions in the phase diagram of Fig. 18 get closer one to another when the phase shift is increased.

The above simulations of cellular structures have been performed using no-flux boundary conditions. When some of them were repeated using periodic boundary conditions, no significant influence on the cell dynamics has been found.

Inside the region HT in Fig. 18, amplitude turbulence on the background formed by a cellular structure has been found.

3.5. Localized turbulence

Fig. 20 (a-d) shows examples of intermittent and localized amplitude turbulence in CGLE with fixed global feedback. Each horizontal row in this figure represents a time sequence of frames taken for a different value of the phase shift χ. The spatial distribution of the modulus ρ of the local oscillation amplitude is displayed in gray scale, with darker regions corresponding to smaller values of the modulus.

Cells in Fig. 20a are small and form an almost regular hexagonal array, similar to a steady cellular structure. However, some of the cells have now a dark interior, i.e. the modulus of the oscillation amplitude is decreased there. However, the modulus ρ is only reduced but does not vanish. When the spatial phase distribution is plotted for such a pattern,

we see that the phase is flipped inside active cells in respect to the rest of the medium. Thin bright membranes, that separate the cells and are formed by shocks, are very rigid. They keep their shape even when a cell becomes active. The entire process can be described as random sporadic activity on a regular array. Individual cells suddenly 'flip' and become dark. They remain in this dark state for some time and then return to the normal lightly gray state.

Sometimes the activation destroys a membrane and penetrates into a neighbouring cell, infecting it. This process may lead to formation of turbulent aggregates (such an object is present in the third frame of Fig. 20a). However, as seen in our simulations, these aggregates later die out and the regime with randomly distributed individual active cells is recovered.

Since we did not run our simulations for very long times, it is impossible to say whether the regime with single active cells is fully persistent or it is not eventually replaced by developed defect turbulence when a large turbulent aggregate appears. However, if such a transition occurs, its waiting time should be large.

When the phase shift χ is increased, cells are getting larger but their arrangement is still fairly regular (Fig. 20b). The fraction of active dark cells is now greater and they form clusters or chains. This state is, however, only a transient which is obtained if we start from the initial conditions that represent a hexagonal array. After some time, the pattern loses its regularity and becomes similar to the patterns shown in Fig. 20c, where a larger value of the phase shift is taken.

In this turbulent state, no regular array of cells is observed. The majority of cells are passive and form a background for the active cells that contain amplitude defects. Such active cells have larger sizes. If two neighbouring active cells appear, the membrane between them can

sometimes break. Inside an active cell, the modulus distribution is far from uniform and undergoes irregular variation with time.

Passive cells, though irregular, are relatively rigid in the presence of global feedback. Light membranes, forming their boundaries and representing shocks, do not easily break and the seeds of amplitude turbulence do not grow to large sizes. Often, the amplitude defects die out in a seed region and it disappears. New active cells can appear as amplitude defects spontaneously develop inside some of the passive cells. The entire regime can be described as intermittent amplitude turbulence.

At still larger values of the phase shift, not shown in Fig. 18, localized turbulence, which represents individual turbulent islands surrounded by the area with uniform oscillations, is found. An example showing the appearance of such turbulence is given in Fig. 20d.

Localized turbulence develops through the intermittent amplitude turbulence as the intensity of global feedback is increased. At sufficiently high intensities, lying above the stability boundary of uniform oscillations, passive cells in the background of the intermittent turbulence begin to fade away and then disappear. Active cells, populated by amplitude defects, are however more persistent and continue to exist even when they are surrounded by uniform oscillations. As the neighbouring passive cells disappear, the shock membrane separating an active cell acquires an approximately circular shape, so that this object looks more like a 'bubble'. Apparently, this membrane tends to minimize its total length, thus possessing something similar to the elasticity. These bubbles can form clusters, but individual bubbles are also observed.

Fig. 21 displays the spatial distribution of $\cos\phi$ at subsequent time moments within one oscillation cycle when a single turbulent island is

present in the medium. To indicate the presence of amplitude defects, we have additionally shown as bright light areas the regions where oscillation amplitude modulus is very low ($\rho < 0.05$). Periodic boundary conditions have been used in this simulation.

Inside a turbulent island, individual cells are seen which merge or split as time goes on. A cell is surrounded by a shock membrane that separates it from the region with uniform oscillations or from other cells in the island. In the center of a cell, the oscillation amplitude sometimes suddenly drops down almost to zero and an approximately concentric wave - an extended amplitude defect - is produced. This wave propagates towards the boundary of the cell and dies there out. However, it can also destroy the boundary and penetrate into a neighbouring cell.

When the phase variation in an active cell is followed, we see that the phase undergoes rapid variation across the spreading wave, inside the interval characterized by the greatly decreased modulus of the oscillation amplitude. Qualitatively, the pattern looks as if a source emitting ring-shaped phase flips were located in the center of the cell.

These ring-shaped amplitude defects show a transverse instability. As they spread out and come closer to the cell's membrane, some parts of them get very thin. Breakup of such extended defects also often occurs. Closer to the BF-boundary, where the cells are larger, broken extended amplitude defects form structures that look like fragments of spiral waves, similar to the patterns seen in Fig. 10.

If a breakup has not occurred in a given cell, it usually dies out after a few concentric waves have been generated (this is similar to the last stage of destruction of a spiral wave). Apparently, only the broken amplitude defects, which are associated with phase singularities, can produce internal 'pressure' that would allow a cell to counteract the suppressing influence of uniform oscillations .

Another representation of localized turbulence is chosen in Fig. 22. As the vertical coordinate, we plot here the inverse $1/\rho$ of the oscillation amplitude modulus (with a cut-off above a certain high level of $1/\rho$). The local gray scale shading is used to display the local variable $\cos\phi$. The horizontal plane in this figure corresponds to uniform oscillations where $\rho \approx 1.12$. Subsequent time frames within a single oscillation cycle (from the top left to the bottom right) are shown.

The spatial distribution of the oscillation amplitude inside the island is highly irregular. The amplitude reaches very small values in the points that are not fixed and move inside the cells. Oscillations inside a cell are shifted by about half of the period from uniform oscillations in the rest of the medium. However, the phase distribution inside a cell is far from uniform. Great phase variations are seen in the areas where the oscillation amplitude is smaller. Though we have not performed any special quantitative investigation of this complex process, it is, most probably, chaotic.

If no-flux boundary conditions were applied, a turbulent island tended to move into one of the corners of the systems, as in Fig. 22. Once this position was reached, the island could maintain its operation for a long time. Under periodic boundary conditions the life-time of a turbulent island was significantly shorter.

3.6. Heterogeneous media

To investigate the influence of small medium inhomogeneities, special numerical simulations was performed. A local inhomogeneity was introduced by assuming that inside a small region in the center of the medium the oscillation frequency ω in CGLE was slightly increased by

amount $\delta\omega$ in comparison to the rest of the medium. Periodic boundary conditions were used in these simulations.

We found that even such small medium imperfections, which were not noticeable on the background of uniform oscillations, could serve as nucleation centers and pin the turbulent islands. Fig. 23 shows formation of a small active bubble on the background of a cellular structure. Turbulent islands could also be pinned on the background of uniform oscillations.

Fig. 24 shows time evolution of the synchronization parameter R when we started from the turbulent state without global feedback and then abruptly switched it on in absence (thick line) and in the presence (thin line) of a small inhomogeneity. We see that, although in the homogeneous medium such strong global feedback soon leads to the emergence of synchronous oscillations, even a weak inhomogeneity is sufficient to break the synchronization down and produce localized turbulence in the medium.

4. Discussion

Our study has shown that global feedback essentially influences properties of turbulence in the two-dimensional complex Ginzburg-Landau equation and leads to appearance of new kinds of patterns. Inside a synchronization window, strong feedbacks suppress turbulence and establish uniform oscillations. The action of global feedback depends on its intensity and the phase shift, controlled by the delay time.

By adjusting the delay, the synchronization window can always be reached at sufficiently high feedback intensities. The synchronization develops according to different scenarios, i.e. via formation of hexagonal cellular structures or stripes, via localized turbulence on the

background of uniform oscillations, and via formation of large phase domains. Strong global feedback destroy individual spiral waves. Two kinds of elementary structures play an significant role in these processes - shocks and phase flips.

When uniform oscillations are stable in respect to the Benjamin-Feir instability, shocks result from collisions of two propagating waves. Similar patterns, characterized by a local increase of the oscillation amplitude and a minimum of the oscillation phase, are found when turbulence in CGLE is suppressed by global feedback. Such shocks form boundaries between cells and membranes separating turbulent bubbles from the area with uniform oscillations. Shock boundaries and membranes become increasingly rigid with growing global feedback. The membranes are also apparently 'elastic', since they tend to minimize their length.

In the parameter region where uniform oscillations are stable in respect to the Benjamin-Feir instability, phase flips develop when external periodic forcing or global feedback is applied [33,34]. We have found that these phase flips are destroyed by a strong global feedback. Destruction of a phase flip in a one-dimensional system proceeds through the appearance of a singularity point, where the oscillation amplitude vanishes. At the moment when such a singularity is present, the phase can shift by 2π on both sides of this point, thus eliminating the phase difference of 2π in a phase flip. We thus conclude that the winding number is not generally conserved in the presence of global feedbacks.

Though the profile of the modulus distribution in the phase flip shortly before its disappearance is qualitatively similar to that of the slowly moving BN hole, the phase distribution is different (cf. Fig. 1 and 7). The phase shift in a BN hole is close to π, whereas the phase shift in

a phase flip is 2π. Furthermore, a BN hole is a source of plane waves, whereas behind and after of a phase flip uniform oscillations are found. It means that the destruction of a phase flip does not proceed through the formation of a BN hole and represents another dynamical process.

In two-dimensional systems, destruction of phase-flip waves is possible, as revealed by our simulations of spiral waves under strong global feedback. Based on these observations, the following scenario for breakup of a phase-flip wave in such systems can be proposed:

The modulation of this wave first develops, so that in some part of the wave the phase variation becomes condensed inside a very narrow stripe which we call a *string*. Since the oscillation amplitude is greatly decreased inside the string, it can be classified as an extended amplitude defect. The thickness of the string varies with time. At one of its points, the string becomes infinitely thin, the oscillation amplitude vanishes at this point and the string breaks up, so that two open ends are formed. The remaining parts of the string then shrink and the rupture grows, so that the open ends move further away one from another.

At an open end of the broken string, a phase singularity is located and the oscillation amplitude vanishes. The phase changes by 2π after going around any contour, surrounding the open end, and therefore a topological defect should be located in this region. However, its properties are significantly different from that of a topological defect lying in the center of a rotating spiral wave. Now the topological defect is attached to an end of an extended amplitude defect, i.e. to the string.

We have observed that at some stage in the process of destruction of a spiral wave by global feedback, the pattern may include both a localized amplitude defect, that forms the core of a spiral wave and is located in its center, and a string, that forms the retreating tail of the decaying spiral wave. Attached at the end of this string, a second phase

singularity is found. The spiral wave ultimately dies only when the string reaches its core.

We believe that such strings also play an important role in the processes of localized turbulence. In the BF-stable region, phase flips do not spontaneously appear. However, they can be generated by heterogeneities, i.e. by small regions with an increased oscillation frequency. Such a region behaves then as a pacemaker, periodically sending concentric phase-flip waves [21]. In the BF-unstable region, where uniform oscillations are unstable in respect to phase modulation, phase flips may, however, occur even in absence of any material inhomogeneity, inside the cells formed by shock membranes.

When the cells are small (Fig. 19a), the phase is flipping almost uniformly inside a cell. As the phase shift in increased and the cells get larger, we see in our simulations that flipping of the phase occurs locally inside the cell. Then a ring-shaped phase flip is formed that spreads concentrically towards the cell boundaries. The phase gradient inside the ring grows and the amplitude modulus drops down (Fig. 21), so that the ring can be described as an extended amplitude defect, or a string loop.

As the loop grows, its modulation develops. It gets locally thinner and may break up. However, this process needs time. If the cell is not sufficiently large, string loops do not typically break - they die by colliding with the cell membrane formed by a shock. When breakup occurs inside a larger cell, short string fragments are formed. Sometimes, one of the open ends of a string started to curl and a spiral pattern developed. However, this spiral pattern had no regular shape and did not exist for a long time. String fragments can also locally destroy the membrane and penetrate into a neighbouring cell.

Note that strings observed in our simulations of two-dimensional CGLE with global feedback can be viewed as analogs of strings in the quantum field theory (see [39]). Ends of these strings are occupied by topological charges which, however, possess no own dynamics. The real dynamical objects are the strings which can move and change their shapes, interact and break. In contrast to this, the topological defects are simply attached to the string ends and move together with them or are produced in pairs of opposite signs when a string breaks.

We see that two-dimensional oscillatory systems with global feedback show a rich variety of pattern formation processes. In this context, it should be emphasized that 'controlling' turbulence means not merely its depression by strong feedbacks. Application of a global feedback is also a method for modifying turbulent behaviour and generating new kinds of spatiotemporal patterns. Particularly, the delay time determines the phase shift of the driving force. By varying this time, it is possible not only to rich the synchronization window, but also to influence properties of spatiotemporal patterns observed at intermediate feedback intensities, before the onset of uniform oscillations.

Our theoretical investigations have been carried out for a concrete model of CGLE with global feedback. However, this model is generic since it describes the typical behaviour of a reaction-diffusion system near a supercritical Hopf bifurcation. Its predictions often remain qualitatively valid even farther away from the bifurcation point, where oscillations are not perfectly harmonical and their amplitudes are not small. An important result of our study is that variation of only two parameters, i.e. of the feedback intensity and the delay time, is sufficient to modify properties of observed patterns, induce transitions

to different principal spatiotemporal regimes and, eventually, establish uniform oscillations.

We acknowledge the financial support of the Volkswagen-Stiftung and are grateful to G. Dewel and R. Imbihl for valuable discussions.

References

1. A. Newell, Lect. Appl. Math. 15 (1974) 157

2. Y. Kuramoto and T. Tsuzuki, Prog. Theor. Phys. 54 (1975) 687; 55 (1976) 356

3. Y. Kuramoto, Chemical Oscillations, Waves, and Turbulence (Springer, Berlin, 1984)

4. A. S. Mikhailov and I. V. Uporov, Dokl. Acad. Nauk SSSR 249 (1979) 733

5. J. M. Greenberg, SIAM J. Appl. Math. 39 (1980) 301; Adv. Appl. Math. 42 (1981) 450

6. P. C. Hagan, SIAM J. Appl. Math. 42 (1982) 762

7. N. Bekki and K. Nozaki, Phys. Lett. A 110 (1985) 133

8. P. Coullet, L. Gil, and J. Lega, Phys. Rev. Lett., 62 (1989) 1619

9. T. Bohr, A. W. Pedersen, and M. H. Jensen, Phys. Rev. A 42 (1990) 3626

10. E. Bodenshatz, M. Kaiser, L. Kramer, W. Pesch, A. Weber, and W. Zimmermann, in: New trends in Nonlinear dynamics and Pattern Forming Phenomena, eds. P. Coullet and P. Huerre (Plenum, New York, 1990)

11. B. I. Shraiman, A. Pumir, W. von Saarlos, P. C. Hohenberg, H. Chate, and M. Holen, Physica D 57 (1992) 241

12. I. Aranson, L. Kramer, and A. Weber, Phys. Rev. E 47 (1993) 3231

13. H. Chate and P. Manneville, Physica A 224 (1996) 348

14. A. S. Mikhailov and A. Yu. Loskutov, Foundations of Synergetics II. Chaos and Noise, 2nd enlarged edition (Springer, Berlin, 1996)

15. D. Battogtokh and A. S. Mikhailov, Physica D 90 (1996) 84

16. L. D. Landau, E. M. Lifshitz, Statistical Physics (Pergamon, Oxford, 1980)

17. D. Walgraef, G. Dewel, and P. Borkmans, Phys. Rev. A 21 (1980) 397

18. A. S. Mikhailov, Foundations of Synergetics I. Distributed Active Systems, 2nd revised edition (Springer, Berlin, 1994)

19. R. Imbihl and G. Ertl, Chem. Rev. Chem. Rev. 95 (1995) 697

20. H. Levine and X. Zou, Phys. Rev. Lett. 69 (1992) 204

21. G. Veser, F. Mertens, A. S. Mikhailov, and R. Imbihl, Phys. Rev. Lett. 71 (1993) 935

22. F. Mertens, R. Imbihl, and A. S. Mikhailov, J. Chem. Phys., 99 (1993) 8668

23. F. Mertens, R. Imbihl, and A. S. Mikhailov, J. Chem. Phys. 101 (1994) 9903

24. M. Falke, H. Engel, and M. Neufeld, Phys. Rev. E 52 (1995) 763

25. K. Rose, D. Battogtokh, A. S. Mikhailov, R. Imbihl, W. Engel, and A. Bradshaw, Phys. Rev. Lett. 76 (1996) 3582

26. W. Eckhaus, Studies in Nonlinear Stability Theory (Springer, Berlin, 1965)

27. H. Sakaguchi, Prog. Theor. Phys. 85 (1991) 417

28. H. Chate and P. Manneville, Phys. Lett. A 171 (1992) 183

29. S. Popp, O. Stiller, I. Aranson, and L. Kramer, Physica D 84 (1995) 424

30. M. Bazhenov and M. Rabinovich, Physica D 73 (1994) 318

31. L.D. Landau and E.M. Lifshitz, Quantum Mechanics. Nonrelativistic Theory (Pergamon, Oxford, 1977)

32. K. Kaneko, Physica D 34 (1989) 31

33. P. Coullet and K. Emilsson, Physica A 88 (1992) 190

34. P. Coullet and K. Emilsson, Physica D 61 (1992) 119

35. P. Ortoleva and J. Ross, J. Chem. Phys. 58 (1973) 5673

36. D. Battogtokh, A. Preusser, and A. S. Mikhailov, Computer videos of turbulence in CGLE with global feedback, in: http://afpserver.rz-berlin.mpg.de/~~mex~~ compsys

37. I. Aranson, L. Kramer, and A. Weber, Phys. Rev. Lett. 72 (1994) 2316

38. G. Veser, F. Esch, and R. Imbihl, Catal. Lett. 13 (1992) 371

39. A. M. Polyakov, Gauge Fields and Strings (Harwood, Chur 1987)

Figure captions

Fig. 1. Spatial distributions (a) of the oscillation amplitude modulus ρ and (b) of the phase ϕ/π in a slowly moving Bekki-Nozaki hole ($\varepsilon = 2$, $\beta = -1.4$, $c = 0.354$).

Fig. 2. Spatial distributions (a) of the oscillation amplitude modulus ρ and (b) of the phase ϕ/π in a moving Bekki-Nozaki hole ($\varepsilon = 2$, $\beta = -1.4$, $c = 3.24$).

Fig. 3. The square of the wavenumber k_0 of the first unstable mode as function of the parameter $\nu = -1 - \varepsilon\beta$ for $\varepsilon = 2$ and $\chi = -0.2\pi$ (curve 1). Curve 2 shows the quadratic approximation (41) of this dependence. Curve 3 displays the respective dependence of the wavenumber k_{KS} of the most unstable mode in CGLE without a global feedback, as given by equation (20).

Fig. 4. Stability diagram of uniform oscillations ($\varepsilon = 2$, $\beta = -1.4$). The oscillations are stable in the region above the boundary formed by the curve DABCE. Characteristic points of this curve correspond to the values of the phase shift $\chi_- = -0.6235\ \pi$ (point A), $\chi^* = 0.275\ \pi$ (B), and $\chi_+ = 0.599\ \pi$ (C).

Fig. 5. The wavelength λ_0 of the first unstable mode as function of the phase shift χ for $\varepsilon = 2$, $\beta = -1.4$. The horizontal line shows the wavelength λ_{KS} of the most unstable in CGLE without global feedback for the same values of the parameters ε and β.

Fig. 6. Profiles of the oscillation amplitude modulus (a) and of the phase (b) in steadily traveling phase flips in the BF-stable region of CGLE with global feedback ($\varepsilon = 5.0$, $\beta = 0.5$, $\chi = 0$, $\mu = 0.13$).

Fig. 7. Destruction of a phase flip by strong global feedback ($\varepsilon = 5.0$, $\beta = 0.5$, $\chi = 0$, $\mu = 0.175$). Spatial profiles (a) of the amplitude

modulus and (b) of the phase ϕ/π at subsequent time moments T are shown.

Fig. 8. Phase diagram for turbulence in CGLE without global feedback (from [15]). Phase turbulence is observed between lines L and BF, defect turbulence to the left of line T, and frozen states exist (approximately) to the right of line S_2. The points 1, 2, 3, 4, and 5 indicate the parameter values taken in our simulations.

Fig. 9. Destruction of a spiral wave by increasing global feedback. Spatial distributions of $\cos\phi$ are shown in gray scale at six subsequent time moments (from the top left to the bottom right) for $\varepsilon = 2$, $\beta = -0.55$, and $\chi = 0$. The intensity of global feedback grows with time as $\mu = 10^{-4} \times t$ (dash line in the upper part of the figure). The solid line in the upper part shows the time dependence of the synhchronization parameter R.

Fig. 10. Suppression of spiral-wave turbulence by the growing global feedback. Six subsequent time frames for the real part $\mathrm{Re}\eta$ of the complex oscillation amplitude are shown from the top left to the bottom right; $\varepsilon = 1.3$, $\beta = -0.8$, $\chi = 0$, $\mu = 10^{-3} \times t$.

Fig. 11. A detailed view of the process leading to the destruction of a spiral wave by increasing global feedback. Subsequent frames, corresponding to moments T, show in gray scale the spatial distributions of (a) the oscillation amplitude modulus and (b) the oscillation phase.

Fig. 12. Evolution of (a) modulus and (b) phase distributions during the process leading to destruction of a phase flip in the one-dimensional system. Time is running from T = 110 to T = 115 in the horizontal direction, the coordinate is plotted along the vertical axis. The same parameters as in Fig. 7.

Fig. 13. Phase turbulence in CGLE without global coupling (ε = 2.0, β = -0.75, μ = 0). Spatial distributions of the oscillation phase ϕ are shown at six subsequent time moments. The phase increases between 0 and 2π and then jumps back to 0, the black fronts in this figure display the lines of constant phase $\phi = 2\pi$.

Fig. 14. Suppression of defect turbulence via formation of a cellular structure (ε = 2, β = -1.4, χ = -0.2 π). The upper part shows the growth of the global feedback intensity μ (dash line) and the dependence of the synchronization parameter R on time. The middle part displays the respective evolution of the spatial distribution of the amplitude modulus ρ in the central vertical cross-section of the medium, dark areas correspond to smaller values of ρ. Three frames in the bottom row show spatial distributions of the variable ρ in the entire medium at selected time moments T = 200, 600, and 700.

Fig. 15. Suppression of defect turbulence via development of localized turbulence (ε = 2, β = -1.4, χ = 0). The same notations as in Fig. 13. Three frames in the bottom row are taken at T = 200, 652, and 800.

Fig. 16. Suppression of defect turbulence via development of large phase domains (ε = 2, β = -1.4, χ = 0.3 π).The same notations as in Fig. 13. Time evolution in the middle part is displayed for the times between T = 264 and 1500. Three frames in the bottom row are taken at T = 500, 738, and 1490.

Fig. 17. A cellular structure (ε = 2, β = -1.4, χ = -0.2 π, and μ = 0.245). The same notations as in Fig. 12.

Fig. 18. Phase diagram for cellular structures (ε = 2, β = -1.4). The solid curve shows the theoretical stability boundary of uniform oscillations (see Fig. 4). When moving from the region DMT with

fully developed defect turbulence, turbulence on the background of a cellular structure is found in the region HT. Breathing hexagonal cells appear inside the region BH and steady hexagonal cells are observed in the region H. The cells disappear and are replaced by uniform oscillations inside the region UO, whose boundary lies higher then the solid curve (a hysteresis).

Fig. 19. Cellular and stripe structures at $\varepsilon = 2$, $\beta = -1.4$ for (a) $\chi = -0.6\,\pi$ and $\mu = 0.8$; (b) $\chi = -0.2\,\pi$ and $\mu = 0.3$; (c) $\chi = -0.5\,\pi$, and $\mu = 0.35$; (d) $\chi = -0.63\,\pi$ and $\mu = 1.0$. The gray scale representation is used to display the spatial distributions of the variables ρ (a - c) and $\cos\phi$ (d) at subsequent time moments at a fixed intensity of global feedback.

Fig. 20. Intermittent and localized turbulence at $\varepsilon = 2$, $\beta = -1.4$ for (a) $\chi = -0.6\,\pi$ and $\mu = 0.4$, (b) $\chi = -0.4\,\pi$ and $\mu = 0.25$, (c) $\chi = -0.2\,\pi$ and $\mu = 0.18$, (b) $\chi = 0$ and $\mu = 0.3$.

Fig. 21. Localized turbulence ($\varepsilon = 2$, $\beta = -1.2$, $\chi = 0$ and $\mu = 0.33$). Spatial distribution of $\cos\phi$ is shown in gray scale at subsequent time moments within a single oscillation period (from the top left to the bottom right); small bright regions additionally indicate the areas where $\rho < 0.05$.

Fig. 22. Three-dimensional representation (see the text) of the localized turbulence ($\varepsilon = 2$, $\beta = -1.2$, $\chi = 0$ and $\mu = 0.392$).

Fig. 23. Development of an active pinned bubble on the background of the cellular structure ($\varepsilon = 2.0$, $\beta = -1.4$, $\chi = -0.2\pi$, $\mu = 0.32$); the modulus ρ of the local oscillation amplitude is plotted. Inside the defect of size 5 x 5, located in the center of the medium, the local oscillation frequency is increased by $\delta\omega = 0.35$.

Fig. 24. Turbulence induced by a small defect of size 2 x 2, inside which the local oscillation frequency is increased by $\delta\omega = 0.05$ ($\epsilon = 2$, $\beta = -1.2$, $\chi = 0$).

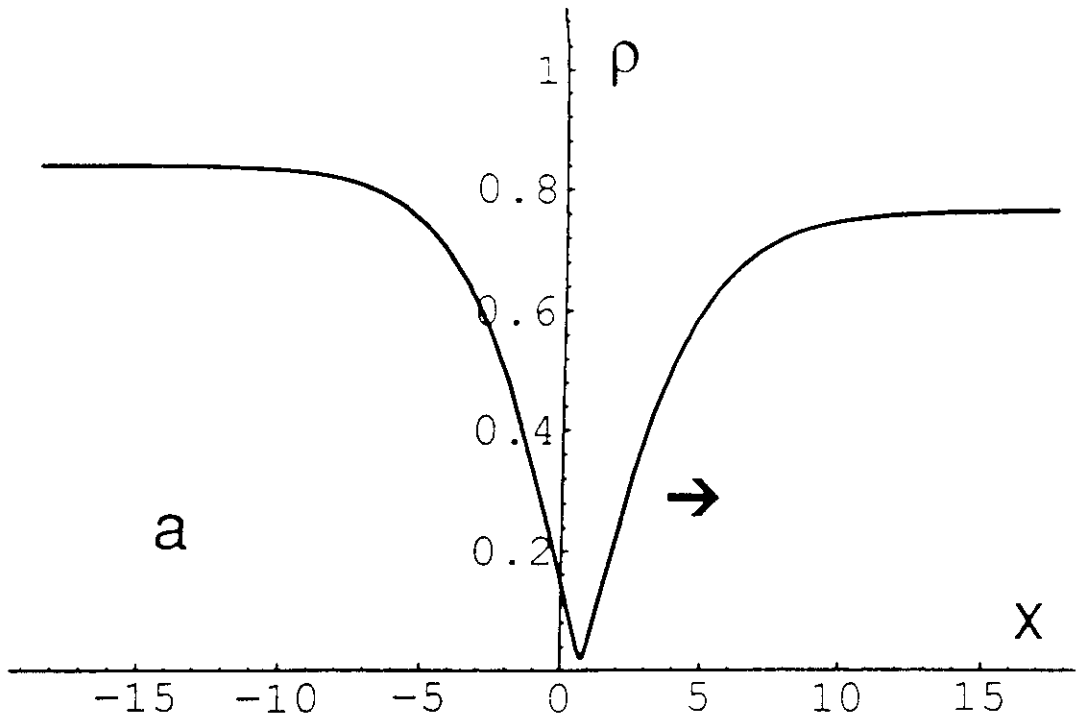

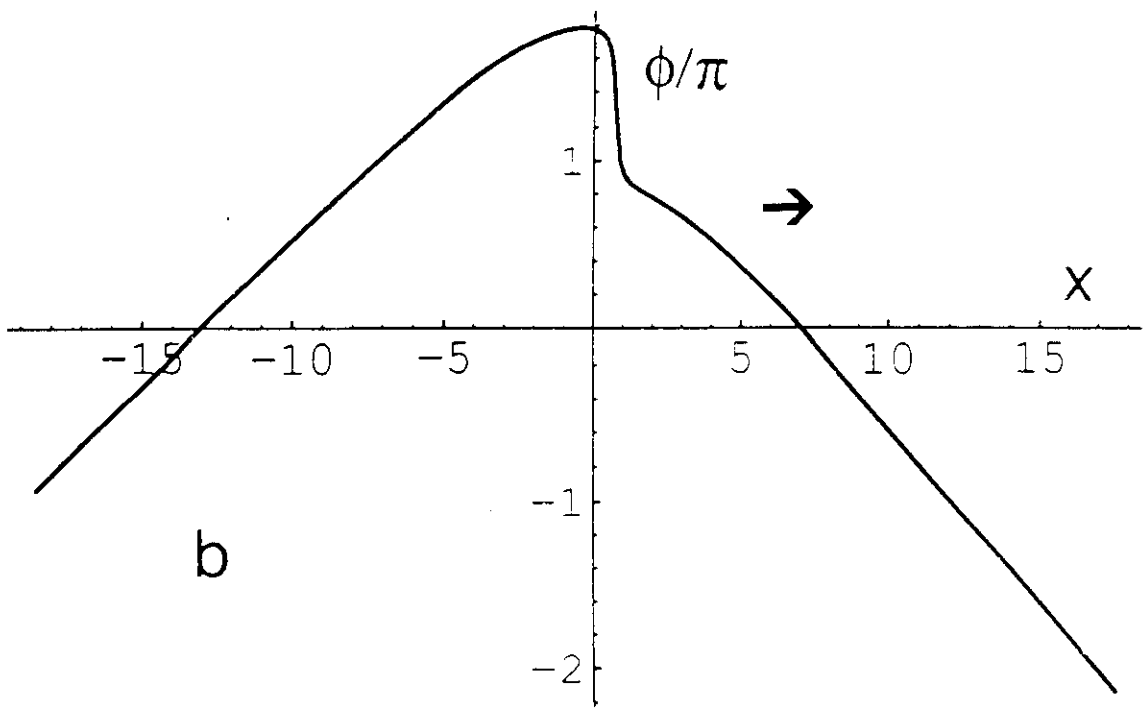

Fig. 1

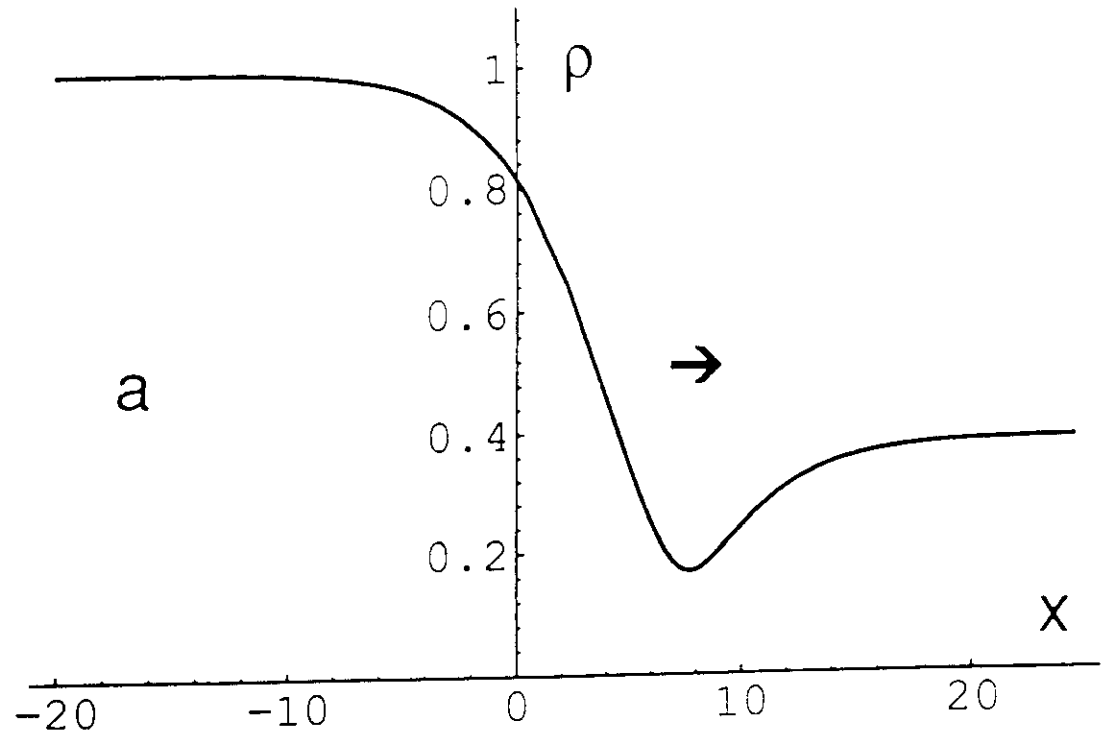

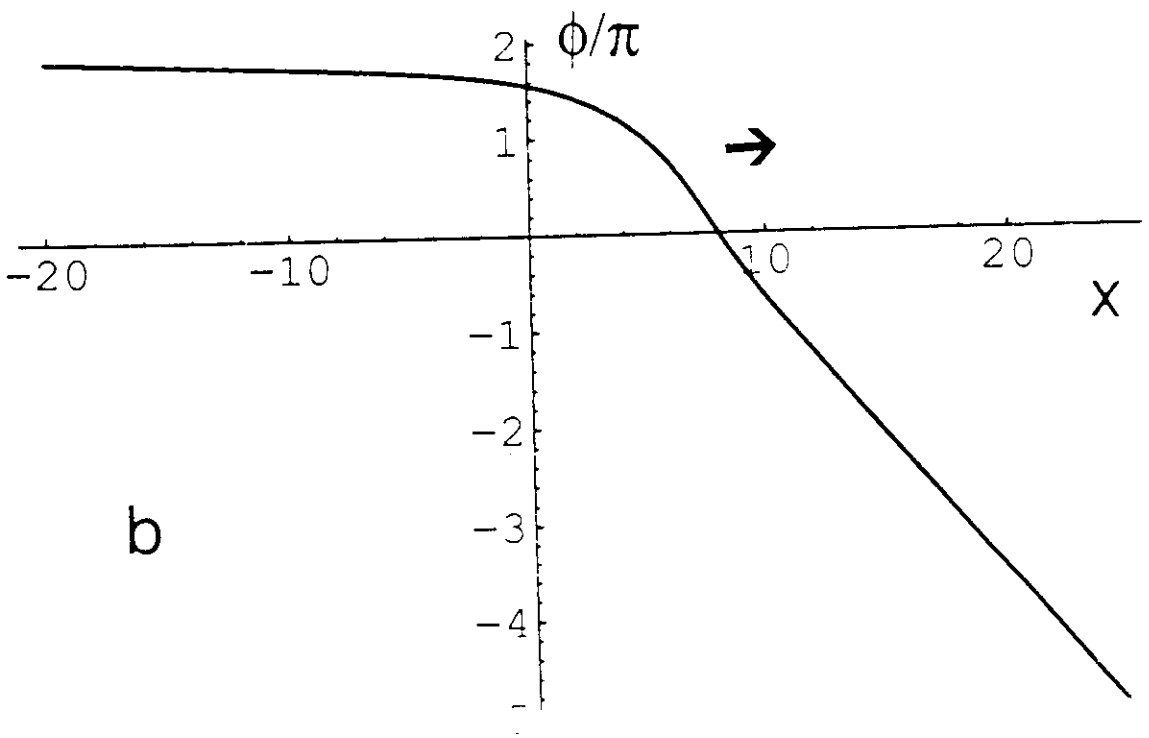

Fig. 2

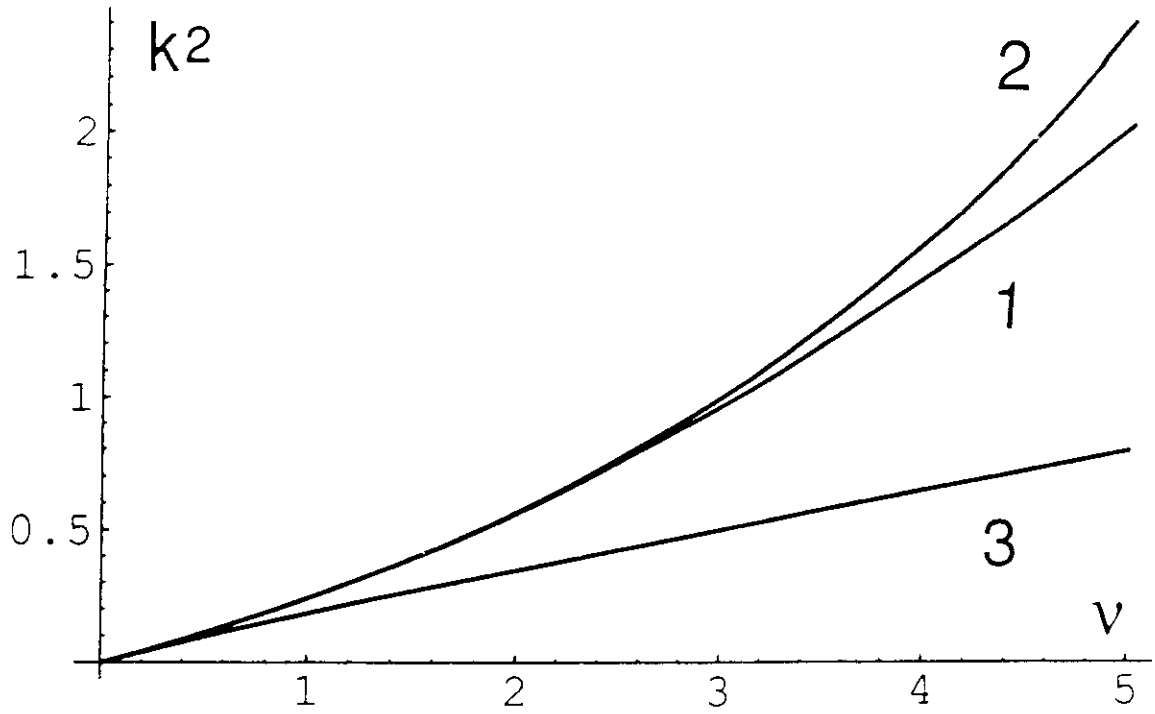

Fig 3

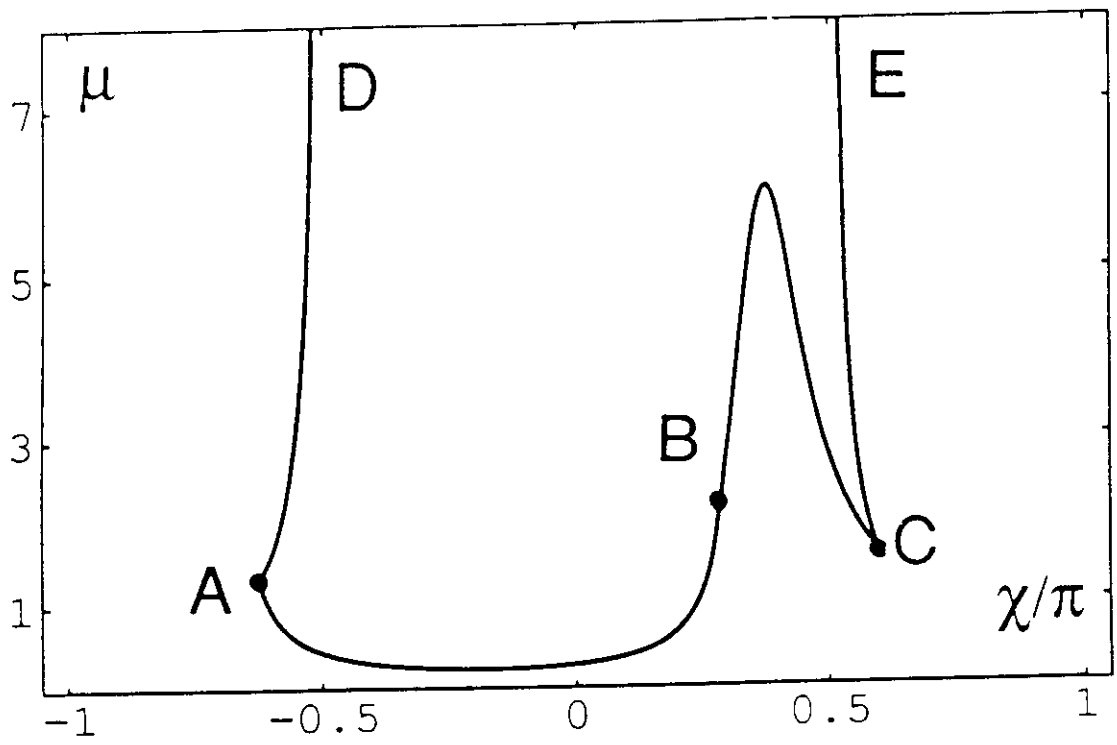
μ
D
E
7
5
3
1
A
B
C
χ/π
−1
−0.5
0
0.5
1

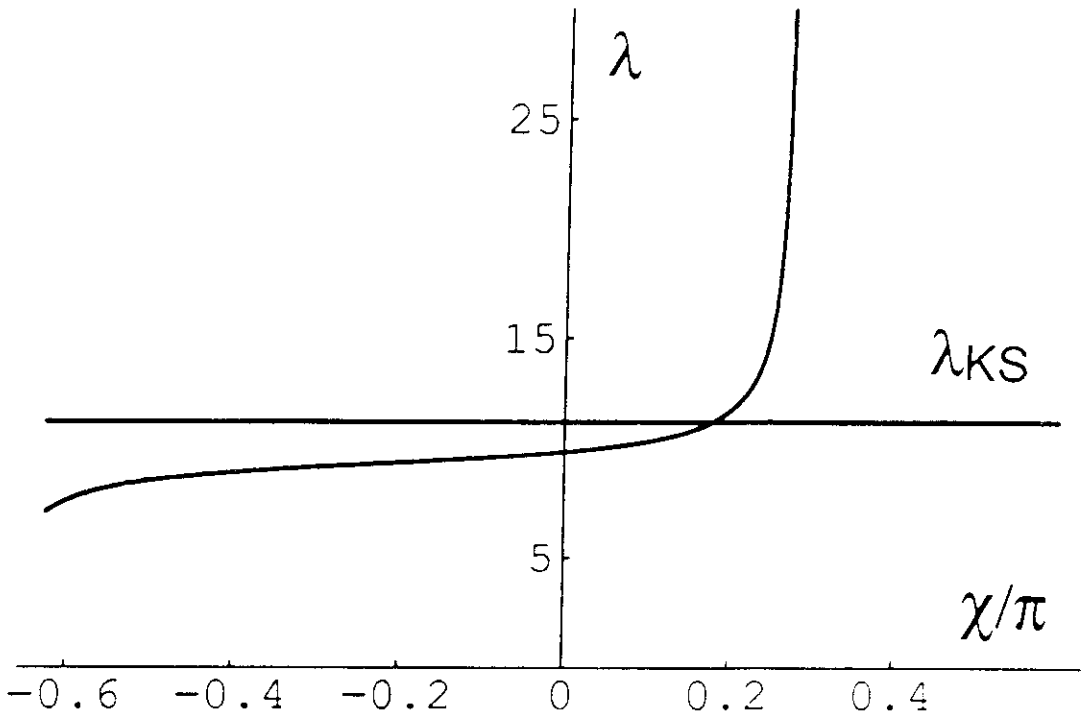

Fig 5

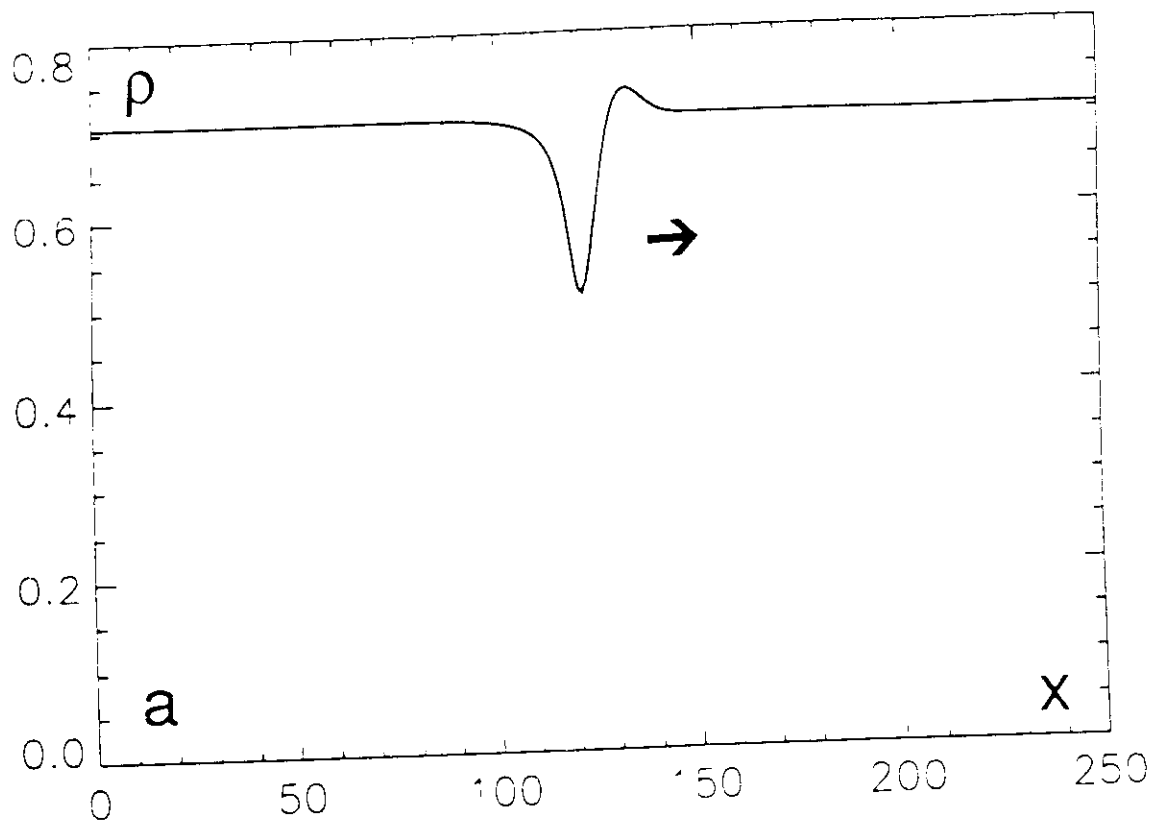

Fig. 6a

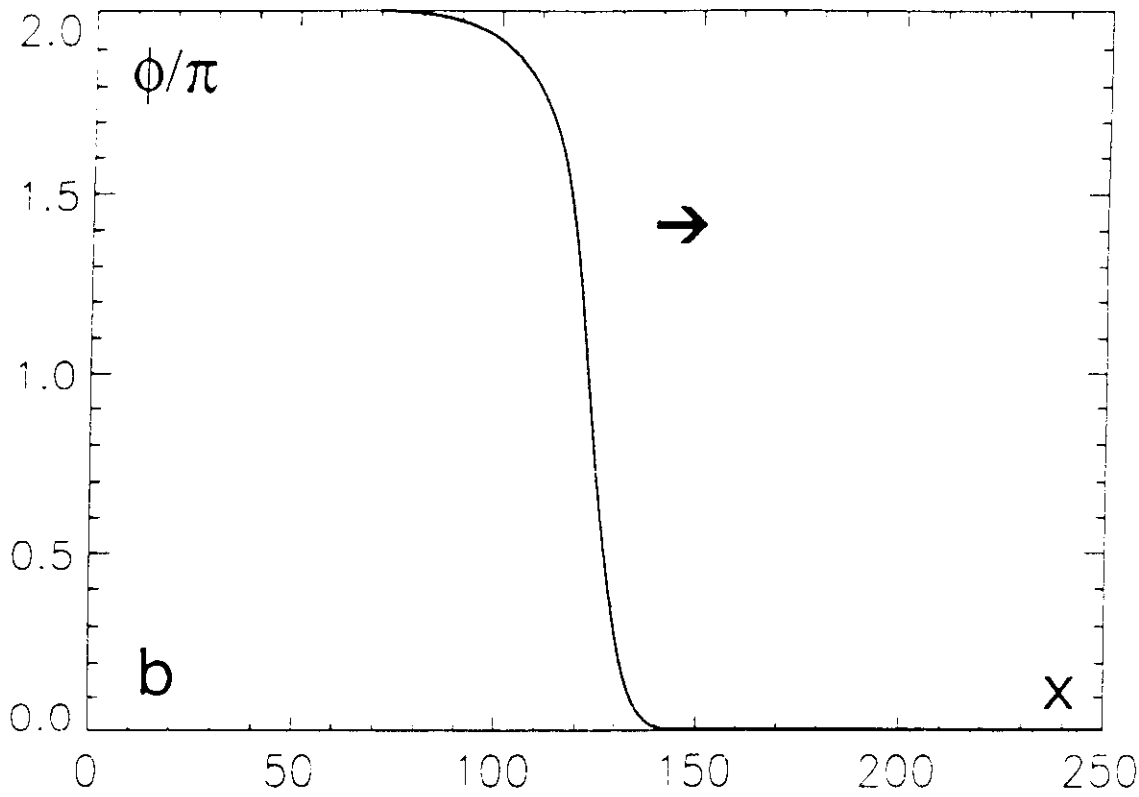

Fig 6b

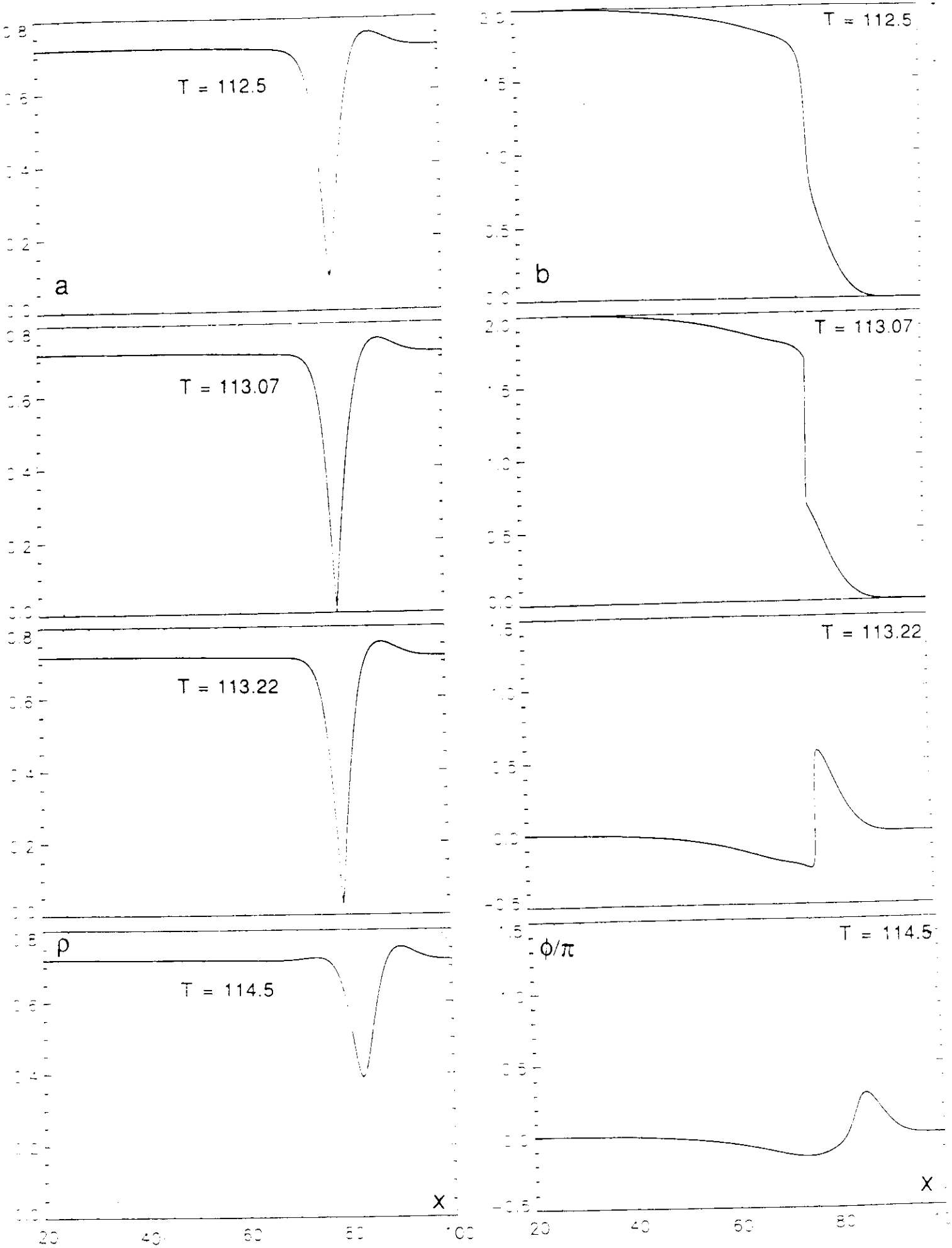
T = 112.5
a
T = 113.07
T = 113.22
ρ
T = 114.5
x
20
40
60
80
100
T = 112.5
b
T = 113.07
T = 113.22
φ/π
T = 114.5
x
20
40
60
80

Fig 7

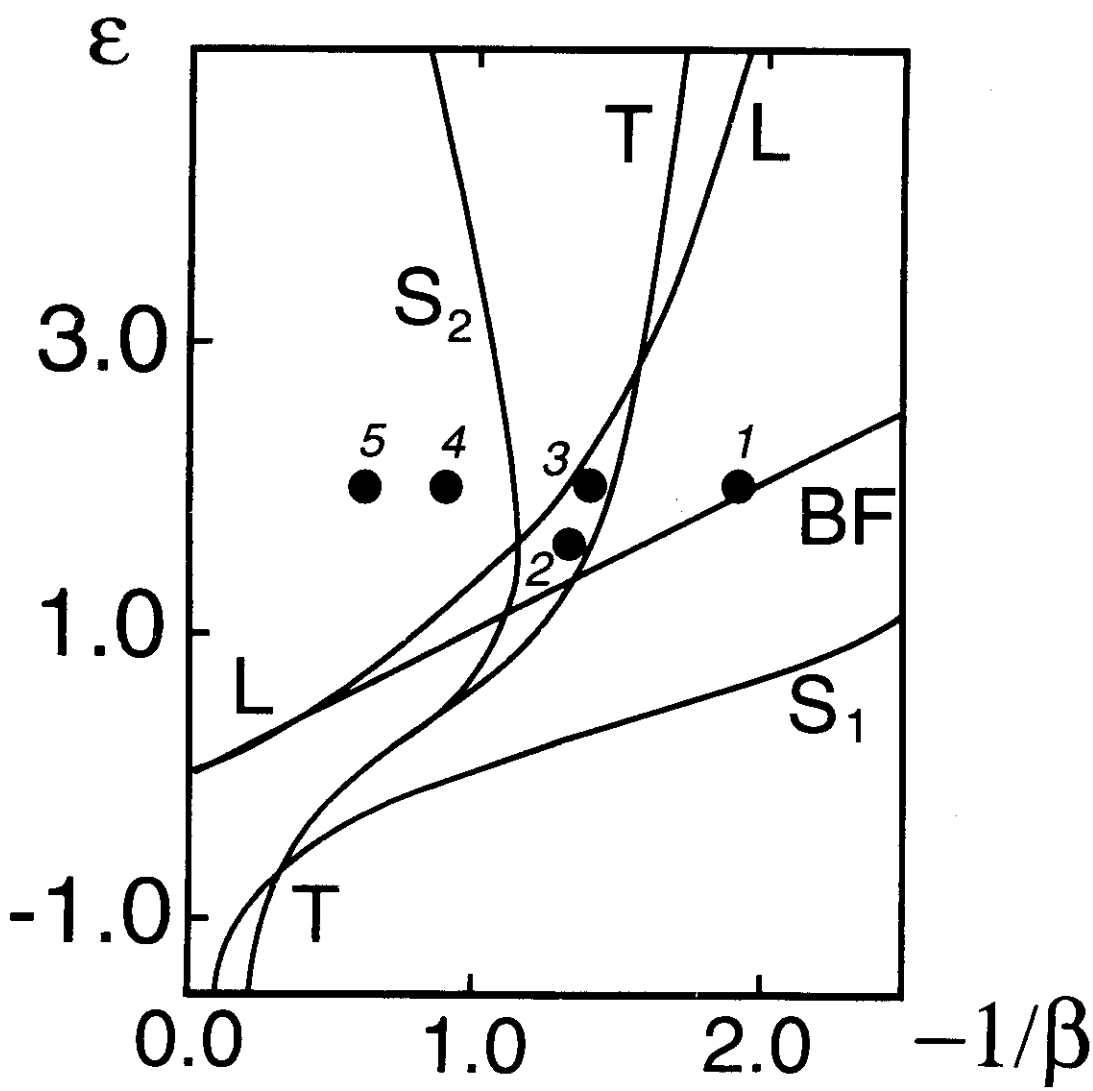
ε
T
L
S2
3.0
5
4
3
1
BF
2
1.0
L
S1
-1.0
T
0.0
1.0
2.0
−1/β

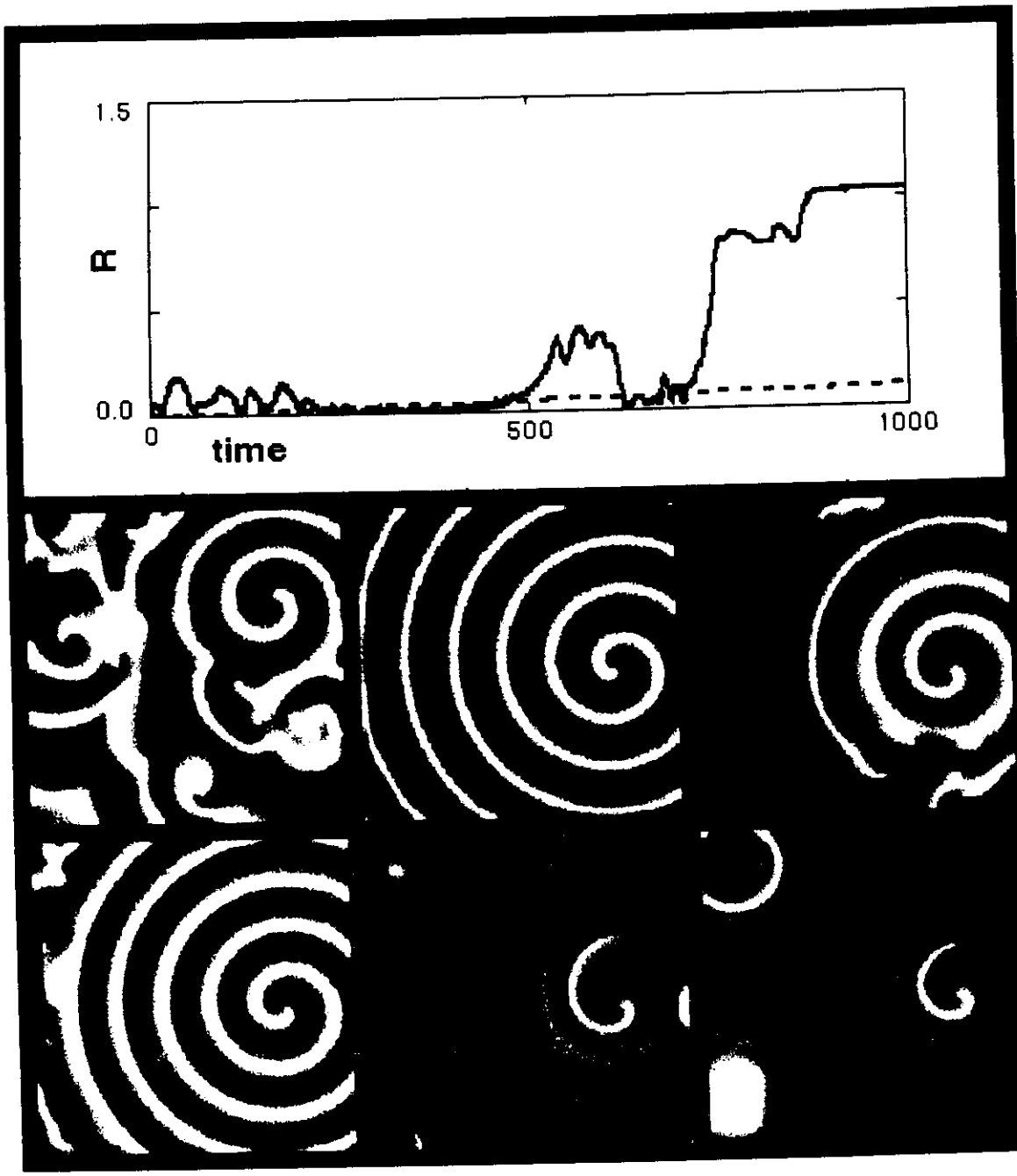
1.5
R
0.0
0
500
1000
time

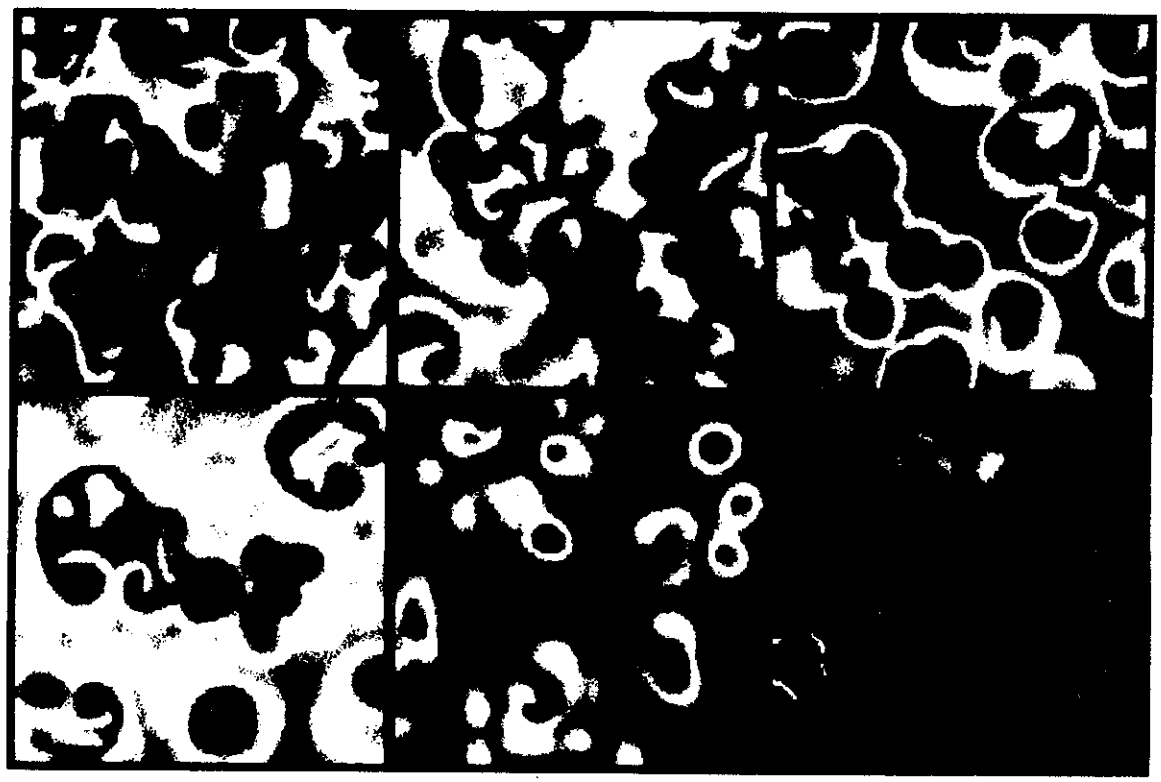

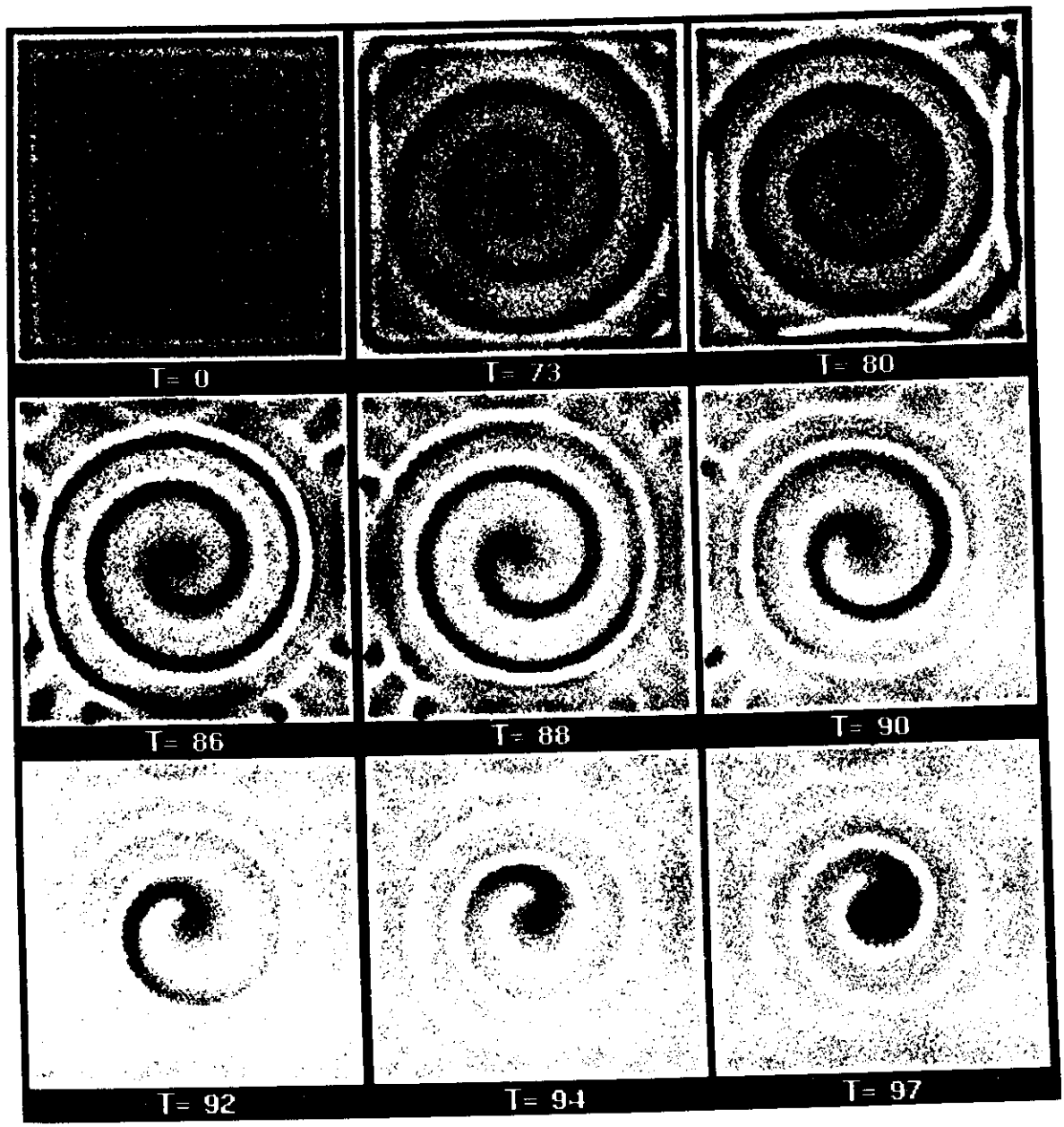
T= 0
T= 73
T= 80
T= 86
T= 88
T= 90
T= 92
T= 94
T= 97

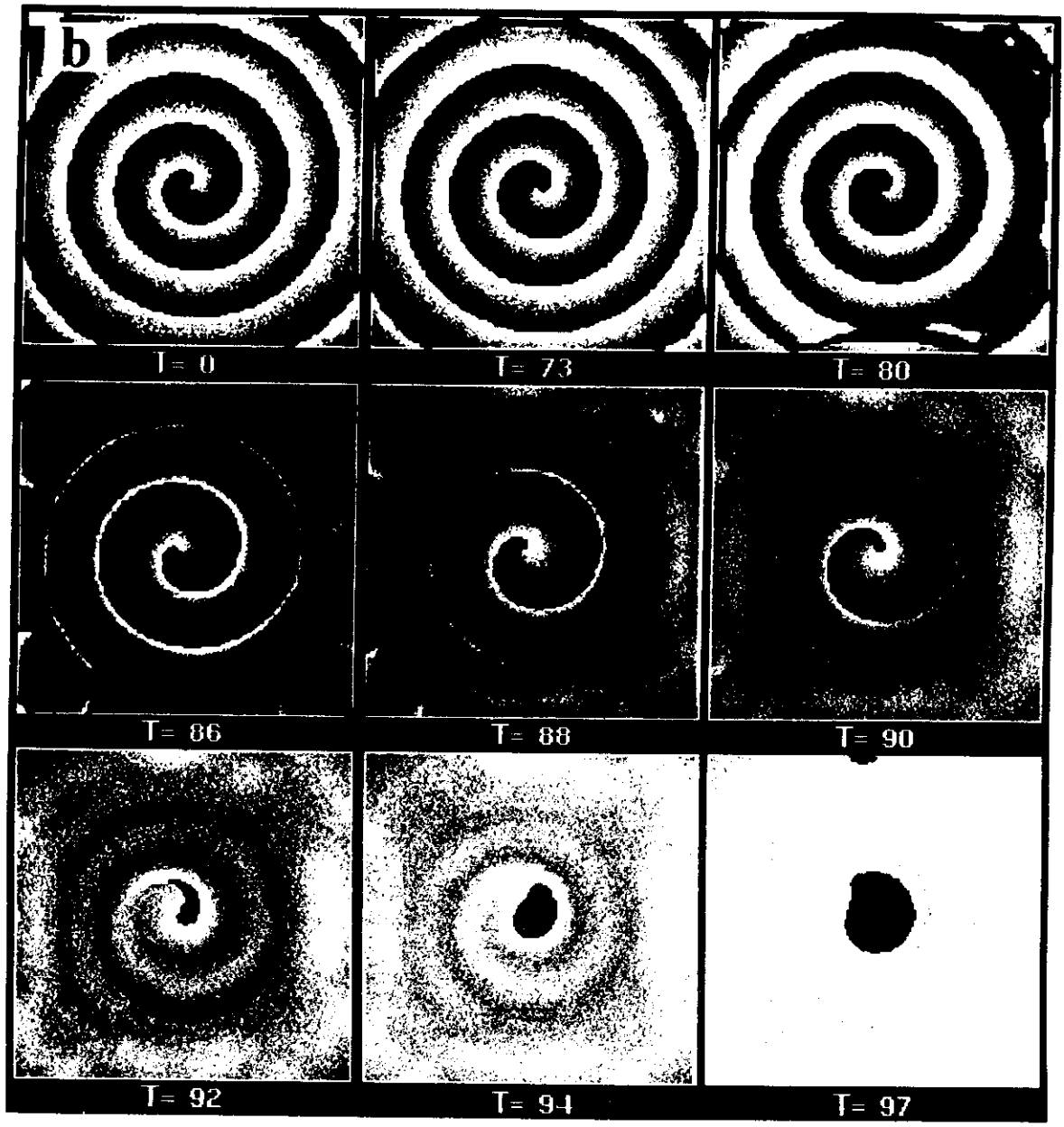
b
T= 0
T= 73
T= 80
T= 86
T= 88
T= 90
T= 92
T= 94
T= 97

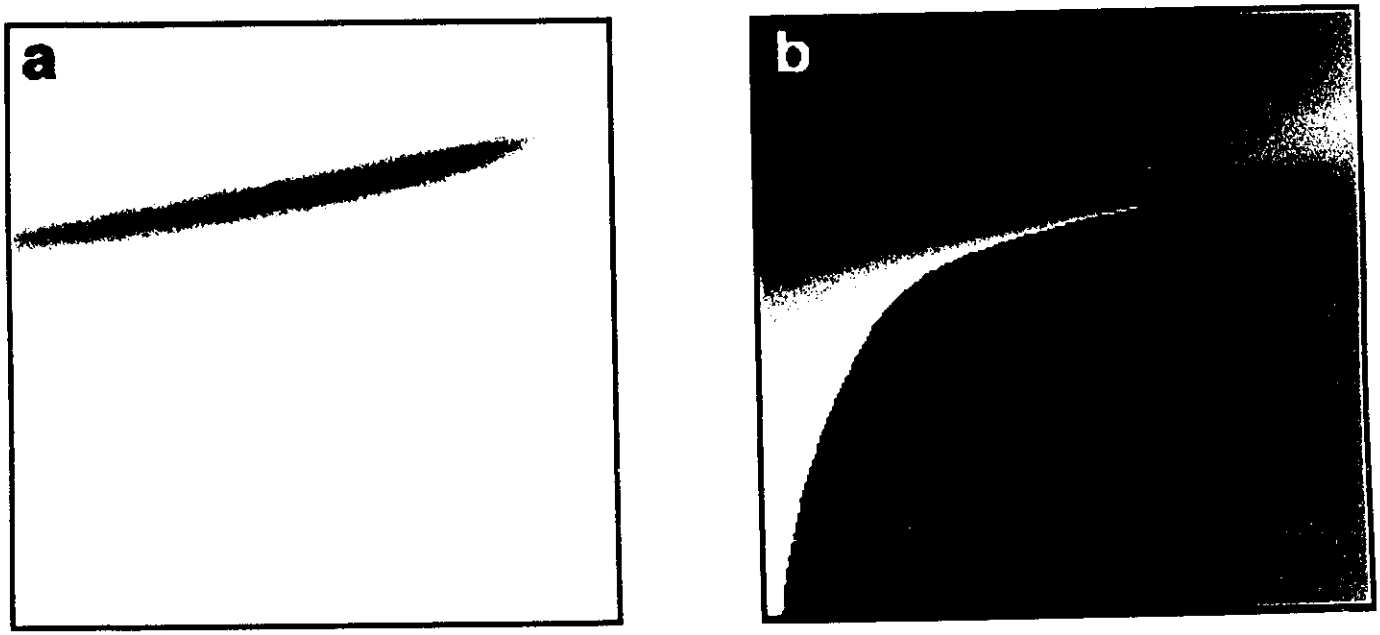

Fig 12

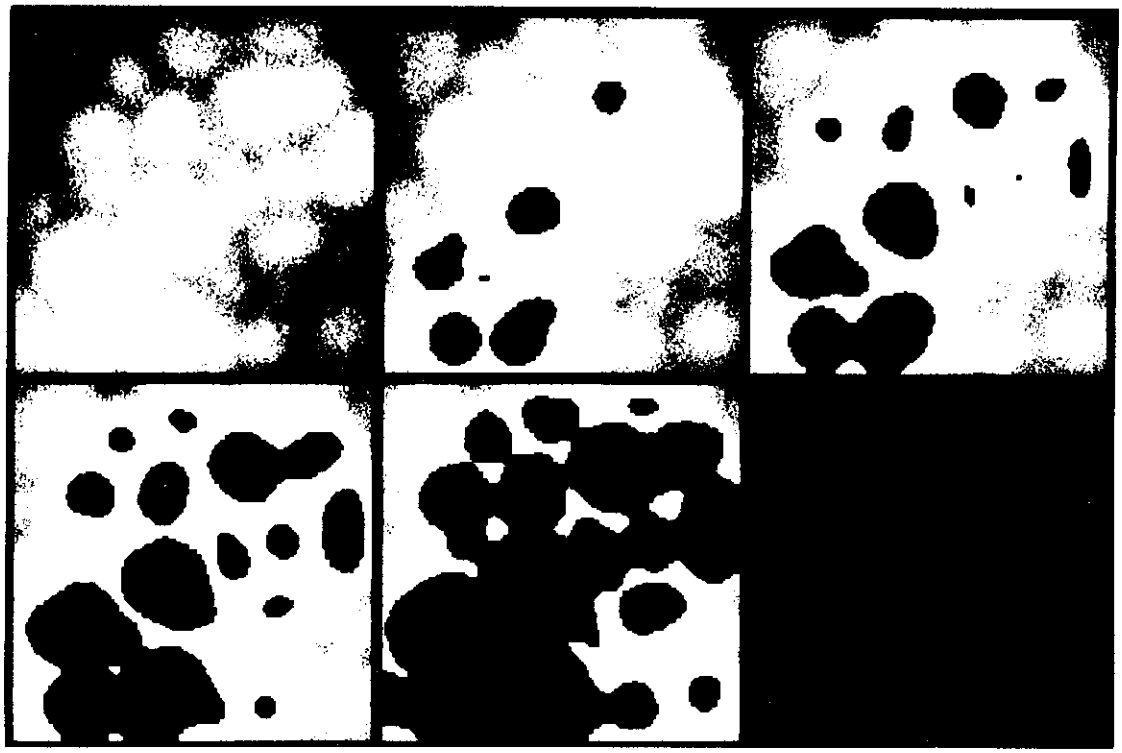

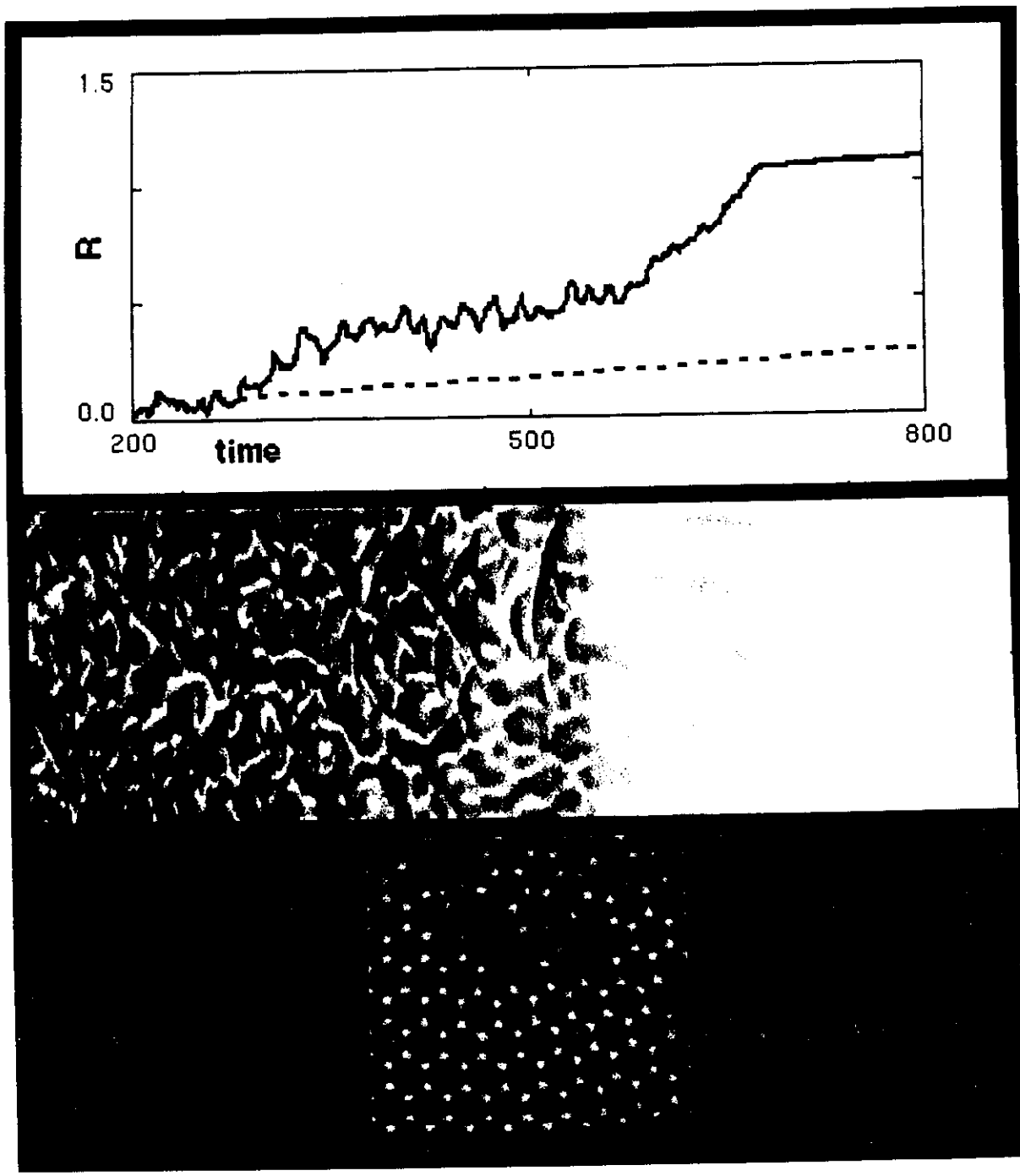

Fig 14

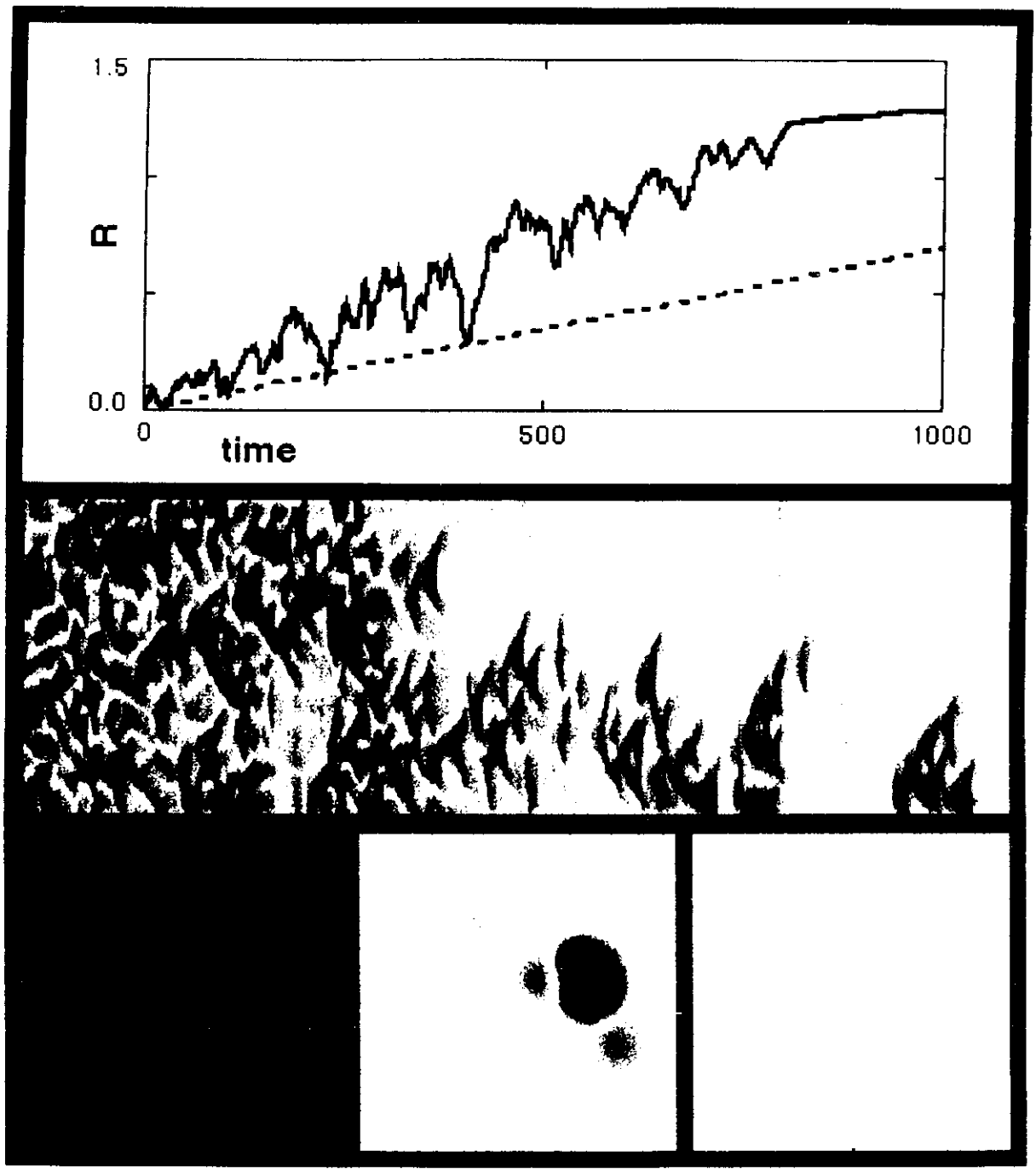
1.5
α
0.0
0
time
500
1000

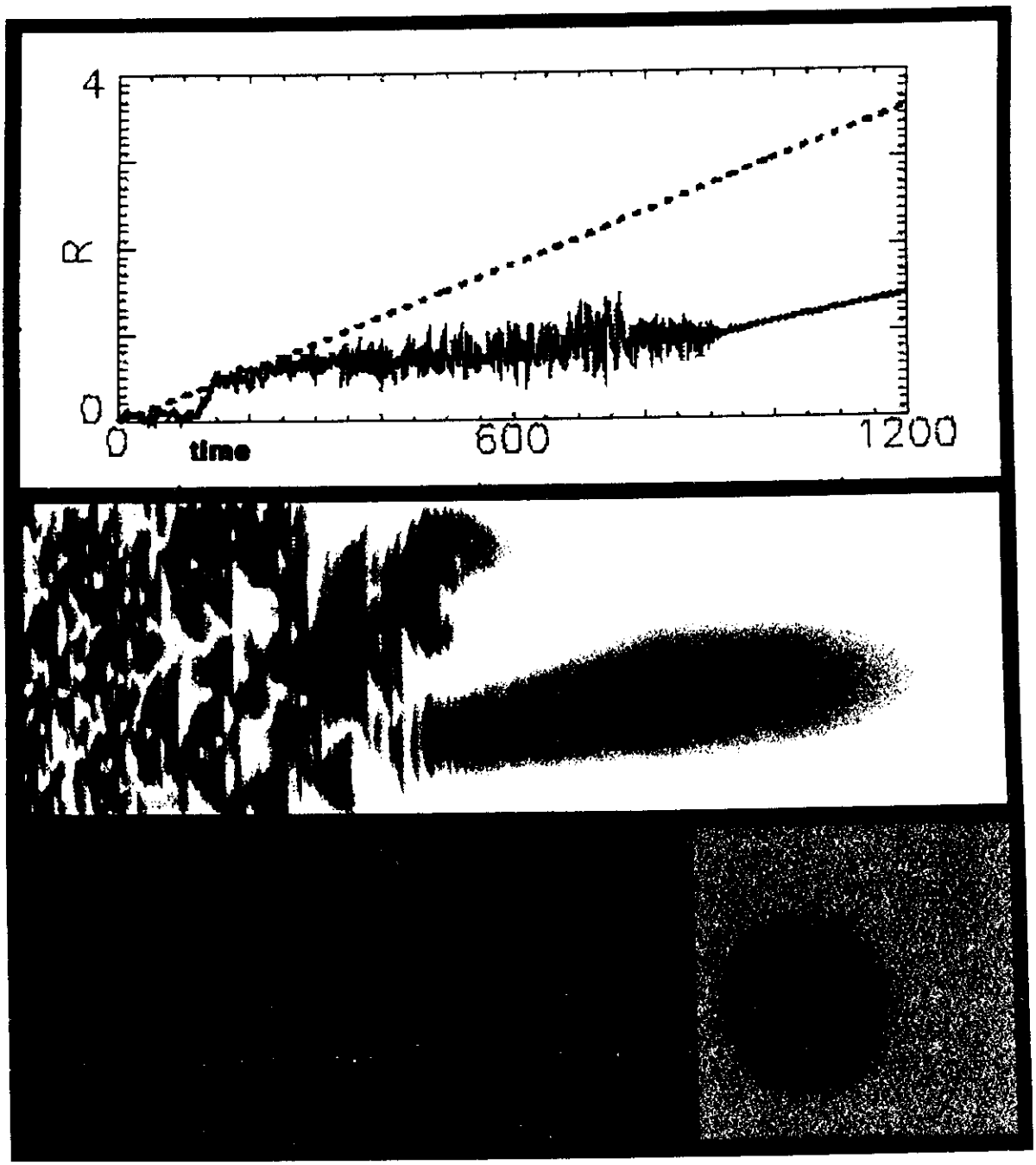

Fig 1A

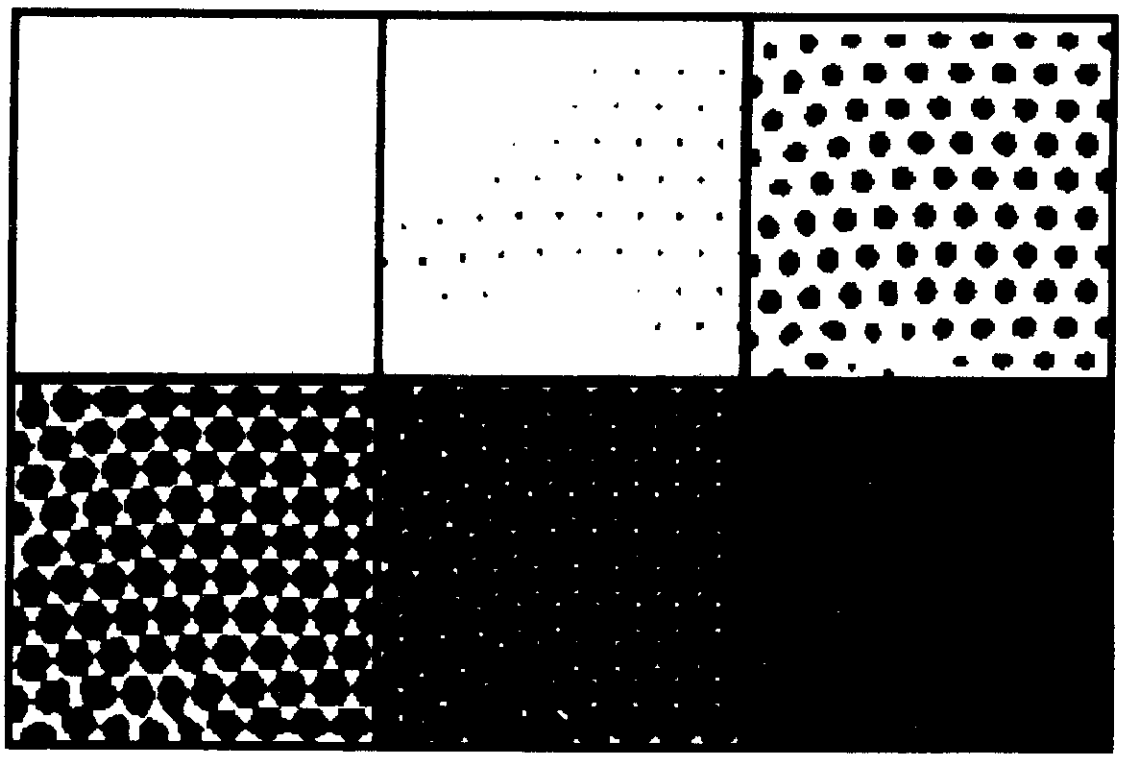

Fig 17

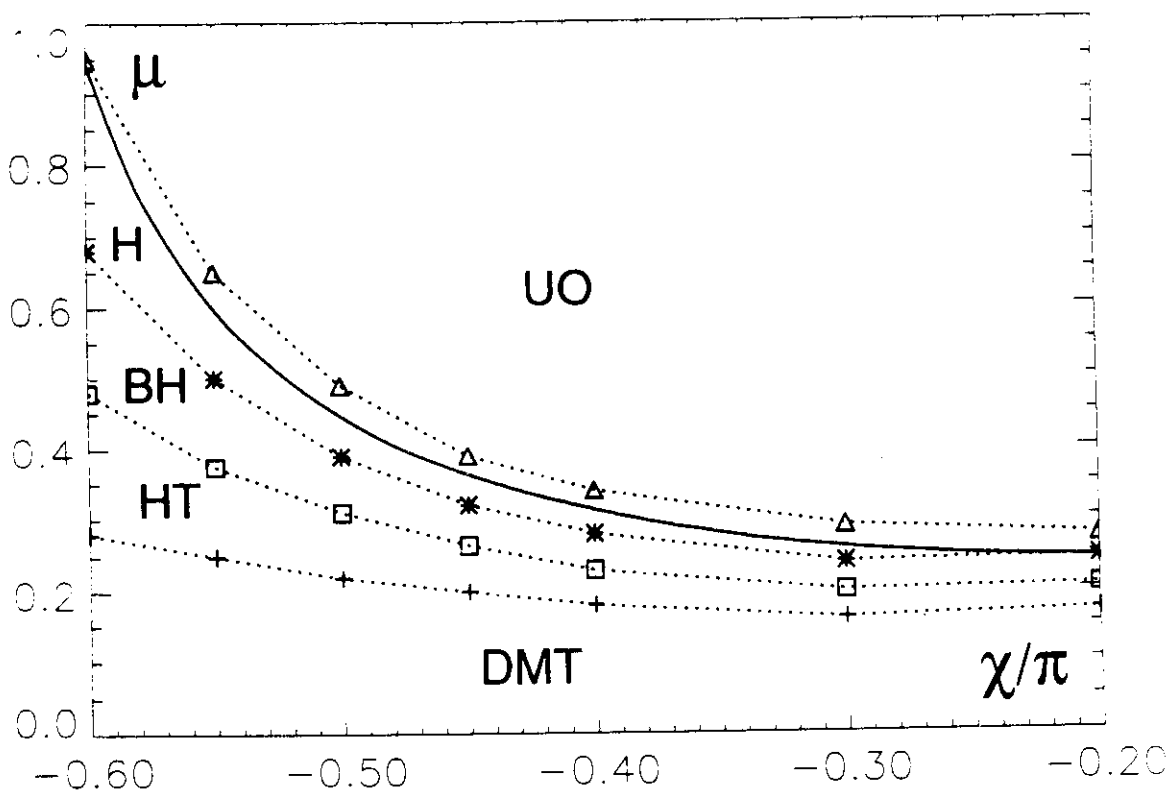
μ
H
BH
HT
UO
DMT
χ/π
0.8
0.6
0.4
0.2
0.0
−0.60
−0.50
−0.40
−0.30
−0.20

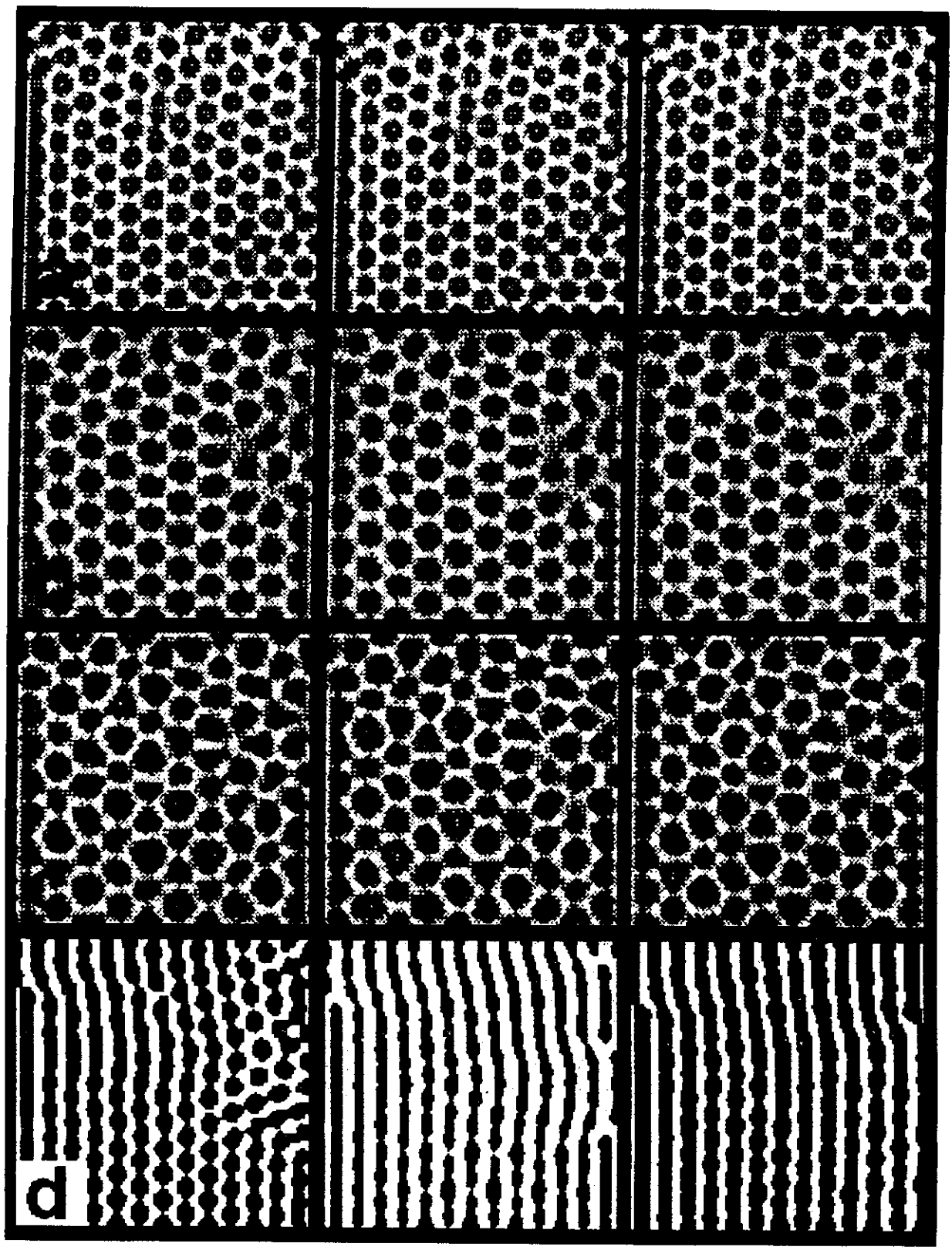
d

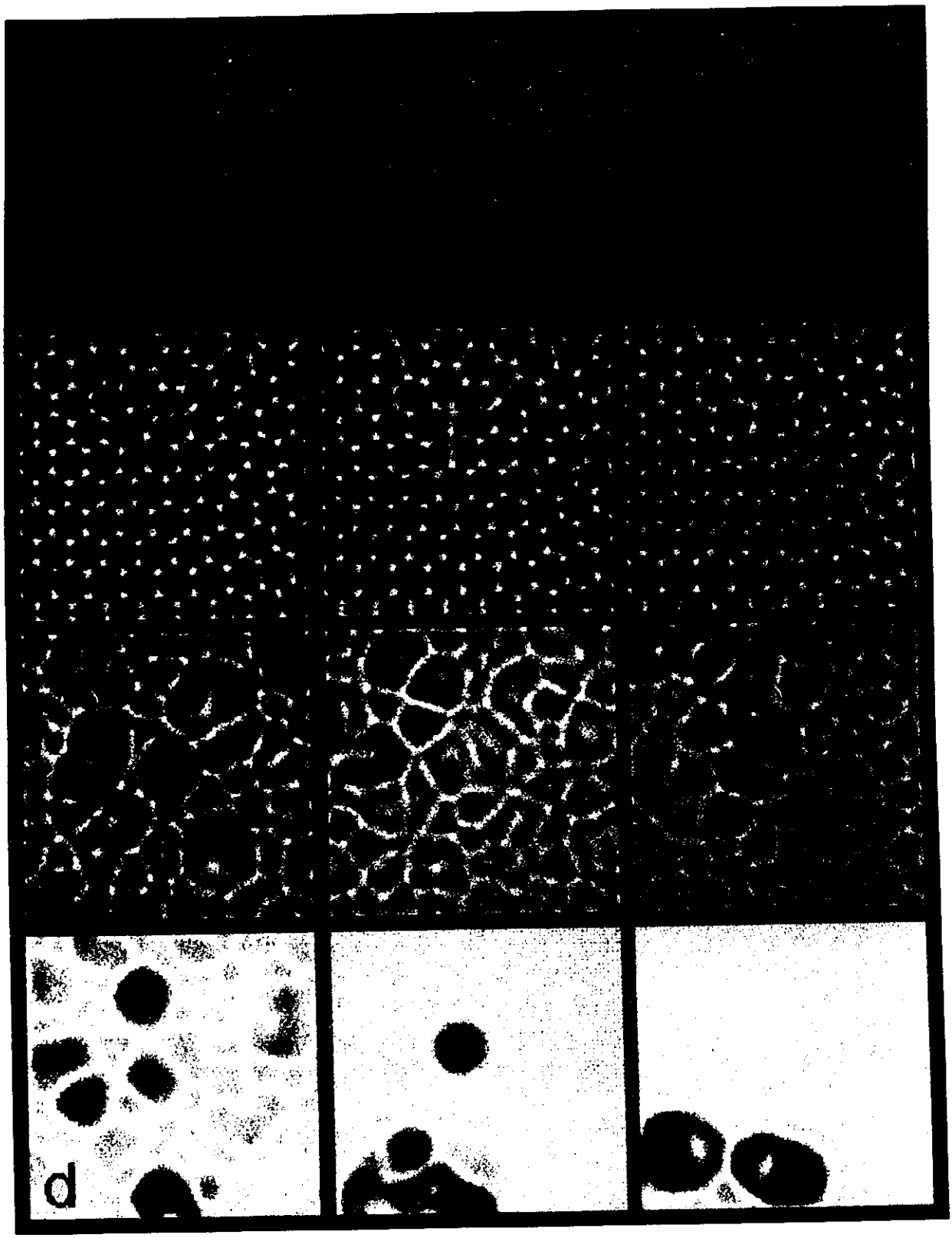

Fig 20

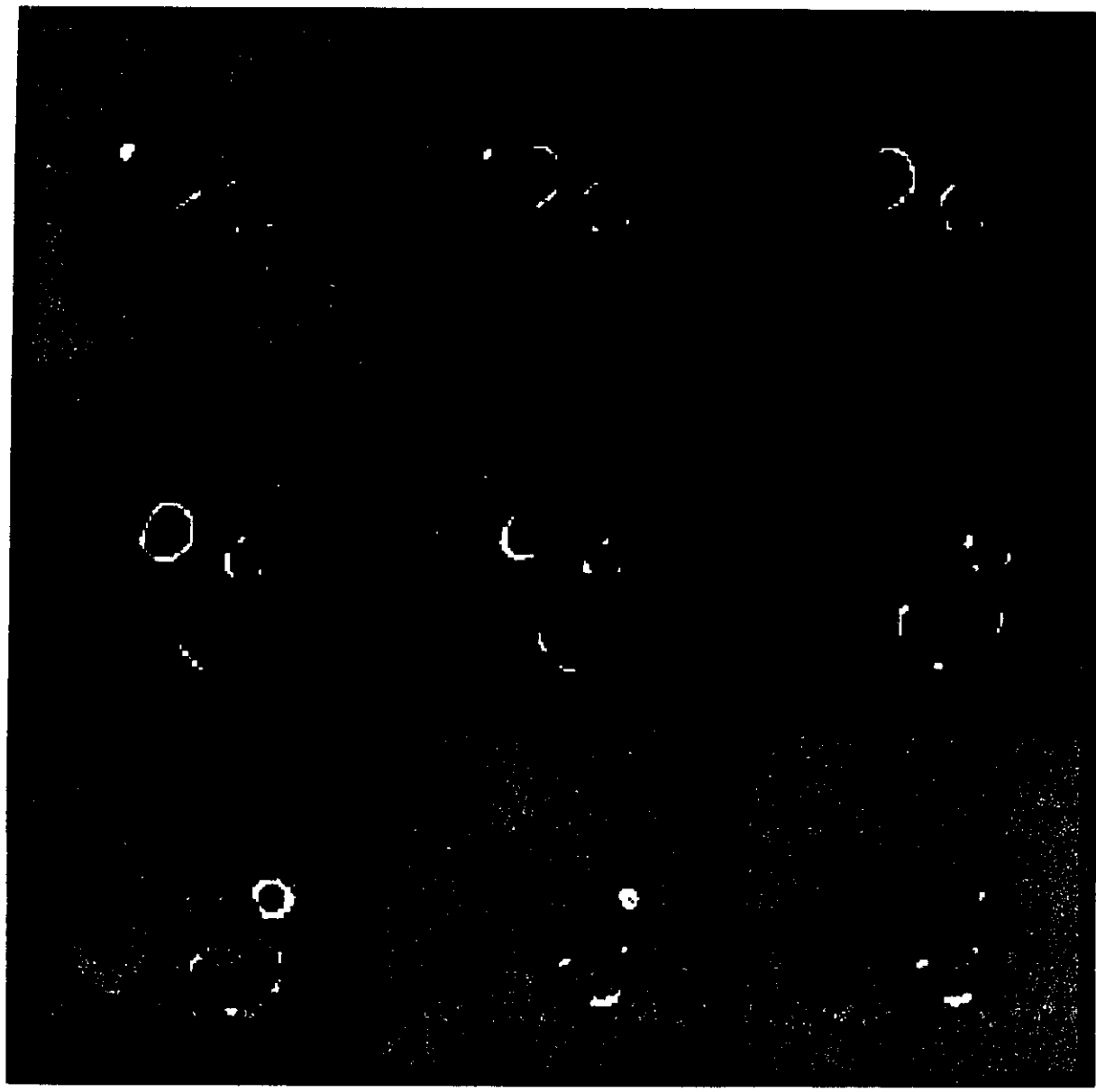

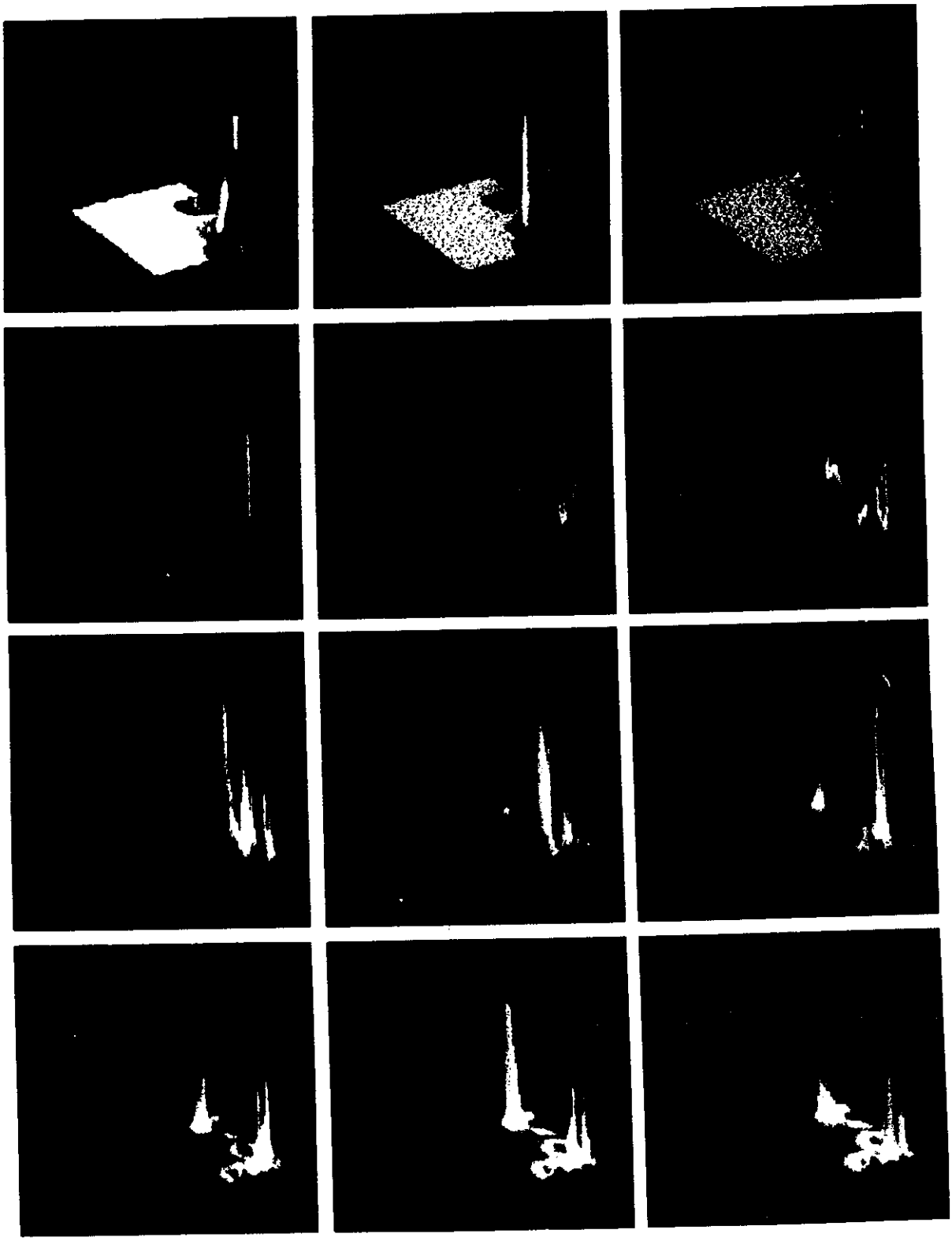

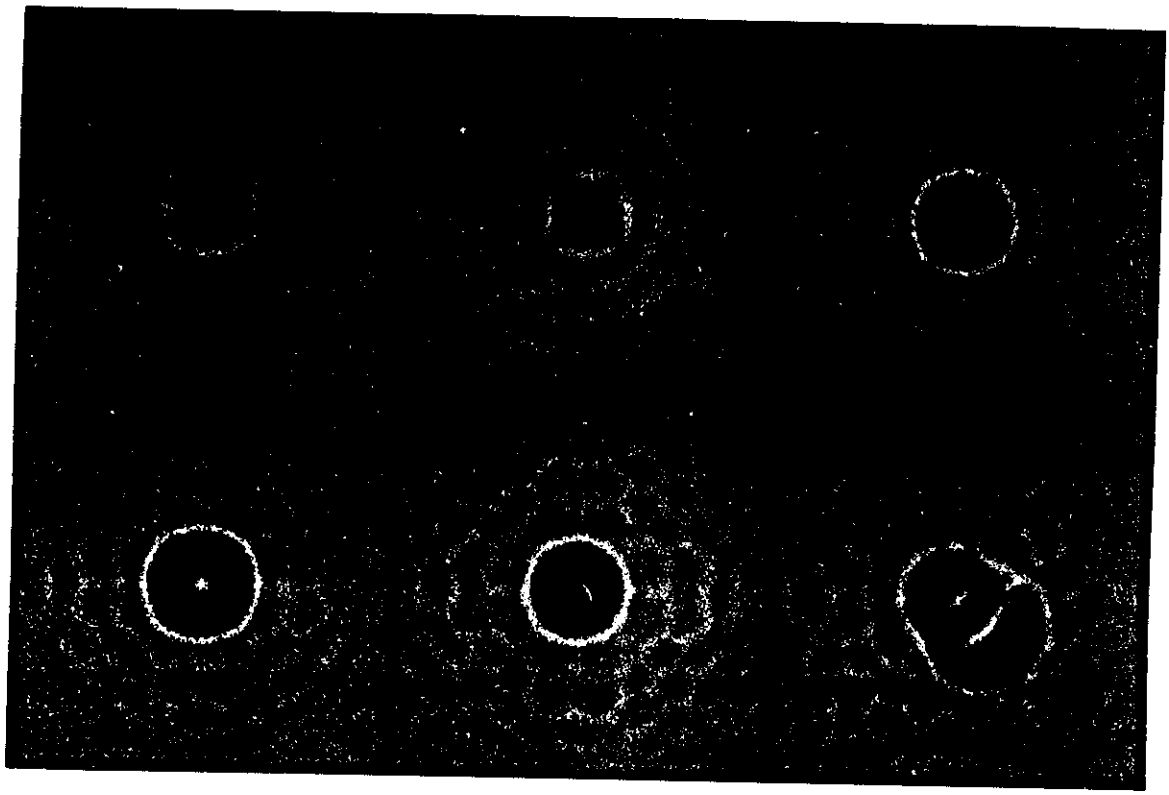

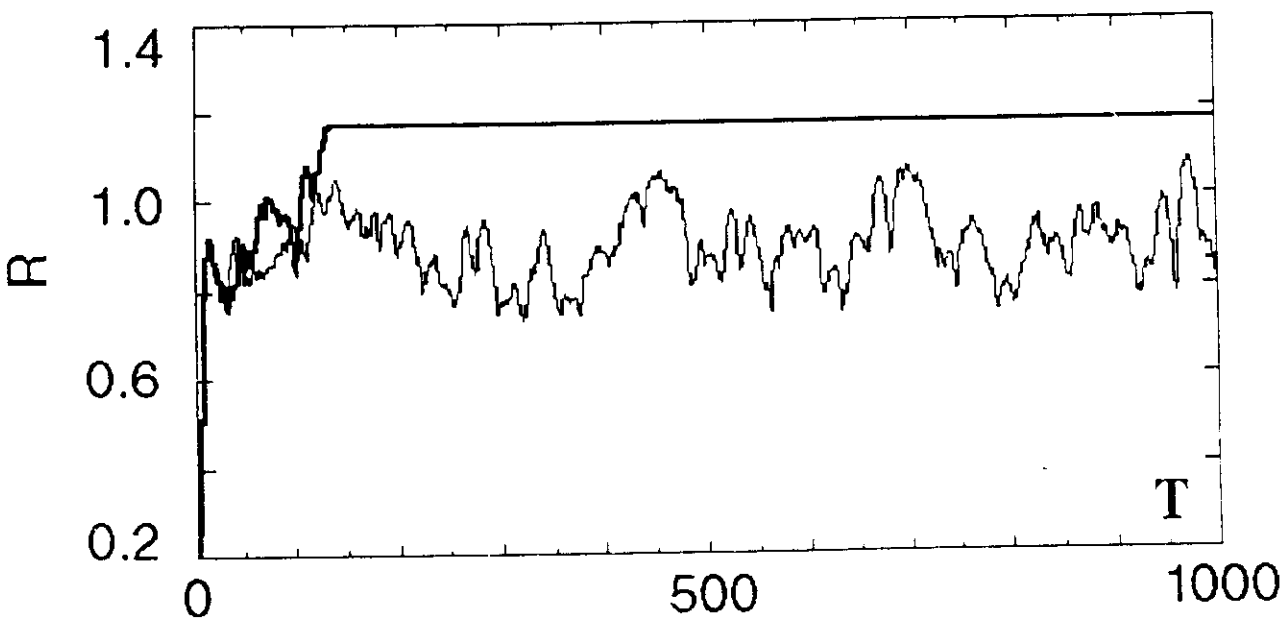
1.4
1.0
0.6
0.2
R
0
500
1000
T